

THE INFLUENCE OF COMPLEX TOPOGRAPHY ON AEOLIAN SEDIMENT
ACCUMULATION AND PRESERVATION: AN INVESTIGATION OF
MORPHOLOGY AND PROCESS HISTORY

Thesis submitted for the degree of

Doctor of Philosophy

at the University of Leicester

by

Alex Hay

School of Geography, Geology and the Environment
University of Leicester

September 2017

Abstract

It has long been understood that topography has an important influence over systems of aeolian sediment transport, accumulation and preservation. There has, however, been a comparative lack of investigation into how aeolian sediment accumulation and preservation responds to the influences of complex topography and variable sediment sources at a landscape (rather than landform) scale. Using the Mojave Desert, California, as a case study, this study demonstrates that the distribution and form of aeolian deposits is related to the topography of the mountain block and is manifest as deposits which represent three accommodation space types, each having a characteristic morphology (sand ramps, sand sheets and valley-fills). The observed aeolian morphologies cannot necessarily be delimited into a discrete patchwork of landforms because, in many cases, they lack distinct boundaries and because of the close association of the different accommodation space types within the landscape. Observed aeolian deposits range from thin veneers of sand to significant (>15m) deposits with visible sections. A series of ages derived from luminescence dating indicate that the aeolian system has operated across the majority of the last 80ka and can be associated with variations in sediment supply and availability. After deposition, topographically-anchored aeolian deposits can be (though are not necessarily) highly persistent features within the landscape, with their preservation potential also related to their accommodation space. Across this time, coarse-grained sediments appear as event-based and highly localised deposits which inter-finger with the predominantly aeolian sediments, indicating that the processes operated contemporaneously rather than switching between states of aeolian and hillslope process dominance.

Acknowledgements

I would like to thank my supervisors, Mark Powell, Andy Carr and Ian Livingstone for their help and guidance throughout my time undertaking this research. I would like to acknowledge to the Natural Environmental Research Council and the University of Leicester for funding this project. Thank you to Simon Benson for his assistance on field work and to Nick Marsh, Tiff Barry, Mike Norry, Colin Cunningham and Adam Cox of the School of Geography, Geology and the Environment at the University of Leicester for their valued assistance with undertaking and interpreting laboratory samples. Thanks also to Rob Fulton and Jason Wallace of the Desert Studies Center (California State University) for their local knowledge and help with fieldwork logistics during this project's two field seasons. In addition, I would like to thank my friends (particularly Hannah, Helena and Ros) and family for their support over the course of this project and, of course, thanks to Emma, for everything.

Table of contents

Abstract	i
Acknowledgements	ii
Table of contents	iii
List of figures	vii
List of tables	xiv
List of abbreviations	xv
1 Introduction	1
1.1 Background	1
1.1.1 Limitations of previous work and research opportunity	2
1.2 Project aim	3
1.3 Thesis outline	3
2 Context for study	5
2.1 Influence of topography on aeolian sediment transport	5
2.1.1 Influence of topography on aeolian process operation	5
2.1.2 Conceptualising topographically-influenced aeolian systems	9
2.1.3 Mapping, identifying and characterising aeolian deposits within the landscape	10
2.2 Determining landscape history in an aeolian system	13
2.2.1 Process history	13
2.2.2 The relationship of process history to boundary conditions	14
2.2.3 The utility of timings of process (in)activity	16
2.3 Objectives:.....	17
3 Field site	18
3.1 The Mojave Desert	18
3.1.1 Aeolian deposits within the Mojave Desert	19
3.1.2 Sand transport corridors	21
3.1.3 Cady Mountains aeolian system	22
3.1.4 Sampling locations.....	22
3.2 Geomorphological setting for study area	24
3.2.1 Geology	24
3.2.2 Contemporary climate.....	25
3.2.3 Palaeoclimate	26
3.2.4 History of palaeo lakes in the eastern Mojave Desert	32

3.3	Influences on geomorphic processes.....	35
3.3.1	Sediment generation	35
3.3.2	Sediment supply.....	35
3.3.3	Sediment availability	38
3.3.4	Sediment transport	40
3.4	Summary	41
4	Methods	42
4.1	Determining the distribution of land cover	42
4.1.1	Data sources and preparation	42
4.1.2	Mapping of land cover using remote sensing data	42
4.2	Mapping surface morphometry	47
4.2.1	Data sources and processing	47
4.2.2	Morphometric parameter determination	47
4.2.3	Scale of analysis.....	49
4.2.4	Analyses.....	51
4.3	Developing a record of process history.....	52
4.3.1	Stratigraphic logs	52
4.3.2	Sediment mineralogy	52
4.3.3	Textural analysis	52
4.4	Luminescence dating.....	53
4.4.1	Fundamentals of luminescence dating.....	53
4.4.2	Considerations for D_e determination	54
4.4.3	Sampling and laboratory protocols for D_e determination.....	56
4.4.4	Determination of the environmental dose rate.....	57
4.5	Summary	59
5	Developing the luminescence dating protocol.....	61
5.1	Quartz luminescence dating	61
5.1.1	Analysis of the quartz OSL signal	62
5.1.2	Composition tests.....	65
5.1.3	The fast ratio as a means to identify reliable quartz aliquots/grains.....	67
5.1.4	Quartz equivalent dose.....	68
5.1.5	Summary	70
5.2	K-Feldspar luminescence dating	71
5.2.1	Bleaching of the post-IR IRSL signal.....	71
5.2.2	Mitigating the effects of anomalous fading	74
5.2.3	Dose-recovery test	78

5.2.4	Additional protocol considerations	78
5.2.5	Summary	82
5.3	Comparison of derived equivalent doses at two sites with independent age control	83
5.3.1	Silver Lake	83
5.3.2	Harper Lake	88
5.4	Deriving equivalent dose estimates	92
5.4.1	Observations of D_e scatter	92
5.4.2	Identifying incomplete bleaching using single grain analysis	94
5.4.3	Summary	99
6	Morphometry of aeolian deposits within the Cady Mountains.....	101
6.1	Large-scale topographic control over the spatial distribution and form of aeolian deposits	101
6.1.1	Large-scale description of the landscape	101
6.1.2	The distribution and form of land cover	105
6.1.3	Relationship between the distribution and form of aeolian deposits and topography	116
6.1.4	Conceptualisation of the large-scale topographic control over the spatial distribution and form of aeolian deposits	117
6.2	Meso-scale morphology and landform classification of aeolian deposits	118
6.2.1	Accommodation space types as a framework for landform investigation	118
6.2.2	Identification and delimitation of distinct landforms between accommodation space types	122
6.2.3	Summary	137
6.3	Synthesis	137
7	Stratigraphy and Geochronology.....	139
7.1	Description and process history from field sites	139
7.1.1	Field sites	139
7.1.2	Geochronology.....	140
7.1.3	Stratigraphic description	142
7.1.4	Textural characteristics and structure of deposits.....	154
7.2	Operation of the aeolian system.....	158
7.2.1	Age-based landscape description.....	159
7.2.2	Timings within the aeolian system	161
7.2.3	Sediment provenance	163
7.3	Process history of the Cady Mountains.....	164
8	Discussion	165

8.1	The relationship between the distribution and form of aeolian deposits and topography.....	165
8.1.1	Distribution	165
8.1.2	Morphology of aeolian deposits within accommodation spaces	166
8.2	Landscape history for the Cady Mountains	167
8.2.1	Updated history of aeolian activity in the region.....	168
8.2.2	Drivers for aeolian deposition and preservation	169
8.3	The influence of complex topography on aeolian deposition and landform development	173
8.3.1	Role of accommodation spaces.....	174
8.3.2	Morphology of landforms	174
8.3.3	Hillslope sediment	176
8.3.4	Landform persistence / preservation.....	177
8.3.5	Summary	179
8.4	Broader considerations	179
8.4.1	Approach.....	179
8.4.2	Timing of lake stands.....	180
9	Conclusions	181
10	References.....	183
11	Appendix.....	208

List of figures

Figure 2.1: Accommodation spaces are locations within the landscape which result from the interaction between the underlying topography and the dominant wind flow pattern. They promote the deposition of aeolian material into landforms, although this process is dynamic as sediment accumulation can be episodic and/or degradation can re-open accommodation spaces within the landscape – with this figure being intended as a representative example where $t = 1$ through $t = 4$	6
Figure 3.1: Location map for this study (main) and its setting within the SW USA (inset). Map data © OpenStreetMap contributors.....	19
Figure 3.2: Aeolian landforms of the central Mojave Desert (Lancaster and Tchakarian, 1996; Lancaster and Tchakarian, 2003). Landsat-8 image courtesy of the U.S. Geological Survey. Map data © OpenStreetMap contributors.	21
Figure 3.3: Map of the nine field sites discussed in this study. Landsat-8 image courtesy of the U.S. Geological Survey. Map data © OpenStreetMap contributors.	23
Figure 3.4: Mean monthly temperature and precipitation data at Barstow (Daggett Airport). Source: NOAA.....	25
Figure 3.5: Contemporary winds within the region are largely from the west, however the effect of topographic steering funnels winds east of Barstow before they separate either across the Cady Mountains or towards the Bristol Playa. Note the northerly wind which travels across Soda Lake to the Kelso Dunes. Wind data adapted from Berry <i>et al.</i> (1981) and ventifact records adapted from Laity (1992). Map data © OpenStreetMap contributors.....	27
Figure 3.6: Moisture sources for the south-western USA referenced in the text. Map data © OpenStreetMap contributors.	29
Figure 3.7: Regional climate synthesis for SW USA lake high stands. Lake high stands show a broad trend of north-south migration in general accordance with the approximate latitude of the NAPJ (records shown: Benson <i>et al.</i> , 2003; Kirby <i>et al.</i> , 2006; Benson <i>et al.</i> , 2011; Reheis <i>et al.</i> , 2012; Benson <i>et al.</i> , 2013; Garcia <i>et al.</i> , 2014; Reheis <i>et al.</i> , 2015) (discussed in the text). The Devil’s Hole speleothem record (lower) (Winograd <i>et al.</i> , 1992; Winograd <i>et al.</i> , 2006) indicates first order variability coherent with trends in Northern Hemisphere summer insolation, global ice volume and global temperature (Martinson <i>et al.</i> , 1987), albeit with a divergence in the timing of the last deglaciation (Moseley <i>et al.</i> , 2016).	30
Figure 3.8: Climatic history for the Manix Basin and related surroundings for the past 120ka. Lake Manix high stand data from Reheis <i>et al.</i> (2012) and Reheis <i>et al.</i> (2015). The SW USA responds to glacial-interglacial cycles, as emphasised by the Devil’s Hole speleothem reconstruction (Winograd <i>et al.</i> , 1992; Winograd <i>et al.</i> , 2006).....	31
Figure 4.1: A subset of the Landsat 8 image of the study region prepared using the EMI false colour composite described in the text (Khiry, 2007). Yellow, blue and red colours correspond to sand, rock and vegetation. Landsat-8 image courtesy of the U.S. Geological Survey.....	44

Figure 4.2: Spectrum of land cover classes observed in the Cady Mountains. Surfaces range from an almost pure sand cover (a) through sands with a stone cover (b) to surfaces of bedrock and/or stones (c). Schematic representation of the relationship between these covers (brown line = stone cover; yellow line = sand cover) is shown (lower).....	45
Figure 4.3: Six morphometric feature classes (modified from Wood, 1996). Pits are excluded from discussion as they account for a negligible proportion of the land surface (0.17%).	48
Figure 4.4: Morphometric classification of a section of the Cady Mountain block performed using three different maximum window sizes: a) 11x11, b) 41x41 and c) 67x67. Landsat-8 image and National Elevation Dataset courtesy of the U.S. Geological Survey. Map data © OpenStreetMap contributors.	51
Figure 4.5: Comparison of U, Th and K derived using ICP-MS/XRF and in-situ gamma spectrometer.	58
Figure 5.1: Aggregate values of recuperation (left) and recycling ratios (right) for quartz SAR data for 120 aliquots.....	63
Figure 5.2: Examples of quartz shine down curves for samples (a) CN13-1-2, (b) SM13-3-1 and (c) HL14-1-1 which highlight the variation in behaviour of quartz grains which exist across the Mojave Desert samples. Sample (a) is an example of the bright quartz signal which is dominated by the fast component similar to that commonly reported for many environments. Conversely, sample (c) is a much dimmer signal which suggests significant contributions from medium and slow signal components which can make the sample unsuitable for dating using the SAR protocol.	64
Figure 5.3: Composition test for samples from this study performed using the method outlined by Lawson <i>et al.</i> (2015). The most quartz-like behaviour plots close to 1,1 and the most feldspar-like behaviour plots close to 0,0. For comparison data are shown for samples as follows: MD1-1 and ROB2 - South African coastal aeolianite, S1A1 - active dune sands in the Venezuelan Llanos savannas (Carr <i>et al.</i> , 2016). Data for non-Mojave Desert samples provided by A. Carr, unpublished data unless stated otherwise. KAZ and ROB samples show typical bright fast-component-dominated quartz signals and are shown to agree with an independent ¹⁴ C chronology.	66
Figure 5.4: The relationship between equivalent dose (D_e) and fast ratio rejection threshold for six exemplar samples. Where a trend can be established it suggests that the D_e derived using the standard SAR protocol is an underestimate of the ‘true’ D_e . The samples shown here are CN13-1-2 (a) CN13-4-1 (b) CN13-7-1 (c) PK14-1-1 (d) DN14-1-1 (e) HL14-1-1 (f) SM13-1-1 (g) and SM13-3-1 (h).....	69
Figure 5.5: When samples were bleached in natural daylight the equivalent dose decreased with time such that the original signal had reduced by >80% after 1-2 hours of exposure. The samples CN13-5-1 (a), HL14-1-1 (b), SL14-3 (c) and SM13-3-1 (d) are shown and were measured using the pIR-IRSL _{50,225} protocol.	72
Figure 5.6: Residual and D_e values for samples from this study. The dotted horizontal line represents the central age for a surficial (~0.3m) sample from a contemporary Mojave River barchan dune which is assumed to be a ‘modern analogue’	73

Figure 5.7: g-values for samples used in this study calculated for the IR ₅₀ and pIR-IRSL _{50,225} protocols. Figure 5.8	76
Figure 5.9: Equivalent dose for samples measured using both the pIR-IRSL _{50,225} and pIR-IRSL _{50,290} protocols.	77
Figure 5.10: Dose-recovery values for samples measured by this study using the pIR-IRSL _{50,225} protocol. All samples were able to recover a known dose within a 10% uncertainty.	78
Figure 5.11: Preheat plateau test for samples CN13-5-1 (a), HL14-1-1 (b), SL14-3 (c) and SM13-3-1 (d).....	79
Figure 5.12. The relationship between equivalent dose (D _e) and test dose size is shown for samples CN13-2-1, CN13-4-1, HL14-1-1, and SL14-1-1. The grey band highlights the size of an acceptable recovery ratio for the given dose of 57.5Gy (±10%), except for SL14-1-1 where the grey band indicates the last lake high stand and the dashed box represents the preceding low stand (Kirby <i>et al.</i> , 2015).	82
Figure 5.13: Stratigraphy (upper) for the measured section at Silver Lake showing the two luminescence sample locations alongside the range of uncalibrated radiocarbon dates reported by Owen <i>et al.</i> (2007). The image (lower) shows the sampling location where the lake floor is to the left of the photo (continuing out of shot), with the quarry exposures lower centre and the spit extending out to the right.....	84
Figure 5.14: Radial plots for samples SL14-1-1 and SL14-1-2 derived using the pIR-IRSL _{50,225} signal (upper). Single grain pIR-IRSL _{50,225} and single aliquot IRSL ₅₀ data are also shown for sample SL14-1-1 (lower).	85
Figure 5.15: SL14-1-1 single grain D _e plotted with ranked grain sensitivity does not appear to show the “declining baseline” described by (Rhodes, 2015) (discussed in the text).	86
Figure 5.16: Site views looking west along the outcrop at Harper Lake (upper) and stratigraphic diagram for the measured section (lower) showing the two luminescence sample locations alongside the geochronology reported by Garcia <i>et al.</i> (2014).....	88
Figure 5.17: K-feldspar ages for HL14-1-2 as derived using three different measurement protocols.	89
Figure 5.18: Radial plots for samples HL14-1-1 and HL14-1-2 derived using the pIR-IRSL _{50,225} signal (upper). Single grain pIR-IRSL _{50,225} and single aliquot IRSL ₅₀ data are also shown for samples HL14-1-2 and HL14-1-1 respectively (lower). The brightest grain represents the grain with the largest net-signal response to the first test dose.	90
Figure 5.19: Single aliquot radial plots for samples (a) CN13-2-1, (b) CN13-3-1, (c) CN13-4-1 and (d) CN13-5-1.....	93
Figure 5.20: Single aliquot radial plots for samples (a) DN14-1-1, (b) DN14-2-1, (c) DN14-3-1 and (d) DN14-4-1.	94
Figure 5.21: Single grain radial plots for the samples CN13-2-1 (a), CN13-3-1 (b), CN13-4-1 (c) and CN13-5-1 (d).	96
Figure 5.22: Single-grain equivalent dose distributions for samples CN13-2-1 (a), CN13-3-1 (b), CN13-4-1 (c) and CN13-5-1 (d) derived using the post-IR IRSL _{50,225}	

protocol. Samples are plotted in decreasing rank order of sensitivity and where samples with filled red symbols (i.e. those until the declining base has decreased by 15%) are those used in D_e determination. The method for D_e determination is described in the text and follows the approach of Rhodes (2015). The dashed line is intended as a guide to highlight the declining base phenomena visible within the four samples displayed here..... 99

Figure 6.1: Shaded DEM of the topography of the Cady Mountains in southern California which shows the study area, the course of the contemporary Mojave River and the location of the former Palaeo Lake Manix bed and fan-delta. Lake Manix high stand data as described in Reheis and Redwine (2008). DEM source: National Elevation Dataset courtesy of the U.S. Geological Survey. Map data © OpenStreetMap contributors. 103

Figure 6.2: Morphometric characteristics of the Cady Mountains. a) Hypsometric curve noting the level of the most recent Lake Manix high stand, (b) distribution of slopes, (c) aspect of surfaces with a slope angle of greater than two degrees and (d) classification of the mountain block by six morphometric classes. 104

Figure 6.3: Morphometric feature classification for the Cady Mountains. Landsat-8 image and National Elevation Dataset courtesy of the U.S. Geological Survey. Map data © OpenStreetMap contributors. 105

Figure 6.4: Land cover map for the Cady Mountains. Landsat-8 image courtesy of the U.S. Geological Survey. Map data © OpenStreetMap contributors. 106

Figure 6.5: Photographs of the land surface at two locations classified as being Stone-Covered Sands. The upper photograph is from the eastern flank of the Cady Mountains and the lower image is from the Valley Center Road area (Figure 6.22) within the western half of the mountain block..... 107

Figure 6.6: Distribution of land cover with elevation within the Cady Mountains. 108

Figure 6.7: Variation in land cover type with aspect. Areas with a slope angle of less than two degrees were considered to have no discernible aspect. Percentages are stacked so that they sum to 100%. 109

Figure 6.8: Spatial distribution of land cover classified by aspect. a) Sand Cover, b) Stone-Covered Sands, c) Rock Surfaces). Aspect of areas identified as having either a Sand Cover, Stone-Covered Sands or Rock Surfaces land cover are shown as a) to c) respectively. Slopes $<2^\circ$ were classed as having no overall aspect. 110

Figure 6.9: Percentage land cover for differing slope angles. Percentages are stacked so that they sum to 100%. 111

Figure 6.10: Percentage land cover for morphometric feature classes within the Cady Mountains. Percentages are stacked so that they sum to 100%. 113

Figure 6.11: Percentage land cover of valleys with differing orientation where percentages are stacked so that they sum to 100% (a). Orientation of valleys within the Cady Mountains as Figure 6.2b. 113

Figure 6.12: Variation in land feature classification within areas of the landscape covered by (a) Sands, (b) Stone-Covered Sands, and c) Rock Surfaces. Landsat-8 image

and National Elevation Dataset courtesy of the U.S. Geological Survey. Map data © OpenStreetMap contributors.....	114
Figure 6.13: Three accommodation space types which represent the principal forms of aeolian deposits within the Cady Mountains.	118
Figure 6.14: Morphometric feature classification for areas determined as being a Mountain Front accommodation space type.	119
Figure 6.15: Morphometric feature classification for areas determined as being a Plain accommodation space type.	120
Figure 6.16: Morphometric feature classification for areas determined as being a Valley accommodation space type.	120
Figure 6.17: Morphometric feature classification for areas determined as being a Composite accommodation space type.	121
Figure 6.18: The following section contains several figures which highlight the variability in the morphology of aeolian accumulations across the Cady Mountains. The locations for these figures within the mountain block. Landsat-8 courtesy of the U.S. Geological Survey. Map data © OpenStreetMap contributors.	122
Figure 6.19: Morphology of aeolian deposit at Soldier Mountain. Landsat-8 image courtesy of the U.S. Geological Survey.....	123
Figure 6.20: Photographs to illustrate the morphology of aeolian accumulation against an unnamed mountain - here referred to as ER. Landsat-8 image courtesy of the U.S. Geological Survey.....	124
Figure 6.21: Photographs to illustrate the morphology of aeolian accumulation against an unnamed mountain - here referred to as MC. Landsat-8 image courtesy of the U.S. Geological Survey.....	125
Figure 6.22: Photographs to illustrate the morphology of aeolian accumulation against an unnamed mountain - here referred to as PK. Landsat-8 image courtesy of the U.S. Geological Survey.....	126
Figure 6.23: Photographs to illustrate the morphology of an aeolian deposit which has developed within an unnamed valley – here referred to as RD. Landsat-8 image courtesy of the U.S. Geological Survey.....	128
Figure 6.24: Photographs to illustrate the morphology of aeolian deposit which have filled an unnamed valley – here the landform is referred to as WC. Landsat-8 image courtesy of the U.S. Geological Survey.....	129
Figure 6.25: Sediments have accumulated within a number of valleys which have coalesced into what may be considered to be either one or a number of landforms. Photographs illustrate the strong variability in morphology which are visible, even within small areas. Landsat-8 image courtesy of the U.S. Geological Survey.....	130
Figure 6.26: A broad and open plain contains a low-relief dune field whose surface is sandy. Many of the creosote bushes exhibit protruding root systems (a), suggesting recent deflation from this surface. Landsat-8 image courtesy of the U.S. Geological Survey.	131
Figure 6.27: A broad and open plain capped by a surface which varies from Sand Cover towards the south to Stone-Covered Sands towards the north. The plain has an	

undulating shape towards the extreme south of the area, with the raised areas commonly showing evidence of W-E aligned ventifaction b) and c). Landsat-8 image courtesy of the U.S. Geological Survey..... 132

Figure 6.28: Photographs to illustrate the morphology of aeolian accumulation against an unnamed mountain and which continues into a number of small but steep-sided valleys – here referred to as CN. Landsat-8 image courtesy of the U.S. Geological Survey..... 134

Figure 6.29: A broad and open plain contains a low-relief dune field whose surface is sandy. This sandy surface wraps up into a sand-covered planar surface to the south. Landsat-8 image courtesy of the U.S. Geological Survey..... 135

Figure 6.30: This area of topography is morphometrically complex as it contains areas of planar, plain and valley shapes which exhibit a combination of Sand Cover and Stone-Covered Sand surfaces. Here the area is referred to as MF. Landsat-8 image courtesy of the U.S. Geological Survey..... 136

Figure 7.1: Map of the nine field sites discussed within this chapter. Landsat-8 image courtesy of the U.S. Geological Survey..... 140

Figure 7.2: Stratigraphy of the aeolian deposit at CN. 143

Figure 7.3: Photographs showing the setting of the CN-Valley field site. 144

Figure 7.4: Stratigraphy of the aeolian deposit at DN. 145

Figure 7.5: Stratigraphy of the aeolian deposit at ER..... 146

Figure 7.6: Stratigraphy of the aeolian deposit at MC..... 147

Figure 7.7: Stratigraphy of the aeolian deposit at PK..... 148

Figure 7.8: Stratigraphy of the aeolian deposit at RD. 149

Figure 7.9: Photograph showing the interior of the sedimentary deposit at SM by profile A. Figure looking south-west (Figure 7.10)..... 150

Figure 7.10: Stratigraphy of the aeolian deposit at SM composed of two profiles (A&B). 151

Figure 7.11: Stratigraphy and geochronology of the aeolian deposit at WC..... 153

Figure 7.12: Grain size distribution data for the sedimentary units listed above. 154

Figure 7.13: Textural characterisation for the sedimentary units described in Section 142. Skewness and sorting parameters after Folk and Ward (1957). 155

Figure 7.14: Photograph showing the interior of the landform at Soldier Mountain indicating the location of profile B (Figure 7.10). 157

Figure 7.15: Lenses of pebbles, gravel and cobbles observed within the Complex Valley (described in Section 6.2) (upper and inset) and within the CN landform and adjacent (< 50m distance) to the sampled stratigraphy (lower). The lens shown in the upper figure shows evidence of cut-and-fill processes, with what appears to be an unconformity present within the close-up photograph (inset). 158

Figure 7.16: Geochronology for the field sites listed in Table 7.1. 159

Figure 7.17: The ratio of K₂O (representing K-Feldspar concentration) and CaO (representing Plagioclase feldspar) for Cady Mountain samples (squares). The typical range for granite or granodiorite sediments is plotted in a) and the range of distributions

reported by Muhs <i>et al.</i> (2003) and Muhs <i>et al.</i> (2017) for comparable deposits are shown as dashed shapes in b).	163
Figure 7.18: Ratios of K/Rb and K/Ba (which represent variability in K-Feldspar composition) for the sedimentary deposits of the Cady Mountains (squares) are shown against the ranges for comparable sediments from Muhs <i>et al.</i> (2003) and Muhs <i>et al.</i> (2017) (shaded shapes).	164
Figure 8.1: Landform classification based upon the three accommodation spaces types from Section 6.2.....	175

List of tables

Table 4.1: Error matrix for the land cover classification, adapted to only show the Sand Cover, Stone-Covered Sands, Rock Surfaces and Other land covers. Numbers in the upper grid relate to the number of validation locations which conform to each category.	46
Table 4.2: An example single-aliquot regenerative dose (SAR) protocol as adapted from (Murray and Wintle, 2000). As the sequence is repeated multiple times the ‘given dose’ (step 1) is varied during each run. During the first run the given dose is 0Gy (to capture the natural signal) and thereafter the given dose is varied during each subsequent run through a number of different doses to form a ‘dose-response curve’. Following this the sequence is repeated twice more using a given dose of 0Gy (to measure recuperation) and finally using a repeat of the given dose during the second run is given (to correct for sensitivity changes during the measurement of the sequence)...	55
Table 4.3: Dose rate data for the luminescence dating samples presented by this study for both quartz and feldspar grains.	60
Table 5.1: Equivalent doses and ages for quartz samples measured using the procedures described in the text. D_e values are presented after the fast ratio rejection criterion was applied and using early background subtraction (described in the text).....	70
Table 5.2: A protocol for measuring the rate of anomalous fading within feldspar samples where the preheat is administered before storage (as Auclair <i>et al.</i> , 2003).....	75
Table 5.3: A protocol for measuring determining whether D_e is independent of test dose size.	81
Table 5.4: Dosimetry data for samples at Silver Lake, CA, from this study with comparable data shown as reported in Owen <i>et al.</i> , 2007. Dose rates were derived independently from Owen <i>et al.</i> , but the values are comparable.	87
Table 5.5: Dosimetry data (measured independently) for samples at Harper Lake, CA, from this study with comparable data shown as reported in Garcia <i>et al.</i> , 2014.....	91
Table 5.6: Equivalent dose (D_e) and age values for five samples from CN derived using single-aliquot and single-grain methods.	98
Table 7.1: Equivalent dose (D_e), fading correction (g-values) and ages for the samples discussed in this study. The fading-corrected age is preferred where it is written in black text, otherwise the fading uncorrected age is preferred (see Section 5.2 for justification). Samples CN13-1-2 to CN13-4-1 inclusive are derived using single-grain ages (see Section 5.4).	141
Table 7.2: Synthesised history of (in)activity within the aeolian system operating across the Cady Mountains during the last 80ka, based on the evidence presented in Section 7.1.	160

List of abbreviations

CA	California
CAM	central age model
CaO	calcium oxide
D _e	equivalent dose
DEM	digital elevation model
D-O	Dansgaard-Oeschger
DRC	dose-response curve
EMI	eolian mapping index
GMT	Greenwich Mean Time
GPS	global positioning by satellite
HCl	hydrochloric acid
HF	hydrofluoric acid
H ₂ O ₂	hydrogen peroxide
ICP-AES	inductively coupled plasma atomic emission spectroscopy
ICP-MS	inductively coupled plasma mass spectroscopy
IR	infra-red
IRSL	infra-red stimulated luminescence dating
K	potassium
K ₂ O	potassium oxide
LGM	last glacial maximum
LPH	Late Pleistocene-Holocene transition
MAM	minimum age model
MIS	marine isotope stage
NAPJ	North American Polar Jet
NIR	near infra-red
NOAA	National Oceanic and Atmospheric Administration
OD	overdispersion
OSL	optically stimulated luminescence dating
pIR-IRSL	post-infrared infra-red stimulated luminescence dating
Rb	rubidium
RS	remote sensing
SAR	single aliquot regenerative
SGS	Société Générale de Surveillance
SST	sea surface temperature
SW	south-west
Th	thorium
U	uranium
UK	United Kingdom
USGS	United States Geological Survey
UV	ultra violet
USA	United States of America
XRF	x-ray fluorescence

1 Introduction

1.1 Background

Aeolian landforms are key components of many dryland environments and vary significantly in form across space and time. A fundamental distinction within aeolian landforms are those which are formed through erosional processes (e.g. the combined effect of abrasion and deflation by the wind flow can create yardangs – Mabbutt, 1977) and those that result from aeolian deposition (notably sand dunes) (Warren, 2013). Commonly-studied aeolian landforms include linear dunes, which can be hundreds of miles long (Lancaster, 1988; Fitzsimmons *et al.*, 2007), through to small and rapidly migrating barchan dunes (Vermeesch and Drake, 2008; Burrough *et al.*, 2012). Aeolian landforms can be classified into those that have accumulated by/against some fixed object (anchored dunes) and those which have not (free dunes) (Livingstone and Warren, 1996). Free dunes are self-organising systems whose form and pattern are strongly controlled by the directional variability of the wind and the quantity of transported sediment. The combined impact of these variables creates a range of responses which include barchan dunes which form under uni-modal wind regimes through to star dunes which form under complex and variable wind regimes (after Wasson and Hyde, 1983). Anchored dunes can form around fixed objects, from large topographic obstacles (termed topographic dunes, discussed below) to pieces of vegetation (e.g. Nebkah dunes) (Warren, 2013). Sand sheets are a form of depositional landform which possess a surface which is too coarse for saltation and typically lack bedforms (Mabbutt, 1977).

Topography constrains the routing and velocity of wind flow through the landscape which in turn (via surface shear stress) controls the location(s) of aeolian deposition/erosion (Pye and Tsoar, 1990; Wiggs *et al.*, 2002; Griffiths *et al.*, 2009). This relationship can be observed across numerous scales from the locations and morphology of dune fields and ergs that are driven by macro-scale topography to individual dunes (form and location) whose characteristics are closely related to the local topographic situation and often depend on the relative angle of incidence of the dominant sand-transporting wind (Wilson, 1973; Wiggs *et al.*, 2002). For a topographically-anchored dune to form, the topography and wind flow patterns must interact in a manner whereby a three-dimensional zone is created within which aeolian sediments can be deposited and any

landform preserved (over relevant timescales), termed an accommodation space (Tsoar, 1983). Additionally, winds must be directionally-persistent as topographically-anchored aeolian deposits do not tend to form where significant variability in sand-transporting direction exists (as this modifies the accommodation space) (Cooke *et al.*, 1993). Topographic dunes have been sub-categorised into those which accumulate upon the upwind and downwind side of a topographic obstacle (climbing and falling dunes respectively) or those which form immediately upwind or downwind of an obstacle (echo and lee dunes) (Evans, 1962; Livingstone and Warren, 1996). The occurrence of any one of these morphologies is closely related to the shape of the topography. The further controls on topographic dune morphology are discussed in Section 2.1.

1.1.1 Limitations of previous work and research opportunity

The influence of topography over aeolian deposition and preservation has been primarily investigated using a reductionist and/or highly localised approach, commonly by seeking to relate the existence of a discrete landform (or cluster of discrete landforms) to their surrounding topography (e.g. Evans, 1962; Rendell and Sheffer, 1996; Bateman *et al.*, 2012; Ventra *et al.*, 2017; Rowell *et al.*, in press). This has led to insights into the relationship between individual discrete landforms and their surrounding topography, be that dunes which have accumulated upon a topographic obstacle (e.g. climbing dunes) or those downwind of some topographic obstacle owing to the knock-on effects on local wind flow patterns. As an example of the latter, Xiao *et al.* (2014) showed a relationship between the form and size of aeolian deposits and the width of the pass between two topographic obstacles. Alternatively, investigation has been conducted at a very large scale where the topography has been viewed as something which bounds aeolian systems, dividing one aeolian system from another. Examples of such systems include the global-scale observations of ergs including Wilson (1973) as well as the pathways of aeolian sand described as flowing through the basins of the Mojave Desert (see Section 2.1.2) (e.g. Zimelman *et al.*, 1995; Clarke and Rendell, 1998). Between these scales, however, less investigation has occurred.

A principal issue is that, when considering the relationship between aeolian processes at a scale larger than that of a single dune and the topography upon/beside which it resides (for example across a whole mountain block), interpreting any relationship is more difficult because aeolian process feedback can be compounded and individual landforms

can coalesce, particularly where the topography is more complex (discussed in Section 2.1). Similarly there has been less examination of how topographically-anchored aeolian landforms develop and are preserved/evolve over long time scales (cf. Lancaster and Tchakerian, 1996; Thomas *et al.*, 1997; Kumar *et al.*, 2017; Rowell *et al.*, in press). Given this gap, it is significant that no study appears to have mapped patterns of aeolian deposition within an area of complex topography and tried to understand how the spatial distribution of aeolian deposits is related to the underlying topography.

1.2 Project aim

The above has provided some context for this study and poses a principal aim:

To understand how complex mountainous topography influences aeolian deposition, and landform development and preservation.

1.3 Thesis outline

To achieve the aim of this project, this thesis will adopt the following approach.

Chapter 2 will provide the context for the study, seeking to understand how topography influences the operation of the aeolian system across both space and time. It will focus on how aeolian systems respond to topography particularly with regards to where in the landscape aeolian sand is stored and preserved.

Chapter 3 justifies the geographical location of this study and provides an account of the boundary conditions of the study area. To this end, it outlines the macro-scale morphology of the landscape and provides a narrative of changes in the environmental conditions in this locale during the Late Pleistocene.

Chapter 4 outlines and justifies the methods adopted by this study. The chapter is divided into four sections which: consider the approach for mapping the surface cover of the study location (Section 4.1); characterise the morphology of the observed landform locations (Section 4.2); create a stratigraphic record which can be used to determine the process history for the aeolian system's location (Section 4.3) and provide timings to this process history using luminescence dating locations (Section 4.4).

Chapter 5 assesses the suitability of various luminescence dating approaches providing a geochronology for the study sites. Two locations with independent age controls for the

samples allowed direct testing of these methods and optimisation of the associated measurement protocols.

Chapter 6 considers the relationships between the occurrence and morphology of aeolian deposition within the Cady Mountains and the morphometry of the mountain block at two spatial scales. Section 6.1 demonstrates that there is some pattern to the distribution of sand at the mountain block scale. Section 6.2 shows that this does not translate into a landscape of unambiguously delimitable characteristic landforms at the meso-scale.

Chapter 7 will develop an understanding of the processes which have created the aeolian landforms observed within the study site and consider whether this relates to the accommodation spaces within which the landforms reside. This necessitated a stratigraphic and sedimentological description and also a geochronology for each of the field sites (Section 7.1). By collating these data across field sites, an understanding of how the process history of the aeolian system has operated can be developed (Section 7.2).

Chapter 8 seeks to develop an understanding of how complex mountainous topography influences aeolian deposition, and landform development and preservation. To achieve this, this section will bring together the outcomes of the preceding chapters and the boundary conditions in order to provide a landform classification.

Chapter 9 lists the principal conclusions of this study.

2 Context for study

This section outlines the current understanding of how aeolian systems respond to topography, particularly with regards to where in the landscape aeolian sand is stored and preserved. This chapter also discusses approaches to achieve the stated aim of the project, particularly with regards to: establishing the role of topography within an aeolian system and the characterisation of landforms (Section 2.1) and approaches to determining landscape history and fitting this into the wider boundary conditions (Section 2.2).

2.1 Influence of topography on aeolian sediment transport

Wind has long been understood as a significant driver of sediment transport in dryland environments and given a supply of sediment available for entrainment and a wind suitable for aeolian transport, sand will be transported downwind through the landscape over time (Kocurek and Lancaster, 1999). Such a model is, of course, a gross simplification which ignores the interplay of the many factors which influence sediment supply/availability and transport capacity (e.g. climate, vegetation cover, sediment supply/availability as well as the presence of any bedrock topography) (Howard, 1985; Lancaster, 1988). The net-result of these processes are a suite of characteristic landforms which develop and are subsequently modified and/or destroyed in an ever-evolving geomorphic system (Evans, 2012) and which at any point in time, constitute archives of the suite of processes which have acted upon them. This section discusses current understanding of how topography influences aeolian deposition and landform development (Section 2.1.1) as well as how these aeolian systems can be conceptualised within the landscape (Section 2.1.2).

2.1.1 Influence of topography on aeolian process operation

As outlined in the introduction, topography exhibits an influence on wind flow patterns, through topographic steering and variably promoting/inhibiting aeolian sediment deposition across the landscape. At the largest spatial scale, Wilson (1973) noted that the positioning of sand seas is related to the macro-scale topography of the region, terminating at defined breaks of slope and anchored by the topography by being confined in a basin (or basins).

Aeolian material which is transported through the landscape will be preferentially deposited at the first point(s) in the topography at which the interaction between wind

flow and the topography promotes deposition, termed an ‘accommodation space’ (term as adopted by Lancaster and Tchakerian, 1996; Bateman *et al.*, 2012; Rowell *et al.*, in press) (Figure 2.1). Because accommodation spaces result from the interaction between wind flow patterns and the bedrock topography, they are direction dependent and their location and size (and any landform that they contain) can alter given a changing wind regime (Cooke *et al.*, 1993). An accommodation space will fill with deposited material until a point of equilibrium is reached where material can no longer be deposited (Lancaster and Tchakerian, 1996), whereafter deposition will transfer on to the next accommodation space(s) downwind. It is uncertain whether material is preferentially deposited almost exclusively at a single/few accommodation space(s) or whether the rate of accumulation between accommodation spaces across a corridor is more even. If the former is the case, then a spatio-temporal pattern of aeolian accumulation is likely to be preserved downwind along the aeolian system. A distinction can be drawn between sand which accumulates against topographic obstacles which protrude into the aeolian transportation zone (i.e. positive topography such as mountain peaks and ridges) (e.g. Evans, 1962) and that of traps in the landscape such as topographic hollows and valleys (negative topography) (e.g. Ellwein *et al.*, 2015). Topography can also influence the formation of dune fields over a wider area where they form in broad natural hollows. For example, on Mars the effect of topography on wind flow in a number of craters has led to the formation of a characteristic dune field in these environments (Cardinale *et al.*, 2012). Variation in the above characteristics (themselves related to topography) drives the morphology of the aeolian deposits which form.

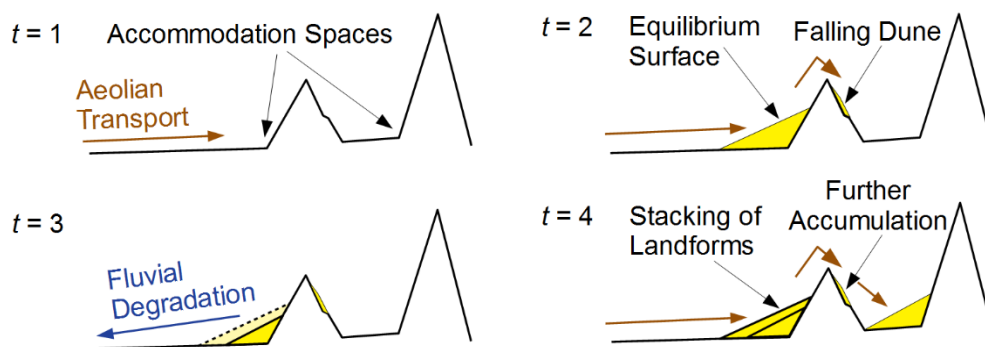


Figure 2.1: Accommodation spaces are locations within the landscape which result from the interaction between the underlying topography and the dominant wind flow pattern. They promote the deposition of aeolian material into landforms, although this process is dynamic as sediment accumulation can be episodic and/or degradation can re-open accommodation spaces within the landscape – with this figure being intended as a representative example where $t = 1$ through $t = 4$.

Where systems of aeolian sand transport interact with topography, landforms are often constructed in the accommodation spaces which this topography creates, with their simplest form being topographic dunes such as climbing and falling dunes (Chojnacki *et al.*, 2010; Warren, 2013). Climbing dunes are formed where the morphology of the landscape consists of a notable topographic obstacle with a 30-50° slope which is roughly perpendicular to the direction of aeolian sand-transport (Cooke *et al.*, 1993; Qian *et al.*, 2011). They typify an influence whereby the morphology of the topography slows the speed of the wind at the base of the mountain, promoting the deposition of sand at this point (Tsoar, 1983; Qian *et al.*, 2011). As the sand accumulates, the effect of the wind on deposition diminishes and sand accumulates on the windward slope until an equilibrium accumulation morphology results. In addition, where sand has accumulated enough for the wind to transport sand up and over a topographic obstacle (Zimbelman *et al.*, 1995), sand can be deposited on its leeward slopes as a falling dune owing to the expansion and separation of the wind flow after the wind has passed over the ridgeline of the mountain (Xianwan *et al.*, 1999; Xiao *et al.*, 2014). Where topographic dunes form appreciable pairs, some studies have differentiated between the climbing and falling components through a combination of understanding of the palaeowind regime such as ventifact evidence (discussed later) and because falling dunes are often steeper, smaller, higher up the topography and different in their grain size distribution and sorting parameters to climbing dunes (Evans, 1962; Lancaster and Tchakerian, 1996). Where they have a sand covered surface, sand ramps appear morphologically similar to topographic dunes, however they represent a different topographically-influenced landform. Bertram (2003: 1) described sand ramps as “sands banked up against mountain fronts or other topographical obstacles” which contain “a variety of sediments formed in different environments, including aeolian, fluvial and [mass movement] deposits”. Their composite structure means that sand ramps sit along a continuum of morphologies which range from topographic dunes (>90% sand) through sand ramps to small lenses of aeolian material within an alluvial fan (Lancaster and Tchakerian, 1996).

Where the slope of the topographic obstacle exceeds 50° then the creation of a standing vortex leads to the formation of echo dunes a short distance upwind of the topographic obstacle (Pye, 1994; Xianwan *et al.*, 1999; Qian *et al.*, 2011; Xiao *et al.*, 2014). Such scenarios only hold true where the ridgeline of any topography is approximately perpendicular to the dominant sand-transporting wind direction. Where the shape of the

landscape is more sinuous or the angle of incidence of the wind is smaller (Wiggs *et al.*, 2002), it is expected that sand will be transported along the mountain front until a point where it can form a climbing dune, or it will travel up and potentially fill gulleys in the mountain front (Cooke *et al.*, 1993). By extension, where a landscape is complex in its topography it is unlikely that simple topographic dune morphologies will develop. Rather a more complex pattern of topographically-anchored aeolian deposits will form where sand has accumulated in depressions and as valley-fills which have merged together. For example, Ellwein *et al.* (2015) described how pairs of climbing and falling dunes form in valleys which are cut into the broader landscape surface (negative topography) where such valleys are roughly perpendicular to the dominant direction of sand transport, owing to a trapping effect which results from the interaction of the topography and wind flow patterns.

The landforms described above occur where sand is deposited upon or within topographic obstacles. However, topography can also affect the accumulation of sand downwind of the obstacle owing to its effect on the wind flow regime, often forming lee or shadow dunes (Pye, 1994). For example, Xiao *et al.* (2014) observed how wind flow slows after leaving a mountain pass. This promotes deposition downwind of the pass where the characteristics of the landform and its distance downwind of the topography are a function of the morphometric shape of the topography. Lee dunes can form downwind of topographic obstacles which range in length from a few metres to tens of km long, depending on the topography (Livingstone and Warren, 1996). Such landforms highlight the large distances downwind which topography can influence the wind flow and hence the nature of sand transport and deposition. One of the major difficulties in establishing the downwind impact of topography on the wind flow (and hence the resultant aeolian accumulations) is that any topographically-induced effects can be super-imposed and compounded. Such an effect would be complicated further if the topography were complex. Accordingly, two previous studies explicitly describe similar areas which they perceived to be morphologically complicated as a result of their topographic situation. Bertram (2003: 29) distinguished *bona fide* sand ramps (my term) from what they describe as ‘*sand ramp complexes*’ around the Jagpan Mountains, Namibia, where they concluded that any attempt to ‘determine their exact number is a matter of opinion’ (thus implicitly requiring ‘proper’ sand ramps to be discrete landforms). Similarly, Telfer *et al.* (2014) noted that, where the topography is more subdued, sand ramps become

morphologically akin to a broad sedimentary cover, rather than discrete (as is the Cat Dune, California – Evans, 1962).

2.1.2 Conceptualising topographically-influenced aeolian systems

Aeolian processes are responsible for the creation of features which range from individual dunes through to enormous sand seas. Many different morphologies of aeolian bedform have been observed, characterised and mapped, with a broad classification for these being presented in Chapter 1. These scales exist as a spectrum, however, and often morphology can be considered as nested and existing at multiple scales simultaneously (Kocurek and Nielson, 1986). For example, though it can be helpful to perceive individual dunes as discrete landforms, they rarely exist in isolation and are often a part of a dune field. For example, barchan dunes commonly exist within corridors wherein they simultaneously act as individuals and interact with each other as a collective (e.g. calving and merging barchans – Bagnold, 1941; Elbelrhiti *et al.*, 2008; Worman *et al.*, 2013). Similarly the interaction between dune morphology and the regional wind flow has caused the Algodones Dune Field, California, to migrate eastwards as a whole body (Sweet *et al.*, 1988; Stokes *et al.*, 1997). Elsewhere, aeolian systems can form sand sheets which are typically low-relief, contain no slip faces or bed forms and can be very extensive and several metres deep (Kocurek and Nielson, 1986). These examples highlight the important association between the dune-scale and the landscape-scale and their interconnectedness in terms of aeolian process operation and feedback.

Dune fields are a common way of conceptualising an aeolian system, often primarily as depositional systems (Warren, 2013). Aeolian transport corridors are another approach to conceptualising aeolian systems of aeolian sediment transportation and deposition in dryland environments (notably Zimbelman *et al.*, 1995), being discussed principally with regards to the Basin and Range province of the SW USA but the idea is generally applicable (e.g. Silvestro *et al.*, 2010a; Yang *et al.*, 2014). They represent an integrated aeolian process system, best broken down into a source area, a zone of sediment transportation and a depositional sink (Zimbelman *et al.*, 1995; Clarke and Rendell, 1998; Chojnacki *et al.*, 2014; Yang *et al.*, 2014). These systems are related to sedimentary basins, the negative topography where the sediments weave along and between the available basin floors. Under such a situation any major topography exists as the boundary for the aeolian system, except for where topographic obstacles interrupt the ‘flow’ of

sediment along the corridors (e.g. Iron Mountains in the Bristol corridor or the Devil's Playground in the Mojave River-Kelso corridor – Zimbelman *et al.*, 1995). The concept of aeolian transport corridors owes its origins to large-scale observations of dune form made from satellite imagery and the associations between these observations of dune form with the locations of possible sediment source areas and the directions of prevailing regional winds (e.g. Zimbelman *et al.*, 1995). Since this period, the study of aeolian transport corridors has benefited greatly from attempts to quantify the system in various ways. These include studies that have sought to identify periods of sediment transport/reworking and accumulation/storage (Lancaster, 1993; Rendell and Sheffer, 1996); studies which have traced the source(s) of the aeolian material (to test whether the notion of a source-to-sink corridor can be observed (e.g. Ramsey *et al.*, 1999; Muhs *et al.*, 2003; Pease and Tchakerian, 2003; Muhs *et al.*, 2017); efforts to develop a sediment budget for the system (Kocurek and Lancaster, 1999) and attempts to frame this understanding within the regional palaeo-environmental record (e.g. Reheis *et al.*, 2012).

2.1.3 Mapping, identifying and characterising aeolian deposits within the landscape

Aerial, and later satellite, imagery has a long history of geomorphological application for mapping land cover and observing landforms (Smith and Pain, 2009). At the simplest level, satellite imagery can be used to visually identify aeolian deposits such as ergs, sand sheets, sand streaks and dune fields (Wilson, 1973; Zimbelman *et al.*, 1995), for example as a means of field reconnaissance. The next step is to identify and map aeolian landscapes often using false-colour composites (combinations of spectral bands from satellite imagery which are understood to highlight or aid the discrimination between land cover of interest) and classification approaches which can facilitate the automated mapping of land cover across a landscape (e.g. Khiry, 2007; Fonji and Taff, 2014).

By combining records of land cover with details of surface form, typically using a digital elevation model (DEM), studies have been used to map areas of sand cover (Khiry, 2007; Teodoro and Goncalves, 2012), landform morphology (Blumberg, 2006; Livingstone *et al.*, 2010; Bullard *et al.*, 2011; Zheng-cai *et al.*, 2015), sediment sources (Ramsey *et al.*, 1999; Mahowald *et al.*, 2003) and to posit likely pathways of sand transport. Indeed, the discipline of geomorphometry is focussed on using these data to extract descriptions of generalised form within the landscape (Pike *et al.*, 2009). Geomorphometry is particularly concerned with distinguishing between *land surface form* and *landforms*, with the former

being purely descriptive and the latter also being used to imply process operation (Evans, 2012). This represents the distinction between specific and general geomorphology (Evans, 1972), that of visualising the variability of form as a continuous surface or as a patchwork of features respectively. Both approaches are scale-dependent, best highlighted by the nesting of landforms within a landscape. Furthermore, this indicates how scale-appropriateness must be determined not by ‘correctness’ but by geomorphological utility (Hengl, 2006). From characterisations of land surface form, morphologies can be determined based upon the observed topographic settings of sediment deposition. These may represent features common across many landscapes (e.g. valleys and peaks – Wood, 1996) or geomorphological forms such as sand sheets or dune forms. As an example of the latter, Bullard *et al.* (2011) mapped the distribution of aeolian landforms within the Namibian sand sea and Miliareisis (2000) extracted alluvial fans from the wider landscape using a combination of land cover and morphometric form. As with aeolian geomorphology generally (see above), less attention has been paid to using these approaches to identify and classify topographically-anchored aeolian deposits. A notable recent example includes the mapping of sand ramps in the Drakensberg/Rooiberge foothills of South Africa (Telfer *et al.*, 2014).

Beyond categorising form, a landscape can be divided into landforms where boundaries can be drawn around a feature (Evans, 2012). In ‘simple’ topographic situations (e.g. around lone hills) landforms can be distinct (with an abrupt boundary) from adjacent parts of the land surface as they are characteristically homogeneous in terms of their form and materials and thus there can be little ambiguity in their classification (Evans, 2012). In such conditions the specific geomorphometry approach has worked well for delimiting landforms (e.g. Bateman *et al.*, 2012; Telfer *et al.*, 2012; Rowell *et al.*, in press). Here landform boundaries represent “real” features, such as streams and ridgelines (Fisher *et al.*, 2004; Evans, 2012), termed *bona fide* boundaries (Smith and Varzi, 2000). However, in situations where the topography is more complex, there can be a greater uncertainty in landform extent and classification where boundaries are ambiguous (as exemplified by the ‘sand ramp complexes’ described above). Here the variability of form and materials can be ambiguous because either they are formed of multiple landforms which have coalesced (as per the distinction between alluvial fans and bajadas) or because the features are inherently ambiguous. As an example, Fisher *et al.* (2004) describe the inherent difficulty in extracting the absolute area of a mountain from the earth’s continuous surface

and so they must be defined using interpreted –*fiat*– boundaries (Smith and Varzi, 2000). The distinction between these types of boundaries is itself not unambiguous, because features like breaks of slope are used to delimit landforms, but slope is scale-dependent (e.g. slope is effectively the change in elevation between two points on a line) and thus any thresholds are arbitrary (Fisher *et al.*, 2005; Minár *et al.*, 2013). These examples highlight how a landscape may not necessarily be neatly divided into unambiguous landforms each with a single clear boundary. There do, therefore, exist unresolved questions regarding whether the influence of topography can lead to a complex morphology in which aeolian landforms may/may not be delimited. Further discussion regarding morphometric approaches for landform identification, and their direct applicability to this study, is found in Section 4.2.

Given the uncertainty described above, studies of the relationship between aeolian landform development and topography have been principally undertaken using a reductionist approach (Harrison, 2001). Reported examples include wind tunnel studies (Tsoar, 1983; Xianwan *et al.*, 1999) or investigations conducted upon a single (Thomas *et al.*, 1997; Bateman *et al.*, 2012), or a few, dune-scale landforms within a landscape, primarily inselbergs or elongated mountain fronts (Evans, 1962; Bertram, 2003; Telfer *et al.*, 2012; Rowell *et al.*, in press). Similarly, studies regarding the influence of topography on aeolian systems have either been conducted at the macro-scale (Wilson, 1973) or have rested on disparate landforms within either a specified aeolian system (Lancaster and Tchakerian, 2003) or a wider landscape. What has not been attempted is to examine the influence of topography on an aeolian system by investigating this effect across a whole mountain block topography on the operation of an aeolian system, seeking to map the distribution and form across the whole mountain block. Complexity arises because the distribution and form of aeolian deposition and landform development within a landscape is not solely related to the influence of the mountain block topography. For example, the climatic history of their environment across time will also influence their development and could lead to a composite morphology resulting from multiple episodes of aeolian activity which have potentially different wind regimes (discussed next). It can be difficult to unpick the effects of these boundary conditions based solely from a mapping exercise. It is therefore necessary to investigate the stratigraphy of the aeolian deposits as these can provide a useful insight into the landscape history within the mountain block.

2.2 Determining landscape history in an aeolian system

2.2.1 Process history

The geomorphic record which is preserved within an accommodation space will comprise the net result of the suite of processes which have influenced its development. Thus, landforms such as sand dunes and ramps provide some evidence of their process history inherently in their form and structure. For example, sand streaks were used to infer long-term sand encroachment and the dominance of a particular wind regime by (Zimbelman *et al.*, 1995); superimposed generations of dune form were used to identify periods of formation and changes in the dominant wind regime by Lancaster (1993); linear dunes have been widely used as an indicator of palaeoenvironmental conditions (e.g. Fitzsimmons *et al.*, 2007; Telfer and Hesse, 2013); and migrating dunes have been used to elucidate sediment transport over contemporary (Silvestro *et al.*, 2010b) and longer timescales (Mason *et al.*, 2011).

Changes within the aeolian system over time (themselves related to regional effective moisture, wind regime, sediment availability) will be recorded within the landforms which are constructed from deposited wind-blown sands as periods of (in)activity (Lancaster, 1988; Kocurek and Lancaster, 1999). Consequently, whilst the net process-balance favours accumulation, aeolian landforms can develop in the accommodation spaces. Conversely, whilst the net balance favours the fluvial/hillslope processes (sometimes interpreted as periods of reduced aridity – e.g. Lancaster and Tchakerian, 1996) then the landform can begin to degrade. If, after a period of time, the system switches back to favouring aeolian accumulation, then another aeolian landform can develop in the accommodation space either in the place of the previous landform or ‘stacked’ upon its remnants (as observed by Kumar *et al.*, 2017). The resulting geomorphic record will comprise the net outcome of the suite of processes which have led to its formation and hence if a record can be reconstructed which will outline these periods of (in)activity then, by collating a number of these records from multiple landforms, a process history for the aeolian system can be developed. These records can potentially provide an important insight into this process history, particularly if constraints on these periods of (in)activity can be established. For example, Roskin *et al.* (2013) and Küster *et al.* (2014) outlined associations between observed phases of aeolian activity and records of human impact on their environment during the Late Holocene. Similarly, by outlining timings for periods of aeolian (in)activity within an aeolian system

then it is possible to develop a landscape history for the chosen study location (at very different spatial scales – e.g. Livingstone *et al.*, 2010; Ellwein *et al.*, 2015).

An important consideration when attempting to reconstruct the process history of a landscape is the influence of landform type on the recorded geomorphic history. The preserved record of aeolian accumulation is influenced by the type of dune being studied, with distinctions drawn between accumulating and migrating free dunes (e.g. Chase, 2009; Telfer *et al.*, 2010), of which the former preserves a longer geomorphic record. Topographically-anchored aeolian landforms, such as sand ramps and topographic dunes, have been recorded to have developed gradually (Lancaster and Tchakerian, 1996) or rapidly (e.g. Thomas *et al.*, 1997; Rendell *et al.*, 2003; Bateman *et al.*, 2012). On the face of it, these scenarios indicate vastly different landscape histories. However, this might reflect rapid landform development at some locations as a part of a gradual spatio-temporal pattern of accumulation at the landscape-scale. Consequently, there exists considerable uncertainty regarding the palaeo-significance of sand ramps (cf. Lancaster and Tchakerian, 1996; Bateman *et al.*, 2012; Telfer *et al.*, 2012; Rowell *et al.*, in press). The possibility of rapid accumulation of aeolian material against individual mountain fronts also raises questions regarding whether large climatic variations are required to explain these periods of locally observed dune (in)activity, as has been the case previously (e.g. Lancaster and Tchakerian, 1996). This is particularly relevant when this is being questioned in other dryland environments (see Chase, 2009). Indeed, the records of individual landforms could represent just a snapshot of a larger system.

2.2.2 The relationship of process history to boundary conditions

Aeolian processes do not occur in isolation and are influenced by the wider environmental conditions – collectively they form the boundary conditions for the aeolian system (Lancaster, 2013). Aeolian systems are related to climate through the influence of wind velocity and the effective moisture (and hence the amount of vegetation cover) (Lancaster, 1988; Kocurek and Lancaster, 1999). This association, coupled with an apparent clustering of ages (e.g. Telfer *et al.*, 2012; Kumar *et al.*, 2017) led to periods of aeolian activity being linked with times of greater regional aridity or humid-arid transitions (e.g. Rendell and Sheffer, 1996; Stokes *et al.*, 1997; Fitzsimmons *et al.*, 2007; Telfer *et al.*, 2012). This process would imply some switching between aeolian-dominated periods and fluvial-dominated periods. However, the association between phases of aeolian activity

and regional aridity has begun to be questioned (e.g. Stone and Thomas, 2008; Telfer and Hesse, 2013; Hesse, 2014), because event-based processes (e.g. debris flows and flash floods) do not necessarily represent (longer-term/regional) significance (Ventra *et al.*, 2017).

Alternatively, periods of aeolian construction can be associated with periods of increased sediment supply and availability (Kocurek and Lancaster, 1999), particularly where significant quantities of sediment are deposited by fluvial systems (Bullard and Livingstone, 2002; Maroulis *et al.*, 2007; Cohen *et al.*, 2010). For example, Ellwein *et al.* (2015) concluded that the aeolian landforms of the Black Mesa Region, Colorado, formed during the Late Pleistocene when conditions were cooler and wetter, but when sediment supply was considerably higher. The increase in stream flow and sediment load (which led to aggradation) understood to have occurred around this time, would likely change the channel morphology towards a wider, braided and sandy channel pattern which is more suitable for deflation (after Muhs and Holliday, 1995). Similarly, Rendell *et al.* (2003) suggested that deflation of fluvial sediments was likely responsible for deposits, perhaps through ephemeral flow or overbank deposits and with palaeosol development during more arid periods. In the Mojave Desert, Muhs *et al.* (2017) associated the construction of the Kelso Dunes with the timings of sediment supply from the Mojave River based upon the similarity of their timings and sediment provenance. This increased sediment supply in the vicinity of the Mojave River provides the significant volume of aeolian materials in both the Cady Mountains and the Kelso Dunes when compared with other areas in the Mojave to the west and south which are comparatively devoid of sand (Kocurek and Lancaster, 1999; Muhs *et al.*, 2017).

Non-aeolian sediments present within some deposits (typically sand ramps – Bertram, 2003) can also provide a useful insight into the processes which have acted upon a landform and, by extension, the drivers which have influenced geomorphic process. For example, periods of fan aggradation can be driven through some interplay of precipitation, temperature and vegetation across Milankovitch and sub-Milankovitch timescales, with a widespread pulse of fan aggradation observed across much of the SW USA and which appears to be related to changes in rainfall seasonality around the Late Pleistocene - Holocene transition (see Section 3.2.3) (Miller *et al.*, 2010; Antinao and McDonald, 2013; Antinao *et al.*, 2016). As described above, the palaeo-significance of

the stone lines within sand ramps remains uncertain. Regardless of the presence of stone lines within a landform, understanding of how the history of a landform relates to its boundary conditions is assisted through the provision of a geochronology.

2.2.3 The utility of timings of process (in)activity

Absolute dates have provided a useful tool for establishing the history of process within geomorphic systems, with applications incorporating reconstructing lake stands (Owen *et al.*, 2007; Reheis *et al.*, 2014), fan development (Spelz *et al.*, 2008; Dühnforth *et al.*, 2017), hillslope events (Winchester and Chaujar, 2002; Fuchs and Lang, 2009) and periods of aeolian landform development (examples below). One major difficulty in reconstructing process history within dryland environments has been the relative scarcity of evidence for the geomorphic and climatic history of the landscape (Singhvi and Porat, 2008), which means that luminescence dating is of critical importance. Records of aeolian activity coupled with timings (absolute dates) for key strata/events have provided a useful tool to develop process histories of aeolian systems (Leighton *et al.*, 2014), with studies frequently seeking to understand system responses to environmental change or to infer palaeoclimatic conditions (for example through interpreting the aeolian record as a record of regional aridity Fitzsimmons *et al.*, 2007; Halfen *et al.*, 2012; Telfer and Hesse, 2013; Leighton *et al.*, 2014; Pan *et al.*, 2014). Records of (in)activity reconstructed from aeolian landforms have been discussed in a manner which provides a more locally-focused process history of how fluctuations in the various drivers of change for an aeolian system (e.g. sediment availability or vegetation cover) might lead to complex local changes within an aeolian system. Such studies might reconstruct the development of lunette dunes as a result of climatic conditions which promote basin desiccation and aeolian deflation (Rich, 2013) or those conditions which lead to a rapid development of aeolian deposits due to changes in the local wind regime or the level of vegetation (Telfer *et al.*, 2012). Further discussion regarding luminescence dating and its direct applicability to this study will be found in Section 4.4 and Chapter 5.

2.3 Objectives:

1. Identify and categorise the morphology of aeolian landforms within the landscape.
2. Determine the history of process operation by developing a geochronology for field sites within the landscape.
3. Relate the above to the boundary conditions of the study area in order to establish the influence of topography over the operation of aeolian processes.

3 Field site

This section describes, and justifies, the geographical location and sampling strategy of this study. The chapter then outlines the macro-scale morphology of the landscape and provides a narrative of changes in the environmental conditions in this locale (as well as can be presently understood) during the Late Pleistocene. It is important to understand the boundary conditions for the aeolian system because they will also have influenced the process history and the morphological outcome of the aeolian deposits. Section 3.1 introduces the study area, with specific focus on its aeolian process systems, and then describes the location and sampling of the field sites. Section 3.2 describes the geomorphological setting for the study area in terms of its geology and climate (current and past). Section 3.3 draws together the history presented in Section 3.2 to provide a synthesis of the boundary conditions for the aeolian system under investigation and its influences on geomorphic process.

3.1 The Mojave Desert

The study location, the Cady Mountains, lies within the central Mojave Desert, 50km east of Barstow, California (Figure 3.1). The Mojave Desert is a physiographic region which forms a part of the wider Basin and Range Province within the SW USA which is characterised by fault-bounded mountain ranges separated by wide flat valleys (Rowlands *et al.*, 1982; Lancaster and Tchakerian, 2003). The contemporary climate of the region is semi-arid, but has been subject to cooler, wetter conditions in the past (see Section 3.2.3). During these periods, the Mojave River, which currently flows ephemerally from the San Bernardino Mountains north and eastwards to its modern terminus at Silver Lake (Figure 3.1), maintained a string of palaeolakes within the region throughout the Late Pleistocene (of which Lake Manix is proximal to the study area) (Enzel *et al.*, 2003). The Cady Mountains, like the Mojave Desert more widely, contain many well defined and mapped aeolian landforms which result from aeolian sand transport systems, many of which are associated with fluvial deposition of sediments (Zimbelman *et al.*, 1995; Lancaster and Tchakerian, 2003).

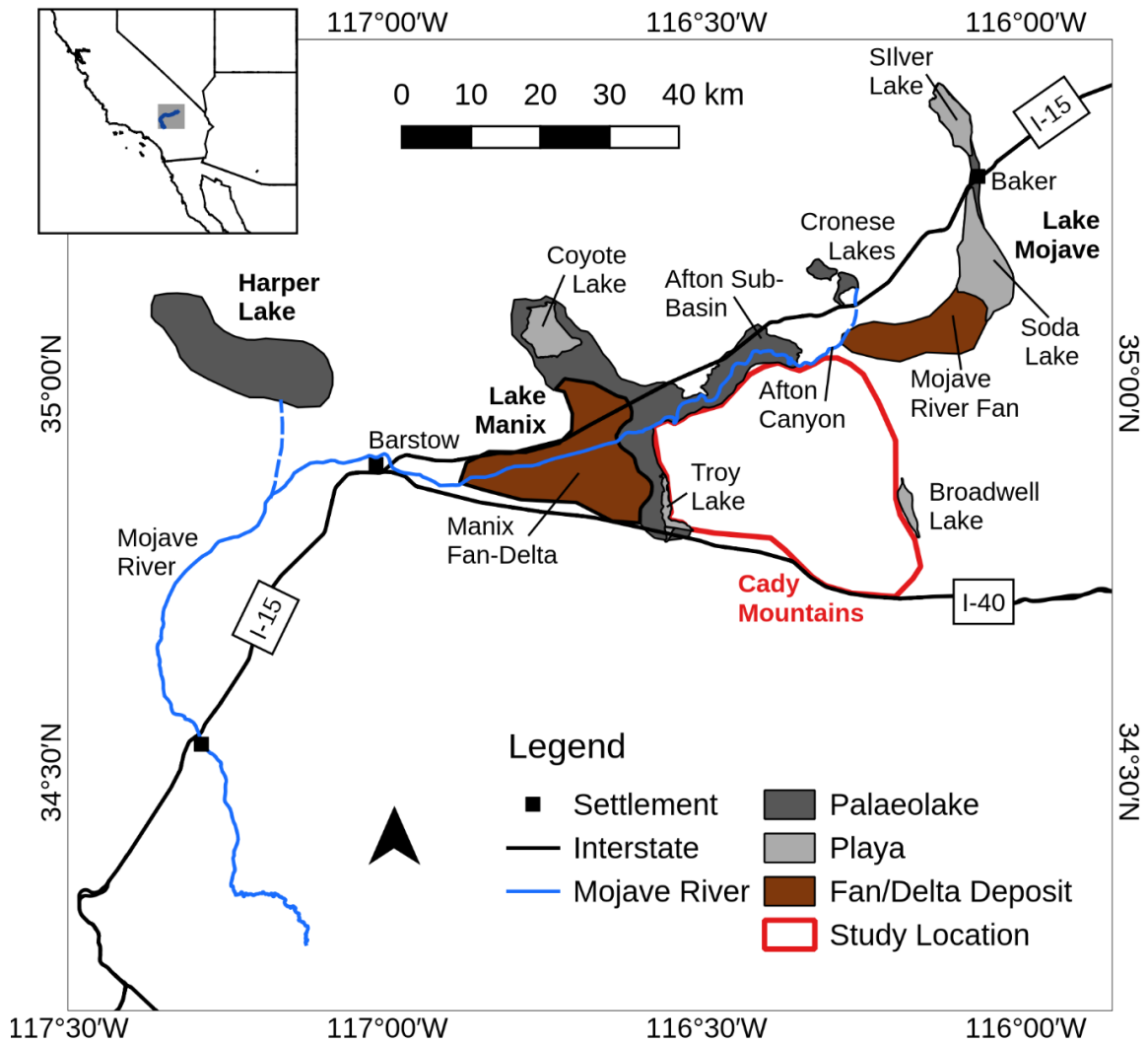


Figure 3.1: Location map for this study (main) and its setting within the SW USA (inset). Map data © OpenStreetMap contributors.

3.1.1 Aeolian deposits within the Mojave Desert

The Mojave Desert contains widespread and significant aeolian deposits, though much historical focus has been on the Kelso Dunes (Figure 3.2) (Sharp, 1966; Smith, 1984; Lancaster, 1994) and the accumulations of the Cadiz and Rice valleys. This earlier work suggested that aeolian transport and accumulation has operated within the region for many tens of thousands of years (Sharp, 1966; Smith, 1984), possibly as multiple phases (Tchakerian, 1989, 1991). The Kelso Dunes are a complex dune field with numerous superimposed morphologies resulting from its variable wind regime and combination of sediment sources (Lancaster, 1993, 1994; Muhs *et al.*, 2017). The aeolian deposits of the Mojave Desert are strongly related to the fluvial systems within the region (e.g. Kocurek

and Lancaster, 1999), though it is also likely that sources of sediment proximal to the dune field are also important. Evidence for this was cited from grain size and sorting characteristics (Sharp, 1966; Lancaster, 1993), wind and ventifact records (Smith, 1984), modern analogues (Clarke and Rendell, 1998), remotely sensed data (Ramsey *et al.*, 1999) and geochemical data (Pease and Tchakerian, 2003; Muhs *et al.*, 2017).

In terms of the influence of complex topography on aeolian accumulation, deposits of aeolian sands have been documented on windward and leeward slopes across the region. For example, Evans (1962) provided a detailed description of the Cat Dune and noted that the deposit contained talus mixed with aeolian sands. Smith (1984) describes topographic dunes on the Cowhole Mountains and Old Dad Mountains as well as topographic dunes, sand streak and tails behind hills within the Cady Mountains. More recently, numerous sand ramps and topographic dunes have been located and mapped across the Mojave Desert, frequently associated with geochronologies from luminescence dating (Lancaster, 1994; Clarke *et al.*, 1995; Lancaster and Tchakerian, 1996; Rendell and Sheffer, 1996; Clarke and Rendell, 1998). It is, however, noticeable that the ages which these studies present feature age reversals which were inconsistent with the stratigraphy and provide strongly conflicting landscape histories (see Section 8.4.1).

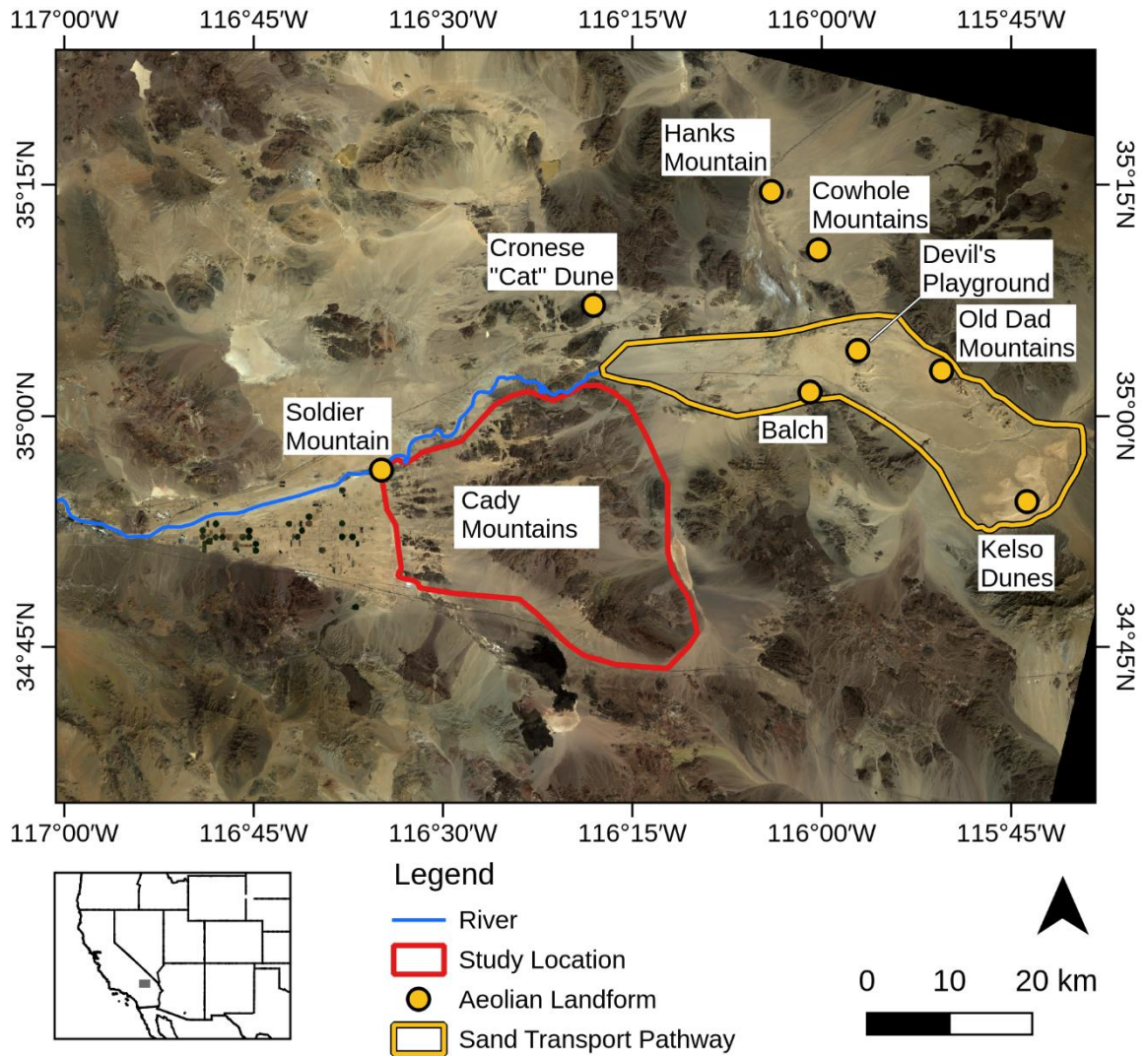


Figure 3.2: Aeolian landforms of the central Mojave Desert (Lancaster and Tchakarian, 1996; Lancaster and Tchakarian, 2003). Landsat-8 image courtesy of the U.S. Geological Survey. Map data © OpenStreetMap contributors.

3.1.2 Sand transport corridors

Large areas of the Mojave Desert contain mountainous topography separated by broad, flat basins. Where these basins connect, significant aeolian systems have been mapped and it has been hypothesised that they formed extensive source-to-sink aeolian sand transport pathways. Three examples being the corridor linking the Mojave River and Kelso Dunes (Lancaster, 1993; Clarke and Rendell, 1998; Kocurek and Lancaster, 1999), the Bristol Corridor and Rice Valley Corridor (Zimbelman *et al.*, 1995). Sand was hypothesised to weave its way along these ‘corridors’, banking up against the topography at the periphery as sand ramps (and sometimes surmounting the topography) as it is transported downwind (after Zimbelman *et al.*, 1995). Subsequently, geochemical

investigation of the “Bristol Corridor” concluded that there was little evidence for any integrated pathway of sand and that locally derived sediments were a more significant sediment source for the development of the studied sand ramps (Pease and Tchakerian, 2003). By contrast, geochemical investigation of the Mojave River to Kelso aeolian system suggests that the Mojave River is the dominant source of material for the aeolian system (Ramsey *et al.*, 1999; Muhs *et al.*, 2017). It might be the case that whereas the Mojave River exists as a significant sediment source to dominate an aeolian system, no similar single source exists within the Bristol corridor.

3.1.3 Cady Mountains aeolian system

The Cady Mountains contain many topographically-anchored aeolian deposits and sand streaks, which have been interpreted as an aeolian system which transports sand from the Manix Basin into the mountain block, principally through studying Landsat images (Smith, 1984; Zimbelman *et al.*, 1995). With the exception of investigation of the sand ramp at Soldier Mountain and the ventifact mapping conducted by Laity (1992) along the western front of the mountain block, the Cady Mountains have received little geomorphological attention.

3.1.4 Sampling locations

The objectives of this study require an investigation of whether some relationship exists between the morphometry of the landscape and the emplacement and preservation of aeolian sediments. In order to investigate this relationship in more detail, a map of the distribution and form of the mountain block (and its aeolian deposits) was created. This mapping and analysis covered a standardised area (Figure 3.3) which was defined to include the Cady Mountains but not the contemporary Mojave River channel, adjacent lake beds (e.g. the Troy and Broadwell playas) or areas of significant human influence (e.g. the agricultural areas of the Newberry Triangle). Within this study area multiple aeolian deposits are described and, from these areas, sedimentary samples for description and laboratory analysis were taken (Chapter 4). Sites were focused on the aeolian deposits which were disproportionately to the northwest of the mountain block (Figure 3.3). All

sites were chosen to be a part of some topographically-anchored aeolian deposit, with the exception of DN which was within a small low-relief dune field.

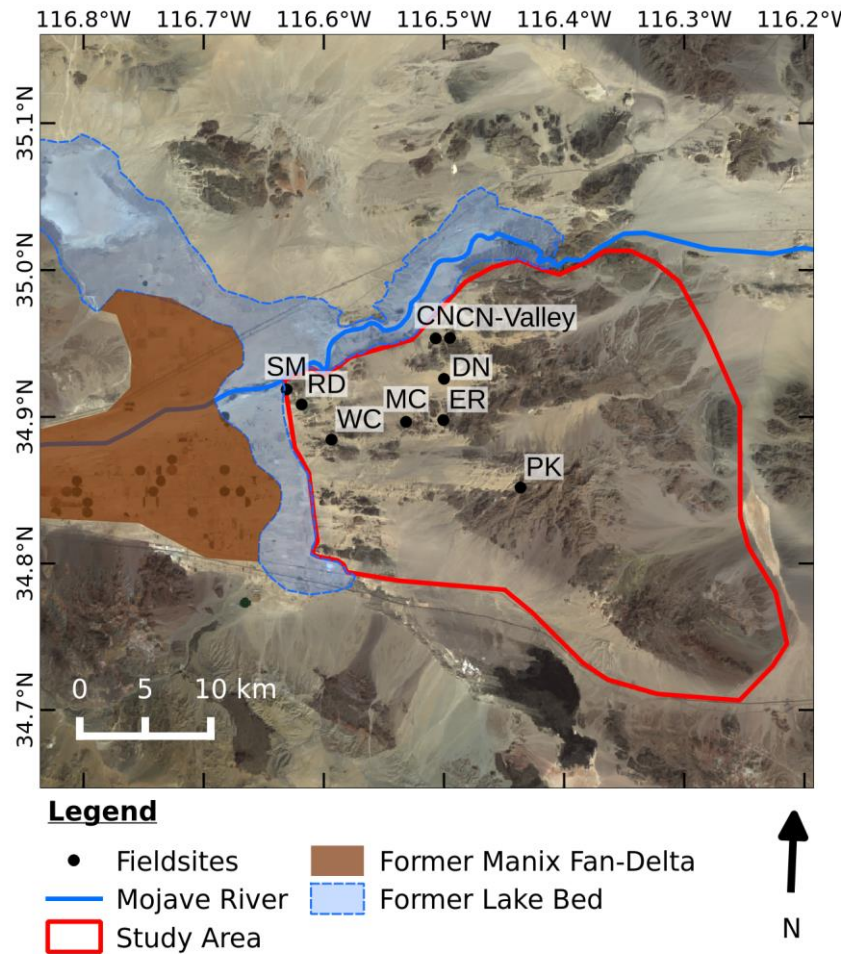


Figure 3.3: Map of the nine field sites discussed in this study. Landsat-8 image courtesy of the U.S. Geological Survey. Map data © OpenStreetMap contributors.

Sampling sites were a combination of fluvially-cut sections and hand dug pits. Pre-existing sections were preferred as they were larger, though pits of two metres were dug to provide an adequate number of sites. Sites were selected to be measured as a single profile whilst providing the thickest depth of visible deposits. Sites were logged upwards from the lowest point in the stratigraphy with the section being divided into units, each of which is described in terms of its texture, stratification and colour (Munsell) (Chapter 7). Such units were commonly divided to characterise changes in the nature of the profile rather than, for example, highlighting every stone horizon in a sand ramp. Multiple samples for luminescence dating (typically four) and grain size analysis were taken to fit within these units (and to bracket notable layers such as palaeosols) rather than being regularly spaced within the section.

3.2 Geomorphological setting for study area

3.2.1 Geology

The Mojave Desert is a physiographic province situated between the large north-south trending basin and range topography of the Great Basin Desert to the north and the San Andreas Fault Zone and the San Bernardino Mountains to the south. The region is characterised by fault-bounded mountain ranges separated by sediment-filled basins (Lancaster and Tchakerian, 2003).

The geological history of the Mojave Desert was significantly influenced by extensional tectonism which led to the uplift of the Transverse Ranges during the Miocene (Dokka, 1986; Glazner *et al.*, 1989). This extensional tectonism divided the region into several rotated blocks separated by fault systems (e.g. Cady and Manix/Afton Faults) which uplifted numerous mountain blocks as they rotated – including the Cady Mountains which is the focus of this study (Dokka and Travis, 1990; Glazner *et al.*, 2002). The uplift of the region during the Miocene significantly impacted drainage (and hence sediment supply/availability) patterns across the region by re-routing the region's primary watercourse – the Mojave River – from flowing southwest to flowing north/northeast into the Victorville Basin (Cox *et al.*, 2003). It was not until 0.5Ma, however, that the Mojave River breached the Victorville Basin to reach the Manix Basin (Jefferson, 2003; Reheis *et al.*, 2012). The San Bernardino Mountains are primarily composed of granitic rocks and gneiss, but also with some arkose (Cox *et al.*, 2003) and so are geochemically similar to much of the Cady Mountains.

The topography of the central Mojave Desert (including the Cady Mountains) is composed of a weathered Mesozoic granitic to quartz monzonite basement variably overlain and intruded by Miocene volcanic and sedimentary complexes (Dibblee and Bassett, 1966; Dokka, 1986; Ross, 1995). The Cady Mountain block has experienced reduced tectonic activity during the Quaternary Period, though the Manix/Afton Fault along its northern border has been recently active (Phelps *et al.*, 2012). The large-scale morphology of the Cady Mountains is described in Section 6.1 and constitutes a large central peak (~1400m) with a series of smaller satellite peaks to the north and south (~1000m) and a row of small peaks (~800m) marking the western front of the mountain block. The mountain block is surrounded by areas of broad, low-lying plains (~600m)

which contain contemporary playa surfaces relating to former palaeolakes (notably Manix and Broadwell lakes) (Enzel *et al.*, 2003; Phelps *et al.*, 2012).

3.2.2 Contemporary climate

The Mojave Desert is currently a semi-arid region with cool winters ($\sim 10^{\circ}\text{C}$) and hot summers ($>30^{\circ}\text{C}$) (Figure 3.4) (Enzel *et al.*, 1989). The study location sits along a precipitation gradient and thus the proximal weather station (Barstow-Daggett Airport) to the field site exhibits an annual pattern between the two endpoints (Figure 3.4). To the east of the field site, the distribution of precipitation throughout the year (measured at Silver Lake) is bimodal, with the majority (66%) of precipitation occurring as cool-season frontal storms and $<40\%$ as summer convectional storms. To the west of the field site, however, these cool-season storms account for 82% of annual precipitation (Enzel *et al.*, 2003; Hereford *et al.*, 2004). Annual rainfall patterns are related to north Pacific sea surface temperature (SST), increases in which are associated with phenomena such as El Niño Southern Oscillation and the Pacific Decadal Oscillation which, in turn, are associated with wetter conditions and larger flow events in the SW USA (Cayan *et al.*, 1999; Andrews *et al.*, 2004). The Mojave River flows from the San Bernardino Mountains inland towards the study area, with lake stands associated with increased cool-season precipitation in the Mojave River headwaters (Enzel and Wells, 1997; Kirby *et al.*, 2012).

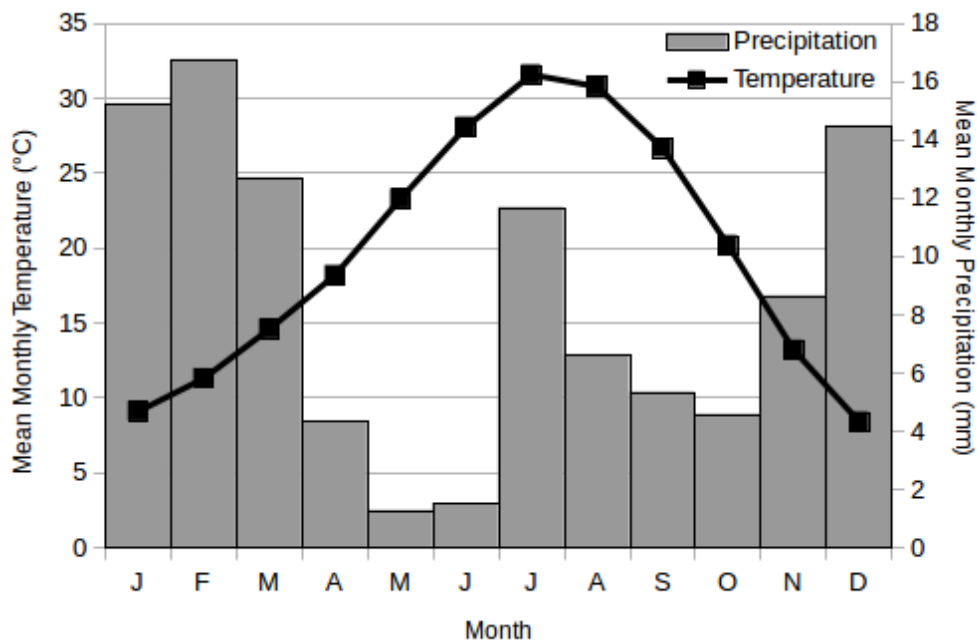


Figure 3.4: Mean monthly temperature and precipitation data at Barstow (Daggett Airport). Source: NOAA.

Under current conditions precipitation events are incapable of sustaining lake stands upon the playa surfaces across multiple years, however particularly large storms can cause significant flow events in the Mojave River (Enzel, 1992; Enzel *et al.*, 1992).

Under current conditions vegetation across the Mojave Desert is dominated by a low density of *Larrea tridentata* (Creosote Bush), *Ambrosia demosa* (Bursage) and several annual species that germinate after late summer storms (Beatley, 1974). The vegetation of the region is controlled by the topography and elevation as well as the presence of any localised water sources, such as areas where groundwater is close to the surface or (in the past) perennial lake stands (Kocurek and Lancaster, 1999). Typically, lower elevations are associated with a lower density of vegetation whereas higher elevations within the Cady Mountains contain a greater prevalence of vegetation, including occasional small *Yucca brevifolia* (Joshua Tree).

The wind regime is an important influence which determines how much sand is transported (through wind speed) and the direction in which any transport occurs. Winds within the region are typically from the west and are strongest in spring and summer, but with some northerly component during the autumn and winter (Figure 3.5) (Berry *et al.*, 1981; Laity, 1992; Zimelman *et al.*, 1995; Muhs *et al.*, 2017). Winds which are sufficient for the transportation of sand are predominately those associated with the passage of winter storms which are also typically associated with westerly winds (Halfen *et al.*, 2015). Topographic steering and sheltering is evident within some wind records, particularly around passes (e.g. where the Mojave River travels between Barstow and Daggett) and along troughs (e.g. Bristol Trough) (Berry *et al.*, 1981).

3.2.3 Palaeoclimate

During the Late Quaternary the SW USA has responded to Milankovitch- and millennial-scale drivers in global climate (e.g. Martinson *et al.*, 1987). Speleothem and lake level records indicate first order variability coherent with trends in Northern Hemisphere summer insolation, global ice volume and global temperature (Winograd *et al.*, 1992; Benson *et al.*, 2003; Winograd *et al.*, 2006; Oster *et al.*, 2009; Lachniet *et al.*, 2014; Railsback *et al.*, 2015; Reheis *et al.*, 2015) (Figure 3.6). Over the last ~120ka the climate of the Mojave Desert generally experienced warm, dry interglacials and cool, wet glacials ($\Delta\sim 6^{\circ}\text{C}$) (Enzel *et al.*, 2003). Associated variability in moisture (quantity and sources) and wind regime has potentially significant implications for geomorphic process history

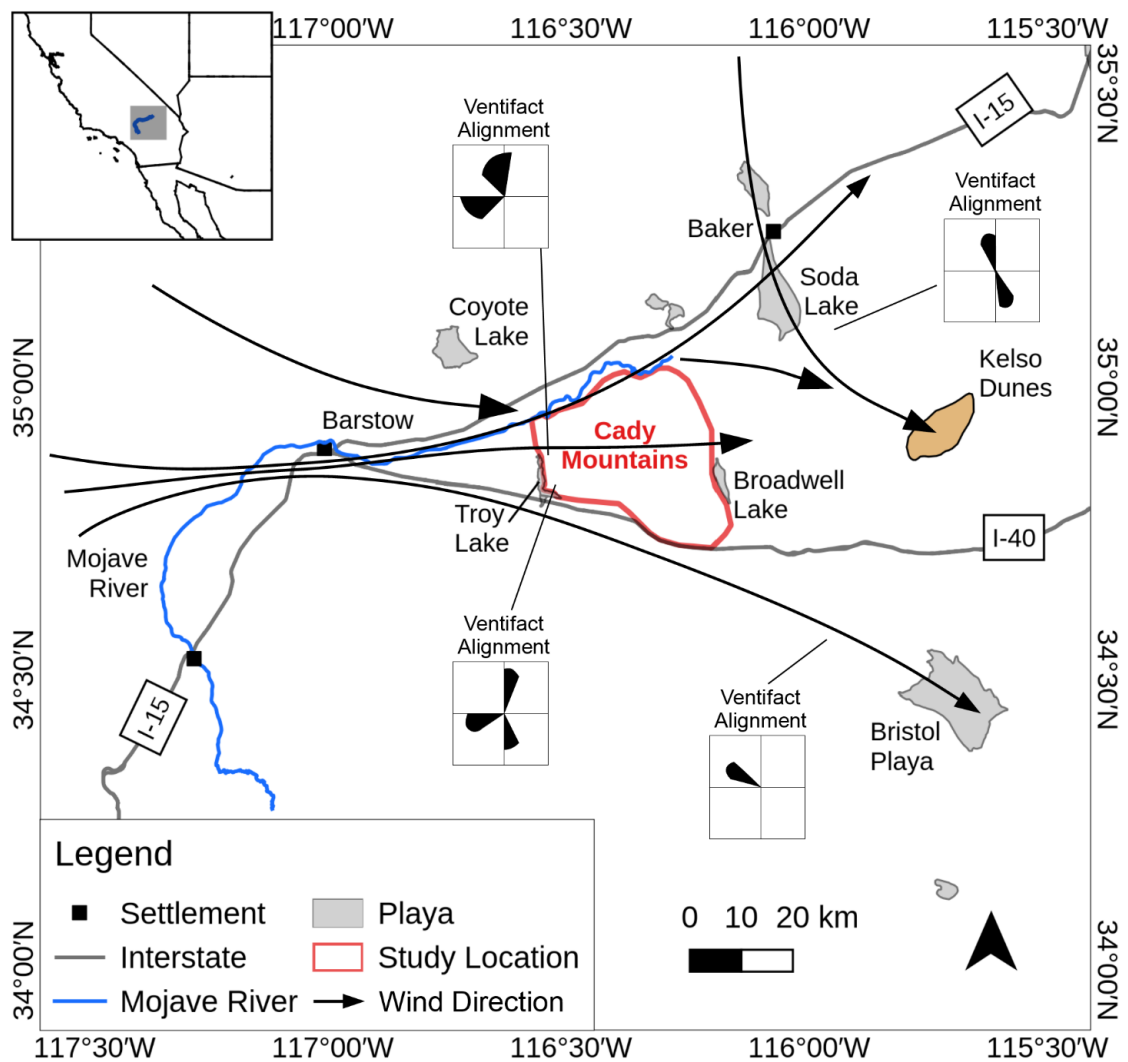


Figure 3.5: Contemporary winds within the region are largely from the west, however the effect of topographic steering funnels winds east of Barstow before they separate either across the Cady Mountains or towards the Bristol Playa. Note the northerly wind which travels across Soda Lake to the Kelso Dunes. Wind data adapted from Berry *et al.* (1981) and ventifact records adapted from Laity (1992). Map data © OpenStreetMap contributors.

(see Section 3.3). This section provides a brief overview of the climate system affecting the Mojave Desert and how it is understood to have responded over the last ~120ka.

The Mojave Desert lies in a key climatic transition zone between coastal areas dominated by Pacific-sourced moisture, commonly associated with cool-season frontal storms (e.g. Enzel *et al.*, 2003; Oster *et al.*, 2009; Kirby *et al.*, 2013), and areas to the east that are affected by the impacts of summer monsoonal systems sourced from the south (Oerter *et al.*, 2016) (Figure 3.6). However, the proximity of the Mojave River headwaters to the Californian coast (Figure 3.6) means that (of these) it is likely that the river has been

sourced from the Pacific. The apparent increase in (Pacific-sourced) moisture and decrease in temperature during glacial periods within the Mojave Desert (e.g. Winograd *et al.*, 1992; Winograd *et al.*, 2006; Railsback *et al.*, 2015) has been related to the movement of the North American Polar Jet (NAPJ) and the associated westerly storm track in response to changes in the positioning of high pressure systems triggered by the expansion of the Laurentide Ice Sheet (Figure 3.7), termed the “dipping westerlies hypothesis” (Enzel *et al.*, 1989; Oster *et al.*, 2009). The hypothesis implies that lake high stands in the Mojave Desert would have been asynchronous with those in the Great Basin to the north as the storm track moved north-south – as driven by the expansion/contraction of the Laurentide Ice Sheet (Figure 3.6) (Enzel *et al.*, 1989; Enzel *et al.*, 2003; Garcia *et al.*, 2014). Lakes Mono, Owens and Searles appear to support this anticipated movement of the NAPJ between $\sim 35^{\circ}\text{N}$ and $>43^{\circ}\text{N}$ as high stands are broadly out of phase with Lakes Harper and Manix to the south (Benson *et al.*, 2003; Kirby *et al.*, 2006; Benson *et al.*, 2011; Reheis *et al.*, 2012; Benson *et al.*, 2013; Garcia *et al.*, 2014; Reheis *et al.*, 2015) (Figures 3.7 and 3.8). Pacific-sourced frontal storms are not the only moisture source for the region, with a combination of Pacific sources being observed under the present climate. An observed asynchrony between Great Basin lake high stands and rainfall patterns along the Californian coast during the last deglaciation (Lyle *et al.*, 2010; Lyle *et al.*, 2012) suggest that tropical or subtropical moisture sources may also have been significant within the region (e.g. Connin *et al.*, 1998; Reheis *et al.*, 2012; Antinao and McDonald, 2013; Wong *et al.*, 2016). Despite accounting for the minority of total precipitation, summer storms have been shown to be geomorphologically significant within the region (e.g. Miller *et al.*, 2010). Such a combination of sources was observed at Bear Lake (Kirby *et al.*, 2012) and Lake Elsinore (Kirby *et al.*, 2013) for (at least) the last deglaciation.

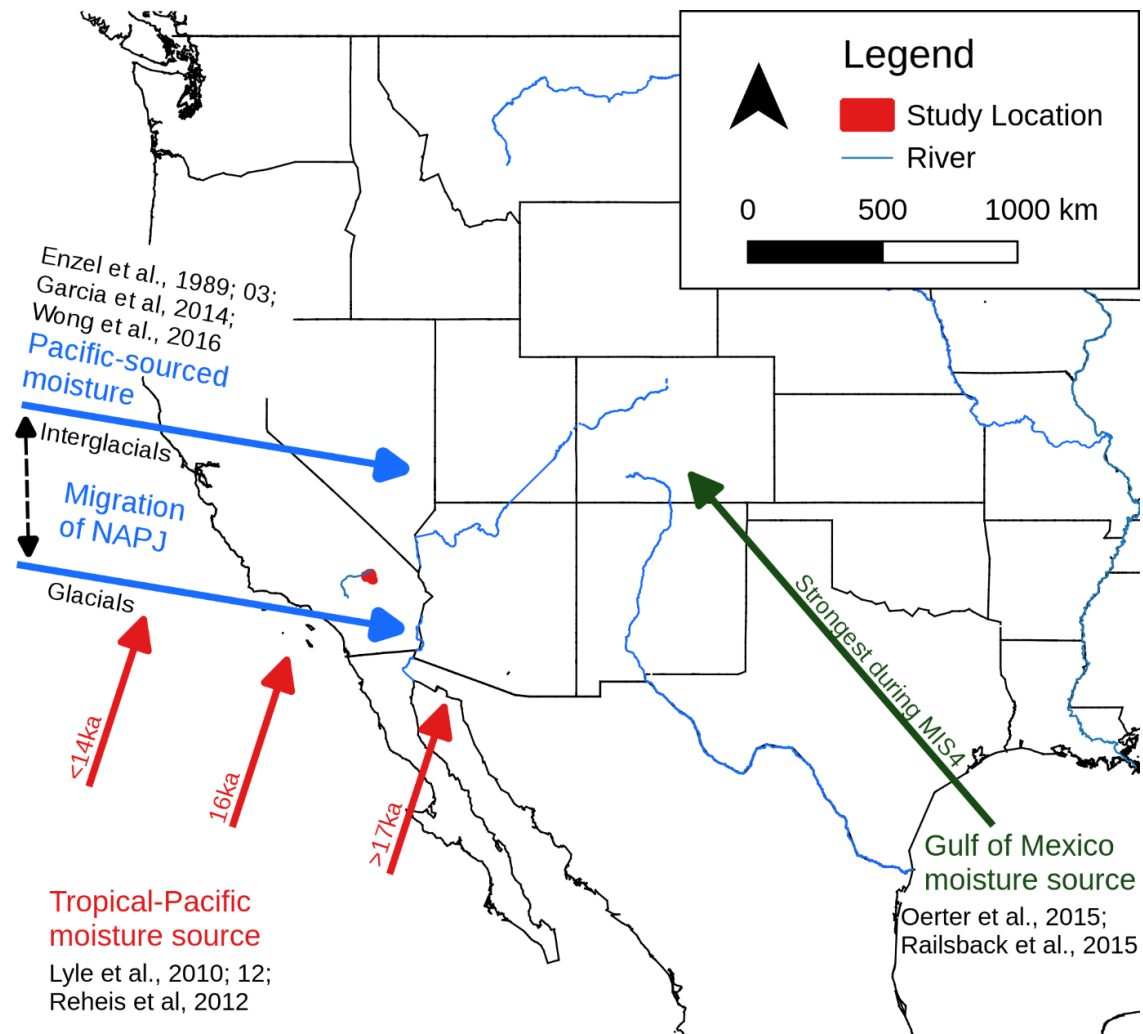


Figure 3.6: Moisture sources for the south-western USA referenced in the text. Map data © OpenStreetMap contributors.

In addition to the regional climatic variability related to glacial-interglacial cycles, southern California shows additional sensitivity to within-cycle variability of insolation and the influence of orbital forcing (Moseley *et al.*, 2016; Glover *et al.*, 2017). The persistence of Lake Manix throughout MIS3, when the westerly storm track was to the north, suggests that the Mojave headwaters experienced a more continuous and higher level of precipitation than other lake systems to the north and east. Such precipitation appears to have been provided through variability in SST gradients along the Californian coast, themselves coeval with Dansgaard-Oeschger events (Enzel *et al.*, 1989; Benson *et al.*, 2003; Bird and Kirby, 2006; Kirby *et al.*, 2012; Reheis *et al.*, 2012; Reheis *et al.*, 2015; Glover *et al.*, 2017).

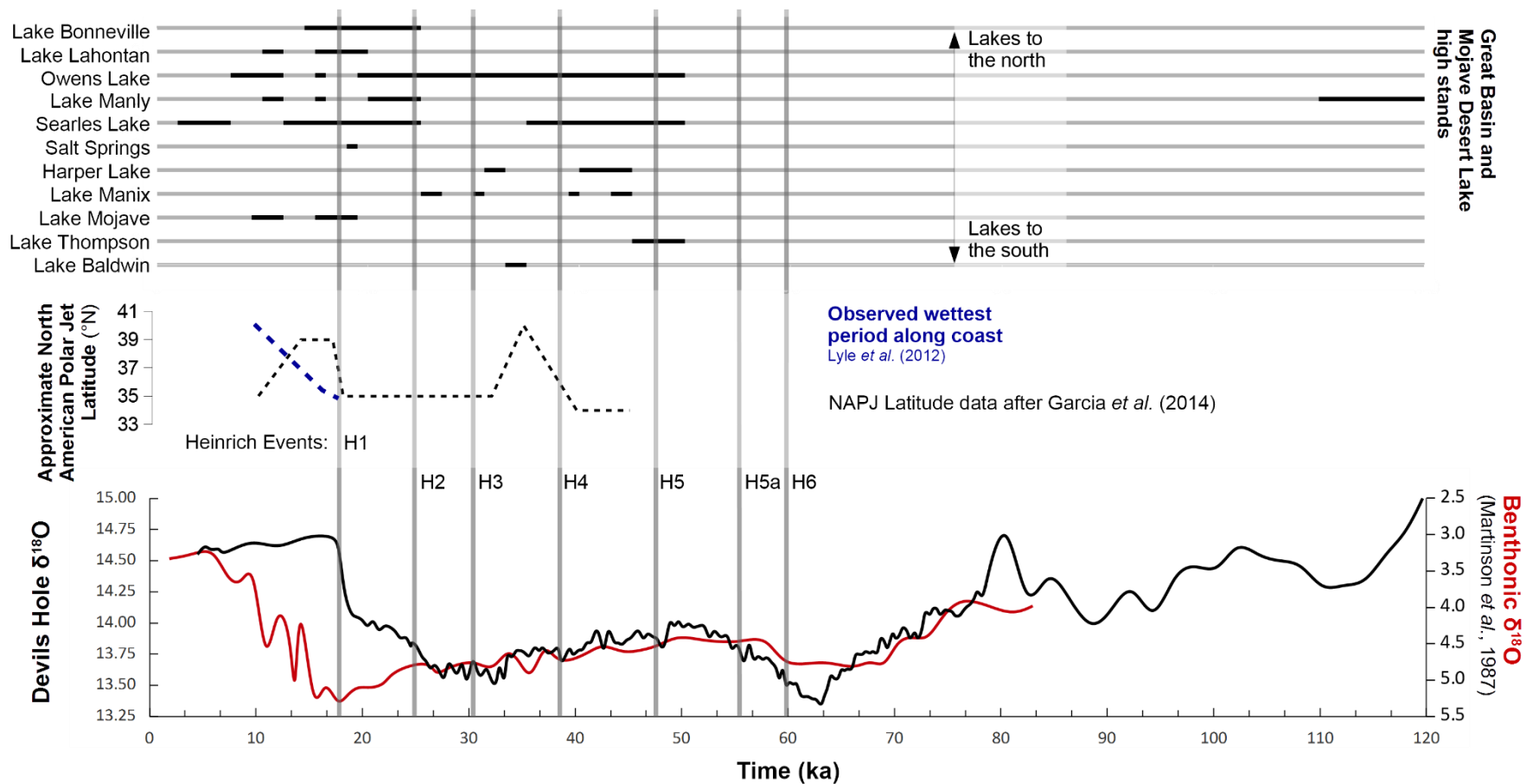


Figure 3.7: Regional climate synthesis for SW USA lake high stands. Lake high stands show a broad trend of north-south migration in general accordance with the approximate latitude of the NAPJ (records shown: Benson *et al.*, 2003; Kirby *et al.*, 2006; Benson *et al.*, 2011; Reheis *et al.*, 2012; Benson *et al.*, 2013; Garcia *et al.*, 2014; Reheis *et al.*, 2015) (discussed in the text). The Devil’s Hole speleothem record (lower) (Winograd *et al.*, 1992; Winograd *et al.*, 2006) indicates first order variability coherent with trends in Northern Hemisphere summer insolation, global ice volume and global temperature (Martinson *et al.*, 1987), albeit with a divergence in the timing of the last deglaciation (Moseley *et al.*, 2016).

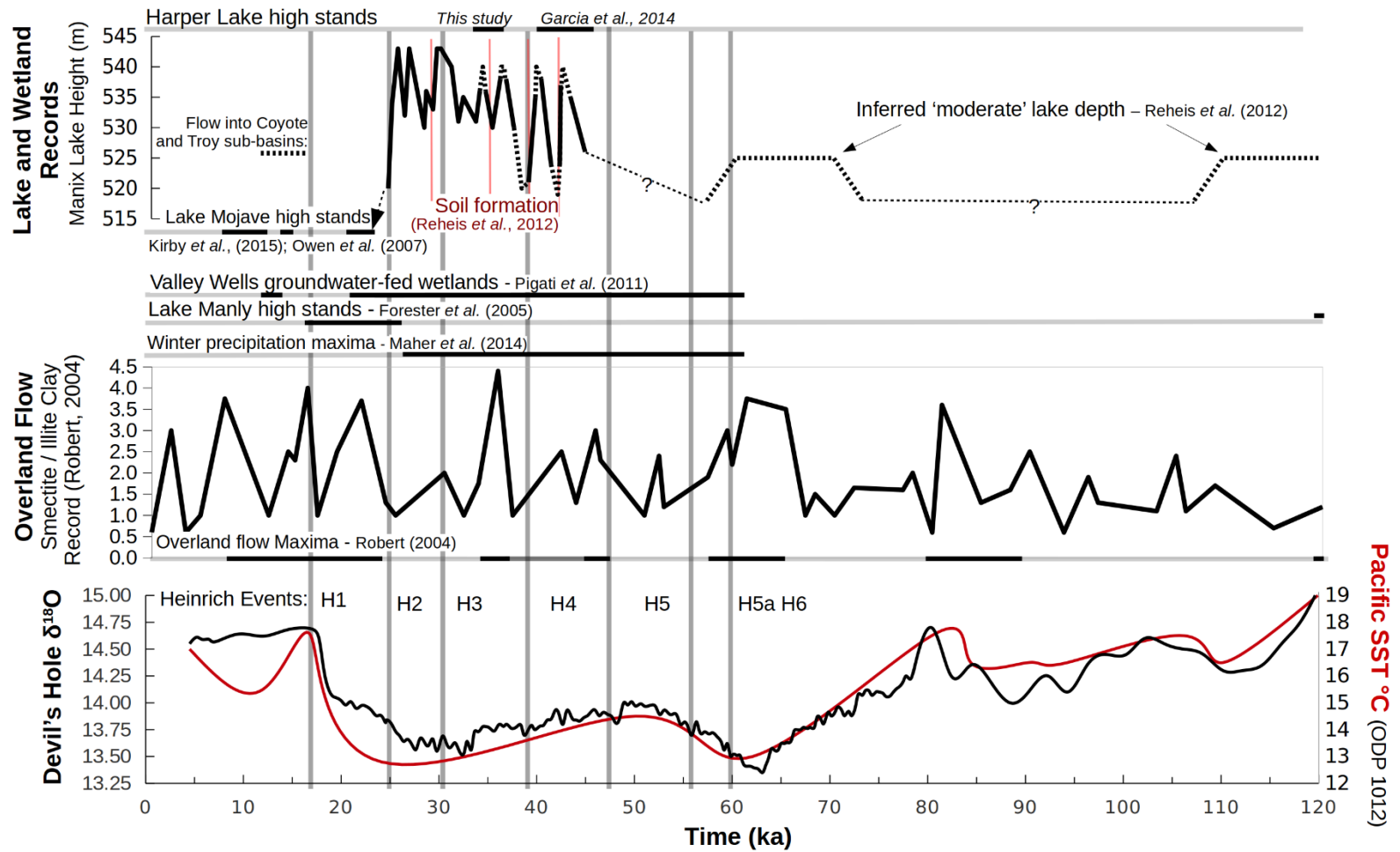


Figure 3.8: Climatic history for the Manix Basin and related surroundings for the past 120ka. Lake Manix high stand data from Reheis *et al.* (2012) and Reheis *et al.* (2015). The SW USA responds to glacial-interglacial cycles, as emphasised by the Devil's Hole speleothem reconstruction (Winograd *et al.*, 1992; Winograd *et al.*, 2006).

Evidence of past vegetation cover, principally reconstructed from Packrat middens, is associated with regional climatic changes. Between 24ka and 9.9ka, areas below ~1000m in the region south of 36°N (which includes much of the Cady Mountains) were dominated by mild mesic woodland characterised by *Pinus monophylla* (less prevalent after 11.5ka), *Juniperus osteosperma* (less prevalent after 9-8ka), *Yucca brevifolia* and *Purshia mexicana*. Above 1000m of elevation vegetation present was likely a similar woodland, but with increased numbers of *Juniperus* as was found in the colder xeric steppe to the north (Koehler *et al.*, 2005). A transition from mild mesic woodland to more desert-adapted vegetation in the vicinity of Lake Mojave and the Granite Mountains occurred from ~8ka. Following the desiccation of the lakes across the Mojave Desert and as the climate warmed after 7ka *L. tridentata* began to dominate the landscape, though the transition to the contemporary vegetation was later at areas of a greater elevation (Koehler *et al.*, 2005).

Overall it appears that, regardless of the ultimate source, variability in moisture within the Mojave Desert was sufficient for lake-level fluctuations throughout the Great Basin, but with the Mojave River catchment receiving enough water to sustain lakes for the majority of the period.

3.2.4 History of palaeo lakes in the eastern Mojave Desert

The Mojave River is presently ephemeral, with flow events correlating with north Pacific SST, increases in which are associated with phenomena such as El Niño Southern Oscillation and the Pacific Decadal Oscillation (Cayan *et al.*, 1999; Andrews *et al.*, 2004; Kirby *et al.*, 2012; Reheis *et al.*, 2012). For example, flow was significant enough to maintain lakes within the Soda and Cronese basins during the Little Ice Age (Enzel *et al.*, 1992). During more humid (glacial) periods, the river was capable of creating and maintaining several Pleistocene lakes along its course at different times. Lake Manix is the most proximal of these to the Cady Mountains, bordering the mountain block on its northern and western flanks (Figure 3.1). The Manix Basin was endorheic until the arrival of the Mojave River at ~500ka (Naggy and Murray, 1996; Cox *et al.*, 2003; Jefferson, 2003). Subsequently the Mojave River maintained a near-continuous lake within the Manix Basin until ~25ka (Reheis *et al.*, 2012). The Lake Manix Basin comprises four sub-basins that operated semi-independently when the lake was not at a full high stand: Cady, Troy, Coyote and Afton. The latter was only

incorporated into the Manix Basin after the breaching of a sill near the Buwalda Ridge ~190ka (Reheis *et al.*, 2012).

Despite its near-continuous existence from 500ka, Lake Manix has varied greatly in its depth, with commensurate evidence for deep water, nearshore and fluvio-deltaic facies mapped within the basin (Jefferson, 2003; Reheis and Miller, 2010; Reheis *et al.*, 2012). River flow to the Manix Basin likely increased after tectonic deformation upstream of Barstow diverted the Mojave River, leading to a greater quantity of water and sediment flowing into Lake Manix at some time around 70ka (Cox *et al.*, 2003). In general, the history of precipitation around the headwaters of the Mojave River over the last 120ka is one of increasing total precipitation and storm frequency from ~45ka peaking about 5ka before the LGM (Robert, 2004; Ibarra *et al.*, 2014; Maher *et al.*, 2014), with this history of effective moisture supporting a fluctuating (low during MIS3) Lake Manix throughout this period (see Section 26). Accordingly, other records from the Mojave Desert show cooler and wetter conditions around Victorville at 43-12ka (Kulongoski *et al.*, 2009), a peak in groundwater levels at Valley Wells 40-32ka (Pigati *et al.*, 2011) and that Lake Baldwin in the San Bernardino Mountains peaked at ~52ka and 45ka but persisted until ~12ka (Kirby *et al.*, 2006; Blazevic *et al.*, 2009; Glover *et al.*, 2017).

Notable precipitation peaks are recorded within a clay proxy record from ocean core ODP893 around the Santa Clarita River (~100km northwest of the Mojave River Headwaters) at 90-82ka, 65-55ka, ~45ka, ~35ka and 24-22ka (Robert, 2004; Cyr *et al.*, 2015), each of which correlates with high stands in Lake Manix (90-82ka is uncertain) and is therefore associated with increased flow in the Mojave River (Reheis *et al.*, 2012; Reheis *et al.*, 2015). Reheis *et al.* (2015) associated millennial-scale lake level fluctuations of up to ~20m between 40ka and 25ka with Dansgaard-Oeschger (D-O) cycles and associated larger precipitation events with Heinrich Events 1-6 (Figure 3.8). Consequently, high stands in Lake Manix correlate with patterns of SST along the Californian coast (ODP 893), the Devil's Hole speleothem record (which tracks Pacific SST) and precipitation near the SBM (Robert, 2004) (Figure 3.8). However, the record of Manix lake level fluctuations proposed by Reheis *et al.* (2015) is limited in that it does not include any history of the lake before ~40ka due to the upper age limits of radiocarbon dating and limited datable evidence from MIS3-5 within the sedimentary record of the previously studied cores (Jefferson, 2003; Reheis *et al.*, 2012). It

is likely that lake level fluctuations before 40ka were similarly related to the patterns of D-O cycling which have been visible in SST changes (associated with the California Current) (Hendy and Kennett, 2000), the peaks in precipitation along the Californian coast (Robert, 2004), large flow events within the Mojave River (Cyr *et al.*, 2015) and the Devil's Hole speleothem record over a much longer period (Winograd *et al.*, 2006).

Inferred avulsions of the Mojave River between the Manix and Harper Lake basins add an additional complexity to the Manix lake level record. The Mojave River fed the Harper Lake basin on numerous occasions from 575-475ka (Cox *et al.*, 2003), recording at least one high stand in the past 70ka. It was hypothesised by Enzel *et al.* (2003) that the Mojave River fed both Lakes Harper and Manix simultaneously as there is little evidence in the Lake Manix record for a hiatus in sediment accumulation during the Late Pleistocene (Jefferson, 2003). Given the limited contemporary analogues for such a system, Meek (2004) considered it more likely that the river alternated between supplying water to the Harper and Manix basins. Garcia *et al.* (2014) identified a single Harper Lake high stand dating to 45-40ka using a combination of radiocarbon and luminescence dating ages. There are, however, a number of limitations to the ages presented by Garcia *et al.* which they acknowledge. Firstly, the radiocarbon ages are close to the usable limit for the technique and it would only take a small quantity of modern carbon to notably affect their conclusion regarding a single high stand. Secondly, the luminescence (IRSL) dating protocol which they used required a large fading correction (~8%) adding a significant uncertainty to the final age (see Section 5). Meek (2000) reported outcrops of lacustrine strata in the basin (without stratigraphic context) which suggested at least two lake stands, one at ~25ka (uncalibrated) and another which gave an infinite age (>30ka).

The cutting of Afton Canyon at ~25ka drained Lake Manix (Reheis and Redwine, 2008). Subsequently the Mojave River has primarily flowed into the Cronese and Soda/Silver Lake basins (Enzel *et al.*, 2003; Reheis and Redwine, 2008). Meek (1990) and Dudash (2006) argued that the Mojave River periodically flowed into the Coyote Basin between 15-12ka. Similarly, subsequent flow into the Troy Lake basin was suggested by Meek (1999), though evidence for such lake stands is limited.

3.3 Influences on geomorphic processes

This section synthesises the climatic history into the related controls on the geomorphic systems: sediment generation, sediment supply, sediment availability and transport capacity.

3.3.1 Sediment generation

Sediment generation is important because it is responsible for weathering bedrock material to a suitable size for aeolian transport (sand-sized), though little aeolian sediment is deflated directly from the bedrock (Bullard and Livingstone, 2002). Weathering in drylands is related to the physical processes associated with thermal expansion within rocks, the expansion of plant roots in cracks in a rock's surface, salt weathering and chemical weathering processes (related to moisture availability) (Cooke *et al.*, 1993). Moisture balance in the region is related to the overall arid-humid cycles of the global climate system (outlined above) and also the specific history of moisture for the SW USA such as was able to sustain Lake Manix even during interglacials. Consequently, the rate of sediment generation is likely to have varied in line with changes in the regional moisture balance (see above), though over the timescales considered by this study it is likely to be insignificant.

3.3.2 Sediment supply

Most sediment supply to aeolian systems is provided as 'secondary supply' from fluvial/alluvial or lacustrine systems rather than being deflated directly from weathered bedrock/hillslope material (Kocurek and Lancaster, 1999; Bullard and Livingstone, 2002). The Mojave River is the most probable source for much of the aeolian sediment within the Cady Mountains, with cores from Lake Manix indicating that inundations from MIS12 to MIS2 deposited >45m of sediment in the basin (Jefferson, 2003; Reheis *et al.*, 2012). Sediment supply to the Manix Basin between 120ka and the cutting of Afton Canyon (~25ka) has been near continuous (supply is expected to diminish when the Mojave River was maintaining Harper Lake high stands, although no obvious break has been presented within the Manix Basin sedimentary record (Enzel *et al.*, 2003)). Sediment supply from the Mojave River likely increased following tectonic changes upstream of Barstow which led to a greater volume of sediment being transported into the Manix Basin after ~75ka (Cox *et al.*, 2003). Peak periods of sediment supply from the Mojave River were concurrent with the precipitation maxima at 90-80ka, 65-55ka, ~45ka, and ~35ka before sediment supply to the

lake was virtually shut down after the cutting of Afton Canyon (Robert, 2004; Reheis and Redwine, 2008; Cyr *et al.*, 2015).

Multiple distinct sedimentary environments existed in the Manix Basin between 120ka and 25ka, with their spatial distribution largely related to their proximity to the Mojave River inflow (or other significant channels) (Reheis and Miller, 2010). The remainder of this section briefly describes the relevant facies of the Manix Basin and their potential significance to the aeolian system. The fine grain sediments which constitute typical lake bed material are of little relevance to the aeolian history of the Cady Mountains as their grain size is too fine (Byers, 1960). However, the Manix Basin also exhibits extensive fluvial-deltaic and shoreline facies with abundant sand-sized sediment, which could provide a viable sediment source for aeolian landforms.

Size and nature of Manix Fan-Delta

Where the Mojave River flowed into Lake Manix a broad deltaic plain formed (Meek, 2004), often referred to as the Manix Fan-Delta (Figure 3.1) (Enzel *et al.*, 2003). The Fan-Delta is characterised by a gradual shift from unconsolidated, parallel-bedded pebbly sands and gravels (proximal deltaic deposits) where the Mojave River enters the Manix Basin (near Yermo), to tan-coloured poorly to moderately sorted sands and silts which are exposed near Soldier Mountain (distal deltaic deposits) (Meek, 1994; Reheis and Miller, 2010; Phelps *et al.*, 2012). Jefferson (2003) argued that the sediments of the fan-delta were deposited at Manix Wash (close to the centre of the basin) from ~60ka. This was attributed to the pulse of sediment associated with the incision of the Mojave River north of Barstow hypothesised by Cox *et al.* (2003). As the fan-delta grew it occupied an increasingly larger proportion of the basin, eventually prograding onto the pre-existing lake sediments of the Coyote sub-basin (Hagar (1966) reported in Meek (1994)). The growth of the Manix Fan-Delta primarily occurred across the broad and flat plain to the south of the Mojave River's contemporary course (the Newberry Triangle – Figure 3.1) and hence it expanded disproportionately towards the Troy sub-basin (Meek, 1990). Jefferson (2003) proposed that the growth of the fan-delta eventually led to the isolation of the Coyote and Troy sub-basins shortly before the cutting of Afton Canyon. Growth of the Mojave Fan-Delta will have been limited after the draining of Lake Manix, however fluvial deposition on the Fan-Delta continued into the mid-Holocene (Meek, 1990). Consequently, the deposition of fine grained Lake Manix sediments

probably centred on the Afton sub-basin during much of MIS4 (Jefferson, 2003) and presumably later (Meek, 2000). In summary, the history of the Manix Fan-Delta indicates that an extensive area (>7m close to Soldier Mountain) of surficial and dominantly sand-sized material was deposited across the western boundary of Lake Manix during the Late Pleistocene.

Sediments of the Coyote Basin

The Coyote Basin provides evidence of sediments suitable for aeolian transport. Across the aforementioned fluvio-deltaic plain, which encroaches into the sub-basin, north-trending inverted palaeo-channel sediments 1-2m above the wider plain were interpreted by Hagar (1966) (and reported by Meek, 1994) to signify a history of aeolian deflation from the surface at this location (presumably of sand-sized material). Further evidence of aeolian (sand-sized) activity on this surface are the ‘mega-ripples’ which Meek (1994) cite as examples of post-depositional reworking by westerly and north-westerly winds before being stabilised under their current lag surface. Corresponding well-sorted dune deposits to the west of the Coyote playa were noted by Byers (1960).

Shoreline and other features

Shoreline deposits such as beach ridges, tombolos and gravel bars (which constitute rounded pebbles and coarse sand) adjacent to the Troy and Coyote playas are attributed to wave action during its multiple Manix high stands (Dibblee and Bassett, 1966; Meek, 1990; Reheis and Redwine, 2008; Phelps *et al.*, 2012). Such features are commonly heavily dissected, suggesting that they were more extensive in the past (Reheis and Redwine, 2008). Though they may have contained quantities of sand-sized material, they likely provided a lesser quantity of sediment than might be expected from the extensive fan-delta sediments, but they remain notable examples of suitable nearshore sediment supply (Meek, 2000).

This section has demonstrated that the Manix Basin contains significant quantities of sediment which is suitable for aeolian deflation, particularly in the Manix Fan-Delta and shoreline features. It is also likely that this sediment supply has been potentially continuous between 120-25ka, but with a number of peaks associated with lake high stands and large river-flow events. Since 25ka sediment supply is associated with Mojave River flow events, especially during the Holocene when the river only flowed ephemerally. Such sediment is

only useful to an aeolian system, however, if it can be made *available* for deflation. This will be the consideration of the following section.

3.3.3 Sediment availability

As outlined in Section 2.2.1, in semi-arid environments sediment availability for aeolian transport is largely modulated by moisture balance, with availability being generally expected to be lower under cooler/wetter conditions owing to the role of moisture for inhibiting aeolian entrainment (Bauer, 2009 #1621 Bauer *et al.*) and promoting greater vegetation cover (Langbein and Schumm, 1958; Lancaster, 1997; Kocurek and Lancaster, 1999). After Lake Manix drained (~25ka – Reheis *et al.*, 2012) and the lake desiccated, significant quantities of sediment will have been made available for aeolian deflation. Subsequent ephemeral deposition of sediment from the Mojave River into either the Fan-Delta (Meek, 1990) or the sub-basins (Meek, 1999; Dudash, 2006) also became available shortly after the flow-event ceased (as per Clarke and Rendell, 1998).

Lake Manix has existed almost continually for ~500ka, having varied in its lake depth/height across this time period and with different facies distributed across the basin (described above). Against this background, the aeolian system has been operating for longer than just since the last deglaciation (Dietze *et al.*, 2016) (Section 7.2). For example, truncation of the sand ramp at Soldier Mountain (Bateman *et al.*, 2012) requires that the ramp pre-dates at least one phase of elevated water levels (altitude approximately corresponds with the ~543m high stand – Reheis and Redwine (2008)). Whilst the Manix Basin contained a perennial lake (before ~25ka), it is expected that even modest lake level fluctuations (~20m – Reheis *et al.*, 2015) exposed sediments previously supplied to the system and thus making them available for deflation. Two modern analogues for such a process are described below.

Analogue 1: Aral Sea

The Aral Sea was a significant inland lake, but whose lake level declined following a wave of abstraction from the rivers that fed the lake which began in the 1960s. The deflation of sediments and aeolian accumulation began to be observed within 15 years and was especially noticeable in deltaic areas (deltas are raised and better drained so desiccate faster). An increase in the rate of abstraction occurred at 1973-77 which further increased the rate of desertification over the following 10-20yrs to the point where previously fixed barchan dunes

were observed to migrate (Saiko and Zonn, 2000). A study of sand drift within the region identified that the sands were deflated rapidly, reaching an initial peak of aeolian transportation at 1966–1970. Further peaks in aeolian transportation were identified at 1984–1986 and 2000–2002 and were related to a combination of irrigation-driven and climatically-driven river flow variability, with sands moving at a rate of $\sim 1000 \text{ t km}^{-1} \text{ yr}^{-1}$ in a south-westerly direction during these events (Issanova *et al.*, 2015). The implication for this example is that the decline in lake level led to the rapid availability of geomorphically significant quantities of sediment from deltaic areas adjacent to the Aral Sea.

Analogue 2: Nile Delta

The Nile River Delta has been a significant sediment source for the Sinai-Negev sand sheet, with the timings for the aeolian system being associated with the combination of sea level and climatic change during the Late Pleistocene and Holocene, through their combined impact of sediment supply and availability. At ~ 35 -13ka the sediments deposited on the Nile Delta were predominately coarse-grained, forming sandy alluvial plains between the braided or anastomosing channels which, because they were seasonally dry, sand could be deflated from these deposits (Stanley and Warne, 1993; Muhs *et al.*, 2013). The implication of this example is that the timings for a significant aeolian system were driven by the supply and subsequent availability of sediments amenable for aeolian transportation, from a seasonally dry-deltaic environment.

Sediment availability will also be spatially variable because the sub-basins of Lake Manix behaved semi-independently due to the presence of a sill (elevation $\sim 541 \text{ m}$) that separates the Coyote sub-basin from the Afton and Troy sub-basins (especially effective when the Mojave River flowed directly into the Coyote sub-basin). Additionally, the growth of the Manix Fan-Delta is understood to have led to the isolation of the Troy and Coyote sub-basins (Cox *et al.*, 2003; Jefferson, 2003; Reheis *et al.*, 2015). It is therefore possible that one sub-basin drained (and hence sediment could become available) while other sub-basins received Mojave River waters (Meek, 2004).

Overall, the history of lake level fluctuations in the Manix Basin will have repeatedly covered and exposed deltaic and shoreline sediments, in turn driving their (un)availability. Following sediment being made available the aeolian processes only have a limited window of

opportunity for deflation and sediment transport before availability is shut down by the exhaustion of sediment, the generation of a lag surface, the raising of lake levels or the re-establishment of vegetation cover (Kocurek and Lancaster, 1999). Furthermore, sediments active within the Cady Mountains' aeolian system need not have been made available from the fluvio-lacustrine system *each time* that they became active. Once aeolian sediment has been transported away from the lake environment then there is also the potential for the remobilisation and recycling of sediments.

3.3.4 Sediment transport

The wind regime of a region is fundamental to sand transport capacity and direction, and hence the operation of any system (Kocurek and Lancaster, 1999). Under current conditions winds within the region are typically from the west and are strongest in spring and summer, but with some northerly component during the autumn and winter (Section 3.2.2) (Berry *et al.*, 1981; Laity, 1992; Zimbelman *et al.*, 1995; Muhs *et al.*, 2017). Winds sufficient for sand transport ($>4\text{m s}^{-1}$) are predominately associated with the passage of winter storms and westerly winds (Bagnold, 1941; Halfen *et al.*, 2015). Topographic steering and sheltering is evident within some wind records, particularly around passes (e.g. where the Mojave River travels between Barstow and Daggett) and along troughs (e.g. Bristol Trough) (Berry *et al.*, 1981; Griffiths *et al.*, 2009).

Reconstructions of large-scale climate across the Mojave Desert suggest an important role for westerly (Pacific-sourced) weather systems across much of the last 120ka. Wind speed will have been adequate for sand transport for much of this period (Halfen *et al.* (2015) – based on wind data modelled by Bartlein *et al.* (1998)). Ventifact evidence from the Cady Mountains (Laity, 1992) is widespread and suggests a dominant history of westerly sand-transporting winds across the region (Figure 3.5). Observed variability within the record does, however, indicate the existence of a notable northerly component (capable of transporting sand) and the influence of topography on local wind flow (and hence sand transport) patterns is evidenced by localised variation in ventifact orientation (Laity, 1992). It is important to remember that ventifact evidence may only be representative of wind direction during the last significant episode of sand transport (Laity and Bridges, 2009). Overall the record of palaeo-winds within the Cady Mountains is relatively unconstrained in

terms of direction, strength and seasonality, but we can expect a strong westerly bias to the wind regime for much of the last 120ka.

3.4 Summary

The purpose of this chapter was to describe the location of the study and its field sites (Section 3.1), to outline the geological and climatic boundary conditions for the study location (Section 3.2) and to synthesise this history into an expectation for the key drivers on the aeolian system in order to facilitate investigation into its historic operation (Section 3.3). The Mojave Desert provides a good region for study because the history of its boundary conditions over the past ~120ka are reasonably well constrained. Sediment supply to the Manix Basin appears to have been broadly continuous over much of the last 120ka, but fluctuating in association with peaks of discharge in the Mojave River. Since the lake drained, sediment supply has been associated with ephemeral river flow events, providing sediment which can become available for deflation over short timescales (in the order of months) (in a manner analogous to that observed by Clarke and Rendell, 1998). Before the lake drained, sediment availability was most probable within the Manix Fan-Delta and shoreline deposits which would have been repeatedly deposited, exposed and reworked by the many lake level fluctuations which operated over the past 120ka. Transport capacity is not understood to be a limiting factor for aeolian systems in the Mojave Desert, with westerly winds being dominant for sand transport (Halfen *et al.*, 2015).

4 Methods

This thesis investigates how complex topography influences aeolian deposition and landform development. The results are split into those which consider the distribution and form of aeolian deposition in relation to the topography of the mountain block area (Chapter 6) and those which establish the process history of the aeolian landscape. This chapter describes the methods used to achieve these outcomes. Mapping the distribution and form of aeolian deposits within the Cady Mountains will require methods for: mapping land cover (Section 4.1); measuring the morphometry of the mountain block (Section 4.2); developing a record of stratigraphy, textural and provenance data for the aeolian deposits (Section 4.3) and combining these with the timings of aeolian activity derived using luminescence dating (Section 4.4).

4.1 Determining the distribution of land cover

This section describes the method for mapping the distribution of land cover across the mountain block using remote sensing data.

4.1.1 Data sources and preparation

The Landsat 8 image acquired from the USGS (via <http://earthexplorer.usgs.gov>) on 27th September 2013 at 18:24 GMT was cloud free. The presence of vegetation can influence the land surface visible in remote sensing imagery because the spectral characteristics of plants differs from that of a bare rock surface. However, the influence of vegetation within the image is thought to be insignificant because the growth of annual plants is severely limited during the summer months (Beatley, 1974) and the adaptations of species prevalent within drylands (e.g *Larrea tridentata*), especially their lower densities and the much lower proportion of the vegetation that is not photosynthetically active, can make dryland vegetation difficult to distinguish from bare surface (Dawelbait and Morari, 2008). This suggests that vegetation should not pose a significant issue for this study. Image preparation and land cover classification of the Landsat imagery were performed using ERDAS Imagine 2013.

4.1.2 Mapping of land cover using remote sensing data

The land cover map was created from a supervised classification of the Landsat 8 image with a spatial resolution of 30m. To maximise the accuracy of the land cover classification an

appropriate combination of the spectral bands was selected for analysis. Various indices have been proposed to aid the classification of land cover types (e.g. Normalised Difference Vegetation Index – after Rouse, 1974). This study utilised the Eolian Mapping Index (EMI) developed by Khiry (2007) which is a false-colour composite which emphasises areas of surficial sand and a low density of vegetation (yellow) thereby rendering them more easily distinguishable from areas with a higher rock cover (blue) or areas with significant vegetation coverage (red). The EMI is performed by displaying the NIR, R and R/NIR bands as the RGB channels respectively and is shown in Figure 4.1. The primary limitation of the EMI is that the above classes cannot be easily distinguished from areas of urban land cover or surface water (Khiry, 2007). The occurrence of these land cover types within this study area is, however, negligible. To perform the supervised classification and assess its accuracy, data on the surface characteristics at the time of acquisition are required. Land cover reference data were acquired through a combination of field survey, geotagged photographs and detailed imagery from Google Earth (see below). This data is required for two distinct purposes: (1) training data for the supervised classification and (2) reference data for performing an accuracy assessment using an error matrix (Congalton, 1991). To avoid using the same data for both purposes, the image was classified using training data derived from areas outside the defined study area.

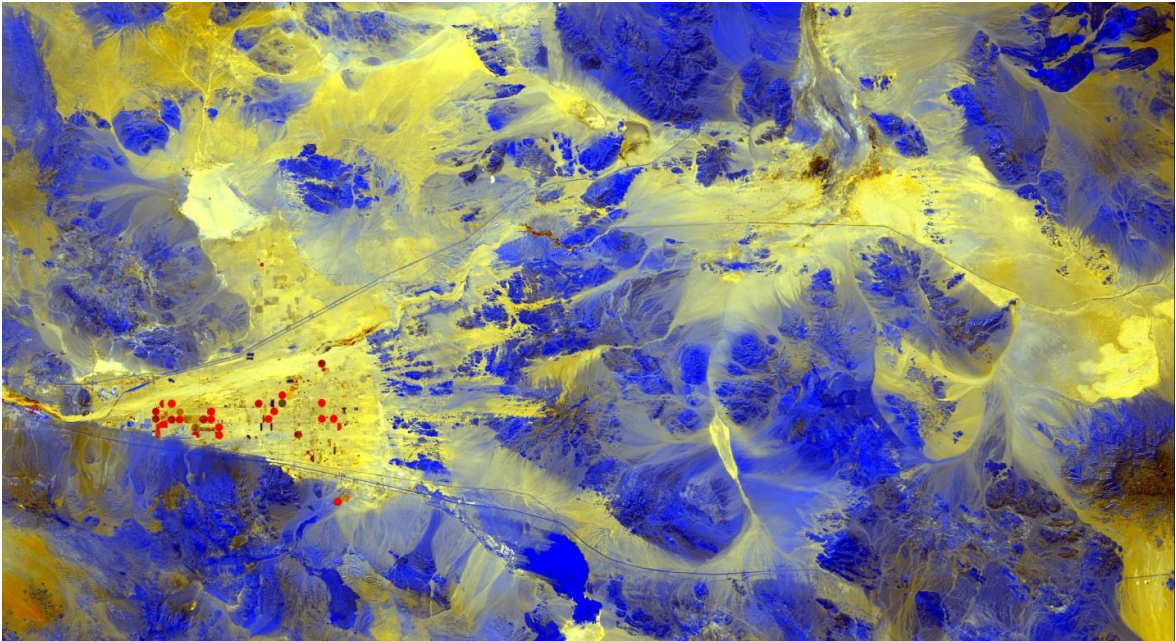


Figure 4.1: A subset of the Landsat 8 image of the study region prepared using the EMI false colour composite described in the text (Khiry, 2007). Yellow, blue and red colours correspond to sand, rock and vegetation. Landsat-8 image courtesy of the U.S. Geological Survey.

Training data was generated by creating polygons with areas of greater than 50 pixels at >10 locations across the Landsat image which were known to possess each of the required land cover classes (as Jensen, 2005). For classification purposes, the land cover of the Cady Mountains was divided into three land cover types: (1) Sand Cover, (2) Stone-Covered Sands and (3) Rock Surfaces (Figure 4.2). A fourth ‘other’ class incorporates any other land cover types. Training data was chosen to represent the three surface classes, where the maximum likelihood classification algorithm determines the absolute spectral boundaries between these classes and their ultimate distribution of these within the landscape (Foody, 1992).

Land Cover Class Exemplars

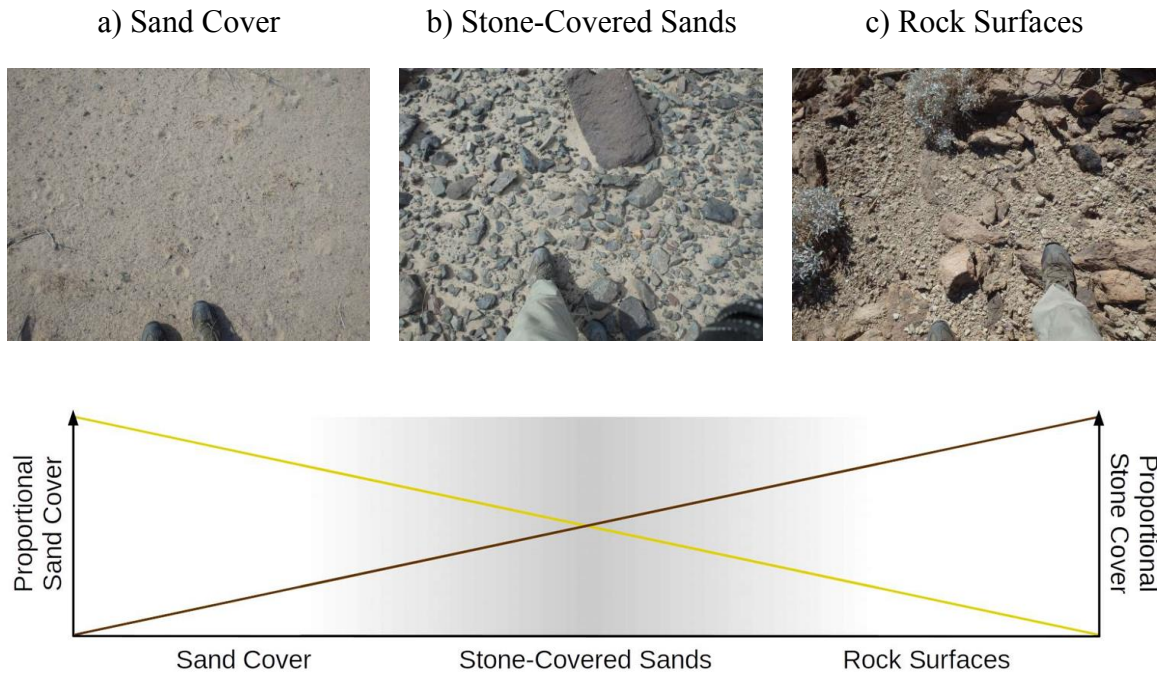


Figure 4.2: Spectrum of land cover classes observed in the Cady Mountains. Surfaces range from an almost pure sand cover (a) through sands with a stone cover (b) to surfaces of bedrock and/or stones (c). Schematic representation of the relationship between these covers (brown line = stone cover; yellow line = sand cover) is shown (lower).

Reference data for the error matrix was acquired using 200 randomly generated points within the study area whereby land cover reference data was determined using a combination of field notes, geotagged photographs and high-resolution Google Earth Imagery. In addition, a further 67 points were used which relate to geotagged photographs (30m location error) which were taken to document the land cover at the field sites used. The use of Google Earth imagery as a tool for the generation of reference data was adopted after being successfully applied by various studies across multiple environments (e.g. Bhattarai, 2011; Chaplin and Brabyn, 2013; Olofsson *et al.*, 2013; Fonji and Taff, 2014). Owing to the lack of heavily vegetated locations within the area of interest, 10 points of reference data for vegetated surfaces were collected outside of the study location (Figure 3.3). To allow for the location error for the GPS devices (~30 m) the reference data and land cover classification were considered to agree if the reference data at each location matched the land cover of more than half of pixels within a 3x3 window of pixels centred on each location. An error matrix compares classified and reference land cover for the different sample locations and is

commonly used to assess the accuracy of the classification. The error matrix creates an estimation of the overall accuracy as well of that relating to errors of omission (user’s accuracy) and commission (producer’s accuracy) and is shown in Table 4.1 (Congalton, 1991). The data analysis for the error matrix was performed using QGIS 2.14.

Table 4.1: Error matrix for the land cover classification, adapted to only show the Sand Cover, Stone-Covered Sands, Rock Surfaces and Other land covers. Numbers in the upper grid relate to the number of validation locations which conform to each category.

		Reference Data				Total
		Sand Cover	Stone-Covered Sands	Rock Surfaces	Other	
Classification Data	Sand Cover	57	7	0	0	64
	Stone-Covered Sands	7	71	5	0	83
	Rock Surfaces	2	14	102	0	118
	Other	0	0	1	10	11
	Total	66	92	108	10	276

Overall Accuracy 87%

<u>Producer’s Accuracy</u>		<u>User’s Accuracy</u>	
Sand Cover	86%	Sand Cover	89%
Stone-Covered Sands	77%	Stone-Covered Sands	86%
Rock Surfaces	94%	Rock Surfaces	86%
Other	100%	Other	91%

The classified image shows an overall accuracy of 87% and has individual user’s and producer’s accuracies greater than 75%. Anderson (1971) suggested that 85% is a suitable threshold for deeming whether a land cover classification is adequate and states that the individual producer/user accuracies should be ‘about equal’. As the accuracies presented in Table 4.1 generally exceed this criterion, the classification performed by this study was deemed satisfactory in order to investigate the pattern of aeolian deposits within the Cady Mountains. The Other class was removed from further consideration because it accounts for a negligible proportion (0.1%) of the final image, being mostly present at an area of high elevation vegetation cover close to the Cady Peak (Figure 6.22). The final classified image is shown in Figure 6.4.

4.2 Mapping surface morphometry

Geomorphometry provides a useful approach to describing the form of the topography within the landscape across a specified range of spatial scales (Section 2.1.3) (Evans, 1972; Wood, 2009). Here a representation of surface form will be achieved by: 1) the mapping of elevation and its derivatives (e.g. aspect, slope) and 2) a morphometric feature classification designed to represent the shape of the landscape through five morphometric shapes: pass, peak, plain, ridge and channel (here the term valley is used instead of channel) (Wood, 1996, 2009). The distribution of these landscape parameters/features will be compared with the mapped distribution of sand in the landscape (as Section 4.42) to investigate the relationship between the form (morphometry) of the mountain block topography and the distribution of sand therein as part of a nested landscape description (Chapter 6).

4.2.1 Data sources and processing

The digital elevation model (DEM) used in this study originates from the USGS National Elevation Dataset and was subset and re-sampled to the same coverage, spatial reference and spatial resolution (30x30m) as the Landsat 8 image described in Section 4.1. The morphometry was classified and mapped using the freeware geographical information system (GIS) ‘Landserf’ version 2.3 (Wood, 2009). Landserf’s primary advantage over other GIS programmes is its ability to consider morphometric parameters such as elevation and its derivatives (e.g. aspect, slope) as well as shape across a specified range of scales (rather than just using a 3x3 grid). This uncouples the scale of analysis from the resolution of the DEM available, which is important because landforms are commonly scale-dependent in their interpretation and extent (Wood, 1996; Fisher *et al.*, 2005). Files were converted into floating point raster type for import into Landserf and were clipped to the study location (Figure 3.1).

4.2.2 Morphometric parameter determination

Landserf derives estimates of slope and aspect (which are first and second order derivatives of elevation – Evans, 1972) using a bi-quadratic polynomial approximation of the surface across a specified window size (or across a range of window sizes) by establishing the rate of change of three orthogonal components (plan curvature, profile curvature and slope) (Wood, 1996, 2009). Where a multi-scale parameter determination is adopted, Landserf generates either an evenly weighted mean value of the parameter for a pixel across the range of window sizes for continuous parameters (i.e. slope and aspect) or an evenly weighted

modal value for the pixel across the range of scales for categorical variables (i.e. the morphometric classification) (Wood, 1996). The process for determining an appropriate range of window sizes is discussed in the next section.

Aspect was calculated as a continuous variable across the raster dataset but was categorised into 16 classes of equal width for presentation. Similarly, slope is shown as a series of classes chosen to represent areas of no discernible slope (0-2°), intermediate slopes (2-11°) and steep (>11°) slopes (adopted as Miliareisis, 2001; Norini *et al.*, 2016). Because much of the sand tended towards the lower angle portions of the piedmont slopes, that class was sub-divided into shallower (2-6°) and steeper (6-11°) piedmont slopes.

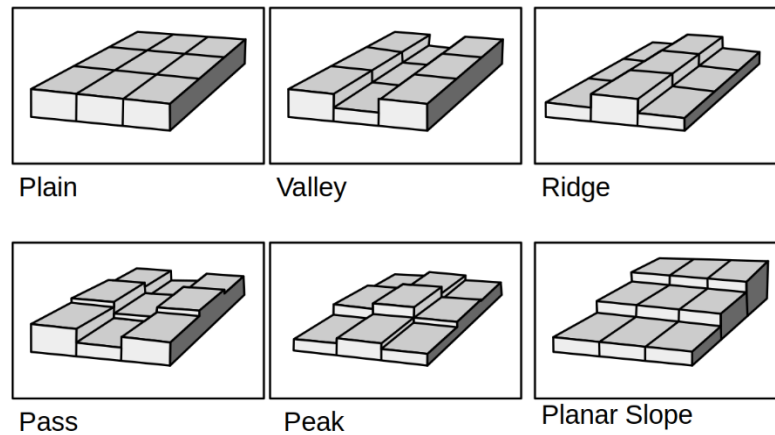


Figure 4.3: Six morphometric feature classes (modified from Wood, 1996). Pits are excluded from discussion as they account for a negligible proportion of the land surface (0.17%).

The morphometric classification utilises the classes of pass, peak, plain, ridge and valley and was derived following Wood (1996) and Fisher *et al.* (2005) (Figure 4.3). The morphometric analysis provided by Landsat portrays surfaces without any significant breaks of slope to be a “plain” (Wood, 1996). Within the area of interest under discussion here this representation of “plains” differs from that of a dictionary definition which describes a plain as an “*extensive tract of flat land or a gently undulating terrain without prominent hills or depressions*” (Whittow, 1984). It can be seen that the latter definition is a subset of the former and distinguishes plains from what are here termed ‘planar slopes’ (e.g. hillslopes or piedmont features) and which have a non-zero slope. The distinction used here is whether these surfaces have a discernible slope, again adopting a slope threshold of 2°. Any relationship between

preferential sand accumulation and preservation and valley orientation was investigated by finding clusters of pixels classified as valleys with a spatial extent greater than 0.5km² (six pixels) and by deriving the main angle for the valley floor visually.

As very few areas have slope and plan/profile curvatures of zero, Landsat sets a minimum tolerance threshold to determine plains. The first, slope tolerance, is used to define how steep a surface must be for it to be considered part of a 'pass', 'peak' or 'pit' and the second, curvature tolerance, is a dimensionless ratio which defines how concave/convex a part of the landscape must be for it to be a morphometric feature (i.e. not a plain) (Wood, 1996). For both parameters, the values of 1° and 0.1 respectively were used and peaks were only classified as such where they had a relative drop to the surrounding topography of more than 50m. All three are arbitrary values which depend on the relative topography and the scale of interest and are chosen by determining the suitability of the resultant classification (as Fisher *et al.*, 2005).

4.2.3 Scale of analysis

Determining an appropriate scale is crucial when discussing morphometry, as landforms can be inherently ambiguous in their spatial extent or landforms of different spatial scales can be superimposed upon each other (Fisher *et al.*, 2004). Because no single "best" scale necessarily exists (Hengl, 2006), multi-scale analyses of morphometry help to mitigate against the scale dependence of morphometric features (Wood, 1996). Here the morphometric parameters/classes were derived from the DEM using a multi-scale analysis which calculates the average value for a pixel across a range of scales. The scales selected in this study range from 3x3-41x41 and allows for the representation of features with length scales between 90m and ~1.2km. This was deemed appropriate for investigating the Cady Mountains because it classifies the major landscape features adequately, but without being significantly influenced by smaller superimposed features. This was established by visually comparing the map of morphometric features created using window sizes of increasing size until an optimum was found. The same window size was used for determining all parameters: aspect, slope and morphometric shape.

To highlight the impact different ranges of window sizes have on the morphometric classification of the landscape, 3D visualisations of the classifications produced using a

minimum window size of 3x3 pixels and maximum window sizes of 11x11 (a), 41x41 (b) and 67x67 (c) are shown in Figure 4.4. The classification derived using the 11x11 maximum window size (Figure 4.4a) classifies landscape features with a length scales of 90-330m. Consequently, the resultant classification identifies much of the small-scale topography superimposed upon the major ridges, hills and mountains. By mapping the small-scale features, the classification provides a poor characterisation of the larger-scale features such as the valley which is marked with a rectangle on Figure 4.4, identifying it as a combination of plain, planar and valley classes. This scale of analysis was deemed to be too noisy for this study which is examining the distribution of sand within the Cady Mountain block at larger scales.

Conversely the classification performed using a 67x67 maximum window size (c) classifies landscape features with a plan-view diameter of 90m - 2.5km. As the influence of any individual window size within this range is evenly weighted, this smoothes out many of the details of the landscape to create a large-scale 'blocky' characterisation of the landscape. The result of this is that many of the smaller, more complex areas of topography which are associated with accumulations of sand are omitted from the feature classification (for example the area within the dashed oval in Figure 4.4).

The classification performed using a 41x41 maximum window size (Figure 4.4b) was selected as most appropriate because it reproduced the meso-scale topography of the mountain block without much of the "noise" associated with the smaller-scale landscape features, but without averaging out many of the small-medium sized topographic obstacles present within the study region. This window size adequately identifies the valley highlighted by the rectangle in Figure 4.4b as well as identifying the pass at the head of the valley. Small changes in the window size (for example adopting a 37x37 or a 45x45 maximum window size) do not significantly influence the determination of parameters. When tested, the variation in the number of pixels being a member of any class/band changed less than five percent. From this it was concluded both that the adopted window size was appropriate for the scale of analysis which was required and that small changes in these variables would have had a significant effect on the output.

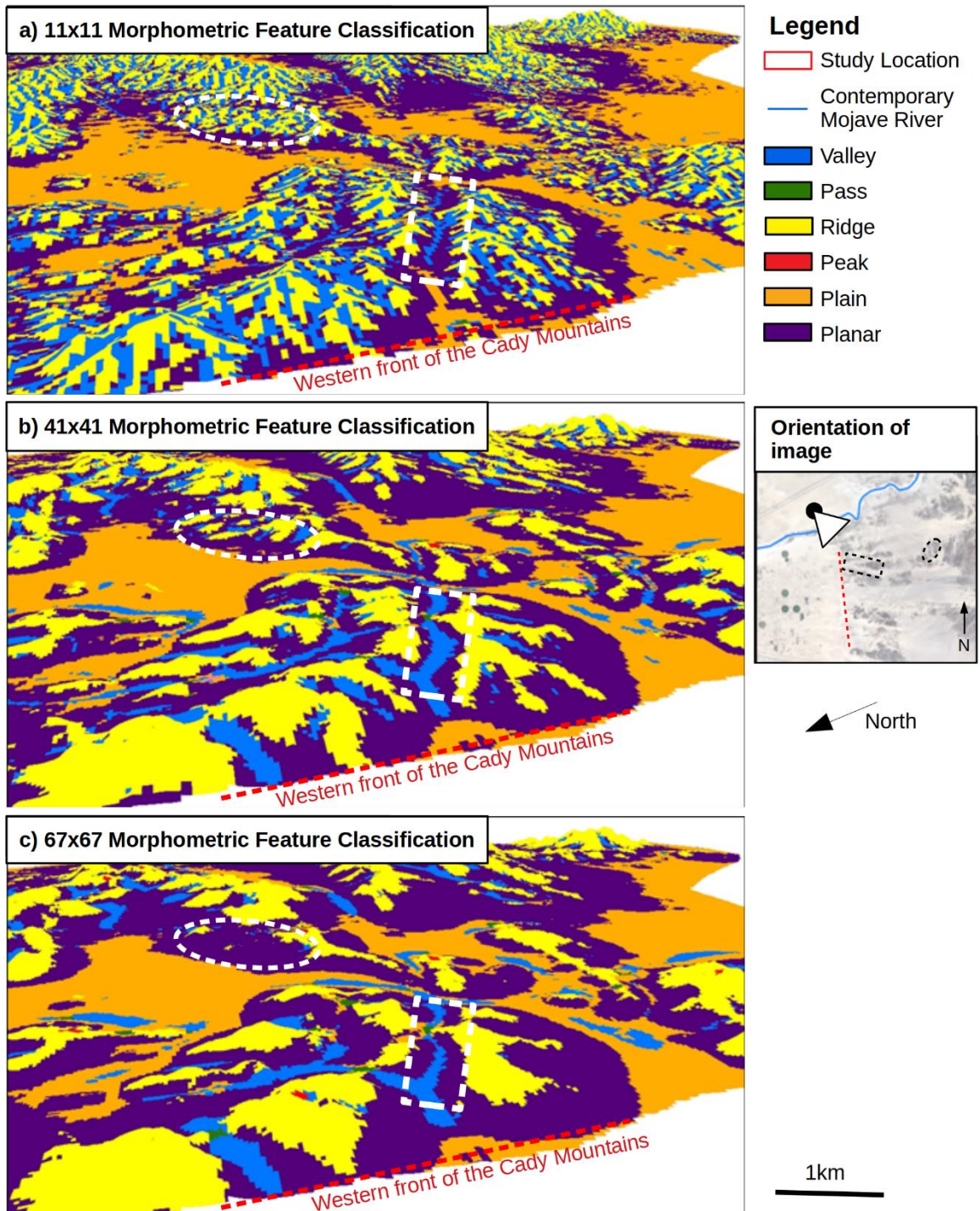


Figure 4.4: Morphometric classification of a section of the Cady Mountain block performed using three different maximum window sizes: a) 11x11, b) 41x41 and c) 67x67. Landsat-8 image and National Elevation Dataset courtesy of the U.S. Geological Survey. Map data © OpenStreetMap contributors.

4.2.4 Analyses

The purpose of this study is to investigate whether a relationship between the distribution of land cover (as mapped in Section 4.1) and the morphometry of the mountain block (as

represented by the morphometric parameters described above) exists. The above datasets can be combined so that the land cover and morphometry of the location are known for each pixel in the landscape (e.g. Sand Cover, 2° slope, southwest-facing, planar...). From this the number (and proportion) of pixels within the landscape which correspond to each parameter/feature can be determined (e.g. X% of Sand Cover is south-facing). Finally, whether the distribution of these land covers across the landscape is systematically related to topography can be assessed using a Chi Square test (Hammond and McCullagh, 1978). These analyses and their outcomes will be described in Chapter 6.

4.3 Developing a record of process history

This section outlines the method used to develop the process history associated with the deposition of aeolian sands within the Cady Mountains including stratigraphic description (4.3.1), sediment provenance (4.3.2), sediment texture (4.3.3) and chronology (4.3.4).

4.3.1 Stratigraphic logs

Stratigraphic logs were created for each of the nine field sites identified in Figure 3.1. At each site, sections were limited to the height of the exposed sediments (sites CN, MC, RD, SM, WC) or to the depths of excavated pits (sites DN, ER, PK) and were cleaned to expose a fresh face before being logged.

4.3.2 Sediment mineralogy

Elemental concentrations were measured using Inductively Coupled Plasma Mass Spectroscopy (ICP-MS), Inductively Coupled Plasma Atomic Emission Spectroscopy (ICP-AES) or X-ray fluorescence (XRF) utilising the same method as the data for the luminescence dose rate (Section 4.4.4). Samples were primarily bulk samples from the luminescence samples, but also included seven samples collected from potential source areas. Because the aeolian deposits are constructed from primarily the sand-sized sediments, some samples also measured only the sand-sized fraction to ensure that the fine-sediment fractions were not significantly influencing their geochemical signature.

4.3.3 Textural analysis

Particle size distributions between 0.01µm and 2000µm were obtained using a Malvern Mastersizer 3000 particle size analyser at the University of Leicester, UK. Samples were run through a 2mm sieve to remove any large particles and dispersed in a calgon solution to avoid

clumping of the sample prior to measurement. The measurement process determines the volume percent of the particles by laser diffraction analysis, and converts the result into weight percent for 100 size classes. Each sample was an average of three sub-samples and the grain-size measurement for each sub-sample was an average of five replicate measurements.

4.4 Luminescence dating

Optically stimulated luminescence (OSL) dating provides an estimate of the time elapsed since grains of semi-conducting minerals (usually quartz and feldspar) were last exposed to light (Wintle and Adamiec, 2017). In the context of aeolian sediments, this reflects the time since the burial of the sediment and is interpreted as representing the formation of that part of the landform (Singhvi and Porat, 2008; Preusser *et al.*, 2009; Rhodes, 2011). This section outlines the general methodological approaches adopted for sample preparation and luminescence measurement. Given the conflicting landscape interpretations resulting from previous chronologies (Section 3.1.1), Chapter 5 will then demonstrate the applicability of the method for use in the Mojave Desert, principally using data from two field sites with independent age control.

4.4.1 Fundamentals of luminescence dating

The luminescence signal is derived from the net-accumulation of electrons at defects in the crystal lattice of quartz and feldspar grains on exposure to ionising radiation (Aitken, 1985). Although this effect is slow, this accumulation of charge leads to a signal which increases with duration of time since the sediments were buried (Murray and Olley, 2002). Because the signal is reset by exposure to daylight or heat, grains of quartz and feldspar can be used as a dosimeter whereby luminescence dating procedures utilise the measurement of electrons trapped at defects within the crystal lattice (Preusser *et al.*, 2009). The most common explanation for these phenomena invokes the interaction of ionising radiation to create pairs of trapped electrons and holes which recombine when stimulated (with light in the case of optically stimulated luminescence) releasing photons in proportion to the number of luminescent recombinations which occur (Duller, 2004). Such defects commonly result from oxygen or silicon vacancies or the impurity of ions, the number of which can vary considerably between grains (Preusser *et al.*, 2009). The accumulation of charge trapped in the lattice of the mineral grains (the natural signal) can be measured via the luminescence

phenomenon to establish the total received radiation dose – termed the equivalent dose (D_e). The D_e can be derived by comparing the natural signal with a dose-response curve created through administering repeated laboratory-induced doses of various sizes before fitting this curve using (typically) a saturating exponential (Wintle, 1997; Aitken, 1998; Lowick *et al.*, 2010; Lowick *et al.*, 2012). By dividing this D_e by a measure of the natural environmental dose rate, the time since the burial of the sediment can be determined (Aitken, 1985).

4.4.2 Considerations for D_e determination

A fundamental consideration for luminescence dating is the mineral selected for analysis. K-Feldspar grains were widely utilised during the 1990s because of their bright infra-red stimulated luminescence (IRSL) signal and because their dose-response curve saturates at substantially higher doses than quartz (Duller, 1997), including (e.g. Wintle *et al.*, 1994; Rendell and Sheffer, 1996). However, K-Feldspar experiences the malign effects of athermal or “anomalous” fading whereby the accumulated charge diminishes unexpectedly owing to instability in some of the traps used by the IRSL signal (Wintle, 1973; Huntley and Lamothe, 2001; Auclair *et al.*, 2003; Lamothe *et al.*, 2003). In response to this, and following the development of the quartz single-aliquot regeneration (SAR) protocol (Murray and Wintle, 2000, 2003; Wintle and Murray, 2006), quartz has become more widely utilised as the target mineral because it does not suffer from anomalous fading and the resulting OSL ages typically demonstrate good comparability with independent dating control (Murray and Olley, 2002; Wintle and Murray, 2006; Rhodes, 2011). Under the SAR protocol the D_e for an aliquot is established by measuring the sensitivity-corrected net natural luminescence signal (often the initial 1.2s minus the final four seconds) and then relating this to a dose-response curve generated on a per-aliquot basis using several regenerated doses (Murray and Wintle, 2000). An example of the SAR protocol (for quartz grains) is shown in Table 4.2.

The SAR protocol was a significant improvement over previous protocols as it allows for the D_e to be determined using a single aliquot, thus minimising the influence of inter-aliquot variation from the measurement (Murray and Mejdahl, 1999), and because it monitors and corrects for changes in luminescence sensitivity during the measurement protocol (Wintle and Murray, 2006). Sensitivity correction is achieved by administering an invariant test dose (T_x) after each regeneration point (L_x), which is used to normalise the OSL signal (L_x/T_x) prior to plotting the dose-response curve (DRC) (Murray and Wintle, 2000). Aliquots are

rejected at the point of constructing the DRC if the repeat (recycling) point is not within $\pm 10\%$ of unity and the presence of a measurable signal following a zero dose is $>5\%$ of D_e (a recuperated signal – Murray and Wintle, 2000) as these are indicative of poor luminescence characteristics (Rhodes, 2011). Before each luminescence measurement of the sample, unstable signal components generated by artificial irradiation are removed by preheating (Wintle, 1997; Murray and Wintle, 2000).

Table 4.2: An example single-aliquot regenerative dose (SAR) protocol as adapted from (Murray and Wintle, 2000). As the sequence is repeated multiple times the ‘given dose’ (step 1) is varied during each run. During the first run the given dose is 0Gy (to capture the natural signal) and thereafter the given dose is varied during each subsequent run through a number of different doses to form a ‘dose-response curve’. Following this the sequence is repeated twice more using a given dose of 0Gy (to measure recuperation) and finally using a repeat of the given dose during the second run is given (to correct for sensitivity changes during the measurement of the sequence).

Step	Action
1	Give dose
2	Preheat (10s)
3	Stimulate for 40s (L_i)
4	Give test dose
5	Cut heat (10s)
6	Stimulate for 40s (T_i)
7	Return to step 1

There are, however, reported instances of quartz OSL proving problematic (including within the same region as this study, the Mojave Desert). In such circumstances quartz grains are observed to exhibit properties that are unsuitable for dating (Pigati *et al.*, 2011; Lawson *et al.*, 2012; Rhodes, 2015). Such properties include dim grains with low grain sensitivity, low bleachability, unstable non-fast signal components and a high thermal transfer, all of which can result in erroneous D_e estimates (Steffen *et al.*, 2009; Roder *et al.*, 2012; Rowan *et al.*, 2012). This suggests a level of quartz unsuitability within the region which can hinder the utility of luminescence dating in these locations. To this end, Lawson *et al.* (2012) observed highly variable quartz properties from six sites across the Mojave Desert which included dim quartz grains and grains which featured significant feldspar signal contamination. Similarly, Roder *et al.* (2012) observed very dim grains and grains with significant contributions from

non-fast signal components for two sites within the region. Given these observations, the suitability of the quartz grains utilised by this study will be investigated in Chapter 5.

Luminescence dating of feldspars is possible with SAR protocols (e.g. Wallinga *et al.*, 2000). The recently developed post infra-red infra-red stimulated luminescence dating (pIR-IRSL) protocols appear to mitigate the effect of anomalous fading (Thomsen *et al.*, 2008; Buylaert *et al.*, 2009; Thiel *et al.*, 2011). The implications and applicability of such a newer feldspar protocol to provide luminescence ages for this study will be discussed in Section 5.2.

4.4.3 Sampling and laboratory protocols for D_e determination

Sample preparation was conducted in the luminescence dating laboratory at the University of Leicester, UK. All samples for luminescence dating were collected using lightproof plastic or steel tubes with lightproof caps from freshly cleaned sediments and based on the sampling approach outlined in Section 3.1.4. The specific preparation methodology follows that adopted by many studies (e.g. Bateman and Catt, 1996; Wintle, 1997). Approximately 2-3cm of material was discarded from the end of each tube to remove material which was potentially exposed to the light during sample collection. This material was retained to estimate sample water content and to provide material for ICP-MS/XRF measurement in the determination of dose rate.

Samples were treated with HCl and H₂O₂ to remove carbonates and organic matter and were then wet sieved to extract the desired size fraction (course-grained, frequently 180-212 μ m). A density separation was performed using LST FastFloat (sodium heteropolytungstates dissolved in water) at 2.7g cm⁻³ to remove heavy minerals and 2.58g cm⁻³ to extract separate quartz and potassium feldspar. After multiple rinses in distilled water the quartz fraction was etched in 48% HF for 45 minutes and the feldspar fraction was etched in 10% HF for 15 minutes in order to remove the outer alpha-irradiated portion of the grain and/or any grain coatings (e.g. Gliganic *et al.*, 2012; Chen *et al.*, 2013). Samples were then dry sieved to remove any heavily etched grains.

All luminescence measurements on small (2 mm) aliquots were performed on a Risø DA20 TL/OSL reader. For quartz, stimulation (60 s at 125°C) was provided by blue LEDs (stimulation wave length 470 nm) at 70% power (delivering ~ 72 mW cm⁻² to the sample). OSL signals were detected with an EMI 9235QA photomultiplier tube with a U-340 detection

filter. For K-Feldspar, stimulation was provided by IR diodes (wavelength 870 nm), with detection of the resulting (blue-violet) IRSL through a combination of Schott BG39 filters and Corning 7-59 filters (detection range 320-450 nm).

4.4.4 Determination of the environmental dose rate

This section describes the approach for calculating the environmental dose for each luminescence sample. An estimation of the environmental dose rate comprising the combined dose from external alpha, beta, gamma, cosmic radiation and, for feldspar grains, the internal beta dose from K intrinsic to the K-Feldspar grain is required to calculate a luminescence age (Aitken, 1985). In this study, the external gamma dose rate was measured in-situ with a gamma spectrometer and the total gamma dose rate determined using the “threshold method” of Guérin and Mercier (2011). The external beta dose rate was calculated from the concentrations of the elements K, Th and U in the tube end material. U and Th were measured using ICP-MS and K was measured using either ICP-AES or XRF spectrometry (as shown in Table 4.3). XRF determination was conducted using a PANalytical Axios Advanced XRF spectrometer and ICP-MS was conducted using a ThermoScientific ICAP-Qc quadrupole ICP mass spectrometer, both at the University of Leicester, UK. Additional ICP-AES analysis was conducted by SGS Canada. All tube end samples were analysed as bulk sub-samples after being milled and homogenised. Concentrations of U, Th and K were also calculated from the gamma spectrometer results using the “windows” method (Aitken 1985). The results compare favourably with those measured using ICP-MS/ICP-AES/XRF with ratios between the two methods of 0.89 ± 0.2 , 0.88 ± 0.3 and 1.07 ± 0.05 for U, Th and K respectively (Figure 4.5). The variability between the ICP-MS and gamma spectrometer data is higher for Th and U when compared with K. This likely reflects the larger clastic material present within

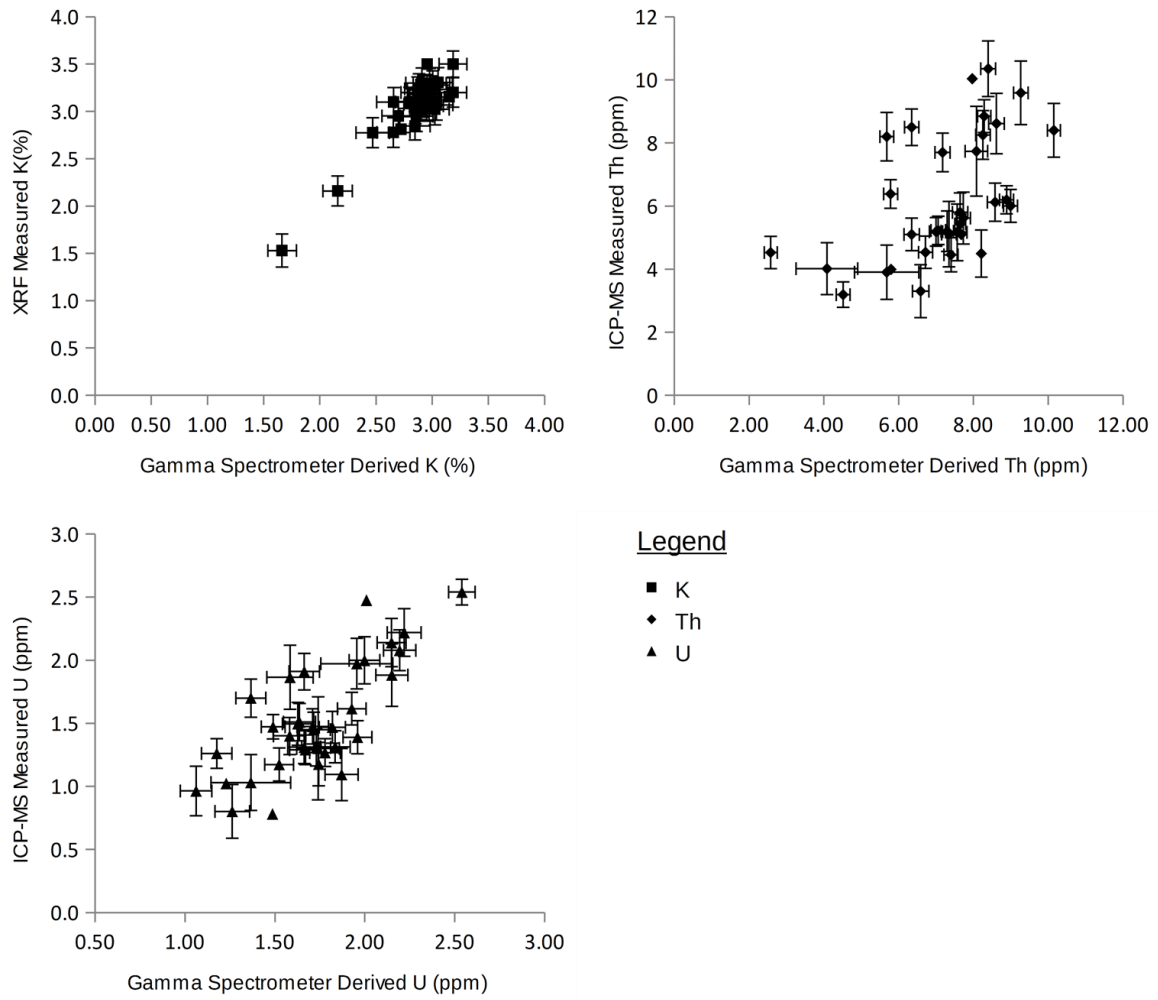


Figure 4.5: Comparison of U, Th and K derived using ICP-MS/XRF and in-situ gamma spectrometer.

the sections which contribute only to the in-situ gamma spectrometer derived concentration. The gamma and beta dose-rate portions were derived using the conversion factors reported by Guérin and Mercier (2011), but incorporating the attenuation due to water (Aitken, 1998) and (maximum) grain size (Mejdahl, 1979; Readhead, 2002). The internal K and Rb concentrations of 12.5 ± 0.5 % and 400 ± 100 ppm respectively were adopted from Huntley and Baril (1997) and Huntley and Hancock (2001) applied to feldspar grains only. The final age uncertainty contains a 3% uncertainty which is intended to incorporate those relating to HF etching, dose-rate conversion, grain size attenuation and water attenuation. Dose rates were attenuated based upon measured moisture contents (following Aitken, 1985) except for the samples from the HL14 and SL14 field sites which used values cited in the papers which

they are attempting to replicate. In addition, a 2% (absolute) uncertainty in water content was propagated into the final dose rate uncertainties (Aitken, 1998).

The cosmic dose was calculated using the method of Prescott and Hutton (1994) and assumes an error of 5% with the overburden as measured in the field. Many studies have recognised that the overburden (and hence the cosmic dose rate) will vary as the landform accumulates or degrades and have attempted to iteratively estimate the cosmic dose rate based upon some understanding of the geomorphic history of the landform under consideration (Munyikwa *et al.*, 2000; Telfer and Thomas, 2007). Such techniques are difficult to apply in this study because the landform history is complex (e.g. there may be erosional episodes within the geomorphic system) and largely unknown. However, the relatively high dose rate in the Mojave Desert renders issues relating to the overburden relatively unimportant (the cosmic dose for all samples accounts for less than 6% of the total dose rate (compared to up to 50% reported elsewhere – Munyikwa *et al.*, 2000) and as a result no correction was made for changes in overburden over time. It is recognised, however, that this will result in additional uncertainty within the ages.

Dose rate data for this study is presented in Table 4.3 and displays values appropriate for both quartz and feldspar grains. The dose rates are high (3-4 Gy/ka) which is typical of the Mojave Desert region (e.g. Rendell and Sheffer, 1996; Owen *et al.*, 2007; Bateman *et al.*, 2012; Garcia *et al.*, 2014).

4.5 Summary

This chapter has outlined the principal methodological components of the study. Chapter 5 demonstrates that the luminescence dating approach is appropriate for dating sediments of the Mojave Desert. Following this, Chapter 6 demonstrates that there is a topographic control over the spatial distribution and morphology of aeolian deposits within the Cady Mountains. Chapter 7 then describes the sedimentology and geochronology for the field sites, highlighting the history of aeolian (in)activity across the mountain block and that each site shows evidence of fluvial/hillslope activity.

Table 4.3: Dose rate data for the luminescence dating samples presented by this study for both quartz and feldspar grains.

Sample	Moisture Content	External Element Concentrations			Gamma	Dose Rate (Gy/ka)	Dose Rate (Gy/ka)
Code	(%)	K (%)	Th (ppm)	U (ppm)	(mGy/a)	for feldspar grains	for quartz grains
CN13-1-1	0.41	3.10 ± 0.16	8.40 ± 0.84	2.14 ± 0.21	1529 ± 73	5.01 ± 0.20	4.17 ± 0.20
CN13-1-2	0.75	3.24 ± 0.16	4.53 ± 0.45	1.27 ± 0.13	1370 ± 66	4.76 ± 0.20	3.91 ± 0.20
CN13-2-1	0.48	3.20 ± 0.16	8.20 ± 0.82	1.70 ± 0.17	1607 ± 77	5.04 ± 0.20	4.19 ± 0.20
CN13-3-1	0.47	3.10 ± 0.16	8.50 ± 0.85	1.91 ± 0.19	1459 ± 70	4.84 ± 0.19	3.99 ± 0.19
CN13-4-1	0.79	3.19 ± 0.16	5.11 ± 0.51	1.09 ± 0.11	1491 ± 71	4.86 ± 0.20	4.01 ± 0.20
CN13-5-1	0.81	3.10 ± 0.16	7.70 ± 0.77	1.51 ± 0.15	1379 ± 66	4.67 ± 0.19	3.82 ± 0.19
CN13-6-1	0.59	3.20 ± 0.16	5.80 ± 0.58	1.45 ± 0.15	1479 ± 71	4.77 ± 0.20	3.92 ± 0.20
CN13-7-1	0.60	2.78 ± 0.14	10.4 ± 1.04	2.08 ± 0.21	1383 ± 66	4.56 ± 0.17	3.71 ± 0.17
CN-Valley	0.51	3.24 ± 0.16	7.46 ± 0.75	1.72 ± 0.17	1325 ± 58	4.74 ± 0.19	3.89 ± 0.19
DN14-1-4	1.30	2.95 ± 0.15	5.43 ± 0.54	1.47 ± 0.15	1279 ± 61	4.52 ± 0.18	3.67 ± 0.18
DN14-1-3	0.91	2.85 ± 0.14	5.20 ± 0.52	1.47 ± 0.15	1357 ± 65	4.52 ± 0.18	3.67 ± 0.18
DN14-1-2	0.87	2.86 ± 0.14	5.23 ± 0.52	1.29 ± 0.13	1298 ± 62	4.43 ± 0.18	3.58 ± 0.18
DN14-1-1	0.64	2.93 ± 0.15	4.45 ± 0.45	1.31 ± 0.13	1475 ± 71	4.63 ± 0.19	3.78 ± 0.19
ER14-1-1	0.42	3.05 ± 0.15	3.30 ± 0.33	0.80 ± 0.08	1211 ± 53	4.43 ± 0.19	3.58 ± 0.19
ER14-1-2	1.58	2.97 ± 0.15	5.19 ± 0.52	1.31 ± 0.13	1258 ± 52	4.52 ± 0.18	3.67 ± 0.18
ER14-1-3	2.04	2.90 ± 0.15	5.62 ± 0.56	1.50 ± 0.15	1246 ± 52	4.49 ± 0.18	3.64 ± 0.18
HL14-1	0.63	3.02 ± 0.15	4.52 ± 0.45	1.17 ± 0.12	1244 ± 51	4.19 ± 0.17	3.34 ± 0.15
HL14-2	0.81	2.85 ± 0.14	4.01 ± 0.40	1.97 ± 0.20	1191 ± 48	4.10 ± 0.16	3.25 ± 0.14
MC13-1-1	0.81	3.50 ± 0.18	3.90 ± 0.39	1.03 ± 0.10	1394 ± 67	4.83 ± 0.21	3.84 ± 0.21
MC13-1-2	0.80	3.30 ± 0.17	5.10 ± 0.51	1.31 ± 0.13	1357 ± 65	4.72 ± 0.20	3.73 ± 0.20
MR14-1-1	0.23	2.70 ± 0.12	8.25 ± 0.83	2.00 ± 0.20	1651 ± 97	4.83 ± 0.19	3.98 ± 0.19
MR14-2-1	0.28	2.47 ± 0.12	8.62 ± 0.86	2.22 ± 0.22	1428 ± 71	4.49 ± 0.17	3.64 ± 0.17
PK14-1-4	0.72	2.92 ± 0.15	6.01 ± 0.60	1.40 ± 0.14	1324 ± 54	4.56 ± 0.18	3.71 ± 0.18
PK14-1-3	0.83	2.94 ± 0.15	8.85 ± 0.89	1.62 ± 0.16	1332 ± 54	4.64 ± 0.18	3.79 ± 0.18
PK14-1-2	1.18	2.98 ± 0.15	6.20 ± 0.62	1.39 ± 0.14	1368 ± 54	4.72 ± 0.18	3.73 ± 0.18
PK14-1-1	2.20	3.04 ± 0.15	6.12 ± 0.61	1.48 ± 0.15	1325 ± 54	4.71 ± 0.18	3.72 ± 0.18
RD14-2-3	1.59	2.95 ± 0.15	9.59 ± 0.96	1.88 ± 0.19	1608 ± 77	5.00 ± 0.19	4.16 ± 0.18
RD14-1-2	1.29	2.91 ± 0.15	7.74 ± 0.77	1.86 ± 0.19	1265 ± 71	4.59 ± 0.18	3.75 ± 0.17
RD14-1-1	2.04	2.87 ± 0.14	5.17 ± 0.52	1.30 ± 0.13	1254 ± 75	4.55 ± 0.18	3.57 ± 0.17
SL14-125	1.90	1.66 ± 0.08	8.99 ± 0.90	4.08 ± 0.41	1230 ± 48	3.96 ± 0.14	3.14 ± 0.12
SL14-3	1.23	1.66 ± 0.08	14.2 ± 1.42	2.54 ± 0.25	1595 ± 59	4.53 ± 0.16	3.72 ± 0.14
SM13-1-1	0.52	2.81 ± 0.14	10.0 ± 1.00	2.48 ± 0.25	1427 ± 68	4.86 ± 0.18	3.87 ± 0.18
SM13-3-1	0.36	3.16 ± 0.16	3.99 ± 0.40	1.02 ± 0.10	1398 ± 67	4.72 ± 0.19	3.87 ± 0.19
SM13-2-1	0.65	3.50 ± 0.18	5.10 ± 0.51	0.78 ± 0.08	1504 ± 72	4.96 ± 0.21	3.97 ± 0.21
WC14-1-2	0.63	3.01 ± 0.15	6.38 ± 0.64	1.26 ± 0.13	1149 ± 51	4.57 ± 0.18	3.58 ± 0.18
WC14-1-3	1.47	2.99 ± 0.15	3.19 ± 0.32	0.96 ± 0.10	1061 ± 50	4.38 ± 0.18	3.39 ± 0.18

5 Developing the luminescence dating protocol

Existing luminescence chronologies within the Mojave Desert have led to conflicting suites of ages, and hence, contrasting landscape histories within the region (Section 3.1.1). Alongside considerations relating to the long-recognised phenomena of anomalous fading in K-Feldspars (Wintle, 1973), recent concerns regarding the reliability of quartz as a dosimeter in the Mojave have also been raised (Lawson *et al.*, 2012; Lawson *et al.*, 2015). Using two palaeo lake sites with independent age controls (Section 5.3), this chapter assesses the utility of both quartz (Section 5.1) and K-Feldspar grains and further seeks to optimise associated measurement conditions (Section 5.2); the latter focusses primarily on mitigating the effects of anomalous fading and assessing the bleachability of K-Feldspar.

5.1 Quartz luminescence dating

Quartz is widely considered a reliable dosimeter as it has a bright, rapidly bleached and non-fading luminescence signal (Rhodes, 2011). The development of the SAR protocol (Murray and Wintle, 2000, 2003; Wintle and Murray, 2006) facilitated the routine use of quartz OSL and it has been shown to provide ages consistent with independent methods (Murray and Olley, 2002; Wintle and Murray, 2006; Rhodes, 2011).

In some regions, however, there are reported instances of quartz OSL proving problematic (Section 4.4). Examples include quartz grains that exhibited low grain sensitivity (low signal to noise ratios and sensitivity to the influence of contaminant minerals), low bleachability, unstable non-fast component signal contributions and high thermal transfer (Steffen *et al.*, 2009; Roder *et al.*, 2012; Rowan *et al.*, 2012; Klasen *et al.*, 2016). In the Mojave Desert, Lawson *et al.* (2012) observed highly variable quartz properties from six sites including dim quartz grains and grains with significant feldspar signal contamination, despite rigorous mineral extraction procedures. Similarly, Roder *et al.* (2012) observed very dim grains and grains with significant contributions from non-fast component signals for two sites within the region. The presence of feldspar inclusions (Jain and Singhvi, 2001) and quartz with a significant thermally unstable medium component can both alter quartz shine-down curve shape and, where the signal is dim, can lead to incorrect D_e determination (Li and Li, 2006; Steffen *et al.*, 2009; Klasen *et al.*, 2016). The underestimation of D_e with respect to expected

age has been reported for quartz at several sites with independent age control (Owen *et al.*, 2007; Pigati *et al.*, 2011; Garcia *et al.*, 2014). This chapter investigates the suitability of quartz samples within the field sites, as well as the applicability of feldspar luminescence dating protocols within the region. Such investigation is important before any consideration of the geochronology of aeolian landforms within the region. Previous geochronologies for the study location (i.e. Soldier Mountain) were made using either non-fading corrected IRSL (Rendell and Sheffer, 1996) or quartz OSL (although Bateman *et al.* (2012) reported no concerns regarding their quartz) and such chronologies are fundamentally inconsistent.

5.1.1 Analysis of the quartz OSL signal

Quartz extracts were obtained from several sites across the study area and were analysed using standard quartz SAR methods. Common aliquot acceptance criteria for the quartz SARs methods are normally considered to provide a quality assurance in D_e estimates. The rejection of large numbers of aliquots on the basis of these criteria is usually considered indicative of samples that may be unreliable dosimeters. These include the recycling ratio and recuperation tests (Murray and Wintle, 2000). For the analysed Mojave samples, all aliquots had acceptable recycling ratios and recuperation values ranged from -1% to 32% of D_e (Figure 5.1), where an acceptable value is considered to be <5% (Murray and Wintle, 2000). Aliquots with an unacceptably high recuperated signal can indicate the presence of a significant contribution of the thermally unstable medium component (Steffen *et al.*, 2009). Recuperation arises from the thermal transfer of charge from deeper traps into shallower traps, typically by the preceding irradiation, preheating or stimulation and can be symptomatic of an unstable medium component within the luminescence signal (Wintle and Murray, 2006). Given that more than a fifth of samples exhibited an unacceptably high recuperation level, the relative influence of non-fast signal components within sample shine-down curves was investigated.

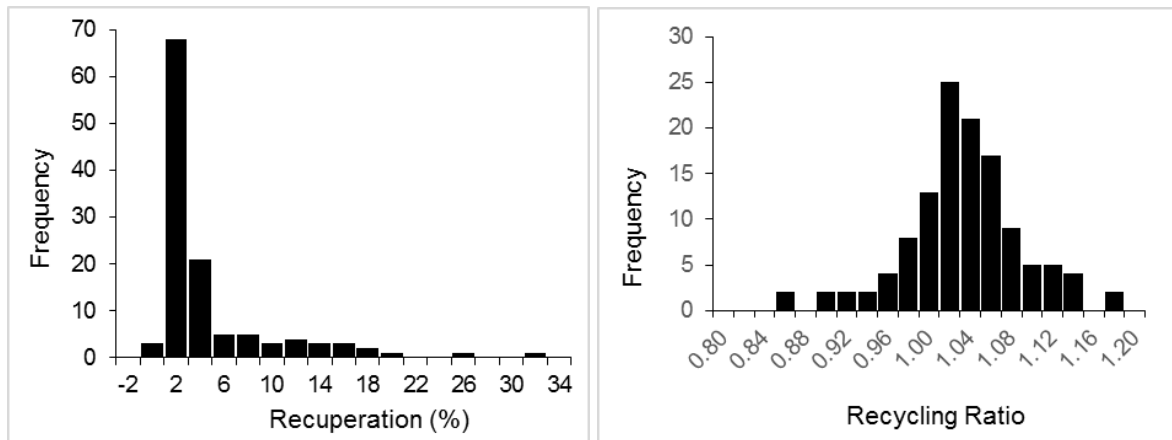


Figure 5.1: Aggregate values of recuperation (left) and recycling ratios (right) for quartz SAR data for 120 aliquots.

Shine-down curves for quartz blue light stimulated OSL typically display a characteristic decay shape (e.g. Figure 5.2a), representing a composite of multiple signal components (Bailey *et al.*, 1997). The total signal has been explained as the sum of several (usually at least 3) OSL signals derived from traps with different depths, electron populations, decay rates and thermal stabilities (Jain *et al.*, 2003; Wintle and Murray, 2006; Wintle and Adamiec, 2017). The quartz SAR protocol is optimised for samples where the initial signal is dominated by the fast component, which is rapidly bleached, thermally stable over geological time (with a calculated trap life time at 20°C of 310 Ma (Bailey *et al.*, 1997; Singarayer and Bailey, 2003)) and has been demonstrated to offer accurate OSL ages in various contexts (Murray and Wintle, 2000; Murray and Olley, 2002; Jacobs, 2008; Bailey, 2010). The fast component can be identified through the subtraction of a background signal from the initial signal (often the first 0.3s of the decay curve) using either a late background method (which often removes the last 4s of signal) or an early background method which removes the background signal immediately following the initial signal (Banerjee *et al.*, 2000; Cunningham and Wallinga, 2010). Additional components include the medium and slow components (Jain *et al.*, 2003), which may in some cases significantly influence the initial OSL signal as they exhibit different thermal stabilities, bleach at different rates and are associated with significant signal recuperation (Li and Li, 2006; Steffen *et al.*, 2009; Bailey, 2010; Cunningham and Wallinga, 2010). All of which means that their contribution to the integrated OSL signal is problematic.

Figure 5.2 shows three shine-down curves from sites in this study, which exemplify the behaviour of Mojave Desert quartz samples. The samples all contrast sharply. Sample (a)

comprises a relatively bright aliquot (~2,800 counts per second per Gy for a small ~3 mm aliquot) where the dominance of the fast component is inferred from a rapidly decaying initial signal with limited remaining signal after 5-10 seconds of stimulation. Conversely, sample (c) is a dimmer and less sensitive aliquot (~400 counts second per Gy for a small ~3 mm aliquot) and is exhibiting characteristics related to the slower decaying “medium” and “slow” signal components. For two samples, the medium or slow components represent the equivalent of 20% of the initial signal which may be problematic.

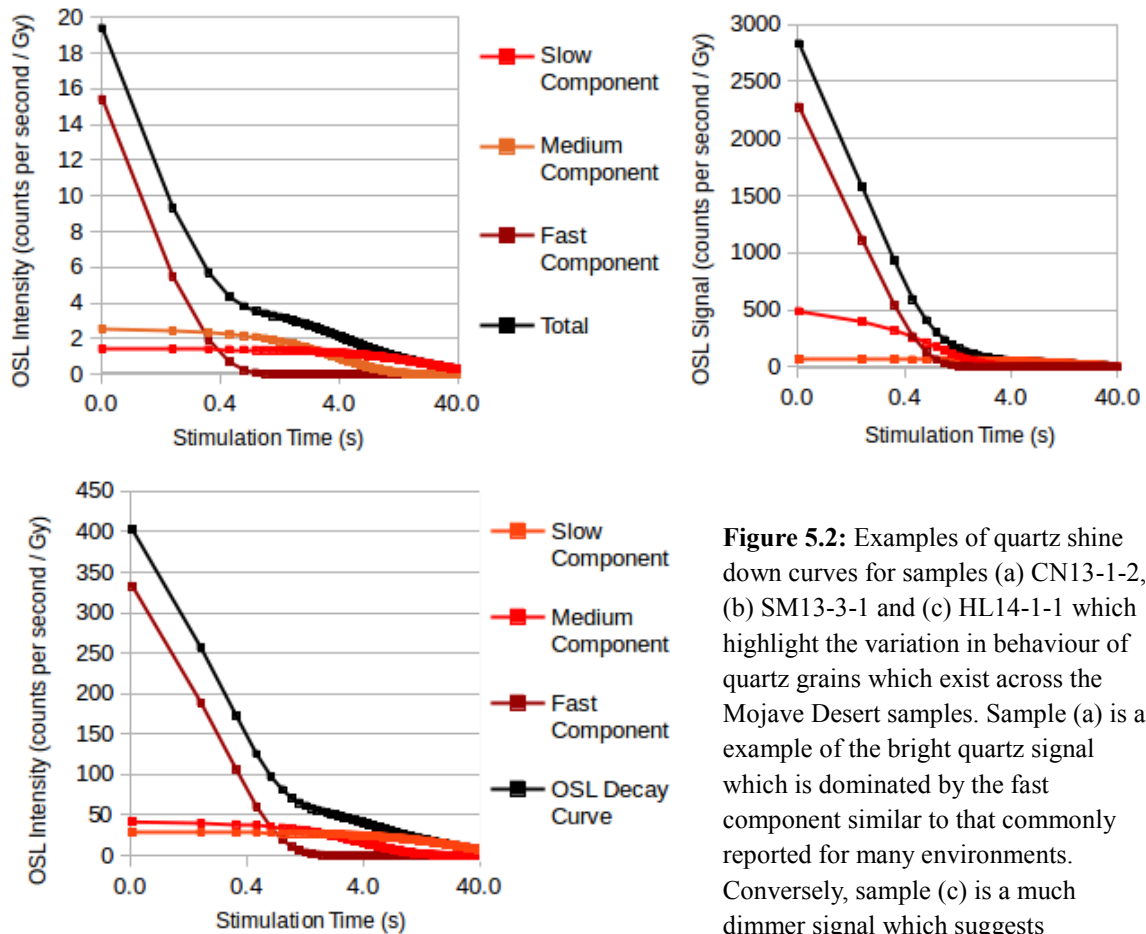


Figure 5.2: Examples of quartz shine down curves for samples (a) CN13-1-2, (b) SM13-3-1 and (c) HL14-1-1 which highlight the variation in behaviour of quartz grains which exist across the Mojave Desert samples. Sample (a) is an example of the bright quartz signal which is dominated by the fast component similar to that commonly reported for many environments. Conversely, sample (c) is a much dimmer signal which suggests significant contributions from medium and slow signal components which can make the sample unsuitable for dating using the SAR protocol.

5.1.2 Composition tests

Purity is important because feldspar also produces OSL (UV) under blue light stimulation (Duller, 2003). A test for quartz purity and for the identification of problematic sample behaviour/signal contamination was proposed by Lawson *et al.* (2015) based on the contrasting of thermal quenching and IR stimulation properties of the two minerals. In quartz a gradual decrease in OSL signal is observed as the stimulation temperature is raised (thermal quenching) (Smith and Rhodes, 1994), which contrasts with feldspars, which typically exhibit an increased IRSL signal with stimulation temperature (thermal assistance) (Wiggenhorn, 1994; Thomsen *et al.*, 2008). An IR depletion ratio can be used to identify signals contaminated by feldspar because, unlike quartz grains, feldspar signals respond to stimulation by infra-red radiation (Duller, 2003). Consequently, an OSL measurement performed on a sample containing K-Feldspar contamination immediately after IR stimulation records a different OSL shine-down curve shape and lower brightness compared with the same sample without such a prior-IR stimulation (Jain and Singhvi, 2001; Reimann *et al.*, 2011). These measurements can be combined and represented graphically by ‘normalising’ the derived quenching and IR depletion values such that the most feldspar-like behaviour observed plots at 0,0 and the most quartz-like observed behaviour plots close to 1,1 (as per Lawson *et al.*, 2015).

Figure 5.3 demonstrates variable degrees of quartz OSL contamination across the study region, with most samples showing a strong divergence from ideal quartz-like properties. The samples from the Silver Lake, Harper Lake and WC14 sites exhibit the least “quartz-like” behaviour, whereas samples from the CN13 and PK14 sites plot with a more “quartz-like” behaviour – though this does not necessarily equate to good behaviour.

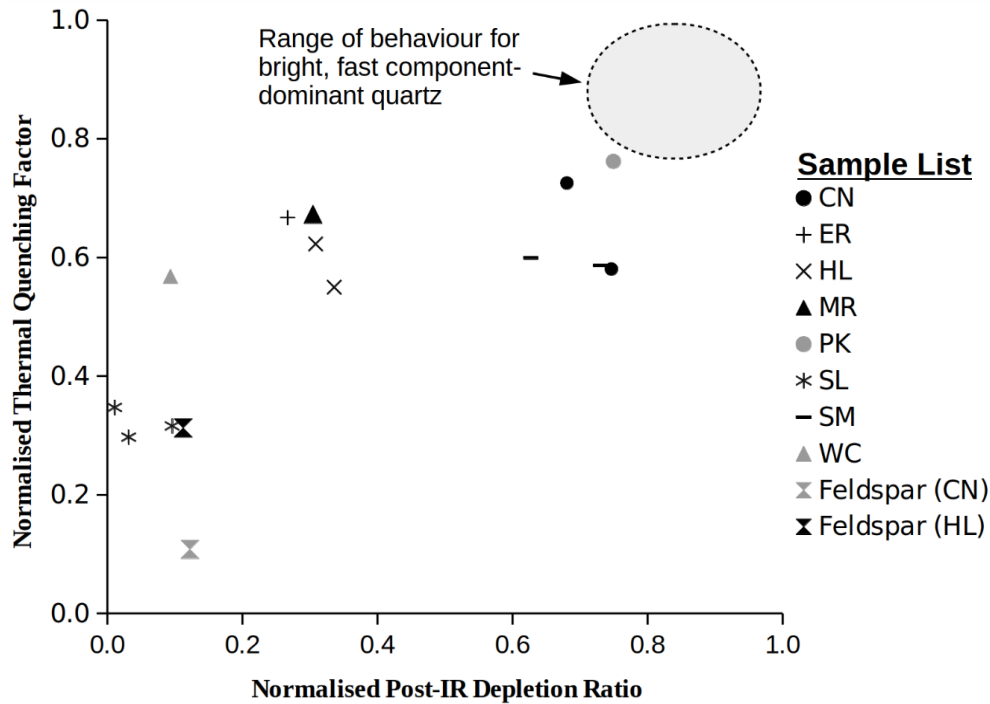


Figure 5.3: Composition test for samples from this study performed using the method outlined by Lawson *et al.* (2015). The most quartz-like behaviour plots close to 1,1 and the most feldspar-like behaviour plots close to 0,0. For comparison data are shown for samples as follows: MD1-1 and ROB2 - South African coastal aeolianite, S1A1 - active dune sands in the Venezuelan Llanos savannas (Carr *et al.*, 2016). Data for non-Mojave Desert samples provided by A. Carr, unpublished data unless stated otherwise. KAZ and ROB samples show typical bright fast-component-dominated quartz signals and are shown to agree with an independent ^{14}C chronology.

Despite the use of standard methods for isolating quartz minerals (Wintle, 1997), Figure 5.3 suggests that many aliquots exhibit feldspar-like properties. The density separation of quartz and feldspar grains followed by prolonged exposure to concentrated (48%) HF, plus post-etch dry sieving means that numbers of individual feldspar grains remaining within the sample should be minimised (Lawson *et al.*, 2012). It is possible that individual quartz grains contain inclusions of feldspar within their crystal lattice (Fragoulis and Readhead, 1991; Lawson *et al.*, 2015). Inclusions pose significant issues for luminescence dating procedures due to their potential effect on the internal dose rate (Aitken, 1985), (as is possible here) because even small quantities of feldspar can produce a bright luminescence signal when the surrounding quartz grain is relatively dim (Jain and Singhvi, 2001; Lawson *et al.*, 2015) and this may result in a different shine-down curve shape (Banerjee *et al.*, 2000).

The composition test, curve fitting and standard aliquot rejection criteria together suggest that the properties of quartz within the Mojave Desert vary considerably and that they often diverge greatly from those optimal for quartz OSL dating. Approaches to minimising the influence of these unsuitable signal components are outlined in the following sections.

5.1.3 The fast ratio as a means to identify reliable quartz aliquots/grains

The fast ratio was proposed by Durcan and Duller (2011) as an objective approach to determining whether a quartz OSL signal is dominated (>90%) by the fast component. When used as an aliquot/grain rejection criterion, it allows the removal of aliquots either dominated by non-fast component-dominated quartz and/or contaminated by other minerals (e.g. feldspar). This rejection criterion was adopted in conjunction with the standard recycling ratio and recuperation parameters in the quartz analysis (Murray and Wintle, 2000) to identify aliquots most likely to be reliable dosimeters (as Jacobs *et al.*, 2013; Feathers and Pagonis, 2015; Trauerstein *et al.*, 2017).

The fast ratio is calculated as:

$$FastRatio = \frac{L1-L2}{L2-L3} \quad (1)$$

where L1 is equal to the number of OSL counts where the fast component dominates the OSL signal (i.e. the first integration window). L2 is the number of counts in the integration window where the fast component has been reduced to 1% of its original signal and L3 represents the average number of counts per integration window where the medium component is reduced to 1% and 0.1% of its original signal.

The values for L1, L2 and L3 are derived from Equations 2 to 5 and relate to the photo ionisation cross-section of the fast and medium components (σ_F and σ_M respectively), where the values of $2.60 \pm 0.06 \times 10^{-17} \text{ cm}^2$ and $4.28 \pm 0.35 \times 10^{-17} \text{ cm}^2$ for σ_F and σ_M respectively are adopted (as Durcan and Duller (2011), Jain *et al.* (2003) and Singarayer and Bailey (2003)). Therefore L1-L3 are estimated as:

$$t_{L1} = 0 \quad (2)$$

$$t_{L2} = \frac{1.95 \times 10^{-15}}{\sigma_F \rho} \quad (3)$$

$$t_{L3(start)} = \frac{1.95 \times 10^{-15}}{\sigma_M \rho} \quad (4)$$

$$t_{L3(end)} = \frac{2.92 \times 10^{-15}}{\sigma M \rho} \quad (5)$$

where ρ is the stimulation power (mW cm^{-2}) of the blue LEDs in the TL/OSL reader.

A Fast Ratio rejection criterion of 20 retains only aliquots/grains for which the fast component contributes >90% of the integrated OSL signal (Durcan and Duller, 2011). Duller (2012) suggested that for samples where not all grains are dominated by the quartz fast component, the number of usable grains decreases considerably (~84% Jacobs *et al.*, 2013) and the average D_e changes as the Fast Ratio rejection threshold is progressively increased. This may form a plateau of D_e if only fast component dominated aliquots are selected (as per Feathers, 2015). Table 5.1 demonstrates there were no aliquots for samples CN13-7-1, CS14-1-1, SL14-125, SM13-1-1 and SM13-3-1 in which the fast component provided > 90% of the OSL signal and that at least four fifths of aliquots were rejected for samples CN13-1-2, CN13-4-1, CP14-1-1 and HL14-1-1 on the same basis. In seven of the eight cases, there was also no observable plateau in D_e as the Fast Ratio threshold was increased, though this may relate to having rejected all but one or two grains (as Jacobs *et al.*, 2013).

5.1.4 Quartz equivalent dose

A final D_e estimate, as obtained using only aliquots with an acceptable Fast Ratio and using an early background subtraction approach (Cunningham and Wallinga, 2010) was compared with the D_e using standard quartz SAR protocol and acceptance criteria and late background subtraction (Table 5.1). Using the first approach for five samples all aliquots were rejected (by the fast ratio criterion) and four samples had a final D_e estimate based upon a very few aliquots (<5). Of these, only the two CN14 samples resulted in D_e values within uncertainties of each other. The D_e obtained with the standard approach for HL14-1-1 was a significant underestimate as was quartz OSL from Garcia *et al.* (2014) while Fast Ratio early background D_e ($n=1$) was broadly in agreement with the IRSL and ^{14}C ages for the site (Garcia *et al.* ; Section 5.3.2). There was also a significant discrepancy between the late background subtracted D_e and the early background subtracted D_e at PK14-1-1.

Overall, the results imply that some Mojave quartz grains may be suitable dosimeters and that single grain analysis may allow the isolation of a statistically significant number of grains with sufficiently high Fast Ratios from which to derive an OSL age. However, given the high rejection rates using the Fast Ratio this is likely to be a highly time-consuming approach.

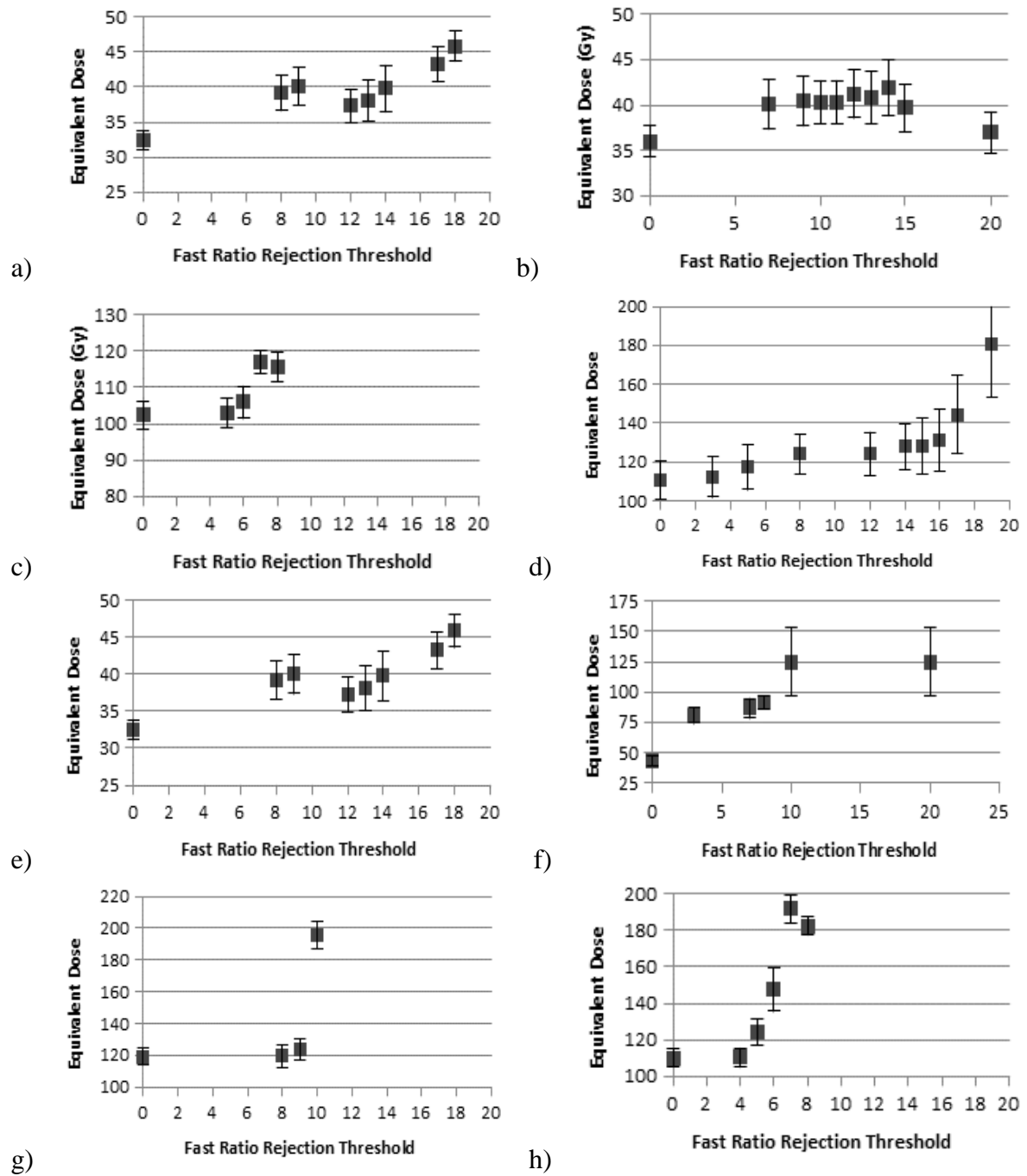


Figure 5.4: The relationship between equivalent dose (D_e) and fast ratio rejection threshold for six exemplar samples. Where a trend can be established it suggests that the D_e derived using the standard SAR protocol is an underestimate of the 'true' D_e . The samples shown here are CN13-1-2 (a) CN13-4-1 (b) CN13-7-1 (c) PK14-1-1 (d) DN14-1-1 (e) HL14-1-1 (f) SM13-1-1 (g) and SM13-3-1 (h).

Table 5.1: Equivalent doses and ages for quartz samples measured using the procedures described in the text. D_e values are presented after the fast ratio rejection criterion was applied and using early background subtraction (described in the text).

Sample	Standard D_e			D_e for aliquots which passed the fast ratio criterion			
	#	D_e (Gy)	Age (ka)	Fast Ratio Range	#	D_e (Gy)	Age (ka)
CN13-1-2	15	36.1 ± 1.8	9.8 ± 0.50	7.6 – 50.8	1	37.57 ± 1.6	10.2 ± 0.4
CN13-4-1	20	35.8 ± 1.6	9.4 ± 0.41	8.3 – 65.7	4	38.72 ± 2.3	10.2 ± 0.6
CN13-7-1	10	102.9 ± 3.5	27.7 ± 0.94	5.7 – 23.4	0		
DN14-1-1	12	29.6 ± 4.0	8.5 ± 1.13	0.0 – 18.1	0		
HL14-1-1	20	43.5 ± 3.9	11.5 ± 1.00	1.5 – 25.3	1	118.96 ± 26.4	36.0 ± 8.0
PK14-1-1	11	109.0 ± 9.0	24.5 ± 2.63	2.5 – 60.8	1	173.9 ± 23.6	47.0 ± 6.4
SL14-1-1	8	9.7 ± 1.1	3.0 ± 0.30	0.5 – 1.1	0		
SM13-1-1	10	107.6 ± 3.8	27.8 ± 0.98	7.0 – 13.0	0		
SM13-3-1	20	109.8 ± 4.7	29.8 ± 1.28	4.6 – 42.0	0		

5.1.5 Summary

This section has demonstrated that quartz grains in samples from the study area are highly variable in their properties and exhibit a number of problematic behaviours, potentially rendering them unsuitable for luminescence dating. The composition test indicated that the quartz often contains an unavoidable (at least practically) contribution from K-Feldspars. Furthermore, many observed aliquots contain a significant medium component (Li and Li, 2006; Steffen *et al.*, 2009; Klasen *et al.*, 2016). Under such conditions, the Fast Ratio is a rigorous means of aliquot rejection (as Duller, 2012; Jacobs *et al.*, 2013). Applying the Fast Ratio for the majority of samples suggests that the quartz data may underestimate the “true” D_e (Feathers, 2015) and few aliquot can be considered “acceptable”. This finding is in accordance with other studies in the Mojave Desert which have reported strong underestimations of quartz ages compared with independent dating (Mahan *et al.*, 2007; Owen *et al.*, 2007; Pigati *et al.*, 2011; Garcia *et al.*, 2014). Consequently, this study will now investigate the utility of feldspar luminescence protocols for deriving D_e values in the Mojave Desert (as Klasen *et al.*, 2016).

5.2 K-Feldspar luminescence dating

K-Feldspar typically produces a bright, light-sensitive IRSL signal that in many ways should be an effective dosimeter for luminescence dating (Duller, 1997). Until recently its widespread application, including in the Mojave Desert (e.g. Wintle *et al.*, 1994; Rendell and Sheffer, 1996), was hampered by the near ubiquitous issue of anomalous fading (Wintle, 1973; Huntley and Lamothe, 2001). In the last 10 years it has been proposed that the effects of this phenomenon can be minimised by using a revised SAR protocol comprising an initial low temperature IR stimulation to evict the most fading-prone electron traps, followed by a higher temperature stimulation that derives IRSL from less fading-prone traps (Thomsen *et al.*, 2008; Jain and Ankjær, 2011). Such protocols are termed “two-step post-infra-red infra-red stimulated luminescence” (pIR-IRSL_{T1,T2} – where T1 and T2 denote the two temperatures at which the sample is stimulated). Buylaert *et al.* (2009) outlined a two-step SAR protocol where T1=50°C and T2=225°C and they demonstrated that this protocol led to a significant reduction of that fading rate. Kars *et al.* (2012), Reimann *et al.* (2011) and Roberts (2012) show agreement with quartz OSL and independent age constraints for pIR-IRSL protocols using T1=50°C and T2 is between 180°C and 230°C. The downside of pIR-IRSL protocols is that they may access traps that are more difficult to bleach, potentially leading to an overestimation of D_e (Kars *et al.*, 2014a).

This section focuses on the suitability of the pIR-IRSL_{50,225} protocol within the Mojave Desert, particularly with regards to the trade-off between ensuring bleaching (Section 5.2.1) and mitigating the effects of anomalous fading (Section 5.2.2). The ability of the adopted protocol to recover a known dose is fundamental to any dating approach and so is investigated (Section 5.2.3). Finally, luminescence ages at two sites with independent age chronologies are analysed to assess how ages derived using the quartz and feldspar methods compare (Section 5.3).

5.2.1 Bleaching of the post-IR IRSL signal

A fundamental assumption of luminescence dating methods is that all electron traps are emptied (bleached) prior to deposition and accrual of the burial dose of interest. Incomplete bleaching at the time of deposition leads to an overestimation of the D_e and age. The ability of grains to be bleached depends on several factors, most fundamentally the properties of the mineral itself. K-Feldspars generally bleach more slowly than quartz grains (Godfrey-Smith

et al., 1988), but the bleaching rate and the magnitude of any residual signal varies with stimulation temperature. The IRSL₅₀ signal is the most easily bleached, while the pIR-IRSL signals at 225°C and 290°C bleach increasingly slowly (Thiel *et al.*, 2011; Reimann *et al.*, 2012; Kars *et al.*, 2014a; Li *et al.*, 2014; Smedley *et al.*, 2015). Li and Li (2011) observed that 2% of the IRSL₅₀ luminescence signal remained after one hour of light exposure in a solar simulator, whereas 12% of the signal remained when measured using a pIR-IRSL protocol. By contrast, Thomsen *et al.* (2008) reported no difference in bleachability of the IRSL₅₀ and pIR-IRSL_{50,290} signals, but in some cases residual signals of up to 40Gy have been reported (e.g. Stevens *et al.*, 2011). Another significant factor influencing the bleaching of grains includes the conditions at the time of bleaching (e.g. night-time).

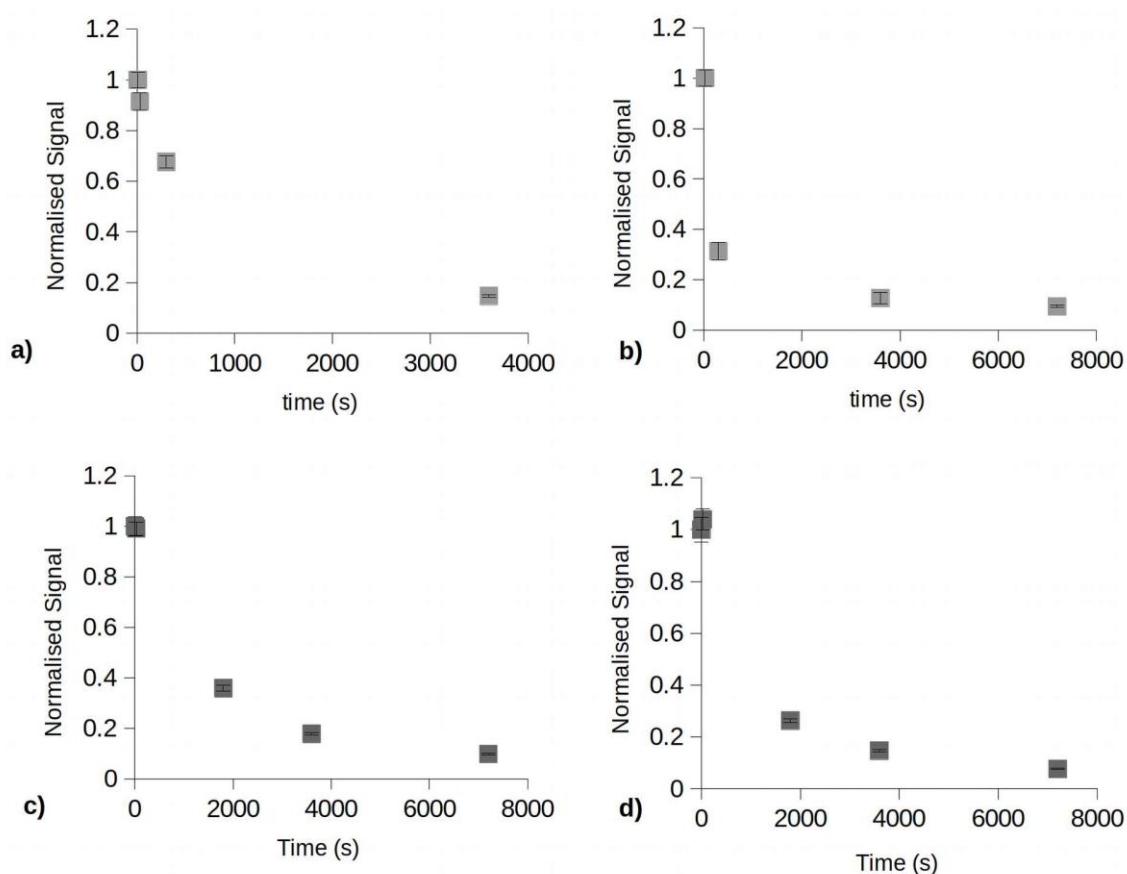


Figure 5.5: When samples were bleached in natural daylight the equivalent dose decreased with time such that the original signal had reduced by >80% after 1-2 hours of exposure. The samples CN13-5-1 (a), HL14-1-1 (b), SL14-3 (c) and SM13-3-1 (d) are shown and were measured using the pIR-IRSL_{50,225} protocol.

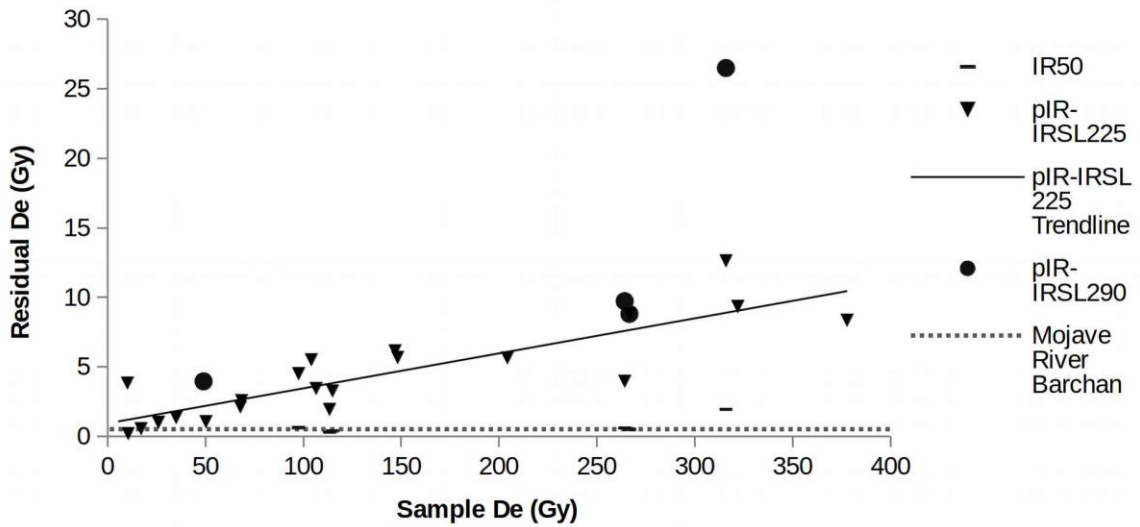


Figure 5.6: Residual and D_e values for samples from this study. The dotted horizontal line represents the central age for a surficial ($\sim 0.3\text{m}$) sample from a contemporary Mojave River barchan dune which is assumed to be a ‘modern analogue’.

These observations suggest that an assessment of the bleaching of pIR-IRSL signals should be undertaken. This problem is somewhat related to the D_e of the sample because the impact of any residual or remnant signal becomes less significant in relative terms for older samples, whereupon the presence of fading becomes a more central concern (Auclair *et al.*, 2003). Consequently, careful selection and testing of protocols is essential (Thiel *et al.*, 2011). Two approaches were adopted to assess this: (1) a selection of Mojave samples were bleached in natural daylight (Leicester, UK) before being measured and (2) samples from an active barchan dune crest were measured as these should have a modern age. With regards to the former approach, Figure 5.5 shows that the naturally acquired pIR-IRSL_{50, 225} (measured at 225°C) signal is reduced by >80% within 1-2 hours. The relative size of the unbleached signals is comparable to the size of those reported by Li and Li (2011), with a value of <20% after one hour of exposure.

To assess the magnitude of any unbleachable signal (Li *et al.*, 2013), three small (2mm) aliquots from each sample (30 aliquots in total) were exposed to daylight for two days before measurement using the pIR-IRSL_{50,225} protocol. For more than 95% of samples the resulting equivalent dose (i.e. residual D_e) was less than 10Gy. Figure 5.5 displays the relationship between the D_e and measured residual D_e . The regression line for pIR-IRSL_{50,225} samples

intercepts at the measured age of a modern analogue sample, an active barchan dune in the contemporary Mojave River (MR14-1-1) with an intercept of 0.94 ± 0.60 Gy. The figure highlights the greater residual signal components associated for the higher temperature pIR-IRSL_{50,225} protocol compared with the IRSL₅₀ protocol, although the residual signal for the former is still generally less than 1% of the sample D_e. The pIR-IRSL_{50,290} has much higher residuals, consistent with the reported lower bleachability of this higher second stimulation temperature (Thiel *et al.*, 2011). Overall, this section demonstrates that the pIR-IRSL_{50,225} signal appears to be bleachable under ideal conditions.

5.2.2 Mitigating the effects of anomalous fading

The rate of anomalous fading can be assessed using a laboratory fading test, most commonly the method proposed by Huntley and Lamothe (2001), itself based upon (Aitken, 1985). This method relies on measuring the fading rate in the laboratory (the rate of which is quantified as the g-value) and then extrapolating this rate to geological timescales to correct the initial calculated age for a sample. This is based upon a series of assumptions about the growth curve Huntley and Lamothe (2001), Auclair *et al.* (2003) and Lamothe *et al.* (2003) (e.g. Reimann *et al.*, 2011; Thiel *et al.*, 2011). The g-value equates to the proportional loss of luminescence signal per decade (order of magnitude time). The value is derived from measurements of the luminescence signal (using the approach outlined in Table 5.2) after various post-irradiation storage times and is fitted with a log-linear regression (Wallinga *et al.*, 2000; Auclair *et al.*, 2003). Kars *et al.* (2012) calculate the delay (storage) time as:

$$\text{delay time} = \frac{\text{irradiation time}}{2} + \text{preheat time} + \text{storage time} \quad (6)$$

For the IRSL₅₀ signal, fading rates between 2% and 10% per decade have been observed (Huntley and Lamothe, 2001) whereas for the pIR-IRSL_{T1, T2} signals observed fading rates are commonly ~0-2.5% per decade (Buylaert *et al.*, 2009; Buylaert *et al.*, 2012a). Where appropriate, ages were corrected from their measured g-values in the R software environment using the package “Luminescence” (Kreutzer *et al.*, 2012), which implements the method of (Huntley and Lamothe, 2001). This approach is therefore only considered applicable for the low-dose ‘linear portion’ of the dose-response curve. Consequently, there is an upper age-limit for correction which is sample dependent, but is typically 25 and 50 ka (Huntley and

Lamothe, 2001; Li and Li, 2008; Kars *et al.*, 2014a). Here the limit is interpreted as being at ~140 Gy (~30ka) after visual interpretation of the dose-response curves.

Table 5.2: A protocol for measuring the rate of anomalous fading within feldspar samples where the preheat is administered before storage (as Auclair *et al.*, 2003).

Step	Activity
1	Bleach Sample
2	Give Dose
3	Preheat
4	Storage
5	Measure Luminescence Signal (L_x) This may require multiple measurements at different temperatures if using a pIR-IRSL _{T1, T2} protocol
6	Give Test Dose
7	Preheat
8	Measure Luminescence Signal (T_x) This may require multiple measurements at different temperatures if using a pIR-IRSL _{T1, T2} protocol
9	Repeat from Step 1 varying the storage time for each new cycle

Figure 5.7 demonstrates a significant variation in measured fading rates for the IRSL₅₀ signal, with g-values of 3-11% decade⁻¹. This compares with g-values of 0-3% decade⁻¹ for the pIR-IRSL_{50,225} protocol, a figure broadly comparable to the pIR-IRSL g-values presented by Buylaert *et al.* (2009) and Buylaert *et al.* (2012a). This observation confirms that the pIR-IRSL_{50,225} protocol isolates a much more stable luminescence signal than the IRSL₅₀ protocol. Furthermore, the higher and highly variable fading rate of the IRSL₅₀ signal provides one probable explanation for some of the discrepancies observed both within and between previous feldspar chronologies in the Mojave Desert (e.g. Wintle *et al.*, 1994; Clarke *et al.*, 1995; Rendell and Sheffer, 1996).

Applications of fading correction on pIR-IRSL ages have ranged from over-corrections (e.g. Buylaert *et al.*, 2009; Reimann *et al.*, 2011; Kars *et al.*, 2012; Li *et al.*, 2014) through to under-estimation after fading correction Wallinga *et al.* (2007). The significance of the fading correction increases with age and for more recent samples (i.e. Holocene) fading corrections are often minimal (Huntley and Lamothe, 2001). For older samples, the uncertainty associated with the fading correction (g-value) can exert a large influence on final D_e uncertainty (Reimann *et al.*, 2011; Kars *et al.*, 2012). Consequently, care must be taken that the fading correction does not greatly increase the uncertainty of the D_e , especially where the fading corrections are small (Roberts, 2012). For samples with a large D_e and where the fading rate for the pIR-IRSL_{50,225} signal is not negligible (defined below), it can be useful to assess the degree to which the pIR-IRSL_{50,290} signal experiences a lower fading rate. The lower fading rate of the pIR-IRSL_{50,290} method implies it is derived from a more stable signal, albeit with a further reduced signal bleachability (Thiel *et al.*, 2011; Buylaert *et al.*, 2012a). To assess the fading rate of the pIR-IRSL_{50,290} signal, samples CN13-2-1, CN13-4-1, CN13-5-1, PK14-1-1 and SM13-1-1 were also measured using the pIR-IRSL_{50,290} protocol as they approximately represent the range of D_e values measured by this study. Figure 5.9 shows that for all samples except PK14-1-1 the pIR-IRSL_{50,290} D_e values are within one sigma error of the pIR-IRSL_{50,225} D_e s. Given this agreement, it is interpreted that the pIR-IRSL_{50,225} signal is not significantly faded for these samples.

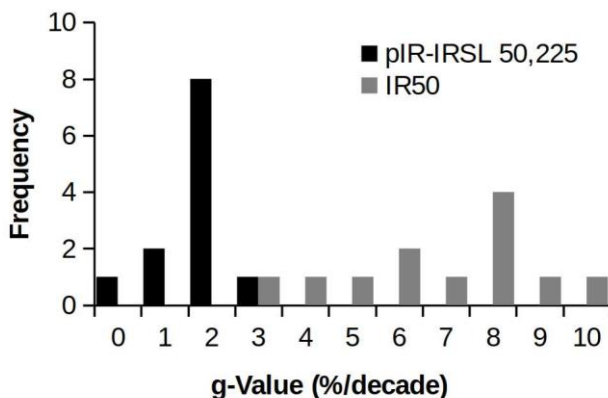


Figure 5.7: g-values for samples used in this study calculated for the IR₅₀ and pIR-IRSL_{50,225} protocols. **Figure 5.8.**

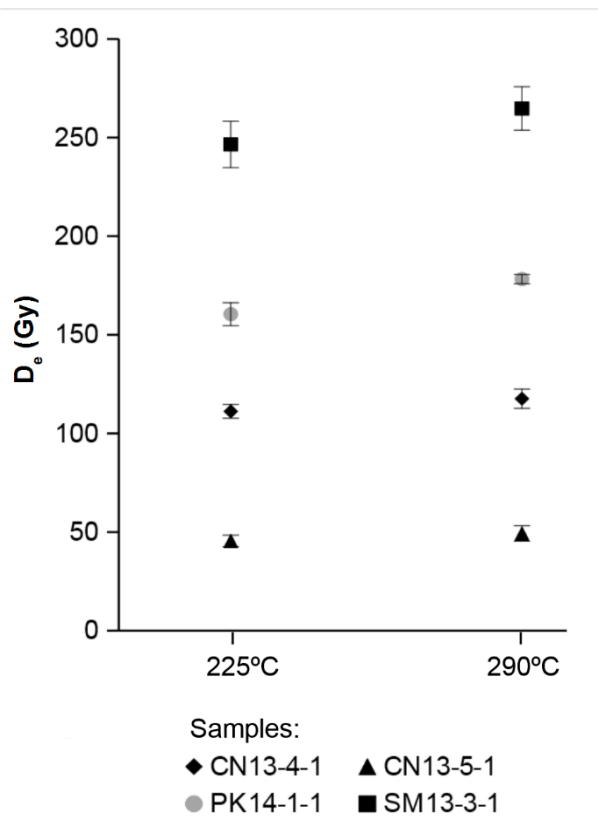


Figure 5.9: Equivalent dose for samples measured using both the pIR-IRSL_{50,225} and pIR-IRSL_{50,290} protocols.

This raises the question of the minimum g-value which should result in fading correction. Fu and Li (2013) argued that with a fading rate of ~1% there is only a small effect on the age of a Holocene sample and, in such a circumstance, a correction may lead to an overcorrection (Li and Li, 2011). Buylaert *et al.* (2012a) and Roberts (2012) suggested that g-values of <1.5% per decade of storage time might be largely an artefact of the laboratory fading tests and indeed might indicate that a stable signal has been reached, given the uncertainty associated with the fading rate measurement. Based on the above, fading correction was not applied where: either (1) the measured rate of fading (g-value) was less than or within uncertainty of 2% per decade of storage time or (2) where the D_e of the sample was too large for the correction procedure to be applied (D_e values which are not within the linear portion of the dose-response curve) (see Section 5.3.4). PK14-1-1 is notable as it shows a fading rate of 2.46 ± 0.2 % decade⁻¹ (which is >2% per decade), but is approaching the usable limit of the fading correction method of (Huntley and Lamothe, 2001) and so it is uncertain whether or not fading correction is appropriate. Fading correction was not applied to PK14-1-1

because the pIR-IRSL_{50,225} and pIR-IRSL_{50,290} D_es are within two sigma uncertainty and because a corrected pIR-IRSL_{50,225} D_e overestimates relative to the pIR-IRSL_{50,290} D_e.

5.2.3 Dose-recovery test

A dose-recovery experiment was performed for each sample for which a D_e was determined (except MR14-1-1 and MR14-1-2). The process comprised bleaching aliquots of each sample under natural light (UK south-facing window) for two days before dosing the aliquot with a known dose (similar to the anticipated equivalent dose) and running the pIR-IRSL_{50,225} protocol as if the dose were unknown. A dose-recovery test represents the most fundamental assessment of the efficacy of equivalent dose determining protocol (e.g. (Murray and Wintle, 2003)). Figure 5.10 shows the aggregate distribution of dose-recovery test results (n=34) and demonstrates that the pIR-IRSL_{50,225} protocol can recover a known dose within a 10% of unity for all of the samples measured across the study region, (average 0.99 ± 0.03). Note that the dose-recovery tests were not residual corrected (after Kars *et al.*, 2014b).

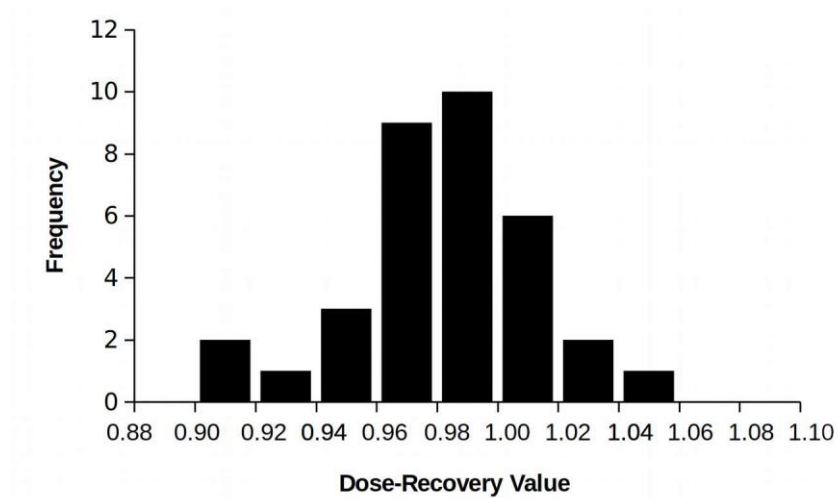


Figure 5.10: Dose-recovery values for samples measured by this study using the pIR-IRSL_{50,225} protocol. All samples were able to recover a known dose within a 10% uncertainty.

5.2.4 Additional protocol considerations

The preceding sections have outlined the trade-off between sample bleachability and finding a non-fading signal. For this study, it appears that the pIR-IRSL_{50,225} protocol is appropriate. Within the protocol, it is important to ensure that the preheating and test dose regimes are suitable.

Sample preheating

Preheating is performed prior to optical or infra-red stimulation to mimic the natural charge transfer that occurs during burial, and to remove unstable charge accrued during laboratory irradiation (Rhodes, 2011; Li *et al.*, 2014). Consequently, a suitable preheat temperature should be chosen that removes all unstable charge, but is low enough to avoid depleting the targeted luminescence signal (Wallinga *et al.*, 2000). When using the SAR protocol, preheating tests typically seek to identify a plateau in D_e across different preheat temperatures, indicative of a range of preheating temperatures that have no effect on the D_e (Murray and Olley, 2002). Accordingly, Reimann *et al.* (2011) observed a plateau of D_e with preheat temperatures between 160°C and 260°C for pIR-IRSL for young coastal sediments. Roberts (2012) observed a preheat plateau between 250°C and 280°C for measurements of Alaskan Loess, but a strong relationship between preheat temperature and D_e at higher temperatures implying D_e overestimation for preheats greater than 300°C. From this they concluded that the preheat temperature had a larger influence than stimulation temperature

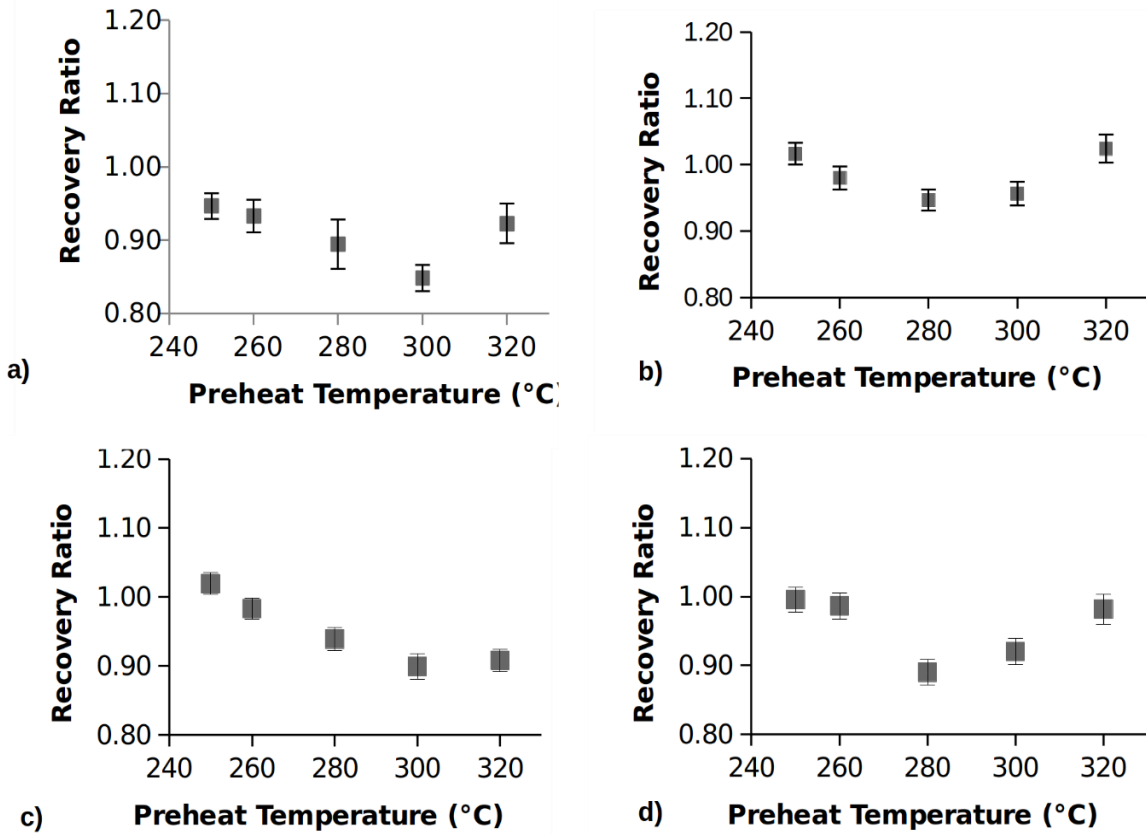


Figure 5.11: Preheat plateau test for samples CN13-5-1 (a), HL14-1-1 (b), SL14-3 (c) and SM13-3-1 (d).

over D_e estimation. There remains some debate on the relative roles of preheat and stimulation temperatures as the drivers of variability in pIR-IRSL D_e estimation, but this suggests that a preheat plateau test should be performed prior to using the pIR-IRSL_{T1,T2} protocol in any given area (Li *et al.*, 2014).

Preheat plateau tests were conducted as part of a dose-recovery experiment. Fifteen aliquots of each sample were sunlight-bleached for two days. Each aliquot was measured using one of five preheat temperatures between 250°C and 300°C with stimulation temperatures of 50°C and 30°C less than the preheat temperature (except for the 250°C preheat temperature which was only 25°C lower). A preheat temperature was considered acceptable if it led to a recovered dose within 90-110% of the given dose. By this measure D_e is independent of preheat temperature for the samples HL14-1-1, SL14-3 and SM13-3-1 but with sample CN13-5-1 underestimates the D_e when measured using a 300°C preheat (Figure 5.11). Overall, the ability to successfully recover a given dose using preheat between 250°C and 300°C indicates the appropriateness of the pIR-IRSL_{50,225} protocol to the samples from the Mojave Desert.

Test dose

The SAR protocol uses the test dose (T_x) to sensitivity correct the luminescence signal (L_x) (Murray and Wintle, 2000). It is important that the D_e is independent of the test dose size and this is broadly seen to be the case. However, Colarossi *et al.* (2017) demonstrated that, for pIR-IRSL signals, the test dose response can be dependent on the magnitude of the regenerated luminescence signal owing to the carry-over of charge from the L_x measurement. Other studies have observed small decreases in D_e with an increase in the test dose (e.g. Qin and Zhou, 2012) or an independence of D_e and test dose size (e.g. Buylaert *et al.*, 2012b; Nian *et al.*, 2012). Here a test was conducted whereby discs of a number of different samples (three per different test dose) were given a known dose (57.5Gy) before being measured using the standard SAR protocol varying only the size of the test dose, which was varied from 15% to 19% of the D_e . The results for this test, shown in Figure 5.12, indicate that the D_e measurements in the study are independent of the test dose size for the samples tested. A test dose of 60s was considered appropriate, as a smaller test dose minimises measurement time.

Table 5.3: A protocol for measuring determining whether D_e is independent of test dose size.

Step	Activity
1	Bleach Sample
2	Give Dose
3	Preheat
5	Measure Luminescence Signal (L_x) This may require multiple measurements at different temperatures if using a pIR-IRSL _{T1, T2} protocol
6	Give Test Dose Groups of three aliquots receive a test dose equivalent to either 15%, 30%, 45%, 60% and 90% of the D_e and which are consistent throughout the experiment.
7	Preheat
8	Measure Luminescence Signal (T_x) This may require multiple measurements at different temperatures if using a pIR-IRSL _{T1, T2} protocol
9	Repeat from Step 1 varying the storage time for each new cycle

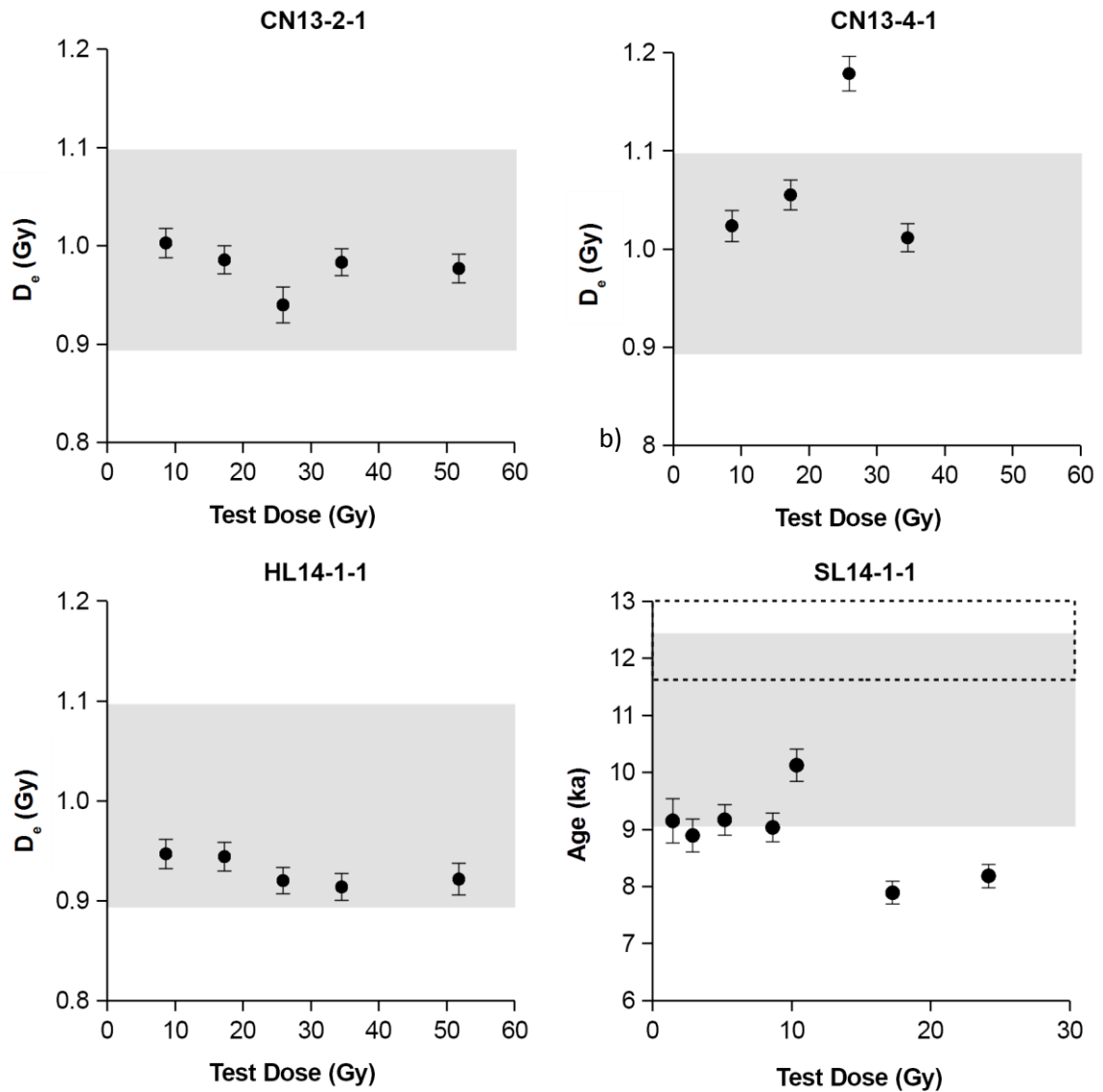


Figure 5.12. The relationship between equivalent dose (D_e) and test dose size is shown for samples CN13-2-1, CN13-4-1, HL14-1-1, and SL14-1-1. The grey band highlights the size of an acceptable recovery ratio for the given dose of 57.5Gy ($\pm 10\%$), except for SL14-1-1 where the grey band indicates the last lake high stand and the dashed box represents the preceding low stand (Kirby *et al.*, 2015).

5.2.5 Summary

This section has demonstrated that the pIR-IRSL_{50,225} signal is bleachable under natural conditions, that it exhibits a much lower rate of fading compared with the IRSL₅₀ signal and that the protocol can consistently recover a known-dose in the samples. It is therefore concluded that the pIR-IRSL_{50,225} protocol provides a suitable trade-off between signal bleachability and mitigating the effects of anomalous fading, as demonstrated by comparison

with data obtained using a pIR-IRSL_{50,290} protocol. Thus, based upon common acceptance criteria, the measurement protocol ought to be suitable for the Mojave Desert samples in this study.

5.3 Comparison of derived equivalent doses at two sites with independent age control

In order to consider this further, this section provides a direct test of the accuracy of this method through a direct comparison with independent chronologies at two independently dated palaeo-lake sites, both of which have comparable sediment provenances (ultimately the Mojave River).

5.3.1 Silver Lake

Silver Lake playa is located north of Baker, CA, and forms the contemporary terminus of the Mojave River. The Mojave River has probably been the most significant sediment source to Silver Lake for at least the last 20ka (Meek, 1999; 2003; Enzel *et al.*, 2003; Reheis and Redwine, 2008; Reheis *et al.*, 2012; 2015). During the Late Pleistocene Silver Lake formed a part of pluvial Lake Mojave and experienced high-stands at 14.4-13.6 cal yr BP (Mojave I) and at 11.7-8.7 cal yr BP (Mojave II) and a potential desiccation 13.6-11.6 cal yr BP (Wells *et al.*, 2003; Kirby *et al.*, 2015) (see Section 3.2.4). The site under discussion (“Silver Quarry” – Wells *et al.*, 2003) comprises a spit and shoreline system at the north end of the playa, which was exposed by quarrying (Figure 5.13). This locale was subject to a detailed, multi-method (¹⁴C, U-series, OSL, AAR) dating inter-comparison study (Owen *et al.*, 2007), which provided the reasonably robust age constraints required here. The exposures at the site today very closely match the diagrams and descriptions in Owen *et al.* (2007) and as such it was possible to confidently identify Lithofacies associations (LFA) 8 (their sample UCR125) and LFA6 (their sample SL3). Thus, samples SL14-1-1 and SL14-1-2 correspond (respectively) to UCR-125 and SL-3 as described in Owen *et al.* (Figure 5.13).

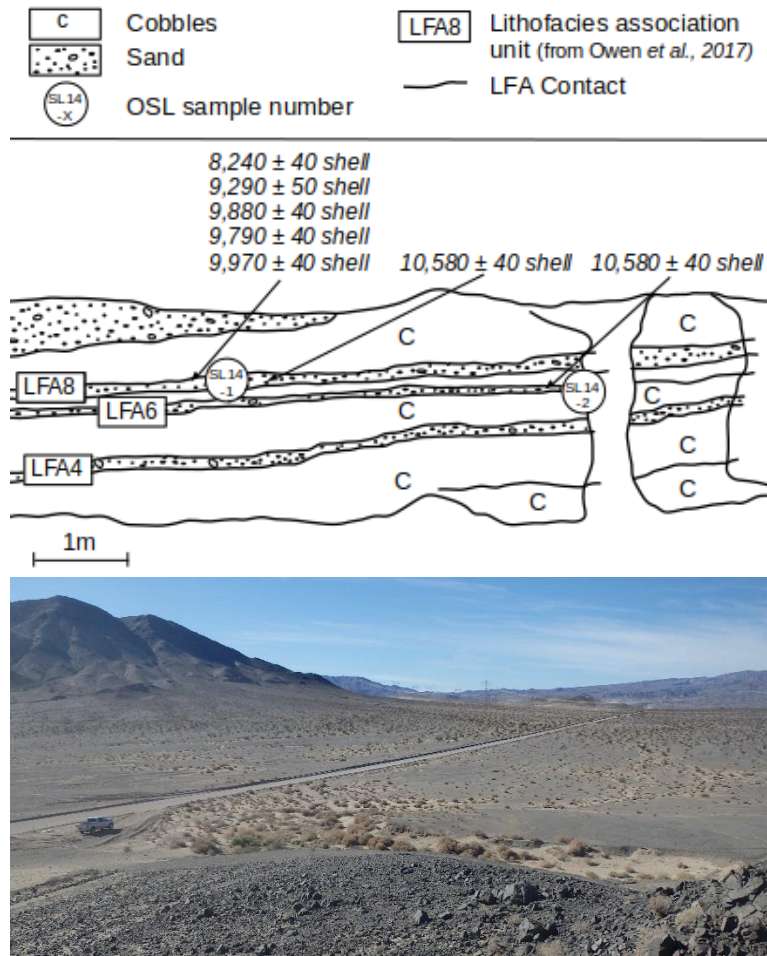


Figure 5.13: Stratigraphy (upper) for the measured section at Silver Lake showing the two luminescence sample locations alongside the range of uncalibrated radiocarbon dates reported by Owen *et al.* (2007). The image (lower) shows the sampling location where the lake floor is to the left of the photo (continuing out of shot), with the quarry exposures lower centre and the spit extending out to the right

reported feldspar IRSL₅₀ (multi-aliquot additive dose) sample ($9.4 \pm 1.5\text{ka}$ – uncorrected age where no fading rate was reported for sample SL14-123). The single grain D_e is marginally lower than the single aliquot D_e for sample SL14-1-1 ($7.4 \pm 0.7\text{ka}$) (Figure 5.15 – discussed below).

Uncorrected single aliquot feldspar pIR-IRSL_{50,225} ages SL14-1-1 ($8.8 \pm 0.4\text{ka}$) and SL14-1-2 ($11.4 \pm 0.5\text{ka}$) in Table 5.4 correspond with the range of radiocarbon ages for these units reported in Owen *et al.* (2007). Dose recovery ratios for the two samples are 1.00 ± 0.01 (SL14-1-1) and 0.99 ± 0.01 (SL14-1-2).

Because of the young age and as measured fading rates for these samples were low ($2.1 \pm 0.3\% \text{decade}^{-1}$ and $0.7 \pm 0.3\% \text{decade}^{-1}$ respectively), both fading-corrected and uncorrected ages for the pIR-IRSL_{50,225} and IRSL₅₀ signals are within uncertainties of each other, the radiocarbon dates and the previously

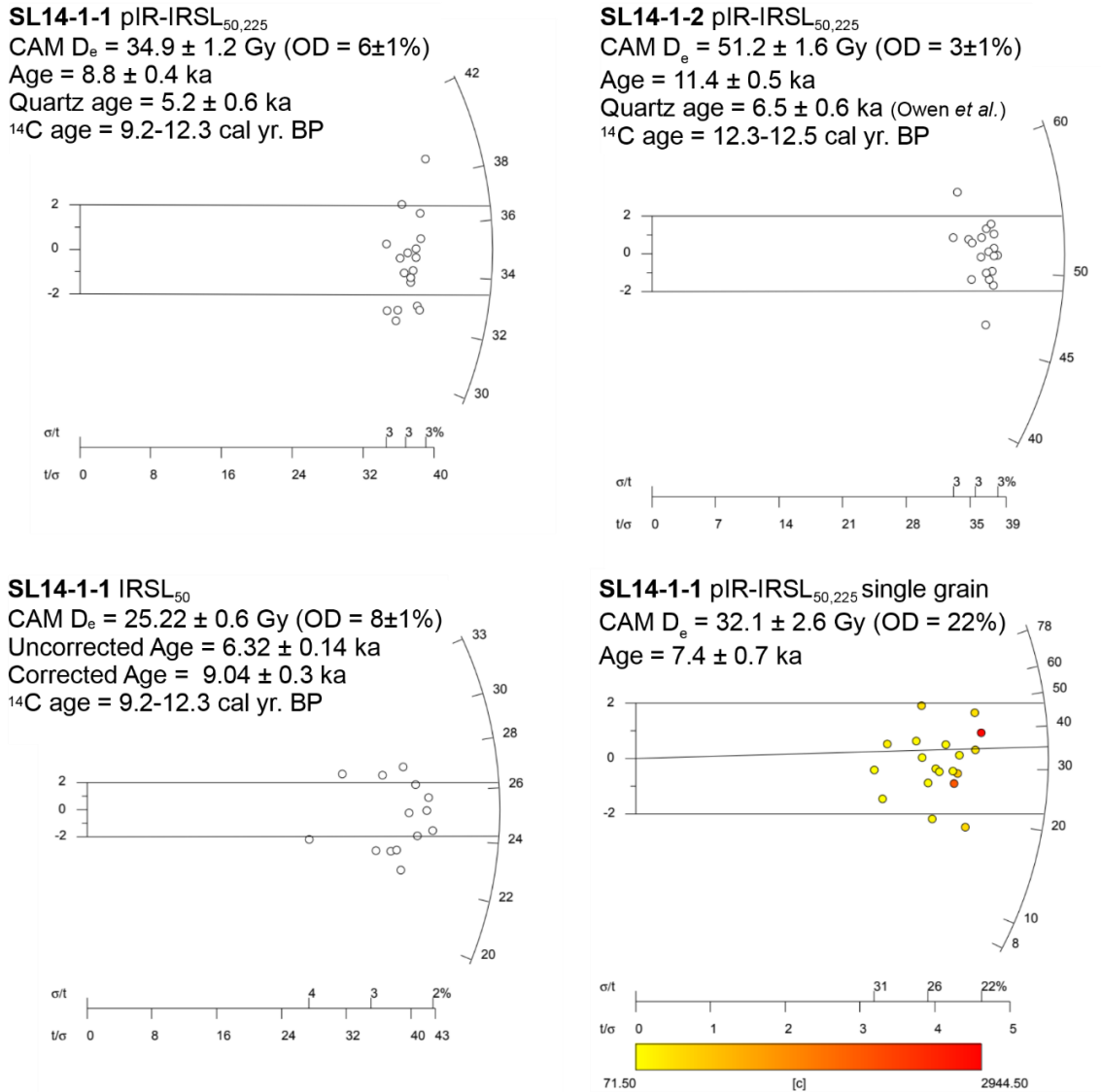


Figure 5.14: Radial plots for samples SL14-1-1 and SL14-1-2 derived using the pIR-IRSL_{50,225} signal (upper). Single grain pIR-IRSL_{50,225} and single aliquot IRSL₅₀ data are also shown for sample SL14-1-1 (lower).

The majority of the OSL ages reported by Owen *et al.* (2007) were derived using quartz, and in all cases presented age underestimations relative to the radiocarbon dating (and considerable D_e scatter was reported). An explanation of this underestimation is now afforded by the analysis of the new SL14 quartz extracts. All aliquots analysed were rejected by the fast ratio criterion (Durcan and Duller, 2011) (see Section 5.1.3). A “best” estimate of the quartz age, based on D_e s derived using the early background subtraction method (Cunningham and Wallinga (2010) – Table 5.4) produced an age of 5.2 ± 0.6 ka, which cannot

be correct as it post-dates the early Holocene inundation of Silver Lake, as recorded in the Silver Lake core presented by Kirby *et al.* (2015). Thus, quartz ages represent an underestimation of approximately one third compared with K-Feldspar ages (Owen *et al.*, 2007). Pigati *et al.* (2011) reported similar findings at Valley Wells ~50km to the East of Silver Lake. Section 5.1 demonstrated that this underestimation results from the vast majority of quartz grains not being fast component dominated. Both the presence of feldspar contamination and/or a proportionally high signal contribution from thermally unstable medium component can explain the observed D_e underestimation (Li and Li, 2006; Steffen *et al.*, 2009; Klasen *et al.*, 2016).

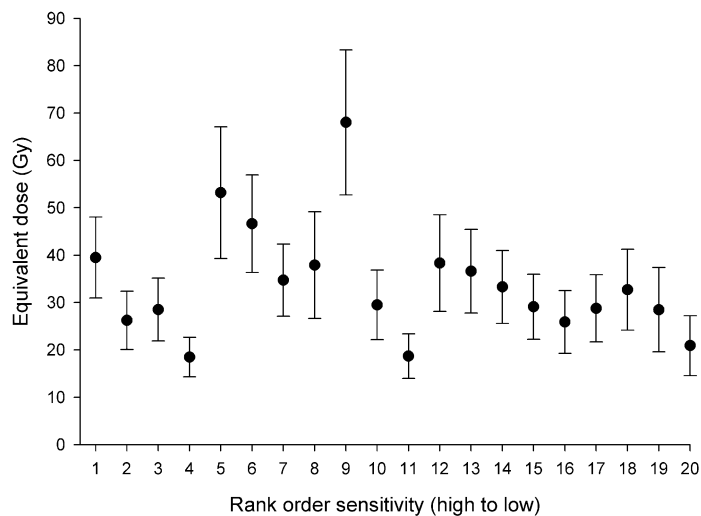


Figure 5.15: SL14-1-1 single grain D_e plotted with ranked grain sensitivity does not appear to show the “declining baseline” described by (Rhodes, 2015) (discussed in the text).

Table 5.4: Dosimetry data for samples at Silver Lake, CA, from this study with comparable data shown as reported in Owen *et al.*, 2007. Dose rates were derived independently from Owen *et al.*, but the values are comparable.

Study	Sample	Depth (m)	Water Content (%)	Dose Rate (Gy/ka)	D _e (Gy)	g-value (%/decade)	Age (ka)
This study	SL14 – 1-1 F	0.4	10±5 (1) ^a	3.96 ± 0. 14	34.9 _b ± 1.2	2.10 ± 0.3	8.8 ± 0.4
	SL14 – 1-1 Q	0.4	10±5 (1) ^a	3.14 ± 0. 12	16.3 ^c ± 2.0		5.2 ± 0.6
	SL14 – 1-2 F	1.2	10±5 (1) ^a	4.53 ± 0. 16	49.9 _b ± 1.9	0.71 ± 0.3	11.3 ± 0.5
Owen <i>et al.</i> , 2007	SL14-123 (dup) Q		1 ^a	4.31 ± 0. 18	20.8 ± 1.1		4.8 ± 0.6
	SL14-123 (dup) F		1 ^a	6.35 ± 0. 26	59.9 ± 4.2		9.4 ± 1.5
	SL14-125 Q		10±5 (1) ^a	3.81 ± 0. 26	25.1 ± 7.2		6.6 ± 0.7
	SL14-3 Q		10±5 ^a	2.30 ± 0. 40	12.2 ± 3.7		5 ± 2
	¹⁴ C	Ten Radiocarbon dates stratigraphically equivalent to SL14-1-1					
¹⁴ C	Three Radiocarbon dates stratigraphically equivalent to SL14-1-2						12.3 – 12.5

Notes:

^a Moisture content assumed to be 10±5 as Owen *et al.*, 2007. Value in parentheses is field measured value.

^b D_e measured on 180-212 micron size fraction using a single aliquot post infra-red stimulated luminescence dating (pIR-IRSL_{50,225}) protocol.

^c D_e calculated using the Early Background Subtraction method (Cunningham *et al.*, 2010) as a best estimate value (Table 5.1), though all values were rejected using the Fast Ratio Test (Durcan and Duller, 2011) implying that the quartz-grains are unsuitable for quartz OSL dating using the SAR protocol owing to contamination (see Section 5.1).

Overall, this section has demonstrated that the quartz OSL strongly underestimates ages at Silver Lake (in accordance with Section 5.1) whereas the feldspar pIR-IRSL_{50,225} gives ages with good accordance with the independent chronology. Owen *et al.* observed only partial bleaching within the Silver Lake samples, however the agreement between the single aliquot and single grain D_es does not suggest that bleaching poses a significant problem for SL14-1-1. As the sediments form part of a shoreline feature, it can be concluded that water-lain deposits can potentially be adequately bleached.

5.3.2 Harper Lake

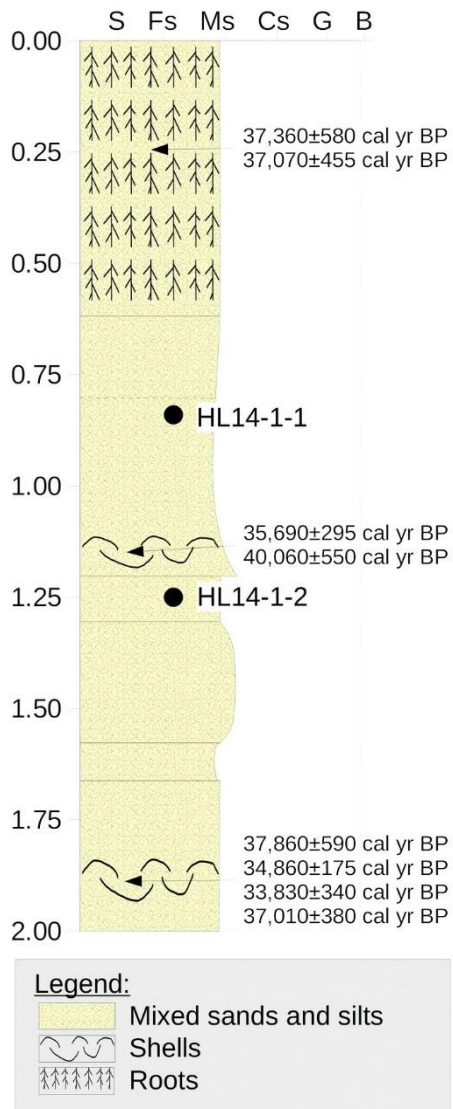


Figure 5.16: Site views looking west along the outcrop at Harper Lake (upper) and stratigraphic diagram for the measured section (lower) showing the two luminescence sample locations alongside the geochronology reported by Garcia *et al.* (2014).

The Harper Basin is situated to the northwest of Barstow, CA. It is a closed basin that episodically received waters from the Mojave River during the Pleistocene, maintaining several pluvial high stands during the last 0.5 Ma (Cox *et al.*, 2003; Jefferson 2003; Meek, 2003; Reheis *et al.*, 2012; 2015). Two recent Harper Lake high stands have been inferred at >30 ka and ~25 ka (uncalibrated) as the Mojave River alternated between terminating in Harper Lake and Lake Manix (Garcia *et al.*, (2014) and references therein). These lake bed deposits, exposed at ‘Mountain View Hill’ (Figure 5.16), were first described by Meek (1999) with a more recent radiocarbon and luminescence dating analysis by Garcia *et al.* (2014). The most recent calibrated radiocarbon dates shown in Figure 5.16 are approaching the upper age limits of radiocarbon dating methods; contamination of modern carbon can significantly affect the dates (as noted by Quade *et al.* (2003) and Pigati *et al.* (2011)). Despite the uncertainty that this introduces, these dates provide a further suite of independent ages for comparison. Here samples were collected adjacent (within <1m) to the same section as Garcia *et al.* (2014) (Figure 5.16).

The new pIR-IRSL_{50,225} signal at both sites produced highly reproducible D_e estimates (HL14-1-1 and HL14-1-2), which are 106.5 ± 3.5Gy and 104.1 ± 3.2Gy. Furthermore, dose-recovery ratios of 0.98 ± 0.01 (HL14-1-1) and 0.97 ± 0.01 (HL14-1-2) were obtained. The age for HL14-1-1 is within uncertainties of one of the fine-grain feldspar ages in Garcia *et al.*, but younger than their fine-grained IRSL ages (Figure 5.16). Fading corrected ages of 29 ± 2 ka (for both samples) are within uncertainty of the lower of Garcia *et al.*'s fine-grained fading-corrected IRSL₅₀ ages (28 ± 2 and 38 ± 2ka – measured fading rate 7.42% decade⁻¹), but are younger than their radiocarbon dates (40-33 cal ka BP – recalibrated with Intcal13). MET-pIR-IRSL age estimates for HL14-1-2 show a significant increase in D_e from the 50°C signal (which is significantly faded – measured fading rate 9.42% per decade) to a plateau of the 200°C, 250°C and possibly the 300°C signals which is in agreement with the radiocarbon chronology (Figure 5.17). This result suggests fading correction for the pIR-IRSL_{50,225} signal may be required. Fading correction of the IRSL₅₀ signal at HL14-1-2 brings the age into alignment with the Harper Lake high stand record of Garcia *et al.*, albeit with a significant imprecision (35 ± 10 ka).

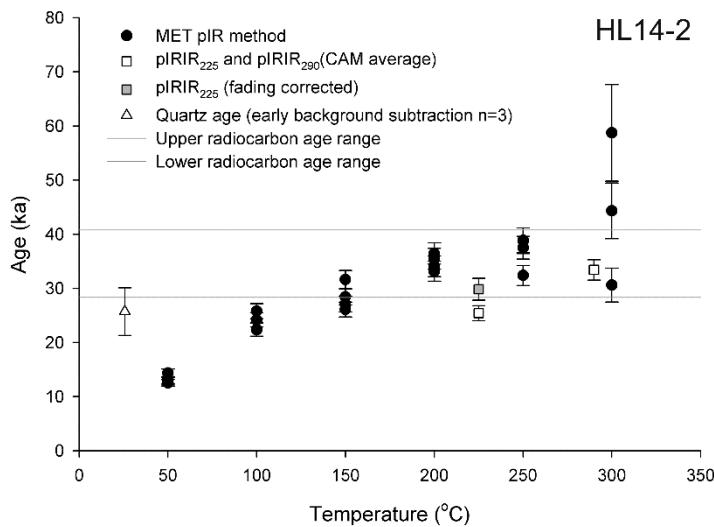


Figure 5.17: K-feldspar ages for HL14-1-2 as derived using three different measurement protocols.

The single grain CAM D_e shows little scatter but is lower than the single aliquot D_e (Figure 5.18d), due to several relatively dim (yellow shaded) grains. When single grain D_es are plotted with ranked grain brightness they show evidence of the “declining baseline” described by Rhodes (2015), with the fading data indicating that, though precision is lower

for the dimmer grains, the declining base does not relate to systematically higher fading rates (discussed further in Section 5.4.2).

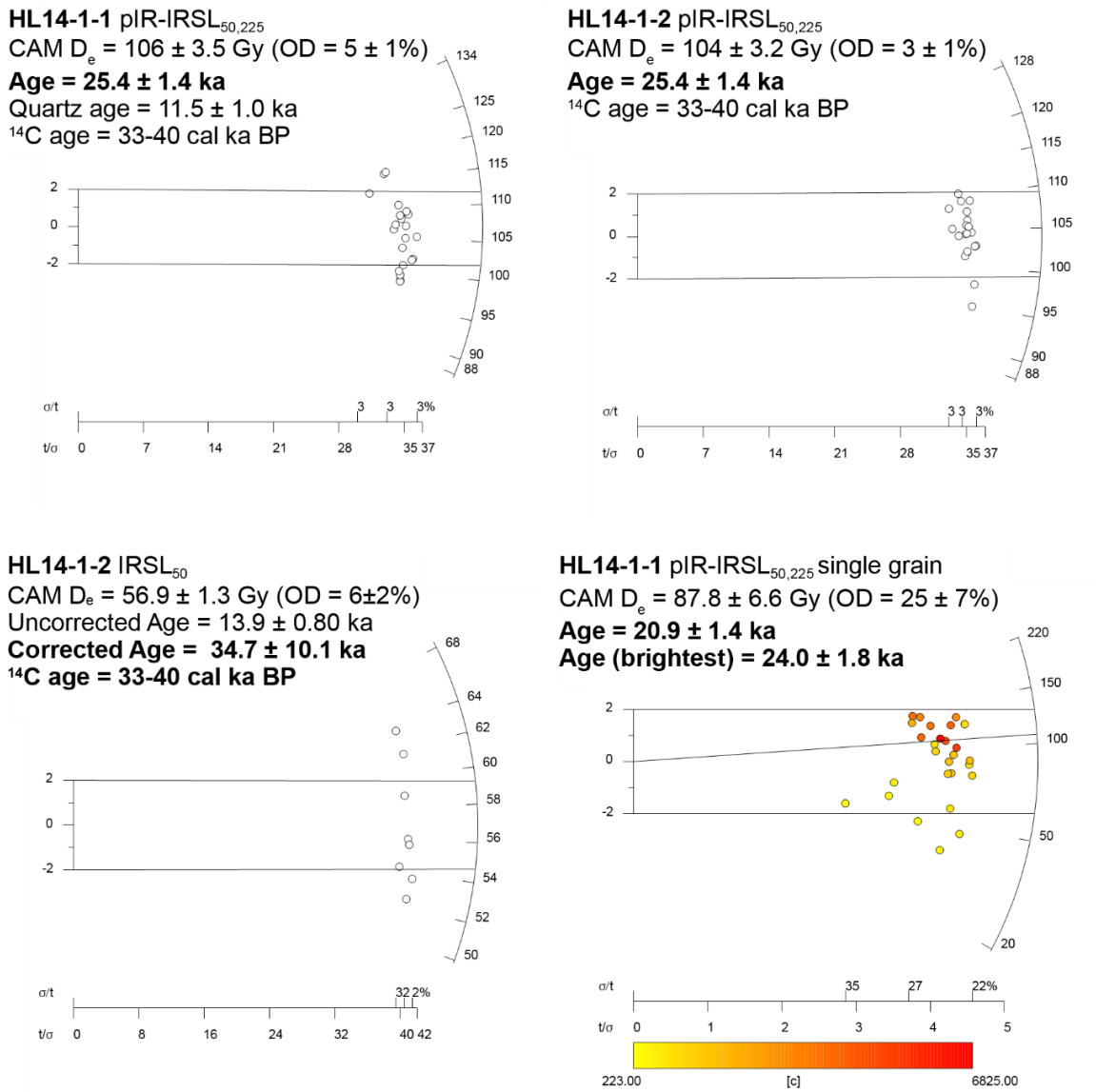


Figure 5.18: Radial plots for samples HL14-1-1 and HL14-1-2 derived using the pIR-IRSL_{50,225} signal (upper). Single grain pIR-IRSL_{50,225} and single aliquot IRSL₅₀ data are also shown for samples HL14-1-2 and HL14-1-1 respectively (lower). The brightest grain represents the grain with the largest net-signal response to the first test dose.

The Quartz OSL age for HL14-1-1 is 11.5 ± 1 ka ($n=20$) and represents an underestimation of approximately two thirds compared with the corrected feldspar ages and the radiocarbon chronology from Garcia *et al.* (2014). Applying the fast ratio rejection criterion (Section 5.1.3) rejects all aliquots but one, with the resulting age of 36 ± 8 ka (Table 5.5) within

uncertainties of the pIR-IRSL ages and the radiocarbon dates. Garcia *et al.* (2014) also presented ages derived using a quartz luminescence method, from which ages of 16-19 ka were obtained.

Table 5.5. Dosimetry data (measured independently) for samples at Harper Lake, CA, from this study with comparable data shown as reported in Garcia *et al.*, 2014.

Study	Sample	Depth (m)	Water Content (%)	Dose Rate (Gy/ka)	D _e (Gy)	g-value (%/decade)	Uncorrected / Corrected Age (ka)
This study	HL14-1 F	0.84	14.5 (1) ^a	4.19 ± 0.17	106.6 ± 3.5 ^b	2.35 ± 0.2 ^d	25.4 ± 1.4 29.1 ± 1.8
	HL14-1 Q	0.84	14.5 (1) ^a	3.34 ± 0.15	89.6 ± 13.8		25.7 ± 4.4
	HL14-2 F	1.25	14.5 (1) ^a	4.10 ± 0.16	104.1 ± 3.3 ^b	2.35 ± 0.2 ^d	25.4 ± 1.4 29.9 ± 1.8
Garcia <i>et al.</i> , 2014	ALG-HL-OSL3 Q	0.70	14.5 (1) ^a	3.56 ± 0.20	63.3 ± 3.9 ^c		18 ± 1
	ALG-HL-OSL3 F	0.70	14.5 (1) ^a	4.55 ± 0.24	78.3 ± 2.4 ^c	7.42 ^e	17 ± 0.5 28 ± 2
	ALG-HL-OSL2 Q	0.70	14.5 (1) ^a	3.56 ± 0.20	98.7 ± 2.5 ^c		17 ± 1.5
	ALG-HL-OSL2 F	0.70	14.5 (1) ^a	4.55 ± 0.24	98.7 ± 2.5 ^c	7.42 ^e	22 ± 0.5 38 ± 2
	ALG-HL-OSL1 F	1.40	13.5 (3) ^a	4.76 ± 0.34	130 ± 2.7 ^c	7.42 ^e	27 ± 0.6 46 ± 3
					120 ± 2.5 ^c	7.42 ^e	25 ± 0.5 42 ± 3
	¹⁴ C	0.2					37 ± 1
¹⁴ C	1.1					35 - 40.5	

Notes:

- ^a Moisture content assumed to be 50% of the saturated value measured by Garcia *et al.*, 2014. Field moisture content is shown in parentheses.
- ^b D_e measured on 180-212 micron size fraction using a single aliquot pIR-IRSL_{50,225} protocol.
- ^c D_e measured on 4-11 micron size fraction using multiple aliquot additive dose (MAAD) protocol.
- ^d Fading measured on sample HL14-2 with a t_c of 548 seconds.
- ^e Fading measured on sample ALG-HL-OSL1.

Harper Lake has greater chronological uncertainties than Silver Lake as the radiocarbon dates are closer to the limit of the technique. However the pIR-IRSL_{50,225} are close to the lower range of these and hence are in broad agreement with the independent chronology presented by Garcia *et al.* (2014), and indeed other records of the Mojave River history (e.g. Enzel *et al.*, 2003; Reheis *et al.*, 2012; Reheis *et al.*, 2015). Consequently, it is inferred that the pIR-IRSL_{50,225} luminescence dating protocol is also appropriate for dating at the Harper Lake site.

5.4 Deriving equivalent dose estimates

Weighted mean D_e values were derived for all samples using the Central Age Model. The model provides a measure of the relative standard deviation of this distribution compared with a central D_e , termed overdispersion (OD), which is a measure of inter-aliquot scatter unaccounted for by individual measurement uncertainties. This additional scatter is thus often considered to represent the “external variation” in D_e , such as incomplete bleaching or post depositional mixing and internal variation such as thermal transfer (though the dose-recovery test suggests that the influence of these should be minimal) (Galbraith *et al.*, 1999).

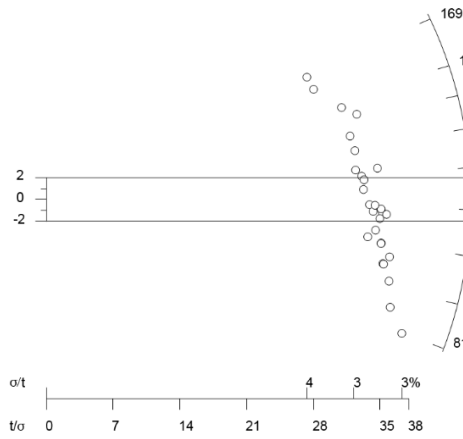
5.4.1 Observations of D_e scatter

High levels of inter-aliquot scatter, often coupled with a large skewness (Olley *et al.*, 1998; Wallinga, 2002a), are usually considered indicative of incomplete bleaching, bioturbation and/or beta dose rate heterogeneity (Murray and Roberts, 1997; Wallinga, 2002a; Mayya *et al.*, 2006; Bateman *et al.*, 2007). Luminescence D_e estimates at five of the Cady Mountains field sites exhibit low levels of inter-aliquot scatter (defined here where $OD < 15\%$ – as Galbraith *et al.*, 1999; Neudorf *et al.*, 2012), whereas three sites show both high OD values (CN13, DN14 and ER14) and age reversals (e.g. Table 5.6).

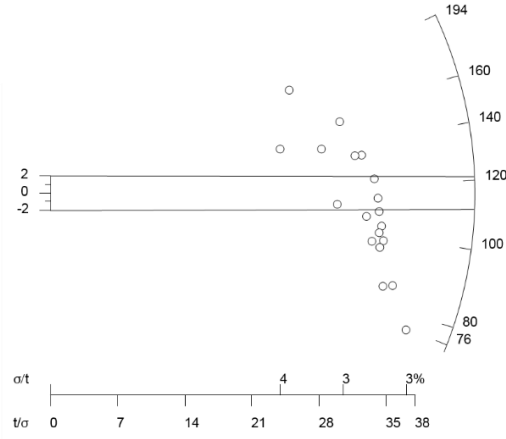
Radial plots for selected samples are visualised as radial plots below (after Galbraith *et al.*, 1999) and which are described here:

- CN13 (Figure 5.19) shows an age reversal in both the upper and lower portions of the section (Section 7.1.2). The upper portion contains five samples, which all give high OD values of 16-25% and show an age reversal for samples CN13-4-1/CN14-3-1. The lower portion contains three samples which all give lower OD values of 8-11% where the upper two ages are within uncertainties and the lowermost age (CN13-7-1) is ~10ka younger than those stratigraphically higher.
- Four single aliquot ages from DN14 (Figure 5.20) are not in stratigraphic order and each has an OD of ~30%.
- ER14 has three ages, with the upper two being ~3ka and the lowermost sample giving an age of ~1.5ka (58% aliquot rejection rate).

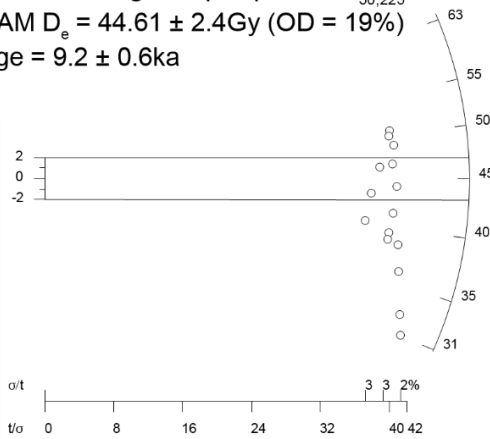
CN13-2-1 single aliquot pIR-IRSL_{50,225}
 CAM $D_e = 111.2 \pm 3.5\text{Gy}$ (OD = 17%)
 Age = $22.1 \pm 1.1\text{ka}$



CN13-3-1 single aliquot pIR-IRSL_{50,225}
 CAM $D_e = 114.9 \pm 7.3\text{Gy}$ (OD = 24%)
 Age = $23.7 \pm 1.8\text{ka}$



CN13-4-1 single aliquot pIR-IRSL_{50,225}
 CAM $D_e = 44.61 \pm 2.4\text{Gy}$ (OD = 19%)
 Age = $9.2 \pm 0.6\text{ka}$



CN13-5-1 single aliquot pIR-IRSL_{50,225}
 CAM $D_e = 245.0 \pm 10.0\text{Gy}$ (OD = 10%)
 Age = $52.4 \pm 3.0\text{ka}$

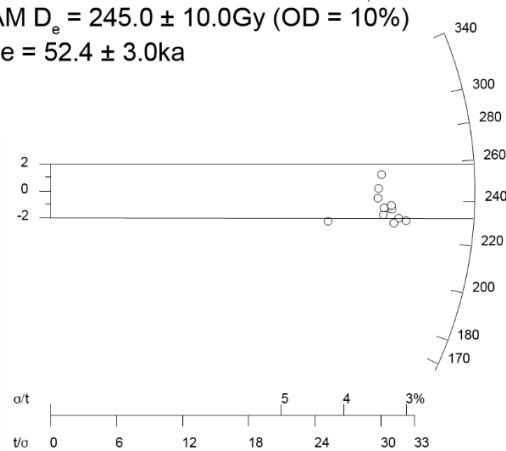
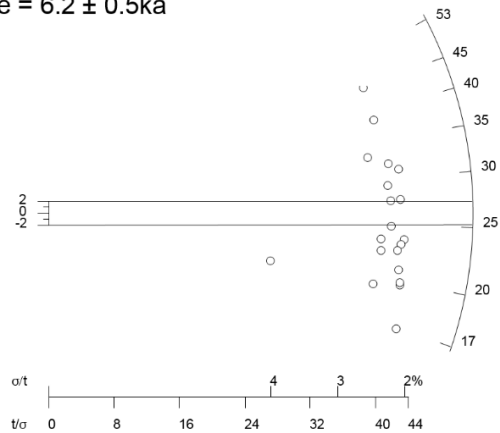
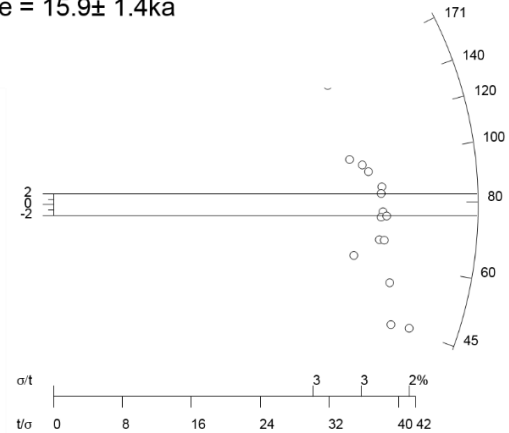


Figure 5.19: Single aliquot radial plots for samples (a) CN13-2-1, (b) CN13-3-1, (c) CN13-4-1 and (d) CN13-5-1.

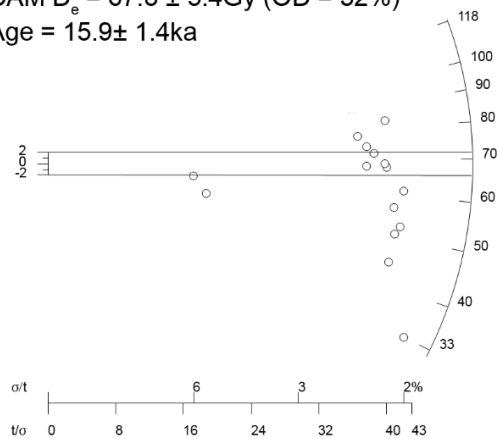
DN14-1-1 single aliquot pIR-IRSL_{50,225}
 CAM $D_e = 26.0 \pm 1.8\text{Gy}$ (OD = 30%)
 Age = $6.2 \pm 0.5\text{ka}$



DN14-1-2 single aliquot pIR-IRSL_{50,225}
 CAM $D_e = 75.2 \pm 6.4\text{Gy}$ (OD = 31%)
 Age = $15.9 \pm 1.4\text{ka}$



DN14-1-3 single aliquot pIR-IRSL_{50,225}
 CAM $D_e = 67.8 \pm 5.4\text{Gy}$ (OD = 32%)
 Age = $15.9 \pm 1.4\text{ka}$



DN14-1-4 single aliquot pIR-IRSL_{50,225}
 CAM $D_e = 35.1 \pm 1.9\text{Gy}$ (OD = 36%)
 Age = $8.0 \pm 0.7\text{ka}$

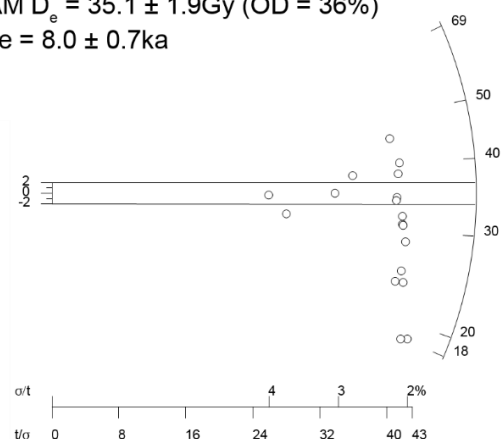


Figure 5.20: Single aliquot radial plots for samples (a) DN14-1-1, (b) DN14-2-1, (c) DN14-3-1 and (d) DN14-4-1.

5.4.2 Identifying incomplete bleaching using single grain analysis

Small aliquots (~3mm) were adopted by this study (Section 4.4.3) as an initial approach to assessing potential inter-grain/inter aliquot scatter. This minimises inter-gain averaging, increasing the chances of identifying the presence of outlier grains/aliquots (Li, 1994; Wallinga, 2002b). However where incomplete bleaching looks probable it can be critical to (additionally) derive D_e s at the single grain level to obviate grain averaging effects within (even) small aliquots (Olley *et al.*, 1998; Rhodes, 2007; Duller, 2008). Furthermore, plotting

the single-grain distribution of an incompletely bleached sample often results in a characteristically skewed distribution featuring a mode surrounding the “true” D_e and a tail of older grains (Olley *et al.*, 1998; Wallinga, 2002a). Under such conditions, the minimum D_e can be a better measure of the true D_e , commonly derived using the minimum age model of Galbraith *et al.* (1999). To investigate the potential for inferred incomplete bleaching at CN13 samples from this site (CN13-1-2 through CN13-5-1), as well as the two lake sites which, on the basis of an initial appraisal of the single aliquot data, are assumed unlikely to be incompletely bleached (HL14-1-1 and SL14-1-1).

A single grain of feldspar was mounted onto each aliquot by hand and measured on the luminescence reader as if a small-aliquot (as per Section 4.4.3). After measuring the grains, the aliquots were observed with a hand lens and only disks confirmed to contain a single grain were retained for the analysis (the remainder had two grains and were discounted from further analysis). Individual D_e uncertainties include the incorporation of an intrinsic OD of 15% (as Rhodes, 2015). Measured OD values for samples in this study, as obtained from dose-recovery tests, ranged from ~4% for SL14 to ~22% for CN13-4-1 (Table 7.1). Dose-recovery experiments were performed on samples CN14-3-1, CN13-4-1 and SL14-1-1, all of which recovered a known dose within a 10% uncertainty.

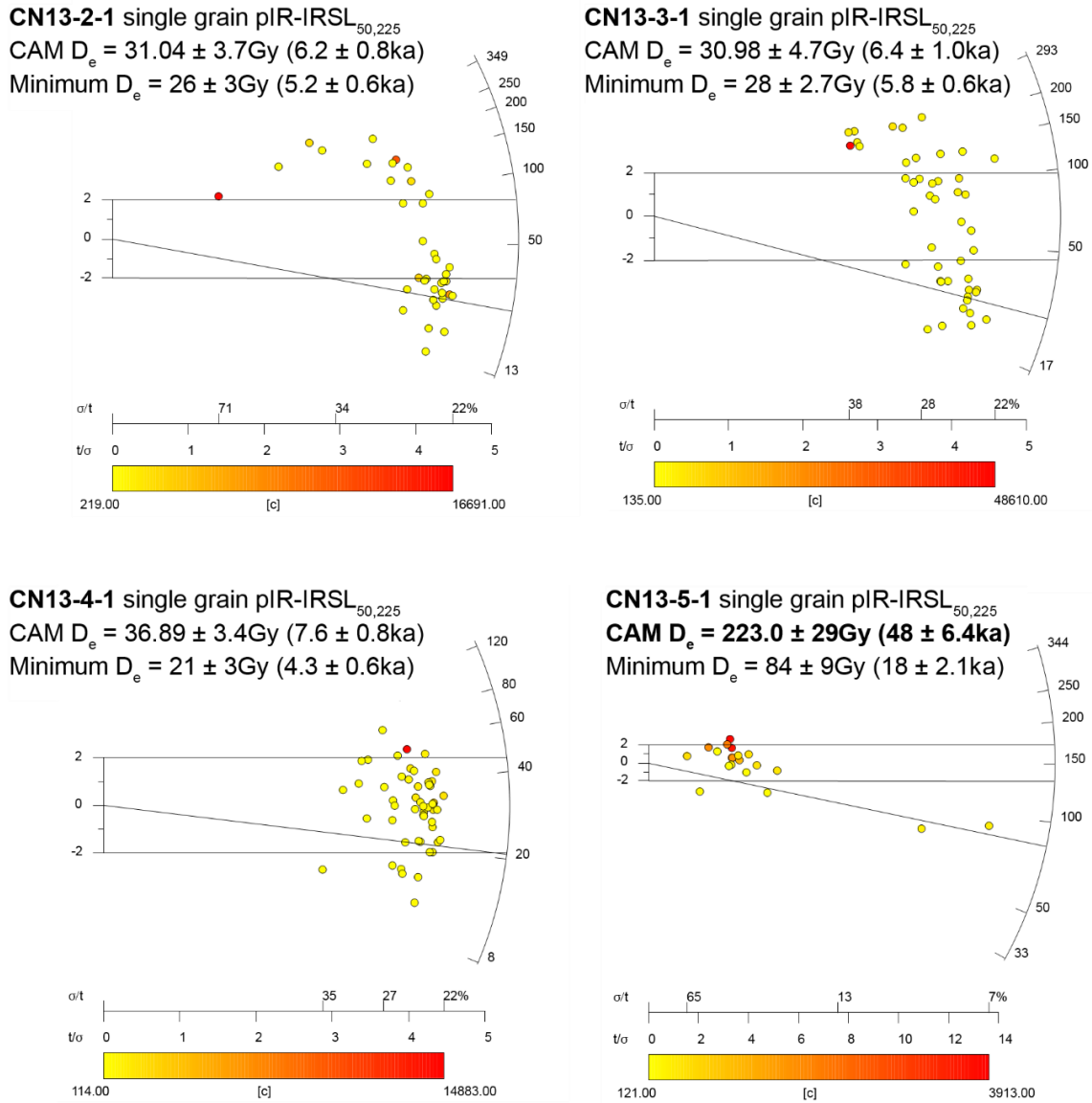


Figure 5.21: Single grain radial plots for the samples CN13-2-1 (a), CN13-3-1 (b), CN13-4-1 (c) and CN13-5-1 (d).

Single grain distributions for samples SL14-1-1 and HL14-1-1 are slightly younger than their single aliquot D_e (Figure 5.14d and Figure 5.18d), but do not indicate that bleaching or bioturbation are significant issues for these samples; both show relatively tight distributions, without any skewness. Single grain radial plots highlight several dim, young grains at HL14-1-1 (Figure 5.14d) and CN13-5-1 (Figure 5.21d), both of which lead to an underestimation of D_e using the minimum age model (MAM) (Galbraith *et al.*, 1999). Dim, small D_e grains were also noted by (Rhodes, 2015), who identified that some Mojave K-Feldspar single grain distributions show a “declining base” – where minimum D_e decreases if grains are plotted in

rank order of sensitivity. Declining bases were observed for samples HL14-1-1, CN13-2-1, CN13-3-1, CN13-4-1 and CN13-5-1 (but not SL14-1-1 or for any dose-recovery tests). The phenomenon may relate to variability in K-Feldspar content between grains (which influences their dose rate), but investigation showed that this declining base is independent of individual grain fading rate. Due to the influence of the declining base on any attempt to apply MAM D_e minimum, D_{es} were derived using an approach following (Rhodes, 2015) and are shown in Table 5.6. The process involved two steps: (1) grains were sorted into decreasing rank sensitivity order and grains were then progressively accepted up to the point where the declining base has decreased by the intrinsic OD value adopted for the dataset (15%) (removing grains significantly affected by the declining baseline); (2) the grain with a D_e which is furthest (largest) from the weighted mean is iteratively rejected until the distribution is consistent with a single population (effectively removing high outliers) (using Galbraith, 2003). For each sample adopted grains are shown as enclosed circles in Figure 5.22.

Applying this approach for all samples from CN13 removes the age reversal within the upper portion of the stratigraphy. Two samples (CN13-4-1 and CN13-5-1) provide single grain D_{es} that are within uncertainties of the single-aliquot CAM D_e after removal of the baseline (Table 5.6). Above these, CN13-2-1 and CN13-3-1 provide ages that are younger than those that were derived using single-aliquot CAM and which also displayed a tail of larger D_e values (Figure 5.22), suggesting that incomplete bleaching is an issue for these samples. This incomplete bleaching presumably relates to the significant volumes of locally-derived coarse-grained material present within the upper portion of CN13 (Section 7.1.3), which are more likely to be incompletely bleached as they will be transported by fluvial or colluvial processes which are less easily bleached in nature (Clarke, 1996; Fuchs and Wagner, 2003). Based on the above, the single grain rather than single aliquot D_{es} were adopted, giving ages in correct stratigraphic order of increasing depth with age. Consequently, the final ages for the samples CN13-2-1 and CN13-3-1 shown in Section 7.1.2 relate to the single-grain rather than single-aliquot method.

Table 5.6: Equivalent dose (D_e) and age values for five samples from CN derived using single-aliquot and single-grain methods.

Sample	Single Aliquot		Single Grain				
	De (Gy)	Age (ka)	De (Gy)	n	Recovery Ratio	Uncorrected Age (ka)	Corrected Age (ka)
CN13-1-2	68.92 ± 3.7	14.50 ± 1.0	30.20 ± 2.50	56	-	6.30 ± 0.60	7.90 ± 0.75
CN13-2-1	111.21 ± 3.5	23.20 ± 1.2	31.04 ± 3.73	37	-	6.15 ± 0.74	7.71 ± 0.96
CN13-3-1	114.92 ± 7.3	24.40 ± 1.8	30.98 ± 4.66	46	0.99 ± 0.05	6.40 ± 0.96	8.03 ± 1.23
CN13-4-1	44.61 ± 2.4	9.20 ± 0.6	36.89 ± 3.44	54	1.00 ± 0.05	7.58 ± 0.71	9.53 ± 0.90
CN13-5-1	259.05 ± 11	55.44 ± 3.3	222.98 ± 28.5	20	-	47.72 ± 6.40	-
SL14-1-1	34.9 ± 1.2	8.8 ± 0.4	32.1 ± 2.6	27	-	7.4 ± 0.7	-
HL14-1-2	106 ± 3.5	25.4 ± 1.4	87.8 ± 6.6	19	-	20.9 ± 1.4	-

Time constraints meant that site DN14 was not analysed at the single grain level. Given that the single aliquot samples have similarly high over-dispersion values to those from CN13 which suffer from incomplete bleaching, it is interpreted that the two younger single-aliquot ages should be viewed as a better representation of the “true” burial age than the two older ages.

This section has demonstrated that, although incomplete bleaching does not appear to be an issue for the majority of sites investigated here (as confirmed at HL14-1-1 and SL14-1-1), where it is suspected single grain data can be targeted to resolve issues such as age reversals (as was achieved at CN13).

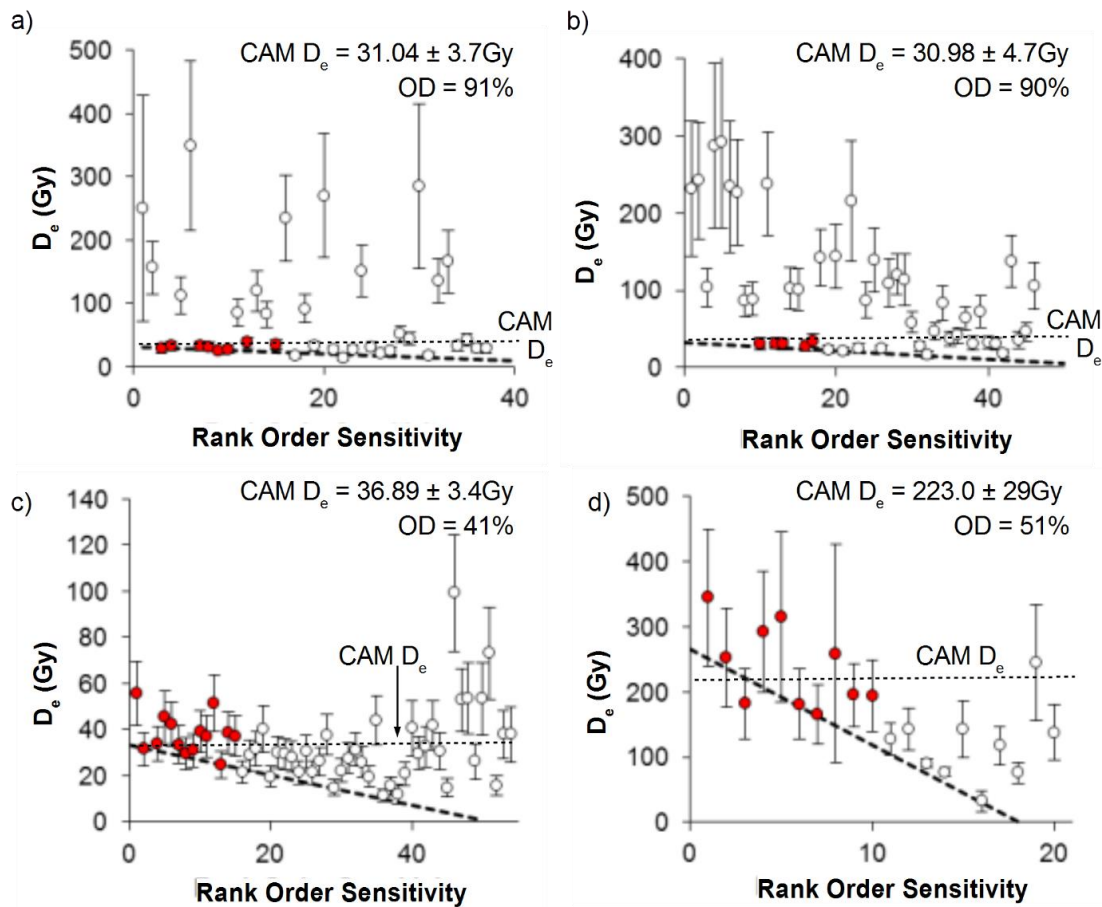


Figure 5.22: Single-grain equivalent dose distributions for samples CN13-2-1 (a), CN13-3-1 (b), CN13-4-1 (c) and CN13-5-1 (d) derived using the post-IR IRSL_{50,225} protocol. Samples are plotted in decreasing rank order of sensitivity and where samples with filled red symbols (i.e. those until the declining base has decreased by 15%) are those used in D_e determination. The method for D_e determination is described in the text and follows the approach of Rhodes (2015). The dashed line is intended as a guide to highlight the declining base phenomena visible within the four samples displayed here.

5.4.3 Summary

This chapter has demonstrated that quartz grains from the study area have highly variable properties and exhibit a number of behaviours rendering them unsuitable for reliable dating. Section 5.1 applied a rigorous means of rejecting aliquots that exhibited unsuitable behaviour (i.e. the fast ratio). A very small number of non-rejected aliquots from four sites agree with feldspar pIR-IRSL_{50,225} ages and (in the case of HL14-1-1) independent radiocarbon ages, but given the rarity of such aliquots this approach is shown to be time consuming and impractical, without guarantees of success. The pIR-IRSL_{50,225} feldspar luminescence

method was found to be appropriate in terms of having a bleachable signal under ideal conditions, and fading rates that are greatly reduced compared to IR₅₀ measurements, greatly reducing the uncertainty associated with applying fading correction (where necessary). Section 5.3 demonstrated that the pIR-IRSL_{50,225} signal shows excellent correspondence with independent chronologies available at two study sites, providing confidence in the application of this approach. In Section 5.4, CN13 single aliquot scatter and a stratigraphic age reversal were considered in detail. Single grain analysis demonstrated that incomplete bleaching of some grains had occurred, with a sub-optimal bleaching environment leading to an overestimation of D_e for the samples affected. It is hypothesized that these grains are derived from slopes surrounding the sand ramp, which will have potentially afforded short and brief transport distances/times wherein complete bleaching is far from certain. A revised single grain chronology was presented for this site (Table 5.6). The final geochronology for the field sites will be presented in Chapter 7.

6 Morphometry of aeolian deposits within the Cady Mountains

The aim of this thesis is to understand the influence of complex topography on aeolian deposition and landform development. Achieving this requires three steps. Firstly, the distribution and form of aeolian deposits within the mountain block will be mapped and their relationship to topography considered (Chapter 6). Secondly, a process history for the aeolian deposits (Chapter 7) will be created to establish how their history fits into the broader boundary conditions (from Chapter 3). Finally, Chapter 8 will unpick the effect of the boundary conditions over time, to see what understanding can be gained regarding the effect of the complex topography of the mountain block on aeolian deposition and landform development. To this end, this chapter demonstrates that there is a topographic control over the spatial distribution and morphology of aeolian deposits within the Cady Mountains. Section 6.1 describes the large-scale form of the landscape and shows that, within this landscape, the distribution and form of the aeolian deposits is related to the topography of the mountain block and is manifest as deposits which represent three accommodation space types. Section 6.2 describes the meso-scale form of exemplar sites to demonstrate that each accommodation space type exhibits characteristic landforms, but which vary in how simple they are to delimit.

6.1 Large-scale topographic control over the spatial distribution and form of aeolian deposits

This section describes the large-scale form of the landscape and then disaggregates this landscape into land cover classes in order to show that the distribution and form of aeolian deposits within this landscape is related to the mountain block topography. From this, a relationship is inferred between aeolian deposits and topography which is manifest as three categories of accommodation spaces.

6.1.1 Large-scale description of the landscape

The topography of the Cady Mountain block constitutes a large central peak network rising to an elevation of 1400m.a.s.l. (A in Figure 6.1) and two smaller peak networks of lower

altitude (~1000m.a.s.l.) to the north and south (B and C in Figure 6.1). The western margin of the mountain block comprises a row of smaller (~800m.a.s.l.) north-south trending peaks which border the former Lake Manix bed at ~550m.a.s.l. (D in Figure 6.1), hereafter referred to as the Western Front. Between these peaks are broad plains of 5-20km² in extent (Figure 6.3). The overall distribution of elevation within the mountain block varies between 388m.a.s.l. and 1390m.a.s.l., with most of the landscape located between 550m.a.s.l. and 800m.a.s.l. (Figure 6.2a).

The percentage of the landscape associated with any given aspect is shown in Figure 6.2b and indicates a dominance of north-facing through east-facing and southwest-facing slopes. The percentage of the total land area with any given slope angle shows a positively skewed distribution with a mode of ~2.5° and limited areas with slopes <1° or >6° (Figure 6.2c).

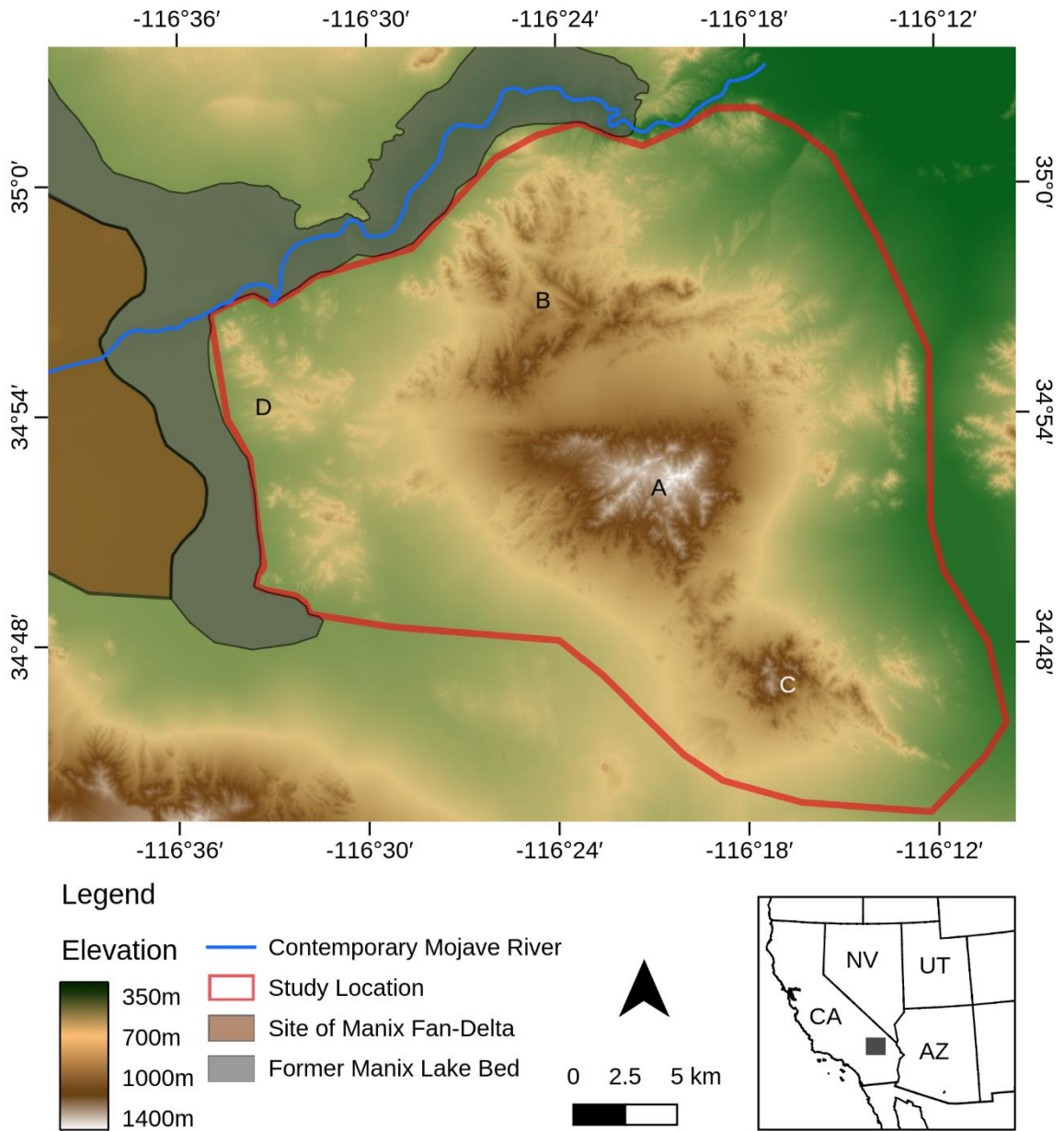


Figure 6.1: Shaded DEM of the topography of the Cady Mountains in southern California which shows the study area, the course of the contemporary Mojave River and the location of the former Palaeo Lake Manix bed and fan-delta. Lake Manix high stand data as described in Reheis and Redwine (2008). DEM source: National Elevation Dataset courtesy of the U.S. Geological Survey. Map data © OpenStreetMap contributors.

The landscape was classified into morphometric features (e.g. peaks, ridges, valleys, plains etc.) as outlined in Section 4.2.2. The proportion of the landscape exhibiting each feature class is shown in Figure 6.2d. Planar is the most common morphometric feature class within

the Cady Mountains (47% of the landscape), with plain and ridge being the second and third most extensive morphometric features, each accounting for 21% and 19% of the landscape respectively. Mountain peaks and passes are the least common landforms accounting for only 0.02% of the landscape combined. The distribution of valley orientation is shown in Figure 6.2b, with valleys tending towards north and east facing (>50% combined). This generally mirrors the relationship of aspect for the landscape as a whole (Figure 6.2c and Figure 6.3).

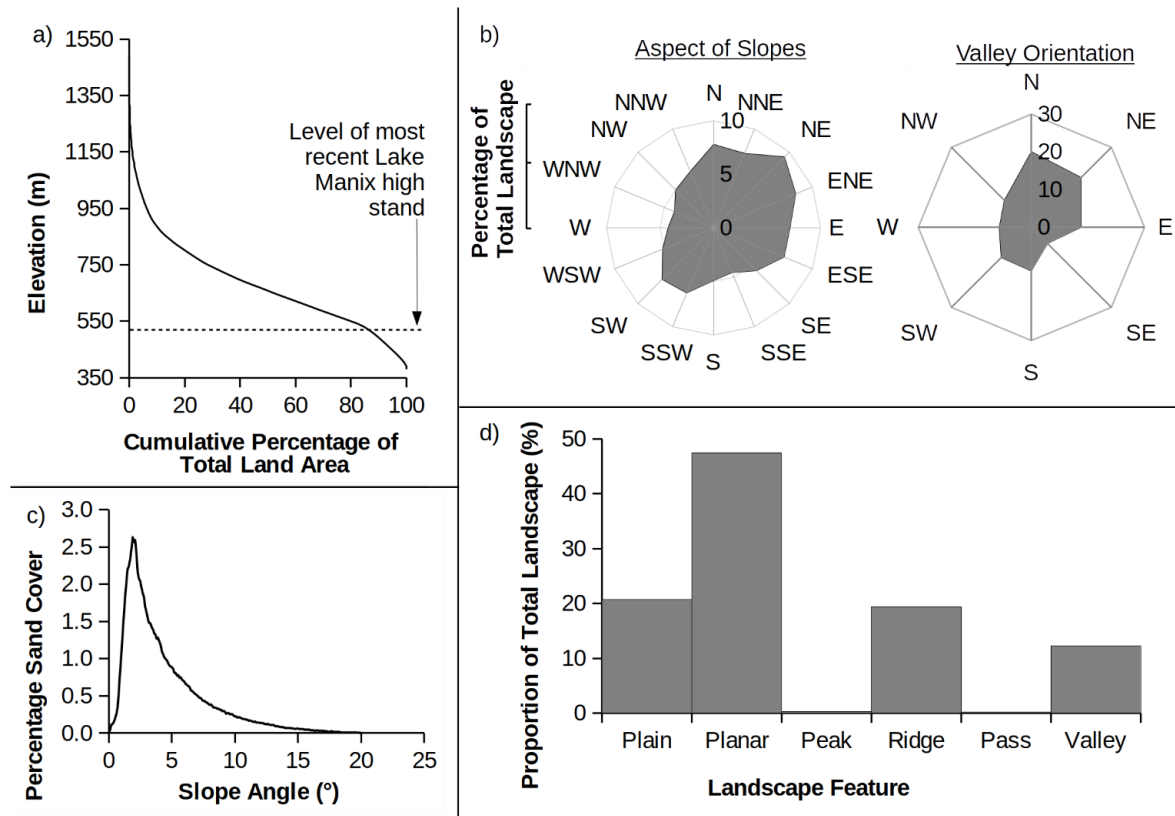


Figure 6.2: Morphometric characteristics of the Cady Mountains. a) Hypsometric curve noting the level of the most recent Lake Manix high stand, (b) distribution of slopes, (c) aspect of surfaces with a slope angle of greater than two degrees and (d) classification of the mountain block by six morphometric classes.

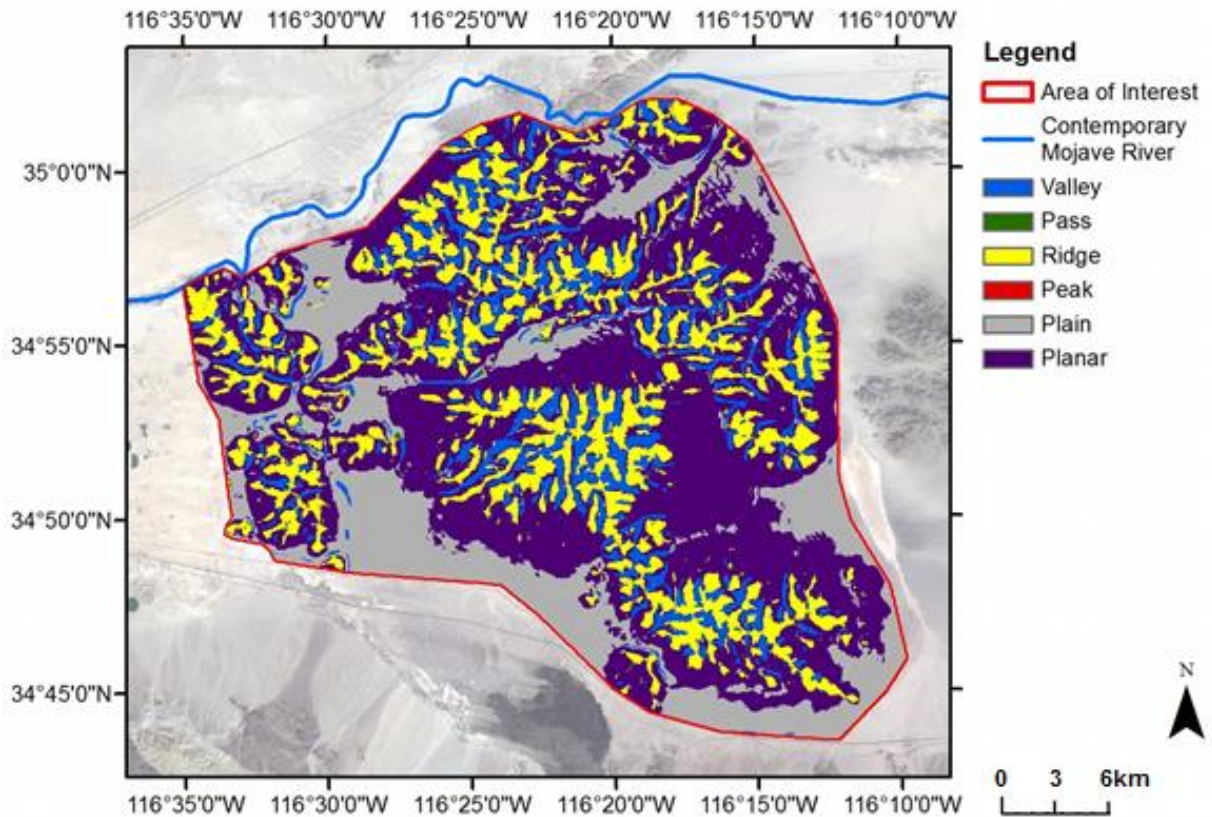


Figure 6.3: Morphometric feature classification for the Cady Mountains. Landsat-8 image and National Elevation Dataset courtesy of the U.S. Geological Survey. Map data © OpenStreetMap contributors.

6.1.2 The distribution and form of land cover

This analysis of the land cover of the Cady Mountains is primarily concerned with three cover types: Sand Cover, Stone-Covered Sands and Rock Surfaces, as derived from a semi-supervised image classification (Section 4.1.2). Most of the landscape comprises the Rock Surfaces class, reflecting the prevalence of rock slopes across the mountain block (Figure 6.4). Stone-Covered Sands is the second most extensive land cover (28%). Sand Cover is the least extensive class, covering only 12% of the landscape.

The distribution of land cover classes is not akin to a pattern of random noise, but is clustered into areas. If both the Sand Cover and Stone-Covered Sand classes are combined, they form a broadly continuous surface which encapsulates a large expanse of the western half of the mountain block. The majority of the Sand Cover and Stone-Covered Sands classes lie to the west of $116^{\circ} 18' W$ and to the north of $34^{\circ} 50' N$ (Figure 6.4) and thus the eastern flank of the mountain block is significantly less sandy than the western flank. Despite this bias to the

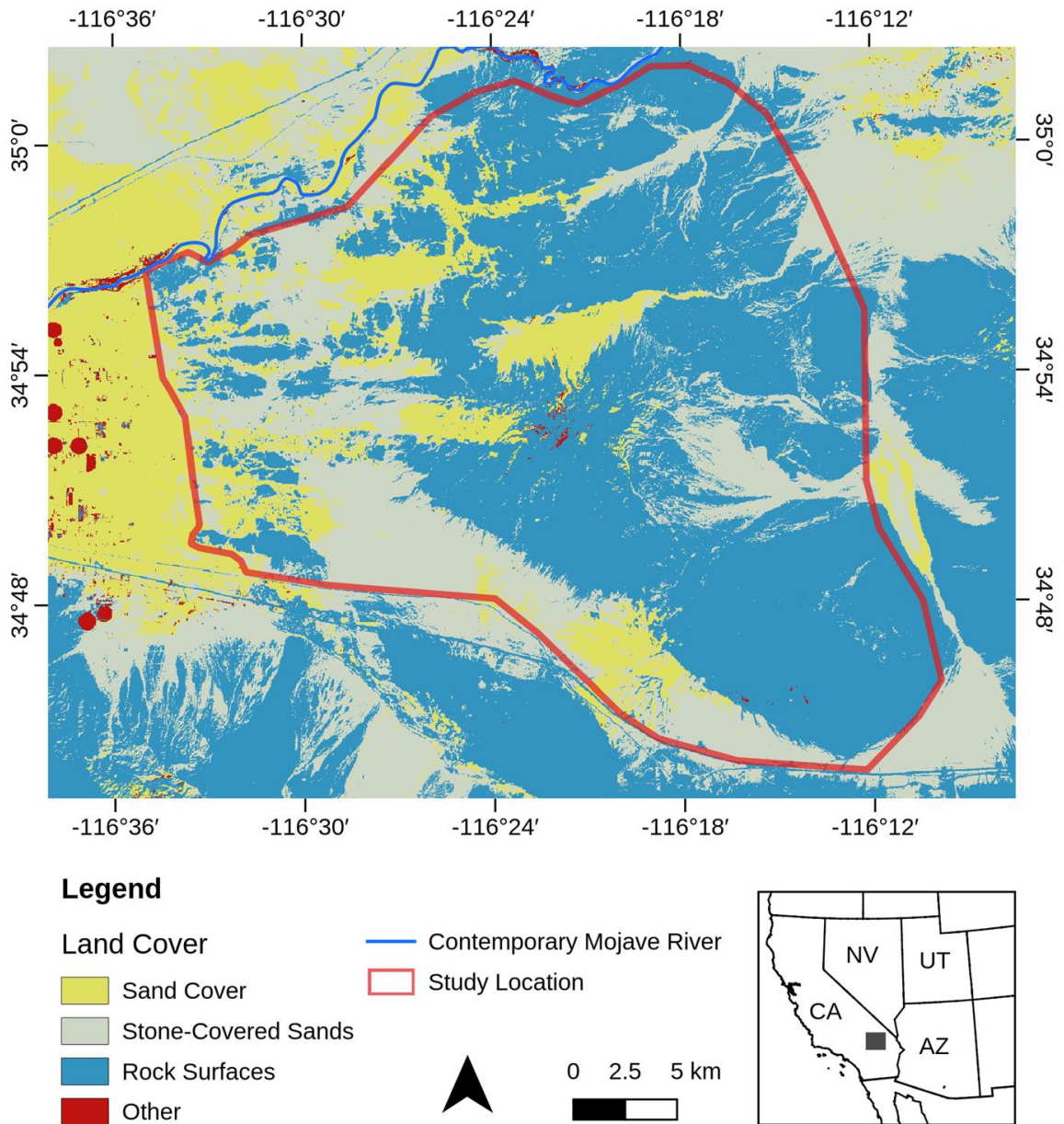


Figure 6.4: Land cover map for the Cady Mountains. Landsat-8 image courtesy of the U.S. Geological Survey. Map data © OpenStreetMap contributors.

west, significant areas of Stone-Covered Sands were observed along the eastern flank of the mountain block with field investigation showing their composition to be a mixture of surface sands, pebbles and cobbles, interpreted as being predominately fluvial in origin (Figure 6.5). By contrast, the western flanks of the mountain block are covered by broad stone-covered plains/planar surface, covering the sands beneath. Crucially, they are classed in a single spectral class despite sub-surface differences (as shown in field investigation (see Section 4.1)).



Figure 6.5: Photographs of the land surface at two locations classified as being Stone-Covered Sands. The upper photograph is from the eastern flank of the Cady Mountains and the lower image is from the Valley Center Road area (Figure 6.22) within the western half of the mountain block.

The relationship between elevation and land cover

The systematic variation in the percentage cover of the three primary land cover classes with elevation is shown in Figure 6.6 (see Chi Square in Appendix 1). Sand occurrence is closely linked to elevation. It is largely absent below ~550m.a.s.l., varies between 10% and 40% of the landscape up to about 1100m.a.s.l. and then decreases to between 0 and 30% at higher altitudes. The highest percentage of sand cover occurs at 820m.a.s.l. Stone-Covered Sands are most extensive between 400m.a.s.l. and 800m.a.s.l., accounting for around 40% of land cover at such elevations, before dropping to ~5% cover over 700m.a.s.l. Rock Surfaces account for more than 70% of areas with elevations between ~400m.a.s.l. and ~550m.a.s.l., but are comparatively under-represented (15-35%) at intermediate elevations before becoming dominant (>80%) above 800m.a.s.l.

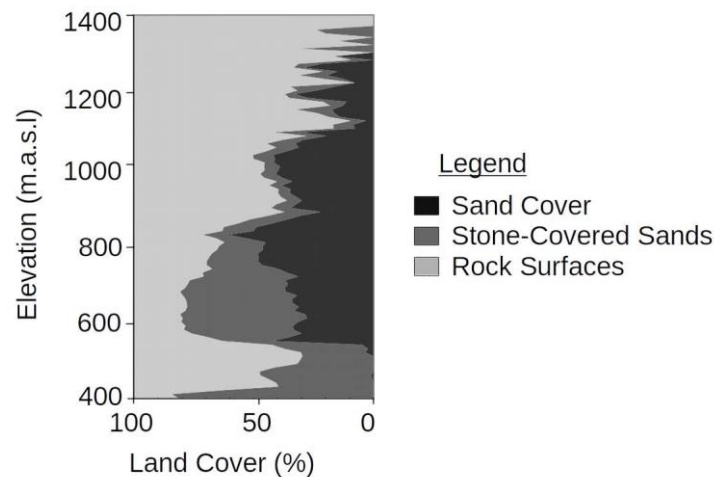


Figure 6.6: Distribution of land cover with elevation within the Cady Mountains.

The relationship between aspect and land cover

Figure 6.7 implies a systematic variation of land cover with respect to slope aspect, confirmed with a Chi Square test (see Appendix). Sand preferentially accumulates on west- and southwest-facing slopes. Stone-Covered Sands have a less tight distribution with a broad mode between south-west and north-west facing slopes and another mode relating to east-south-east facing slopes. Correspondingly the Rock Surfaces class is most abundant on north and east-facing slopes.

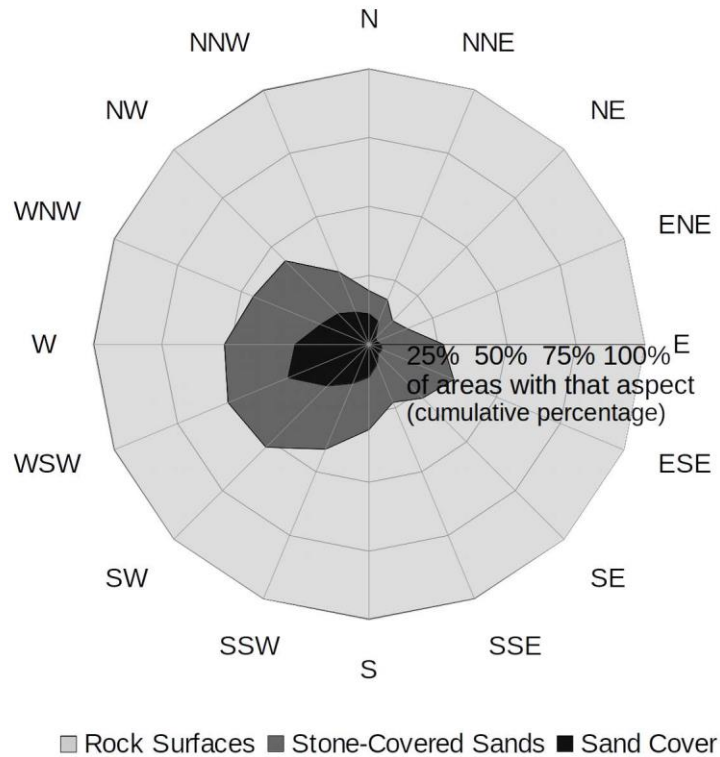


Figure 6.7: Variation in land cover type with aspect. Areas with a slope angle of less than two degrees were considered to have no discernible aspect. Percentages are stacked so that they sum to 100%.

The spatial distribution of land cover classes with respect to aspect is summarised in Figure 6.8. The Sand Cover class comprises several large contiguous west-facing (green) areas towards the western and central portions of the mountain block, which compares with very little Sand Cover on east-facing areas (red). A large valley present towards the north of the image appears as two corresponding east- (red) and west-facing (green) slopes (Figure 6.8a). The presence of several sand-filled north and west orientated valleys (Figure 6.11) which are notable along the border of the former Lake Manix (Figure 6.12) suggests that the valleys may have some control over the emplacement and presence of sand in the region. Much of the Stone-Covered Sand class occurs on areas with no discernible aspect (Figure 6.8b), while the Rock Surfaces class is represented preferentially on east-facing slopes, evident in the large areas coloured red in Figure 6.8c

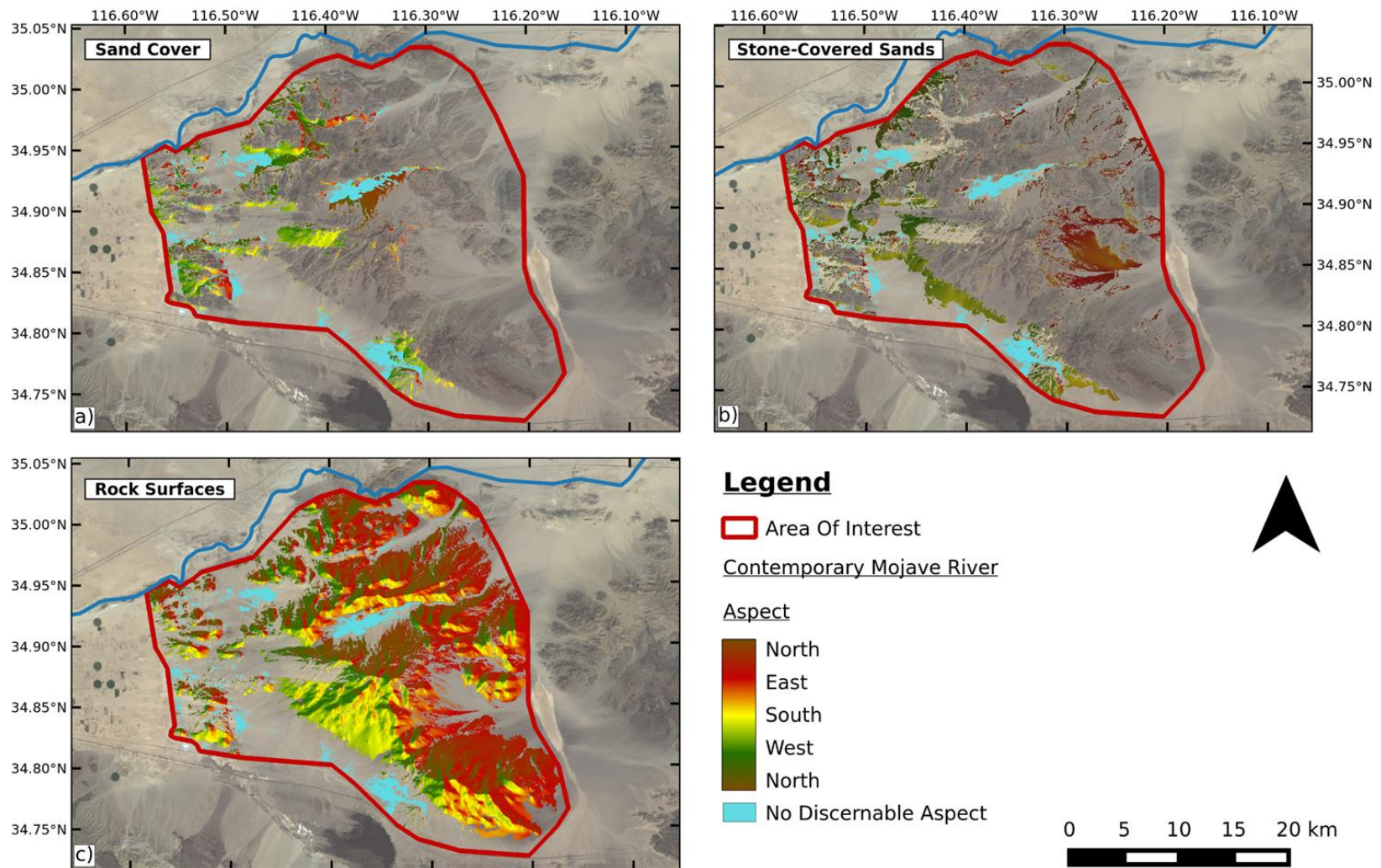


Figure 6.8: Spatial distribution of land cover classified by aspect. a) Sand Cover, b) Stone-Covered Sands, c) Rock Surfaces). Aspect of areas identified as having either a Sand Cover, Stone-Covered Sands or Rock Surfaces land cover are shown as a) to c) respectively. Slopes $<2^\circ$ were classed as having no overall aspect. Landsat-8 image and National Elevation Dataset courtesy of the U.S. Geological Survey. Map data © OpenStreetMap contributors.

The relationship between slope and land cover

Figure 6.9 shows that land cover is systematically distributed with respect to slope angle, with both Sand Cover and Stone-Covered Sands being disproportionately present on or as low angled slopes (confirmed by a Chi Square test – see Appendix). The Sand Cover and Stone-Covered Sand classes are dominant for slopes of less than two degrees, with 86% and 94% of these classes being present on slopes of less than six degrees respectively. The Rock Surfaces class is the dominant land cover for slopes steeper than five degrees, accounting for >80% of such areas.

The results also highlight that it is comparatively uncommon to find Rock Surfaces with negligible slope. However, a small proportion of the landscape has been mapped as such and is mostly confined to one area in the south-east of the mountain block where Sand Cover is rare. This area was identified as being potentially erroneous by the error investigation of the land cover classification. Field data for the verification assessment (Section 4.1) indicates that these small areas contain a contemporary cover of coarse material which is either of a lithology that is darker or which shows evidence of desert varnish.

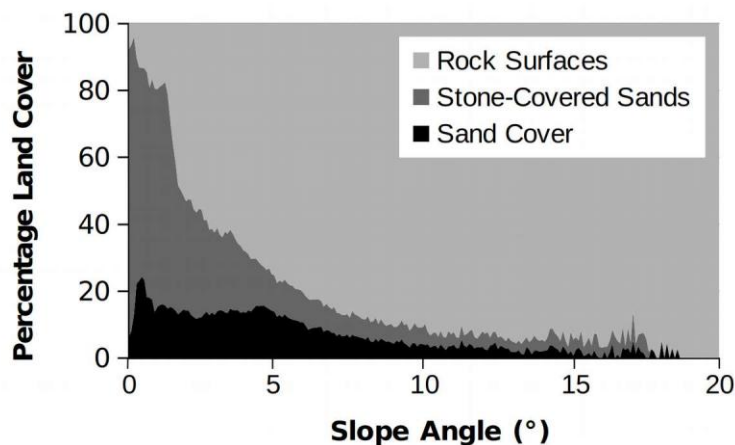


Figure 6.9: Percentage land cover for differing slope angles. Percentages are stacked so that they sum to 100%.

The relationship between morphometric feature classes and land cover

Up to this point the analysis has been concerned with simple morphometric parameters such as elevation, aspect, and slope angle at a given point. This section demonstrates that land cover classes are systematically distributed with respect to morphometric features (see Section 6.1) (confirmed using a Chi Square test – see Appendix 1).

Figure 6.10 shows that Sand Cover is well-represented on plains (14%), planar slopes (13%), passes (12%) and in valleys (12%) and is less well-represented on peaks (11%) and ridges (7%), which compares with a Sand Cover of approximately 12% for the total landscape. Stone-Covered Sands are well-represented on plains (58%), passes (30%) and planar slopes (25%) and poorly represented in valleys (13%) and on ridges (8%) and peaks (8%), compared with an average Stone-Covered Sand surface of 28% for the Cady Mountains as a whole. Extensive stone-covered plains (coloured orange in Figure 6.12) are present across the western half of the mountain block and along its extreme boundary. A large stone-covered planar surface (coloured purple in Figure 6.12) is present within the eastern half of the mountain block. Rock Surfaces are very well represented on ridges (84%), peaks (80%), in valleys (74%) and on planar slopes (64%) and are less-well represented on plains (26%), compared with a total cover of 60% for the Cady Mountains as a whole.

As noted above, the land cover classes are not randomly distributed throughout the mountain block but are disproportionately present to the west of the mountain block. It is therefore noteworthy that valleys tend to be towards the eastern portion of the Cady Mountains (Figure 6.12) which, as discussed above, are disproportionately classified as Rock Surfaces (74%). Furthermore, land cover within valleys can be related to valley orientation, with north-westerly orientated valleys having the largest Sand Cover and Stone-Covered Sand cover (Figure 6.12), which differs markedly from the distribution of valleys as a whole (Figure 6.2b) and the distribution of land cover with respect to aspect (Figure 6.7) (see Chi Square in Appendix 1).

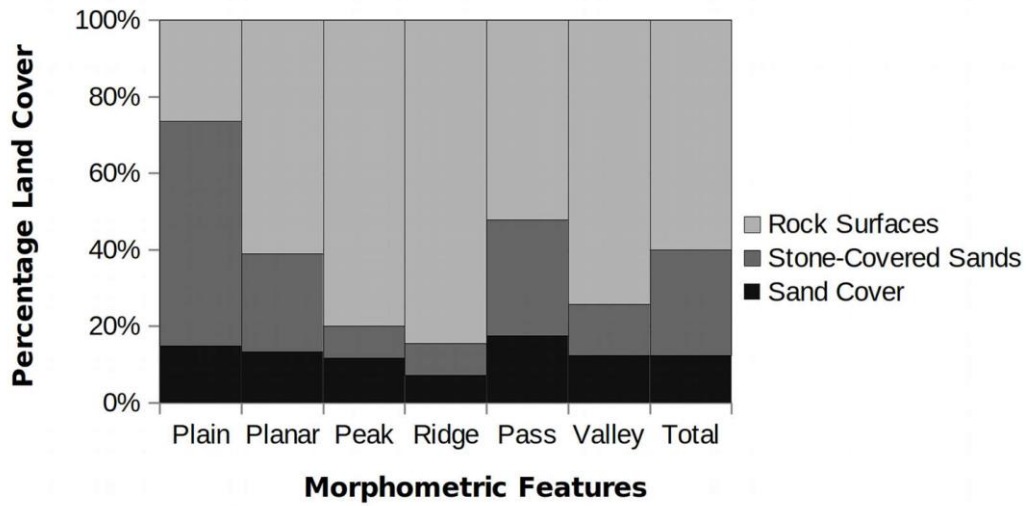


Figure 6.10: Percentage land cover for morphometric feature classes within the Cady Mountains. Percentages are stacked so that they sum to 100%.

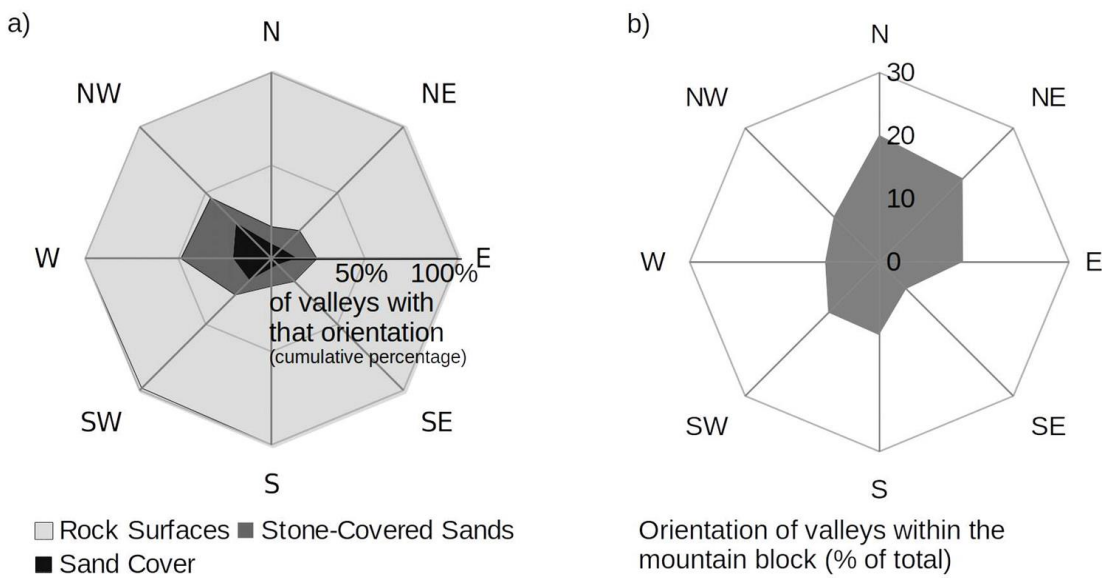


Figure 6.11: Percentage land cover of valleys with differing orientation where percentages are stacked so that they sum to 100% (a). Orientation of valleys within the Cady Mountains as Figure 6.2b.

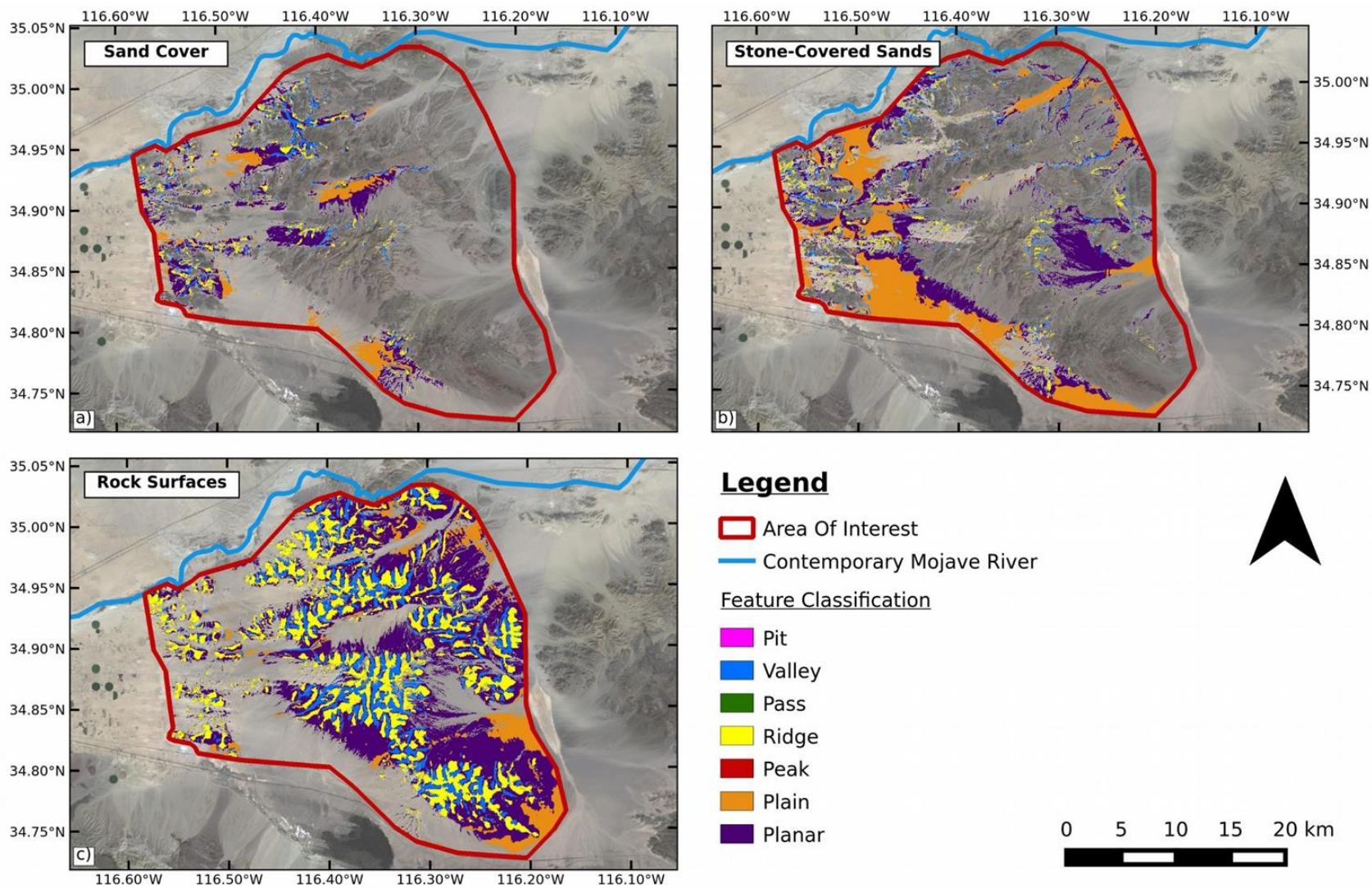


Figure 6.12: Variation in land feature classification within areas of the landscape covered by (a) Sands, (b) Stone-Covered Sands, and c) Rock Surfaces. Landsat-8 image and National Elevation Dataset courtesy of the U.S. Geological Survey. Map data © OpenStreetMap contributors.

Summary

This section has described the morphometry of the landscape of the Cady Mountains and, within this landscape, the distribution and aeolian deposits at the mountain block scale. Six key observations are found:

- a) Sand Cover is disproportionately concentrated towards the north and west of the mountain block and is predominantly west-facing. By contrast the east and south of the mountain block have a much-reduced relative Sand Cover.
- b) Sand Cover is located at intermediate elevations (550-1100m.a.s.l.) whereas Stone-Covered Sand is typically found on slopes with an elevation of less than 700m.a.s.l. Rock Surfaces are the dominant land cover for areas above 800m.a.s.l.
- c) Sand Cover is most common on WSW facing slopes and accounts for a very small proportion of north and east facing slopes, despite such slopes being disproportionately present in the landscape (contrast Figure 6.2b and Figure 6.7). This relationship is mirrored, though less tightly, by the Stone-Covered Sand class.
- d) Stone-Covered Sand and Sand Cover are disproportionately present as low-angled slopes (accounting for ~80% and 20% of these areas respectively). By contrast, 90% of the landscape steeper than $\sim 6^\circ$ is 'Rock Surfaces'.
- e) In terms of morphology, Sand Cover is well represented on plains, as planar slopes and in passes, but is under-represented on ridges and peaks. Stone-Covered Sand is the dominant land cover class of plains (~60%). Correspondingly, ridges and peaks are dominated by Rock Surfaces.
- f) Valleys orientated towards the north and west have the highest percentage Sand Cover of all valleys. Valleys are disproportionally classified as Rock Surfaces though this is likely related to east-facing valleys being disproportionately present within the eastern portion of the Cady Mountains which is largely devoid of sand.

This section has demonstrated that there is some pattern (as summarised in a-f above) to the distribution of sand at the mountain block scale and that this is related to the complex topography of the mountain block. It is important to remember when interpreting these observations that: (1) the analysis was designed to identify the dominant morphometry of the

landscape across the range of scales between 90 m x 90 m and 1.2 km x 1.2 km (plan shape) and hence the analysis will therefore not capture any relationships at smaller or larger scales and (2) that the morphometric parameters were derived using the contemporary land surface and hence are classifying the morphometry of the net-landform development which does not represent the pre-existing topography.

6.1.3 Relationship between the distribution and form of aeolian deposits and topography

Demonstrating a relationship between the distribution and form of aeolian deposits and the mountain block topography requires a map of both land cover and the underlying topographic shape. A limitation of using characterisations of surface form and materials (a DEM and land cover classification) for this approach is that the sand depth remains unknown. Consequently, the record of the underlying topography is incomplete as it is obscured by the presence of aeolian deposits and is thus only visible in areas of the Rock Surface class. However, field evidence can be used to offset this effect. Because of the relief of the mountain block (e.g. Soldier Mountain shows ~200m of local relief and the valley WC shows ~100m of local relief), it is quite likely that the large-scale shape of the underlying topography can be seen “through” the aeolian sediments (which vary from <50cm to >15m – see Section 7.1.3). Furthermore, the different morphometric parameters and feature classes will vary in their sensitivity to alteration by aeolian deposition. The distribution of elevation across the mountain block (Figure 6.2) will be insignificantly altered by the accumulation of a few metres of aeolian material and also quantities of aeolian sediment significant enough to alter the morphometric shape of the landscape are rarely stored upon mountain peaks or ridges (feature classification) (as noted by Lancaster and Tchakerian, 1996). By contrast, the distribution of slopes within the mountain block suggests a dominance of low-angled slopes (Figure 6.2) which represents the development of piedmont features and thus the contemporary surface of aeolian deposits can significantly obscure the bedrock topography, often leading to morphometric classification as planar slopes. The implication of these observations is that, though not all of the bedrock topography is visible, an association between the topography and the mountain block scale distribution and form of aeolian deposits can be inferred. The following section will take this observation one step further;

morphometric features reflect sand accumulation in/on/as different topographic positions (in valleys, on plains and as planar slopes).

6.1.4 Conceptualisation of the large-scale topographic control over the spatial distribution and form of aeolian deposits

A relationship exists between the distribution of sand and the topography of the mountain block. This section will begin to characterise this relationship at the mountain block scale based upon the observation that the Sand Cover and Stone-Covered Sand classes preferentially occur as planar slopes and plains whereas Rock Surfaces are disproportionately the land cover present on ridges and peaks. The occurrence of Sand Cover in valleys was variable, being common in west- or north-facing valleys and their associated passes (as these are typically forming valley-heads). Passes were discounted from further investigation because they account for only 0.2% of Sand Cover and Stone-Covered Sands combined and are often associated with valley features. Hence the aeolian deposits of the Cady Mountains can be characterised as occurring as one of three morphometric feature classes (Figure 6.13), each of which represents a different topographic position for sand accumulation (i.e. *in* valleys, *on* plains and *as* planar slopes). It is here proposed that these three topographic positions represent three different accommodation space types within the landscape: Plain, Mountain Front and Valley (Figure 6.13). Each of these accommodation space types is defined through a combination of the form of the aeolian deposits and the morphometry of the topography (the geometry of neighbouring topography). Plains are defined as expressing both a flat (or near-flat) sand surface and the absence of any significant adjacent topography. Mountain Front features exist as a planar slope of sediment which has developed against some topographic obstacle. Valleys are bounded on two sides by the mountain block topography, with sand accumulation occurring within the lowest point of the valley.


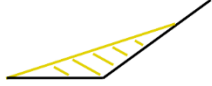

Topographic Position of Aeolian Deposit	Morphometric Feature	Accommodation Space
	Plain	→ Plain
	Planar Slope	→ Mountain Front
	Valley	→ Valley

Figure 6.13: Three accommodation space types which represent the principal forms of aeolian deposits within the Cady Mountains.

6.2 Meso-scale morphology and landform classification of aeolian deposits

Given the emergent relationship between the distribution and form of aeolian deposits and the topography of the Cady Mountains at the mountain block scale, this section will use twelve sites to investigate whether these three accommodation spaces types are evident at the meso-scale and whether these accommodation spaces are associated with characteristic morphologies which can be delimited based on their form and materials.

6.2.1 Accommodation space types as a framework for landform investigation

The twelve sites under discussion here comprise the nine field sites outlined in Section 3.1 and an additional three sites which were selected to balance out the categories and add some highly complex examples where not everything fits neatly. The twelve sites were categorised into the most appropriate accommodation space type. Because some sites (notably CN) are best represented as multiple accommodation space types which occur in close association with each other, a fourth category of ‘composite’ was created.

Mountain Front

Four landforms were considered as being within a Mountain Front accommodation space because most of their area was identified as a planar surface by the overall morphometric feature classification (subsets shown in Figure 6.14) and because they were directly bounded on at least one side by a topographic obstacle. SM is the best example of the Mountain Front

class as the feature overwhelmingly identified as representing a Mountain Front accommodation space. Though most of ER is planar, the centre of ER is identified as ridge morphometry owing to the slope being convex along its long axis. Most of MC exhibits planar morphometry, though the south-eastern boundary of the landform is characterised as alternating ridges and valleys. Numerous topographic high points protrude from the largely planar surface of PK, which are visible as areas of ridge morphometry and a large valley has cut into the landform in its eastern half (see Figure 6.17).

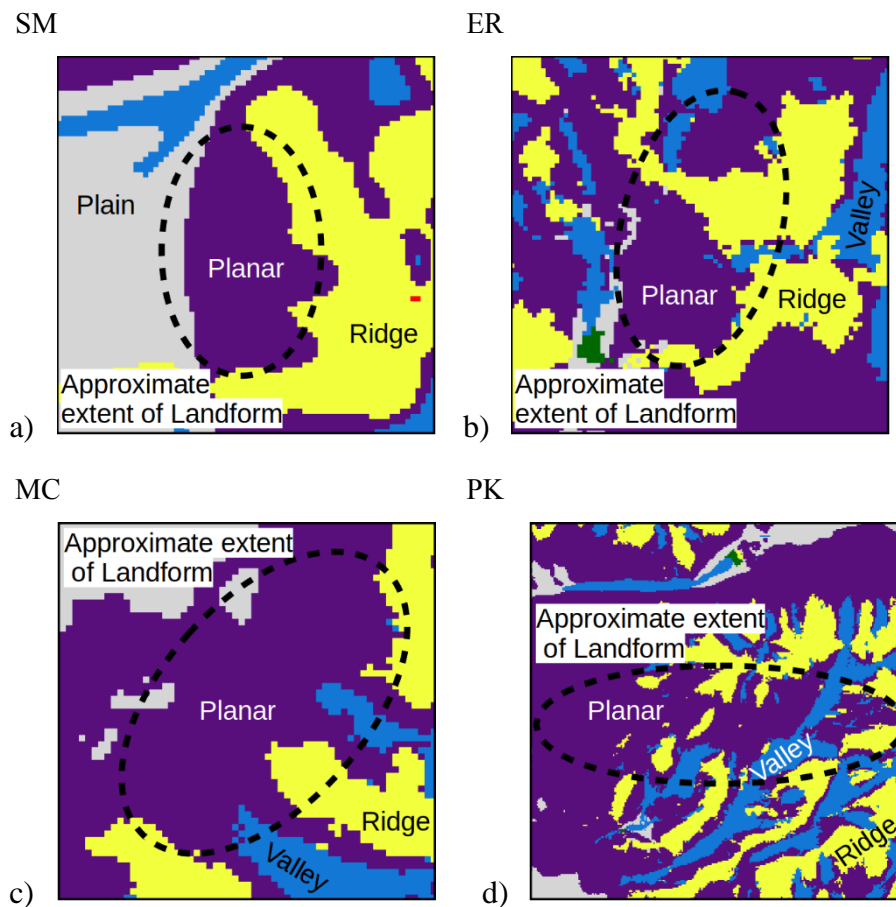


Figure 6.14: Morphometric feature classification for areas determined as being a Mountain Front accommodation space type.

Plain

These field sites were considered as Plain because the majority of the area was identified as such by the morphometric feature classification (subsets shown in Figure 6.15), plus all have negligible topographic bounding. Along the north, south and south-western periphery of the landform some areas of the land surface are steeper than two degrees, leading to these areas being locally classified as planar morphometry.

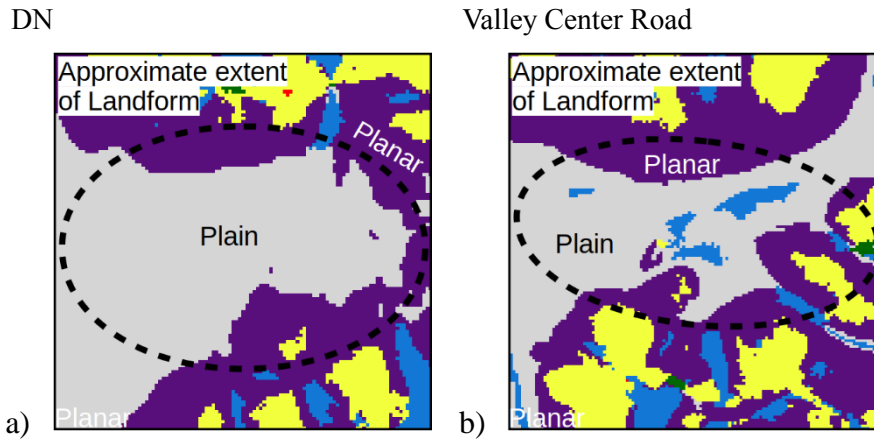


Figure 6.15: Morphometric feature classification for areas determined as being a Plain accommodation space type.

Valley

These landforms were considered as a valley because they are all bounded by topography on multiple sides and contain a significant area in between which was classified as a Valley by the morphometric feature classification, thus identifying the valley floor (subsets shown in Figure 6.16). These valley areas form a single (or forked) main axis at RD and WC respectively. The Valley Complex does not form a closed system with passes, suggesting that an integrated network of ambiguously defined valleys is present.

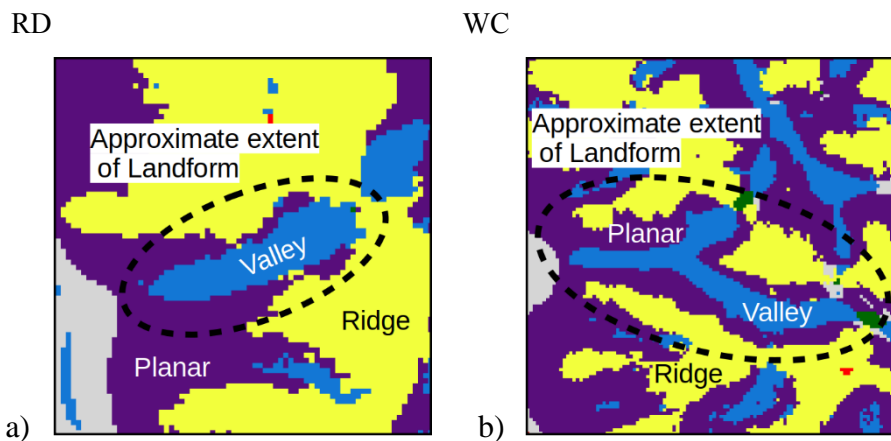


Figure 6.16: Morphometric feature classification for areas determined as being a Valley accommodation space type.

Composite

Three of the exemplar locations did not lend themselves to being classified as any one of the above classes because they show multiple different accommodation space types in close association.

HV (Plain and Mountain Front)

This landform was considered as composite morphometry because approximately half of the area was identified as plain and half as planar by the morphometric feature classification shown as Figure 6.17a, with no obvious boundary between these.

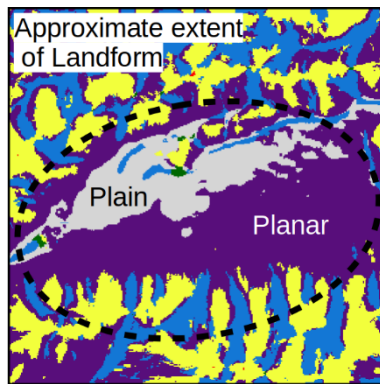
CN (Mountain Front and Valley)

This landform was considered as composite morphometry because, though just over half of the area was identified as planar, three significantly-sized sand-filled valleys were identified by the morphometric feature classification shown as Figure 6.17b.

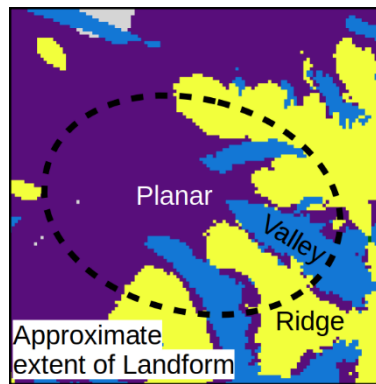
Manix Front (Mountain Front, Plain and Valley)

This landform was considered as composite morphometry because discontinuous and repeating areas of planar, plain and valley morphometry were identified by the morphometric feature classification shown as Figure 6.17c.

HV



WC



Manix Front

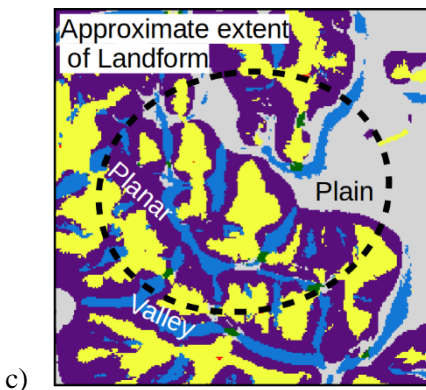


Figure 6.17: Morphometric feature classification for areas determined as being a Composite accommodation space type.

6.2.2 Identification and delimitation of distinct landforms between accommodation space types

This section uses twelve locations described above to show that the accommodation space types are associated with characteristic morphologies at the meso-scale. The section will also describe the landforms to consider how they are manifest within the landscape, particularly with reference to how well-defined the landforms are in terms of their form and materials. The location of the exemplars is shown in Figure 6.18.

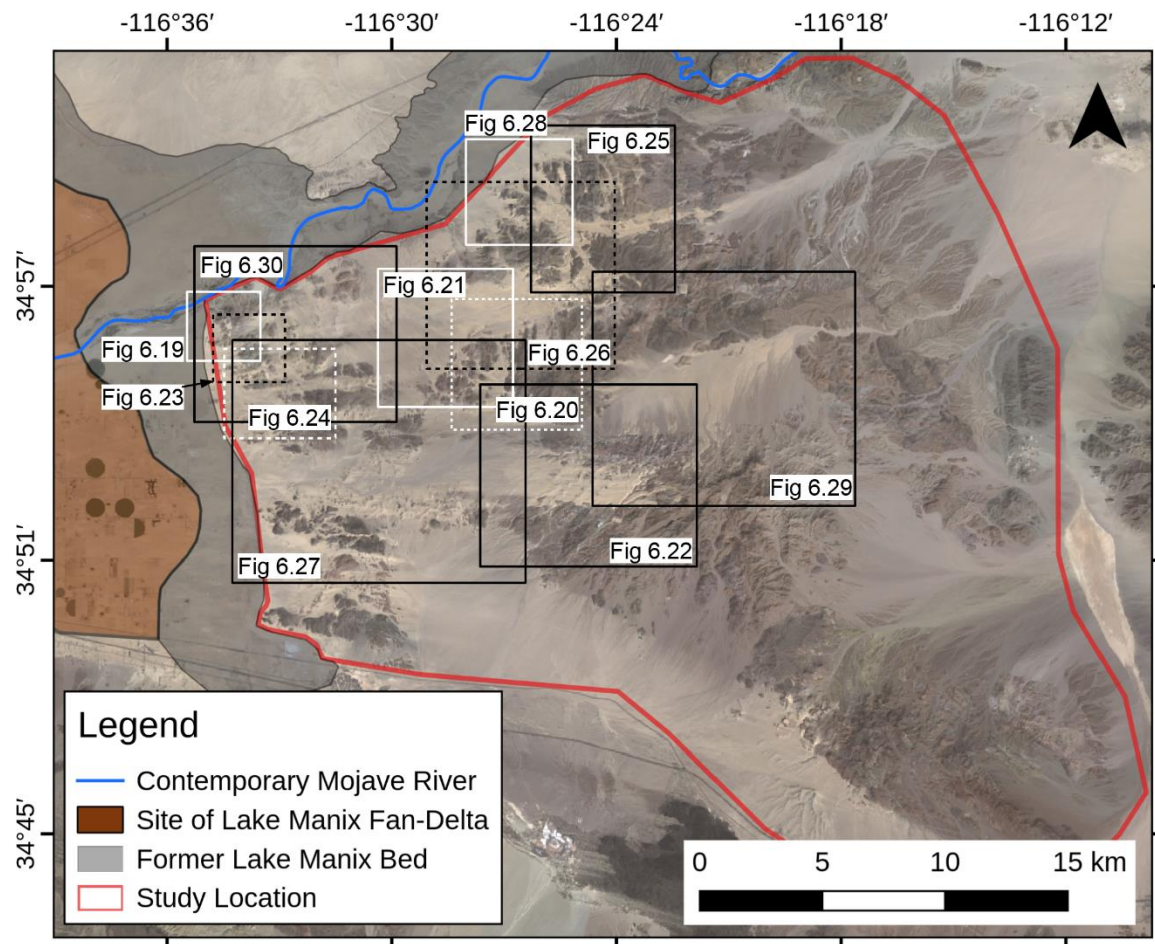


Figure 6.18: The following section contains several figures which highlight the variability in the morphology of aeolian accumulations across the Cady Mountains. The locations for these figures within the mountain block. Landsat-8 courtesy of the U.S. Geological Survey. Map data © OpenStreetMap contributors.

Mountain Front

Four of the field sites were identified as occupying a Mountain Front accommodation space. This section will describe each of these highlighting that, though these sites do exhibit a

characteristic morphometry, this does not necessarily translate into four well-defined and easily delimited landforms of Mountain Front morphology.

Soldier Mountain (SM)

This site has a semi-circular plan form with a planar surface (Figure 6.19b) which sits within a single embayment of the mountainous topography which forms the northern limit of the Western Front (Figure 6.19c). The landform has a slope of 5-7°, is approximately 0.5km² in area and is bounded by the rock slopes of Soldier Mountain where incisions have disconnected it from the hillslopes of the embayment (as Lancaster and Tehakerian, 1996; Bateman *et al.*, 2012), except along the western side where it is bordered by the sands of the contemporary Mojave River. The surface of the landform was classed as a combination of Sand Cover (mostly the landform's toe) and Stone-Covered Sand.

The landform is easily delimited owing to its position within a semi-circular topographic embayment and where it has been truncated by the former palaeo Lake Manix (i.e. with an observable break of slope).

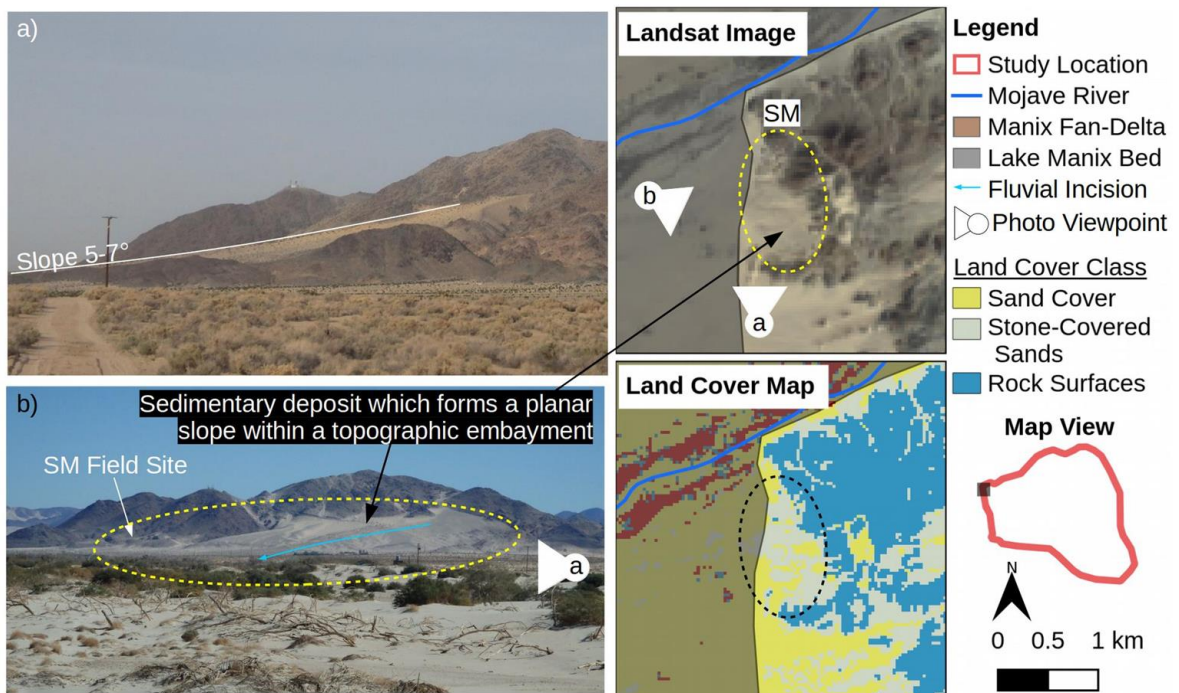


Figure 6.19: Morphology of aeolian deposit at Soldier Mountain. Landsat-8 image courtesy of the U.S. Geological Survey.

East Ramp (ER)

A sedimentary deposit with a planar surface of $\sim 1\text{km}^2$ in area has developed on the western slopes of an unnamed mountain (Figure 6.20), ranging in slope from $3\text{-}8^\circ$. The surface deposits are principally classified as Sand Cover but with some Stone-Covered Sands around its periphery. The landform is incised by several fluvial channels, some of which are large enough to traverse the landform whereas others only extend mid-way down the slope (Figure 6.20c).

Unlike the embayment which bounded SM, this landform has formed as a planar slope which has developed against a topographic obstacle with a broadly linear ridgeline, creating a landform which is rectangular and hence is bounded by topography on only one side. The landform is bordered by stabilised sands to the south and by a low-relief dune field (DN) to the north, being separated from these areas by fluvial incisions. The western border of the landform is more ambiguous, grading into an area of sediments which are woven around the smaller topography. Overall, ER demonstrates similar characteristics to SM (being a planar surface against a single topographic obstacle), though there is some additional ambiguity in defining ER, reflecting that the landform has not accumulated in a well-defined topographic embayment.

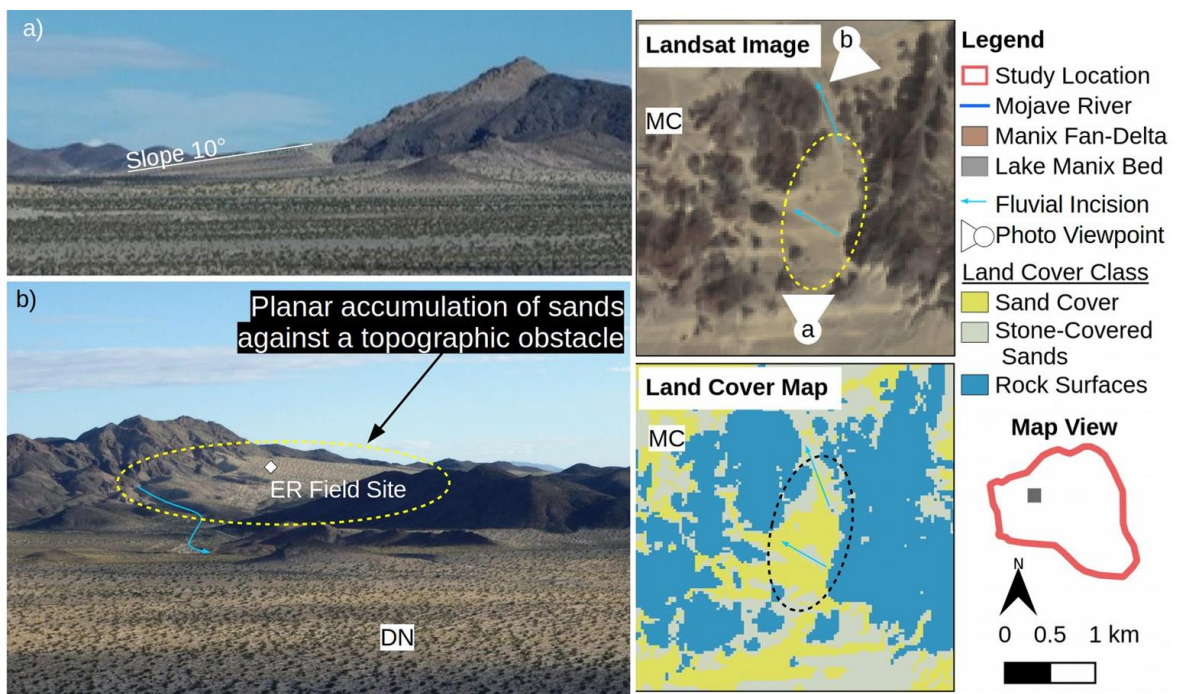


Figure 6.20: Photographs to illustrate the morphology of aeolian accumulation against an unnamed mountain - here referred to as ER. Landsat-8 image courtesy of the U.S. Geological Survey.

Middle Cady (MC)

This site occurs where stabilised sands have formed a deposit with a low angle ($1-3^\circ$) planar surface against a topographic obstacle but which is steeper by the mountain front ($>5^\circ$ locally). The landform's surface is primarily a lag surface of angular to sub-rounded granules and pebbles, but which contains some larger clasts. Consequently, the landform is largely classified as Stone-Covered Sands, but with Sand Cover present as patches across the upper portion of the landform and as a large patch towards the north (Figure 6.21).

Like SM and ER the landform is predominately planar in morphology, but it is significantly more ambiguous in its extent as it grades gently into a plain of stabilised sands to the north

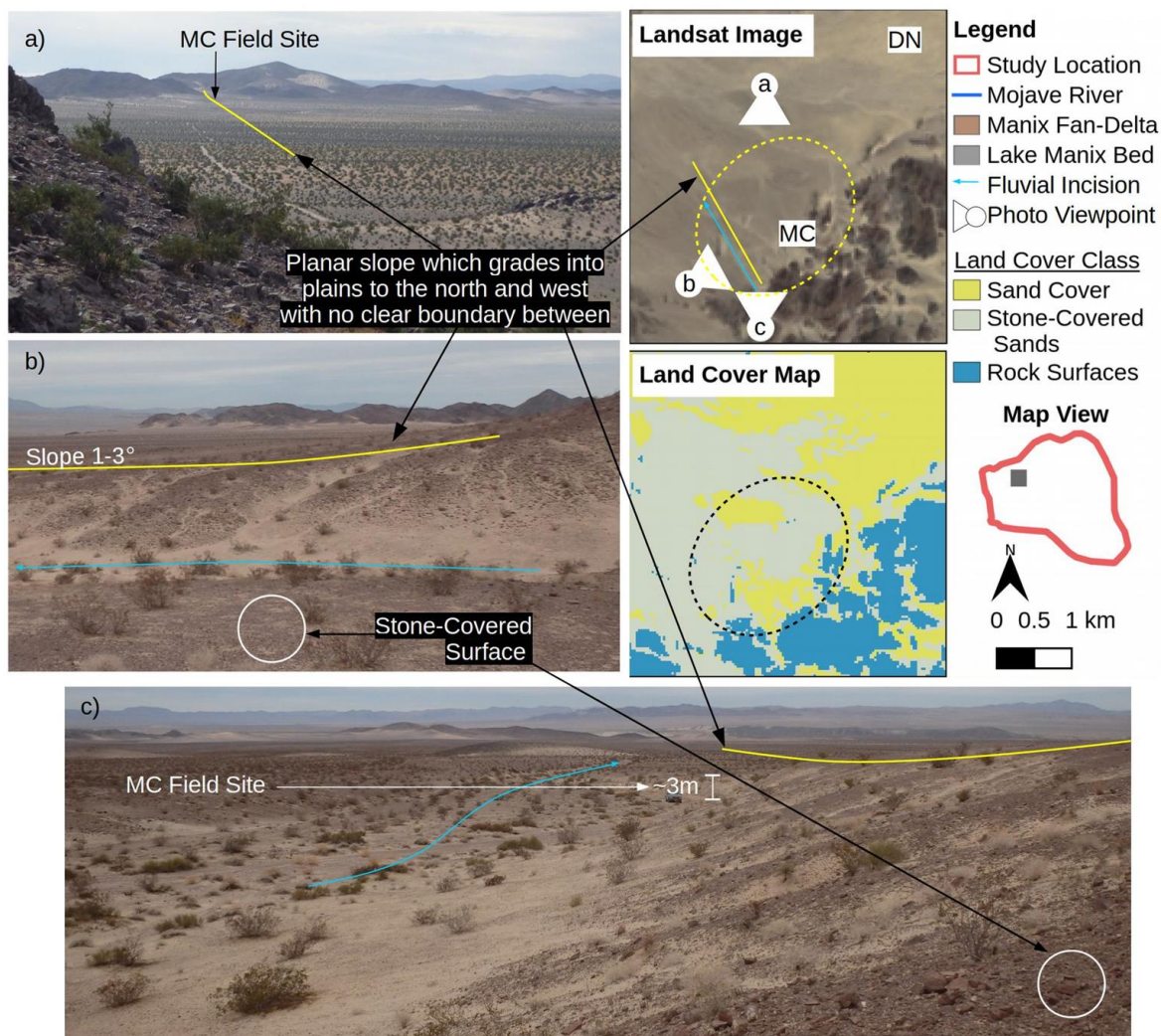


Figure 6.21: Photographs to illustrate the morphology of aeolian accumulation against an unnamed mountain - here referred to as MC. Landsat-8 image courtesy of the U.S. Geological Survey.

and west and a sandy plain (DN) to the north-east. Additionally, it is bounded by multiple topographic obstacles to the south which are separated by a small valley which has become filled with sediments, complicating the extent of the landform in this direction.

Cady Peak (PK)

Sediments have accumulated on the western slopes of the Cady Peak, almost completely burying topographic obstacles, and creating an extensive planar surface (3-5° slope angle) (Figure 6.22b). The landform’s surface is overwhelmingly sandy in composition, but adjacent to some topographic high points the sands have stabilised and become stone-covered. On the assumption that the underlying topography is similar to the topography immediately to the south (~100m vertical difference between ridge and valley floor) then this landform is likely

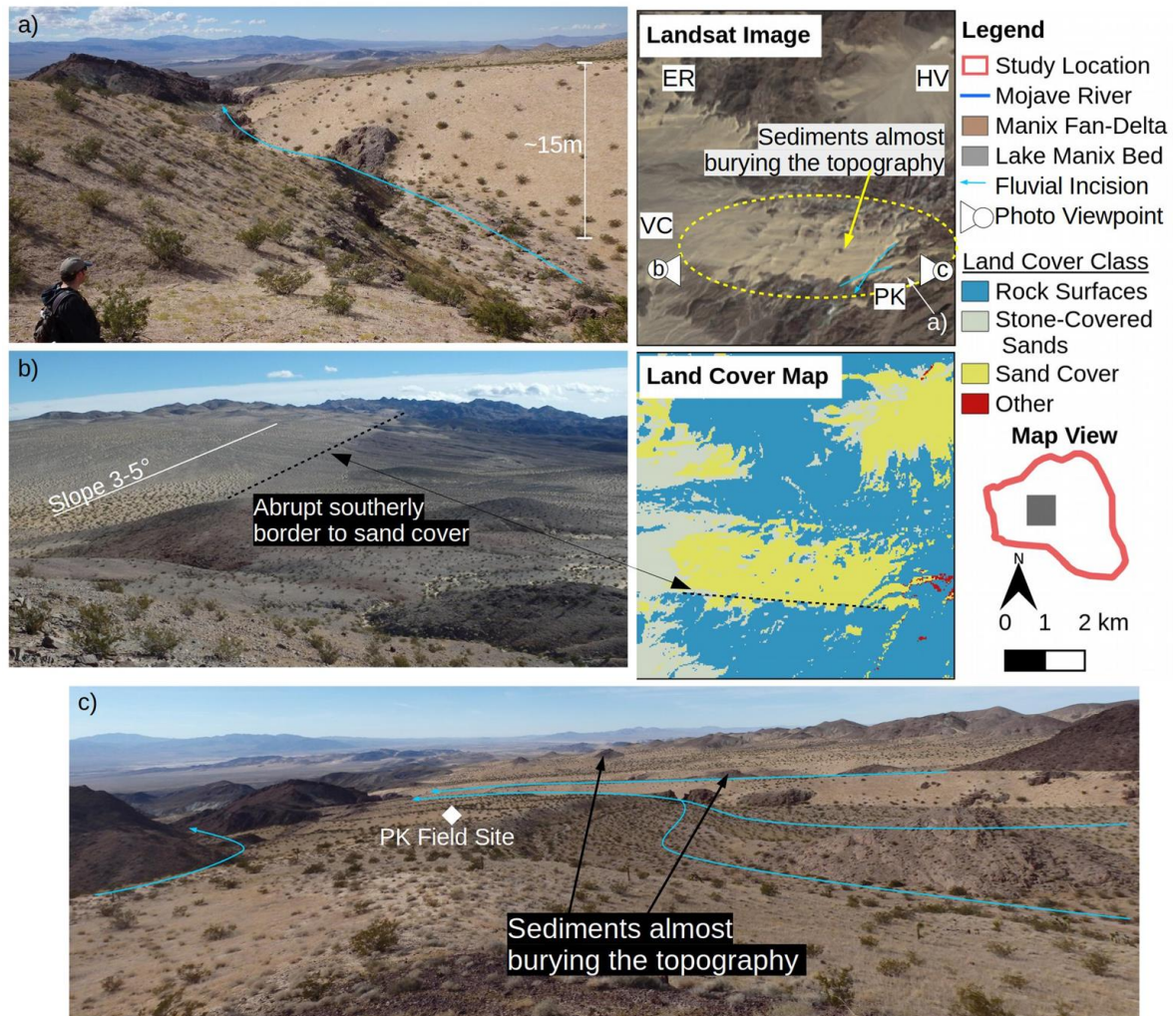


Figure 6.22: Photographs to illustrate the morphology of aeolian accumulation against an unnamed mountain - here referred to as PK. Landsat-8 image courtesy of the U.S. Geological Survey.

to be deep. Additionally, at the easternmost portion of the landform the sands have become incised (>15m), creating several deep incisions into the landform (Figure 6.22a). Figure 6.3 identifies these within the landform as valleys cut into the deposit.

The landform is well defined to the north, east and south by an abrupt boundary, though these do not appear to relate directly to some large topographic barrier (this is particularly noticeable along its southerly boundary – Figure 6.22c). By contrast, the western border of the landform is highly ambiguous as the surface grades into the basin around Valley Center Road without any defined break of slope. The distinction between these landforms will be based on the gradual shift in surface composition between these sites (and hence the boundary's exact location is interpreted).

Summary

This section has described four landforms identified as occupying a Mountain Front accommodation space. The four examples show that, though each of these sites does exhibit planar morphometry, this does not necessarily translate into four well-defined and easily delimited landforms. Two landforms are well-defined whilst two are ambiguous in their extent along at least one axis, grading gradually into adjacent areas.

Valley

Aeolian deposits within valleys were the second accommodation space type observed within the Cady Mountains. This section notes that, where a single valley is tightly bounded by topography, the landform can be straightforward to delimit. By contrast, where multiple valleys meet defining discrete valley landforms can be significantly more ambiguous.

Royalty Drive (RD)

This is a valley-fill deposit on the western margin of the Cady Mountains which is incised by a channel running along the centre of the valley (Figure 6.23). The slope of the landform varies from 1-8° along its long axis to 10-20° where the valley narrows. The surface of the landform is principally of Stone-Covered sands, with the exception of close to the incision down the centre of the valley which has a sandy surface. The thickness of the deposit contrasts sharply to the rest of the mountain front visible from the Mojave River where significant quantities of sand are piled up against the topography as a ramp/valley fill (notably Figure 6.19 and Figure 6.24). It is unknown whether this smaller aeolian accumulation

represents the approximate maximum thickness of valley-fill or whether the landform is significantly degraded.

RD is simple to delimit because it resides in a valley which is tightly defined by the bedrock topography that bounds the landform on all sides, excluding the valley toe.

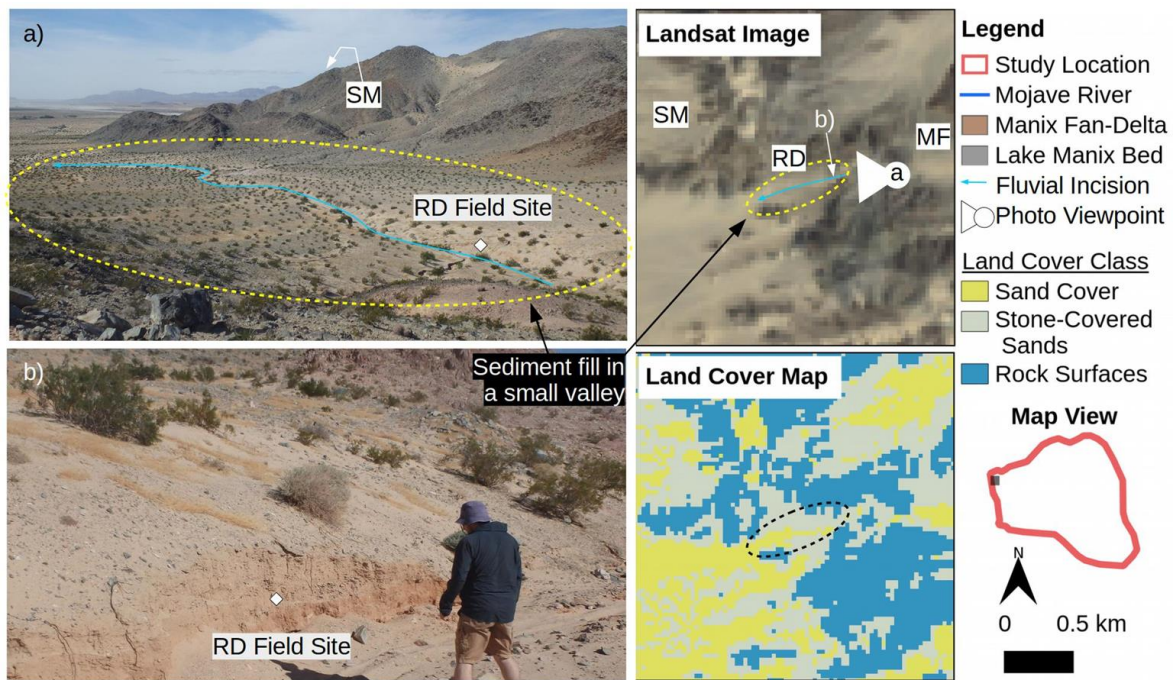


Figure 6.23: Photographs to illustrate the morphology of an aeolian deposit which has developed within an unnamed valley – here referred to as RD. Landsat-8 image courtesy of the U.S. Geological Survey.

West Cady (WC)

This deposit fills a valley along the western margins of the Cady Mountains and has been dissected by a substantial sinuous incision along the approximate centre of the valley (Figure 6.24b and c). Sections within the incision indicated >2m of sand within the valley, which pinches-out towards the mountain fronts (Figure 6.24c). Its surface has a concave low-angle slope (3-5°) which is predominately of Stone-Covered Sand composition but areas of Sand Cover are present, particularly on the south-facing slopes.

The landform is bordered on three sides by topography, although its true extent is somewhat dependent on whether the northerly fork is included (Figure 6.24) and where its western border (valley toe) is perceived to lie. The head of the valley forms a mountain pass which is

devoid of sand, but which contains a significant quantity of W-E orientated ventifacts (Figure 6.24b).

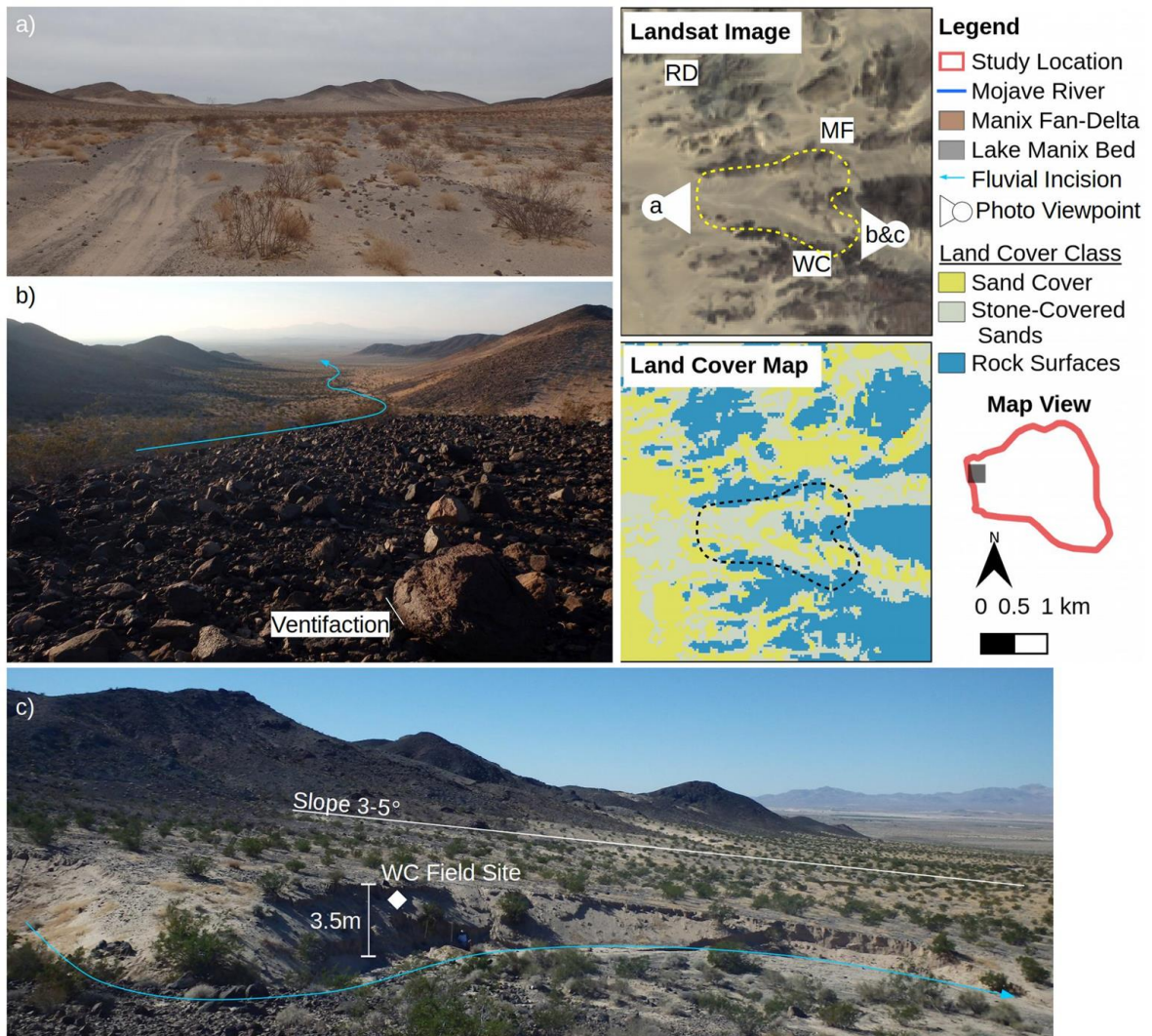


Figure 6.24: Photographs to illustrate the morphology of aeolian deposit which have filled an unnamed valley – here the landform is referred to as WC. Landsat-8 image courtesy of the U.S. Geological Survey.

Valley Complex

Sands fill several long, narrow and steep-sided ($1-25^\circ$) inter-connecting valleys along the northern edge of the mountain block, the largest being $2-2.5\text{km}^2$ in size (Figure 6.25).

This valley is part of a larger $\sim 6.5\text{km}^2$ area of surficial sand comprising multiple joined valleys which meet with DN (Figure 6.25). It is therefore ambiguous whether this area constitutes a single characteristically variable landform or whether the area comprises

multiple distinct valley-fill landforms which are difficult to delimit. Indeed, as these valleys lack any incontestably definable boundary, their (in)distinction is a matter of geomorphological perception (Section 2.1.3).

The three examples of valley-fill aeolian deposits vary considerably in how easily they can be delimited, though all valleys rely on some degree of perception in delimiting their toe. RD is an example of a well-defined landform within a simple valley topography, with WC being similar except that the valley forks and it was a matter of perception whether both forks constitute a single landform or two different landforms. By contrast, the last example showed an extensive network of valleys where no ambiguous dissection of landforms was possible.

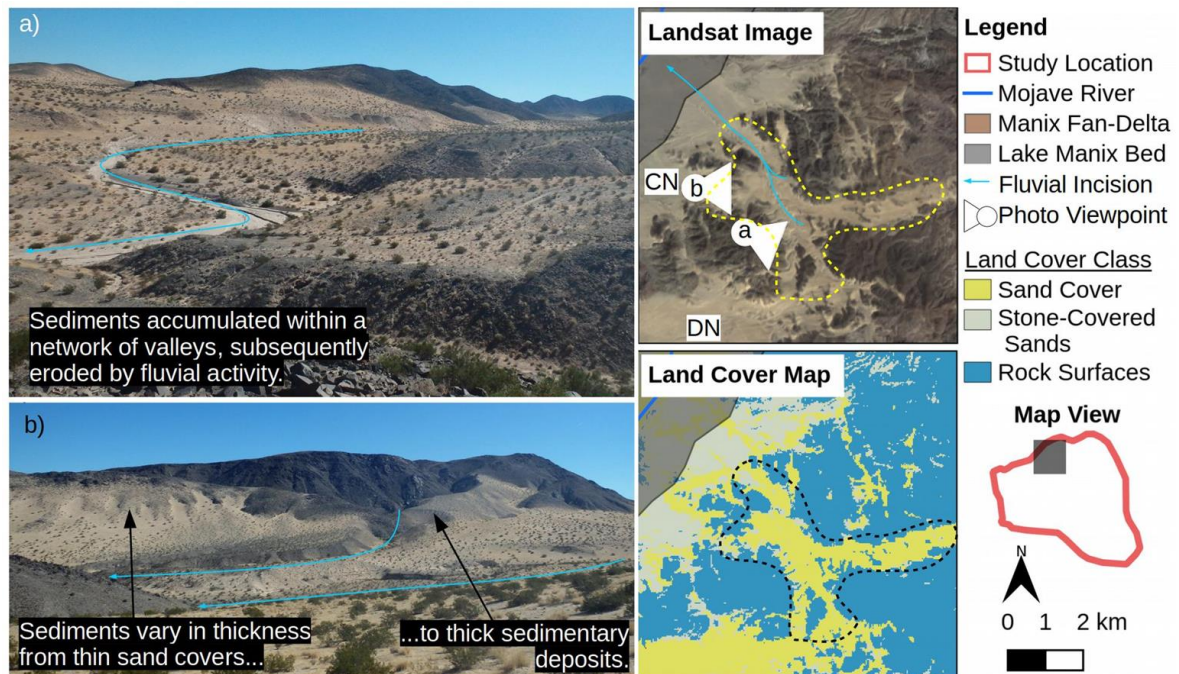


Figure 6.25: Sediments have accumulated within a number of valleys which have coalesced into what may be considered to be either one or a number of landforms. Photographs illustrate the strong variability in morphology which are visible, even within small areas. Landsat-8 image courtesy of the U.S. Geological Survey.

Plain

Aeolian deposits which form as plains are the third accommodation space type under discussion here. As broad areas which grade into adjacent landforms plains, tend to be defined by some perceived boundary, such as a change in land cover or some arbitrary morphometric threshold (e.g. slope). Two examples are described here.

Dune field (DN)

This area constitutes a broad, flat ($<2^\circ$) sand-covered plain which is bounded by steep topography along its northerly and southerly borders (Figure 6.26). Pits dug within this

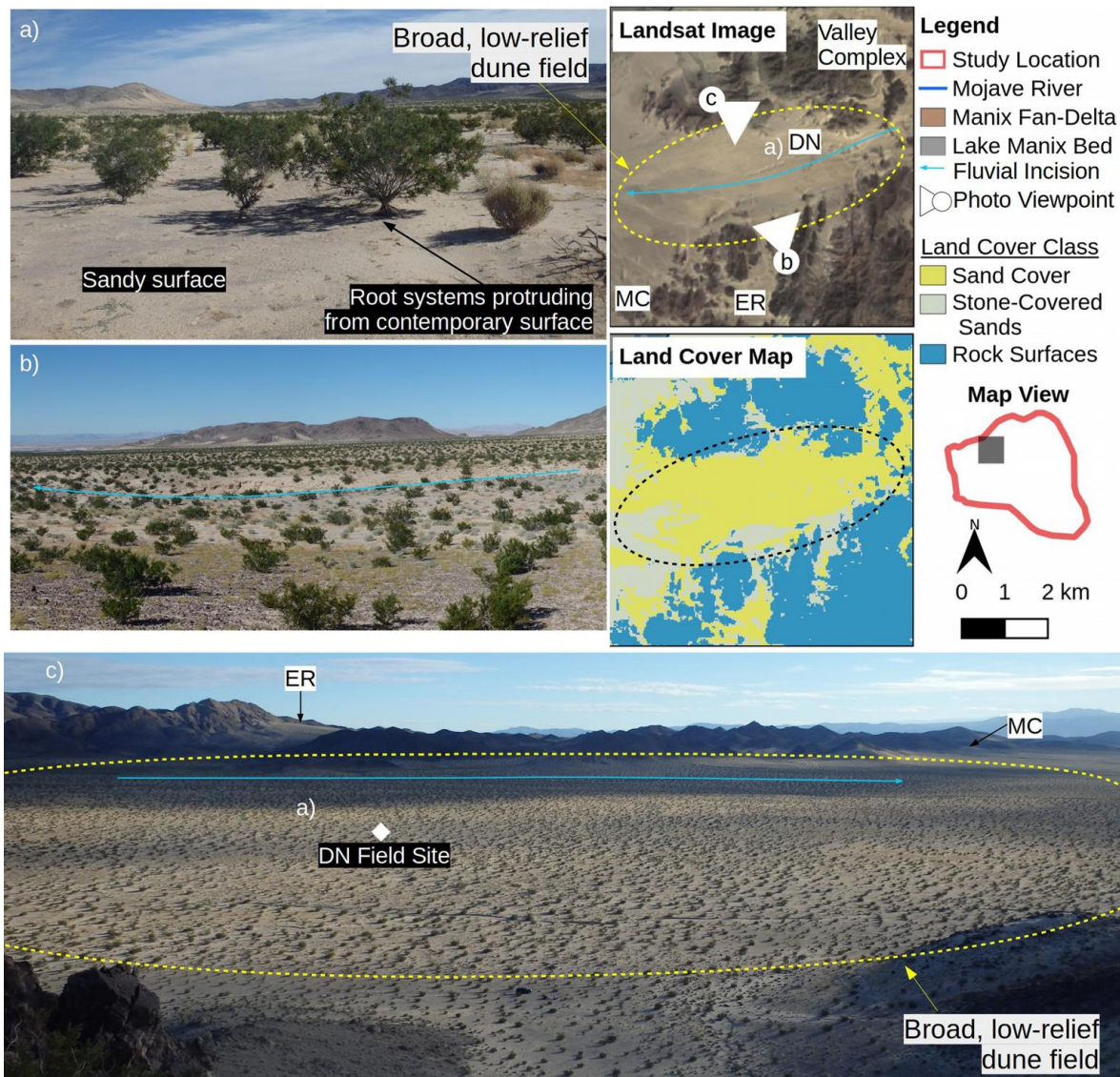


Figure 6.26: A broad and open plain contains a low-relief dune field whose surface is sandy. Many of the creosote bushes exhibit protruding root systems (a), suggesting recent deflation from this surface. Landsat-8 image courtesy of the U.S. Geological Survey.

surface, as well as numerous fluvial incisions (Figure 6.26b), suggest that much of the sand cover on this surface is at least two metres deep. Many of the creosote bushes across the plain have exposed roots (20-40cm exposed) suggesting that sand is currently being deflated from the area (Figure 6.26a).

No definite boundary exists between this plain and the sands of the complex valley discussed above (its eastern border) nor between this plain and the stone-covered sediments around the MC field site which forms its western border. In light of this ambiguity, the change from Sand Cover to Stone-Covered Sands form the southern and western boundary of the landform and the arbitrary threshold between plains and planar slopes (2° – Section 4.2.2) can be considered as forming its northern and eastern boundaries.

Valley Center Road (VC)

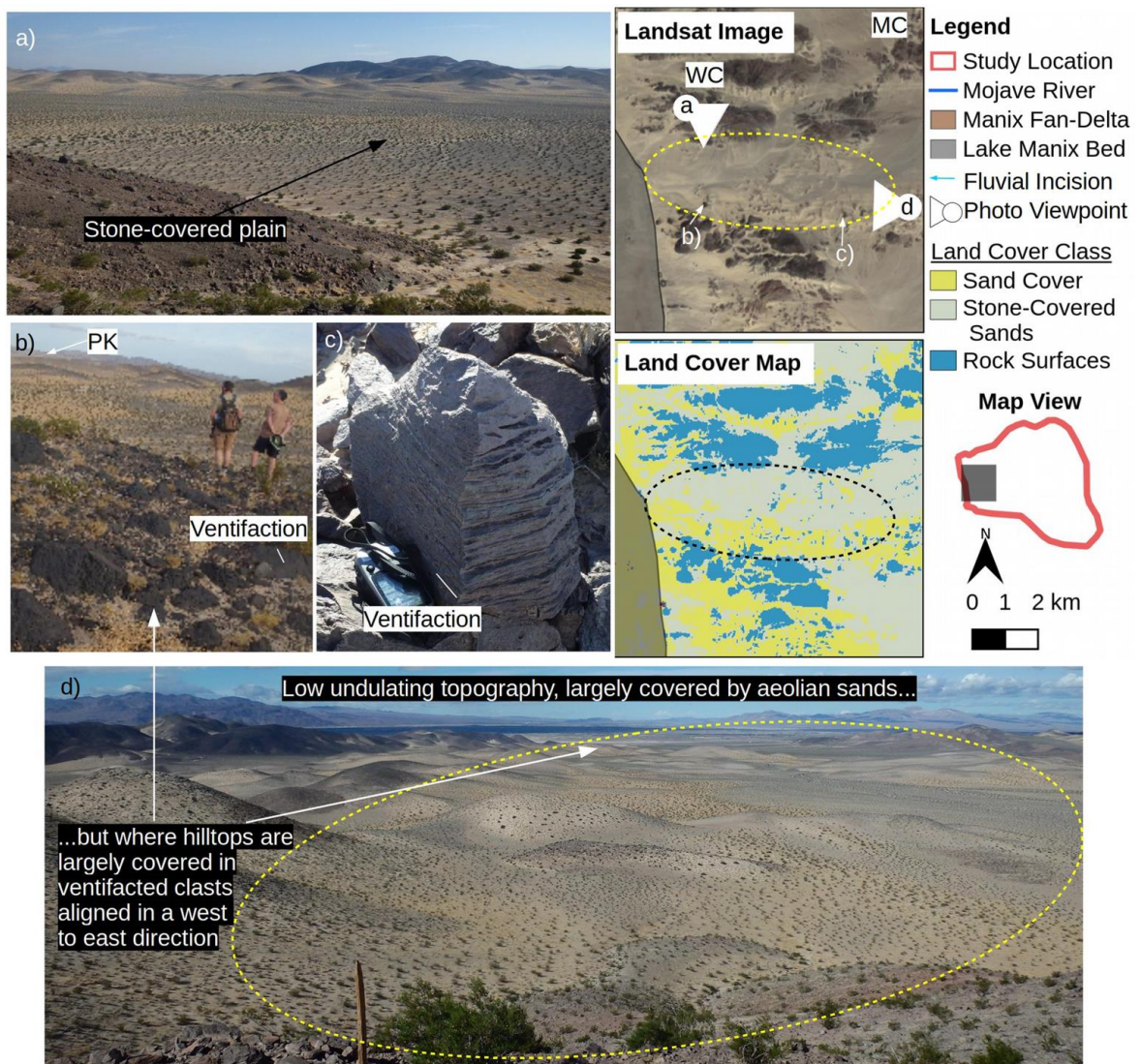


Figure 6.27: A broad and open plain capped by a surface which varies from Sand Cover towards the south to Stone-Covered Sands towards the north. The plain has an undulating shape towards the extreme south of the area, with the raised areas commonly showing evidence of W-E aligned ventifaction b) and c). Landsat-8 image courtesy of the U.S. Geological Survey.

This aeolian deposit is relatively flat when considered at a large-scale ($0-3^\circ$) but contains much small undulating topography with steeper slopes ($<15^\circ$ locally), particularly towards the extreme south of the area (Figure 6.27). The surface of VC varies from Sand Cover towards the south to Stone-Covered Sands towards the north. Pits dug at various points within this area suggest that the sediment is at least 1.5m deep. The uppermost exposed areas of much of the small topography contain abundant evidence of ventifaction aligned in a W-E orientation (Figure 6.27b and c), like those observed by Laity (1992).

The extent of this area is highly uncertain. If only the central area of contemporary sand cover is included then the landform is 14km^2 , but if the area is extended to include the whole plain (including the thick deposits of stone-covered sand) then the landform increases to $>26\text{km}^2$ in size as it occupies the whole low-lying area up to where it potentially meets with PK to the east.

Composite

The three previous classes were of field sites which contain only one accommodation space type. Three areas were observed to contain multiple accommodation spaces (of differing types) in close association with each other, here referred to as Composite sites. This section considered the manifestation of these situations within the Cady Mountains.

Cady North (CN) – comprising Mountain Front and Valley

This landform comprises a low-angle concave surface which increases in steepness from $\sim 2^\circ$ by the Mojave River to 5° by the mountain front, reaching $\sim 30^\circ$ locally on the mountain front and within valleys (Figure 6.28c). It has been incised by numerous channels that emerge from the valleys behind the landform (Figure 6.28b). The surface of the landform is predominately of Stone-Covered Sands, but with some areas of Sand Cover around the periphery of the landform where it steepens against the topographic obstacles. The landform's surface is covered in a network of sinuous incisions (Figure 6.28c) which, coupled with the concave-upwards shape, indicate a history of fluvial activity on the surface.

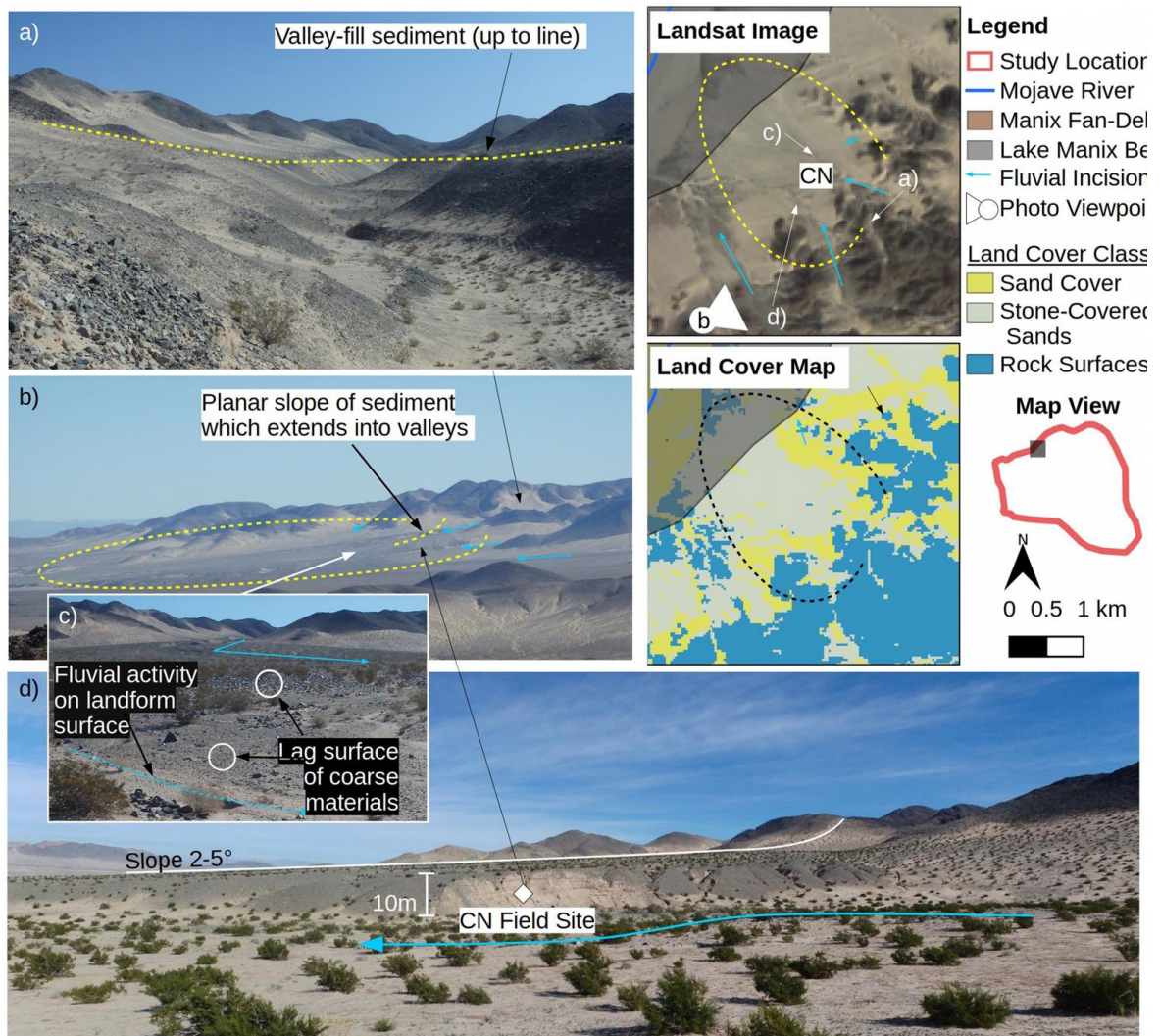


Figure 6.28: Photographs to illustrate the morphology of aeolian accumulation against an unnamed mountain and which continues into a number of small but steep-sided valleys – here referred to as CN. Landsat-8 image courtesy of the U.S. Geological Survey.

This landform is truncated on one side by the Mojave River (and presumably bounded by Lake Manix before ~25ka – see high stand shading in Figure 6.28). It is bounded on its east side by the topography, though the sands of the landform continue into three significant valleys forming valley-fill sediments in each (as in Figure 6.28a). Elsewhere the boundary of the landform is highly ambiguous as the planar slope grades into the surrounding landscape.

Hidden Valley (HV) – Plain and Mountain Front

The Hidden Valley contains a landform which covers $>10\text{km}^2$. The site area is interpreted to have two distinct, though not discrete, landforms. The larger landform is a broad sand-covered plain ($0-2^\circ$). The smaller landform is also sandy with a planar surface $\sim 2\text{km}^2$ in area and slope of $10-15^\circ$. The two landforms have coalesced, lacking any defined boundary (e.g. a break of slope).

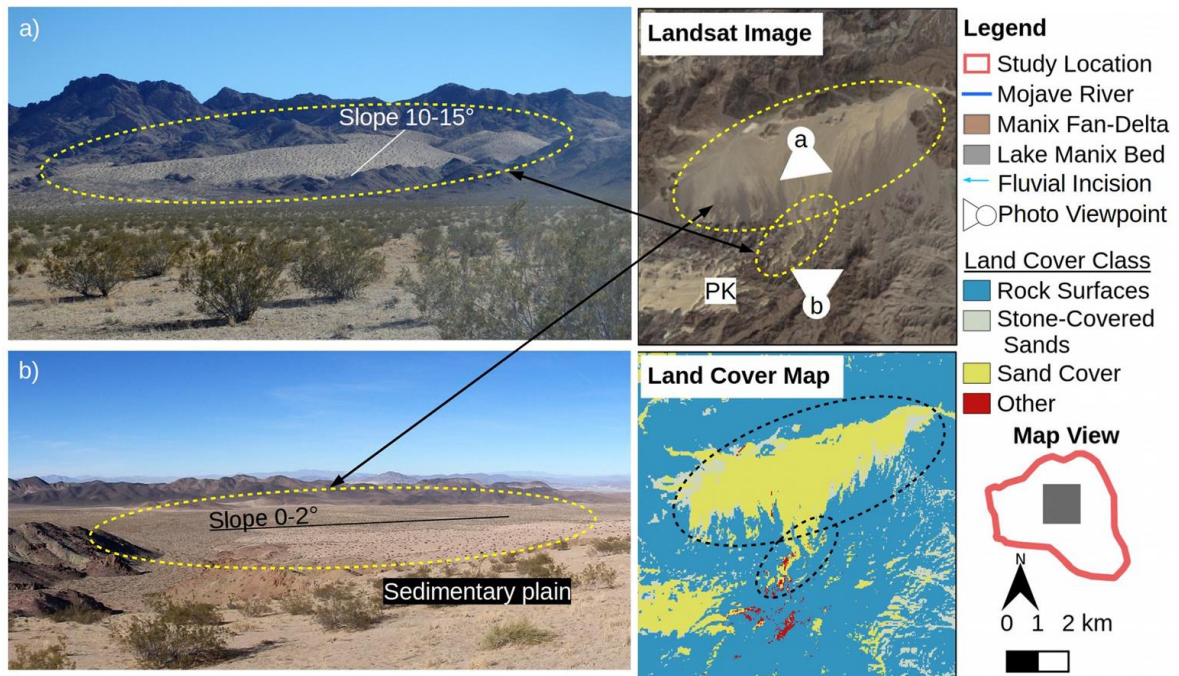


Figure 6.29: A broad and open plain contains a low-relief dune field whose surface is sandy. This sandy surface wraps up into a sand-covered planar surface to the south. Landsat-8 image courtesy of the U.S. Geological Survey.

Manix Front – Mountain Front and Valley

Across this area the complex topography (with a Rock Surface) is flanked and covered by many areas of Sand Cover and Stone-Covered Sands on most sides, forming an aeolian deposit(s) which is highly variable in its morphology. There are situations where sand occupies small hollows ($<100\text{m}^2$), fills valley complexes (similar to Figure 6.25), creates low-slope flats ($0-5^\circ$) and wraps around the topographic obstacles as planar slopes ($5-20^\circ$) (Figure 6.30).

It appears very difficult to attempt to delimit this area into a justifiable patchwork of discrete landforms as it is highly variable in its form and lacks any distinct boundaries, both internally and from adjacent areas. For example, the area visible within Figure 6.30 and marked with a circle is itself connected to the head of the WC valley (northern fork) through a continuous area of Sand Cover and Stone-Covered Sands which wrap around and surmount the topography and hence it is unclear where any boundary should be drawn (therefore these landforms require interpreted boundaries). MF exemplifies many different morphologies within a small area, thus representing well the difficulties associated with any attempt to delimit the aeolian deposits in an area of complex topography into a patchwork of discrete landforms of one (or some number of) distinct morphological classes. Indeed, the situation is compounded by the observation that areas of sediments, even within close proximity, could be described as being of plain, planar and/or valley morphometry simply by considering the landscape at different scales (as noted by Fisher *et al.*, 2004). This situation highlights ambiguity in surface form which can result from the coalescence of landforms within multiple proximal accommodation spaces (of different types).

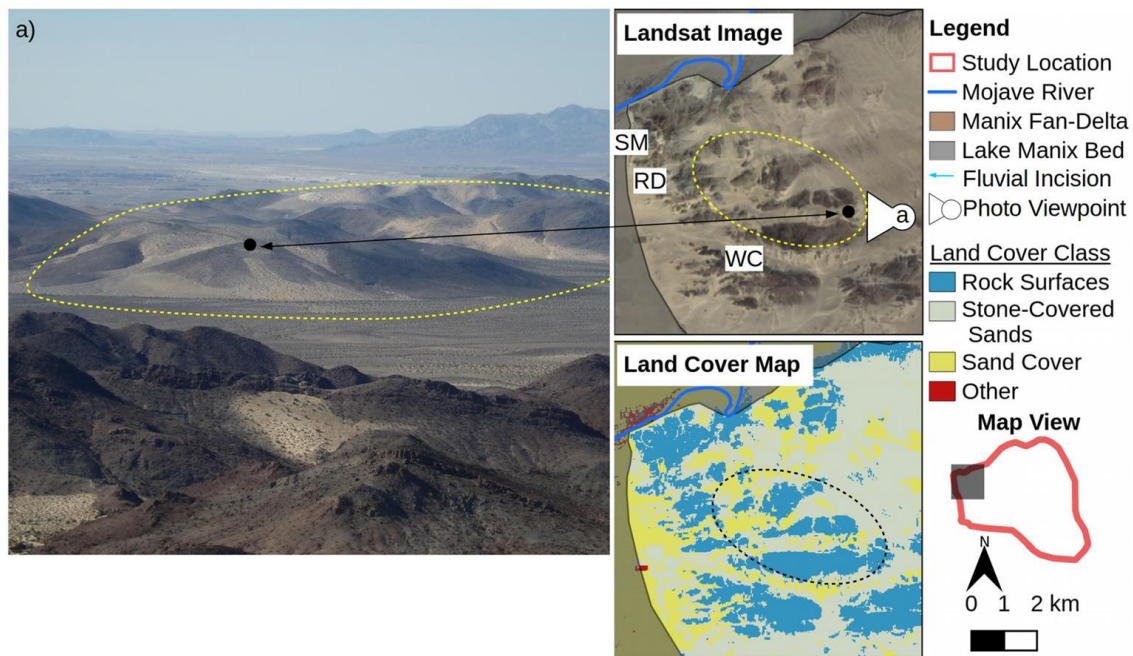


Figure 6.30: This area of topography is morphometrically complex as it contains areas of planar, plain and valley shapes which exhibit a combination of Sand Cover and Stone-Covered Sand surfaces. Here the area is referred to as MF. Landsat-8 image courtesy of the U.S. Geological Survey.

6.2.3 Summary

This section demonstrates that each of the three accommodation space types are associated with a characteristic morphology, however these can vary in their definition depending on the topographic situations present. This variability is due to coalescence of landforms where they either grade into one another (e.g. DN and MC meet) or where multiple accommodation space types occur in close association (e.g. CN) as these situations can make delimiting boundaries between individual landforms highly ambiguous.

6.3 Synthesis

This chapter has shown that aeolian deposits form a broadly continuous cover within the western portion of the Cady Mountains, the distribution and form of which is related to the topography. Section 6.1 proposed that, within this, the form of aeolian deposits can be subdivided based on three accommodation space types. Section 6.2 then showed that each of these accommodation space types are associated with characteristic morphologies but these morphologies can vary in their definability.

The distribution of aeolian deposits forms a broadly continuous cover which is disproportionately present across the western half of the mountain block. Within this cover, landforms vary from those which are easily delimitable landforms (SM) to those which are difficult to delimit because they grade into one another (e.g. MC and DN) or coalesce into a sedimentary apron (MF). This highlights that accommodation spaces do not have to create a discrete patchwork of landforms each with well-defined boundaries because these landforms can coalesce. This observation mirrors those of Telfer *et al.* (2014) when they noted that the aeolian deposits within the Drakensberg foothills, South Africa, varied from discrete landforms through to a discontinuous sedimentary apron which mantled the landscape depending on the local topographic conditions. Telfer *et al.* concluded that the more ambiguous areas reflected a less obvious topographic influence, analogous to the areas in the Cady Mountains where landforms grade gently into each other without an abrupt boundary (e.g. the boundary between MC and DN). This chapter has shown that ambiguity can also result from the close association of multiple accommodation spaces, within each a landform can grow to the point where they coalesce (e.g. at CN or the Valley Complex). As a further example of the complexity arising from landform coalescence, Ellwein *et al.* (2015) noted that the high-relief topography of the Black Mesa region of the Colorado Plateau created a

complex stratigraphy where pairs of climbing and falling dunes coalesced within canyons, which they described as a single valley-fill feature.

This chapter suggests that, if a well-defined accommodation space occurs in isolation and under a consistent wind regime, then a well-defined landform can develop. For example, the landform at Soldier Mountain is a well-defined and isolated accommodation space within an embayment which is the first topographic obstacle reached after the (dominantly westerly – see Section 3.2.3) winds travelled across the Manix Basin. Many similar Mountain Front landforms have been described which are well-defined owing to their position within an accommodation space related to either an inselberg or a simple embayment (e.g. Bertram, 2003; Rowell *et al.*, in press). However, this chapter has demonstrated that, in the Cady Mountains, SM is unusual for being so well-defined by the embayment within which it resides. Across the majority of the Cady Mountains the complex topography (particularly the close association of accommodation spaces and the influence of topography on local wind flow patterns) results in landform coalescence and/or landforms with poorly-defined boundaries.

The distribution and form of aeolian deposition and landform development within the Cady Mountains is not solely related to influence of the mountain block topography. As the climatic history of the Mojave Desert varied during the Late Pleistocene, so did the boundary conditions which controlled their development (see Section 3.2.3). Furthermore, because accommodation spaces result from the interaction between wind flow and the topography, they are somewhat wind direction dependent (see Section 2.1.1) and so can be modified by any significant change in the dominant wind regime. Together these factors could lead to the Cady Mountains exhibiting a composite distribution resulting from multiple episodes of aeolian activity which have potentially different wind regimes. Because it is difficult to unpick these effects based solely on remote sensing data, it is therefore necessary to investigate the stratigraphy of the aeolian deposits as these can provide a useful insight into the landscape history within the mountain block. This will form the essence of the next chapter.

7 Stratigraphy and Geochronology

In seeking to understand the relationship between complex topography and aeolian deposition and landform development the real world setting of this study needs to account for additional complexities controlling the deposition and preservation of aeolian sands, such as variable climatic histories (e.g. changes in moisture availability or wind regime – Chapter 3). Developing a process history is the primary means by which landform development can be investigated within the context of the changing boundary conditions of this locale. To this end, this chapter develops an understanding of the processes that have created the mapped landforms in Chapter 6. This chapter will work at two scales. Section 7.1 provides a stratigraphic description and geochronology for individual field sites, demonstrating the presence of aeolian, fluvial and hillslope sediments. By collating these data across field sites, Section 7.2 presents a new history of the aeolian sedimentation across the mountain block.

7.1 Description and process history from field sites

7.1.1 Field sites

Nine field sites are described in this section (Figure 7.1). They were selected principally based upon the availability of sedimentary sections, although pits were dug at three sites on undissected planar slopes with thick deposits of aeolian sand (ER and PK) and a low lying plain of sediments (DN) (as described in Section 3.1.4).

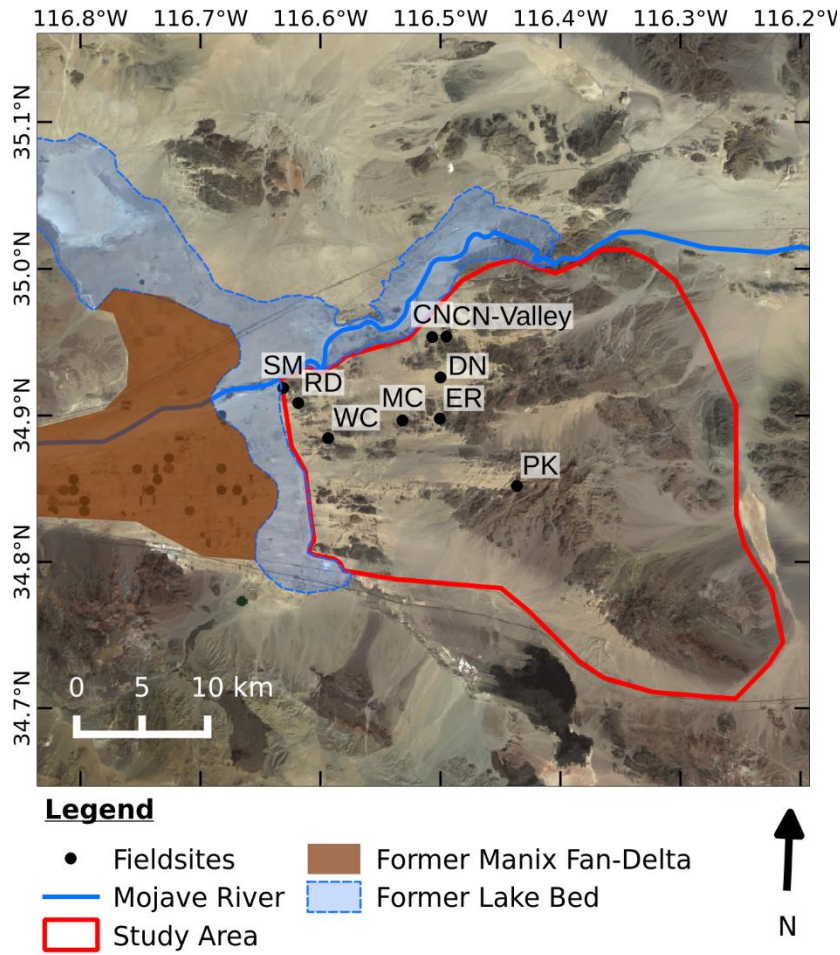


Figure 7.1: Map of the nine field sites discussed within this chapter. Landsat-8 image courtesy of the U.S. Geological Survey.

7.1.2 Geochronology

Ages were established using the protocols outlined in Section 5.2 and these are summarised in Table 7.1.

Table 7.1: Equivalent dose (D_e), fading correction (g-values) and ages for the samples discussed in this study. The fading-corrected age is preferred where it is written in black text, otherwise the fading uncorrected age is preferred (see Section 5.2 for justification). Samples CN13-1-2 to CN13-4-1 inclusive are derived using single-grain ages (see Section 5.4).

Sample Code	Depth (m)	Discs	D_e (Gy)	OD (%)	Uncorrected Age (ka)	g-value (%/decade) ^b	Corrected Age (ka)
CN13-1-2 (SG)	0.8	20	30.20 ± 2.5 ^c	101	6.30 ± 0.6		7.90 ± 0.75
CN13-2-1 (SG)	2.8	28	31.04 ± 3.7 ^c	83.0	6.15 ± 0.7	2.50 ± 0.3	7.71 ± 0.96
CN13-3-1 (SG)	3.8	20	30.98 ± 4.7 ^c	78.0	6.40 ± 1.0		8.03 ± 1.23
CN13-4-1 (SG)	4.6	20	36.89 ± 3.4 ^c	33.0	7.58 ± 0.7		9.53 ± 0.90
CN13-5-1	5.6	28	259.05 ± 11 ^a	9.9	55.44 ± 3.3	2.45 ± 0.2	71.21 ± 4.77
CN13-6-1	7.7	19	264.28 ± 11.7	10.5	58.70 ± 3.5		75.46 ± 5.06
CN13-7-1	8.2	22	204.29 ± 7.3	8.1	44.80 ± 2.3		57.38 ± 2.55
CN-Valley	0.3	18	326.75 ± 13.6	11.4	69.00 ± 4.0	1.95 ± 0.2	83.91 ± 4.47
DN14-1-4	0.8	23	35.10 ± 1.9	36.2	8.00 ± 0.7	2.55 ± 0.3	10.11 ± 0.85
DN14-1-3	1.3	20	67.83 ± 5.4	31.7	15.90 ± 1.4		20.30 ± 1.94
DN14-1-2	1.8	16	75.15 ± 6.4	30.9	17.80 ± 1.7		22.76 ± 2.38
DN14-1-1	2.3	21	25.96 ± 1.8	29.3	6.20 ± 0.5		7.81 ± 0.61
ER14-1-1	0.8	22	10.11 ± 0.4	8.3	2.50 ± 0.1	2.71 ± 0.3	3.16 ± 0.15
ER14-1-2	1.2	16	10.50 ± 0.1	8.8	2.50 ± 0.2		3.16 ± 0.24
ER14-1-3	1.9	11	5.35 ± 0.4	15.1	1.20 ± 0.1		1.50 ± 0.13
HL14-1	0.8	22	107.35 ± 3.5	5.1	25.40 ± 1.4		29.10 ± 1.80
HL14-2	1.3	20	104.32 ± 3.2	2.8	25.40 ± 1.4	2.35 ± 0.2	29.90 ± 1.80
MC13-1-2	2.1	19	323.25 ± 14.9	13.6	71.10 ± 4.5		80.40 ± 5.5
MC13-1-1	3.1	15	340.95 ± 11.5	6.0	74.40 ± 4.6	1.93 ± 0.3	82.44 ± 5.9
PK14-1-4	0.5	20	146.85 ± 5.1	6.8	33.50 ± 1.8		42.78 ± 2.54
PK14-1-3	1.3	28	145.15 ± 5.4	11.0	31.50 ± 1.7	2.46 ± 0.2	40.19 ± 2.34
PK14-1-2	1.6	20	148.22 ± 5.6	9.6	31.42 ± 1.7		40.09 ± 2.38
PK14-1-1	2.0	20	160.47 ± 5.8	9.6	35.10 ± 1.7		44.85 ± 2.28
SL14-125	0.4	20	34.86 ± 1.2	6.2	8.80 ± 0.4	2.10 ± 0.3	10.10 ± 0.50
SL14-3	1.2	19	51.20 ± 1.6	9.1	11.30 ± 0.5	0.71 ± 0.3	11.90 ± 0.60
SM13-1-1	2.0	27	226.42 ± 7.5	6.2	46.63 ± 7.5	2.18 ± 0.3	57.94 ± 10.1
SM13-3-1	5.0	19	246.64 ± 14.1	14.9	54.30 ± 3.4	2.60 ± 0.4	70.98 ± 5.34
SM13-2-1	14.5	17	327.81 ± 12.6	8.3	70.80 ± 3.3		92.92 ± 6.55
RD14-1-3	0.6	7	11.07 ± 2.0	47.5	2.05 ± 0.5		
RD14-1-2	0.9	20	312.71 ± 13.7	13.2	72.20 ± 4.4		
RD14-1-1	1.2	20	318.66 ± 12.2	9.5	77.40 ± 4.4	1.85 ± 0.6	
WC14-1-1	0.7	21	17.10 ± 0.8	7.4	4.00 ± 0.2		5.26 ± 0.34
WC14-1-2	1.9	17	20.44 ± 0.7	8.0	4.50 ± 0.2		5.93 ± 0.35
WC14-1-3	3.5	24	23.18 ± 0.8	8.8	5.50 ± 0.3	3.03 ± 0.4	7.27 ± 0.50

Notes:

^a indicates samples measured using the pIR-IRSL₂₉₀ protocol, others use the pIR-IRSL₂₂₅ protocol. Sample CN13-5-1 has 290 (28 discs) and 225 (20 discs) measurements which are within uncertainty. Sample CN13-2-1 has 290 (23 discs) and 225 (20 discs) measurements which are within uncertainty.

^b g-values were measured using a t_e value of 578 seconds and refer to the pIR-IRSL₂₂₅ protocol unless otherwise stated.

^c samples were measured as single-grains as described in Section 5.4.2.

7.1.3 Stratigraphic description

This section describes the sedimentary units present at each site.

CN (Cady North)

This site is located on the northern front of the Cady Mountains at an altitude of 601 m.a.s.l. (landform surface) (Figure 7.1). It comprises a ~8m fluvially-cut exposure that did not reach the base of the landform (Figure 7.2). The landform accumulated in two phases: Units 1-3 formed between 60-50ka and Units 4-6 developed at 11 ka-7 ka. Between these periods, a well-developed palaeosol implies a dispositional hiatus ~30ka to 11ka (see Section 7.1.4). The oldest evidence for aeolian activity at the site is situated at the CN-Valley site where a lone sample was taken from a small section cut into one of the three large valleys that form the eastern boundary of the CN landform (see Section 6.2) (Figure 7.3). This age (69 ± 4 ka) implies that a longer, unexposed record >65ka also potentially exists in the unexposed material at the CN cutting. Grain size characteristics show a moderately- to poorly-sorted mixture of sands (and some silts) with a dominant mode of ~200 μ m, with samples taken within Unit 6 demonstrating the highest sorting.

Unit 1

The lowermost recorded unit comprises horizontally-bedded sand alternating between layers of paler coloured fine to medium sands and darker and medium to coarse sands. The unit is cemented and contains abundant rhizoliths.

Unit 2

This unit comprises an unbedded supporting matrix of medium to coarse sand with orientated horizontally-aligned clasts of angular material of gravel to boulder in size (~30cm b axis). The unit sits with a sharp contact of coarse sand above the lower unit.

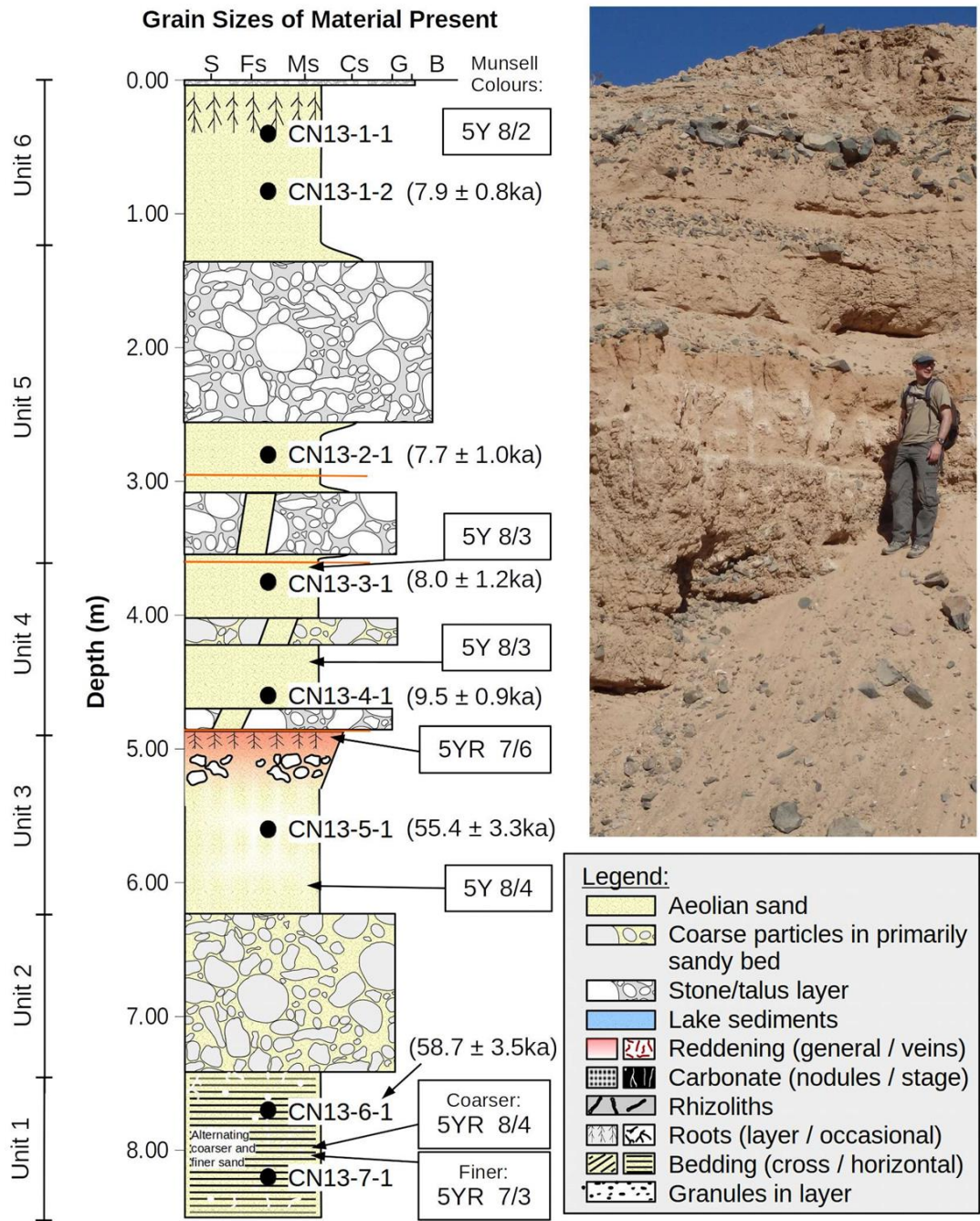


Figure 7.2: Stratigraphy of the aeolian deposit at CN.

Unit 3

This unit comprises unbedded fine to coarse sands and does not contain any clastic material. The lower portion of the unit has significant (Stage 2-3 – Retallack, 1988) carbonate development and the upper portion grades to being reddened at the top. Numerous root traces are observed and there is an abrupt contact with the overlying Unit 4.

Unit 4

This unit comprises a thick layer of fine to coarse sand with discontinuous matrix-supported stone layers. The stone layers vary from two to ten stones in thickness, and range from small granules to particles with a diameter of up to 20cm.

Unit 5

This unit contains two layers composed of granules to angular boulders of up to 1m diameter, separated by fine to medium sands which grade (with an increase in coarse sand) into the clastic layers. The clastic material varies between being clast- and matrix-supported across the unit and are typically of the order of 10-20 clasts thick. The unit contains two (~2cm thick) layers of coarse sand, one of which forms the sharp contact with the unit below.

Unit 6

The uppermost unit comprises unbedded and poorly-cemented sands with few clasts and grading upwards from Unit 5. The landform has a stone pavement surface of angular to sub-rounded pebbles and cobbles.

CN Valley

This sample was taken from the sediments where the CN deposit extends into the valleys behind the mountain front at CN (see Section 6.2.2). There is an isolated OSL sample taken from within a sandy unit which is lightly reddened by the contemporary surface and has an age of $69 \pm 4\text{ka}$ (Figure 7.3).

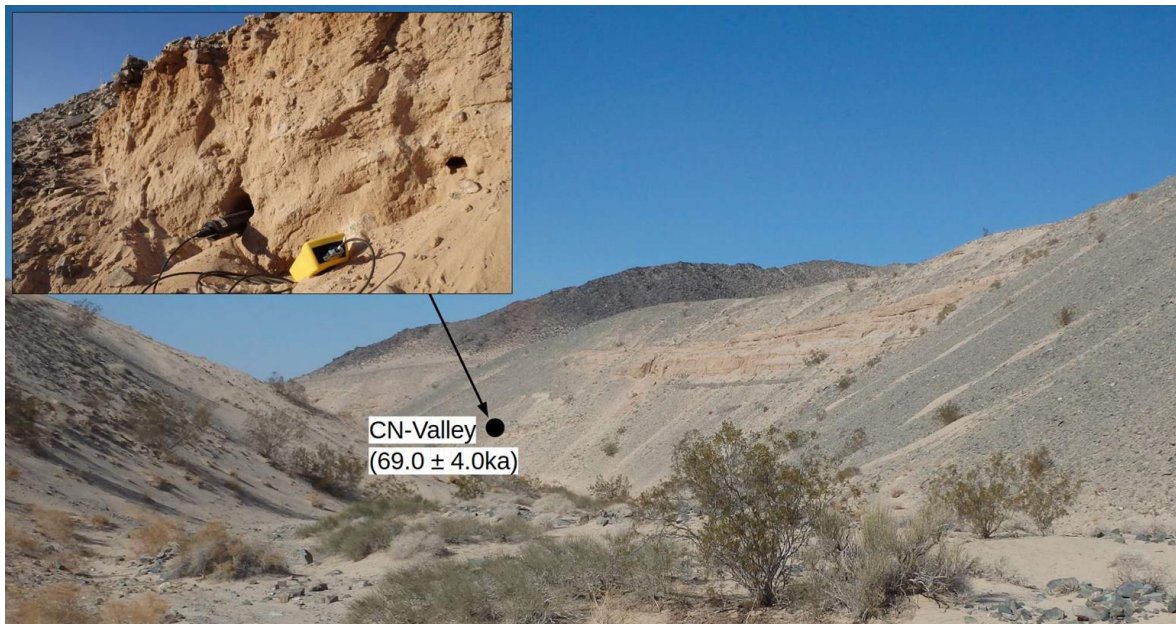


Figure 7.3: Photographs showing the setting of the CN-Valley field site.

DN

This section is situated towards the centre of the DN plain at the north of the mountain block (Figure 7.1). It was sampled to ~2m deep with a hand-dug pit, which did not reach the landform's base (Figure 7.4). The single aliquot ages present a major age reversal (Table 7.1). The younger luminescence ages (7-10 ka) are preferred because these samples are from sands with the least evidence of coarse-sediment input (DN14-1-1 and DN14-1-4) and are supported by them also matching the CN age range (discussed in Section 5.4.2).

Unit 1

The lowermost unit comprises a poorly-consolidated mixture of unbedded sands (mode ~200µm), which features several broadly continuous granule layers (<3mm diameter).

Unit 2

The second unit comprises unconsolidated, unbedded and moderately-sorted fine to medium sands (mode ~200µm) grading to coarser sands above 0.6m and with fine root traces above

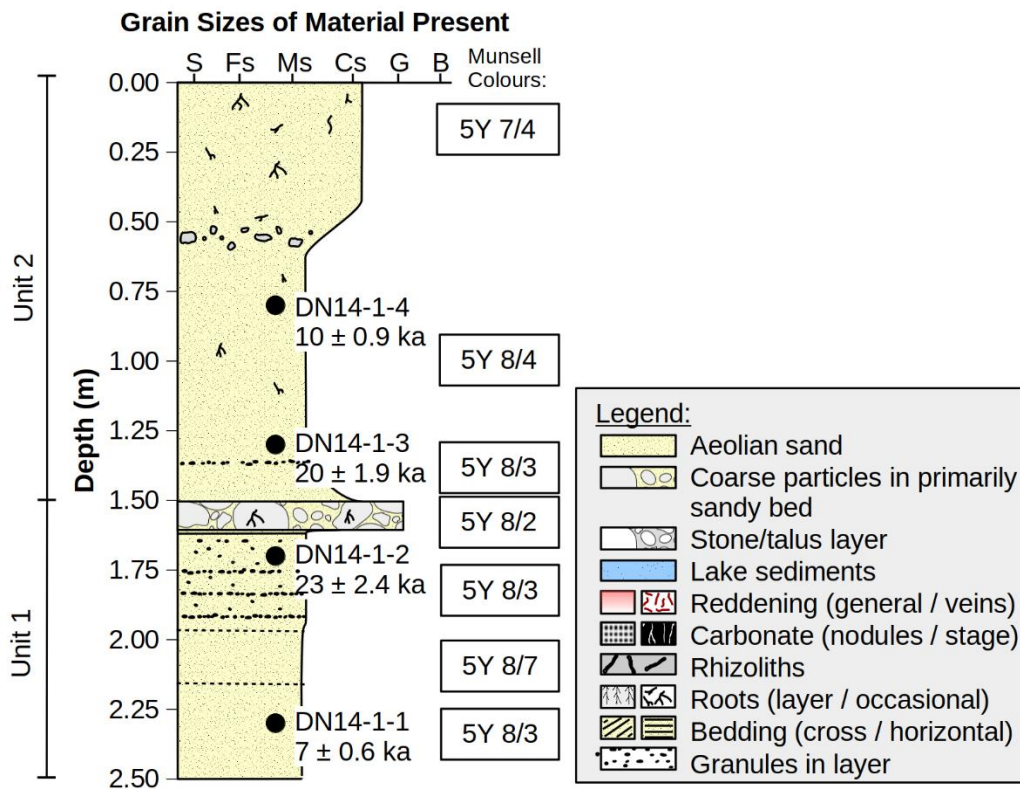


Figure 7.4: Stratigraphy of the aeolian deposit at DN.

1.2m. The base of the unit has a poorly defined contact with Unit 1 and is a mixture of sands through to angular granules (with occasional particles <5cm), which fines upwards and contains root traces. A second discontinuous stone layer at 0.6m contains sporadic sub-rounded stones of 3-7cm in size.

ER

ER is two thirds of the way up a planar slope of sediments which have accumulated against an unnamed mountain (Figure 7.1) and was excavated with a ~2m deep hand-dug pit, which does not sample the whole depth of the landform. The exposed sediment is structureless and homogenous, comprising (Figure 7.5) unconsolidated, unbedded and moderately-well-sorted medium to fine sands (mode ~200µm) with sporadic granules and root traces throughout, but concentrated in the top one metre.

The upper luminescence ages are both approximately 3ka but the lowest age presents an age reversal, being 1.3-1.7ka younger. Though the sample site was deliberately situated away from the larger fluviially-eroded gullies present on the surface of the landform, it is likely that fluvial degradation and reworking is the source of the age reversal (see Section 5.4.2).

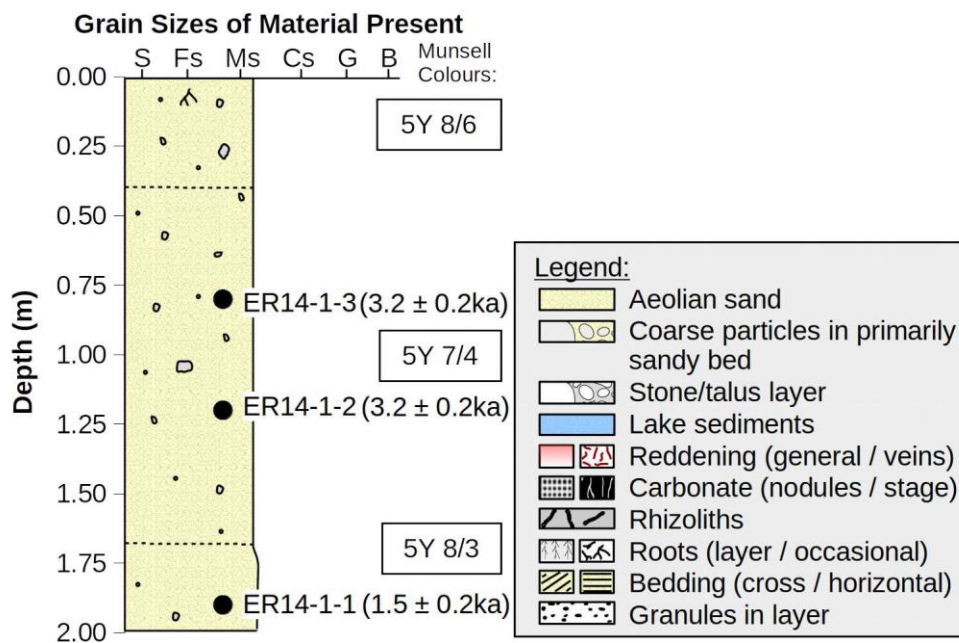


Figure 7.5: Stratigraphy of the aeolian deposit at ER.

MC

This site was sampled at a 3.5m section which did not expose the landform's base and is located on a broad planar slope towards the north-west of the mountain block (Figure 7.1). The sequence comprises three units (Figure 7.6). Luminescence ages are only available for the lowest unit, recording aeolian activity around 65-80ka. A fluvial incision into the landform has exposed a small section which contains ~50cm thick calcrete layer and which was dug to a maximum depth of 3.5m (Figure 6.23d).

Unit 1

The lowest unit is composed of poorly cemented, homogeneous and moderately sorted sands (mode ~200µm, but more coarse sands than units 2/3). Some carbonate nodules are present within the unit which decrease in frequency with depth.

Unit 2

The second unit is a poorly sorted mixture of cemented silts, sands and gravels with diameters of <5cm. The unit shows stage 3/4 carbonate development and root casts which grade out at the base of the unit (Retallack, 1988). The uppermost portion of the unit is lightly reddened.

Unit 3

The uppermost unit comprises uncemented sands (mode ~200µm), capped by granules, pebbles and some larger stones.

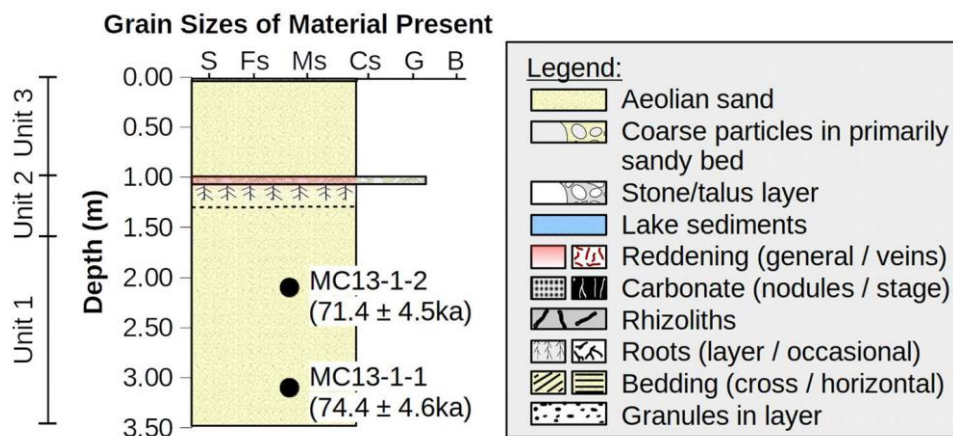


Figure 7.6: Stratigraphy of the aeolian deposit at MC.

PK

This site is situated on a planar surface comprising sand that has buried much of the nearby topography (Figure 7.1). It is undissected and was thus excavated to 2m without reaching bedrock. There are three lightly cemented layers of granules and occasional sub-angular pebbles within the section, with the middle example also expressing carbonate nodule development. Luminescence ages indicate that the sampled portion of the deposit accumulated at 30-36ka. The sediments are homogenous (Figure 7.7) and comprise unbedded and moderately-sorted fine to coarse sands (mode $\sim 200\mu\text{m}$) with occasional granule lenses, and roots in the upper half of the section.

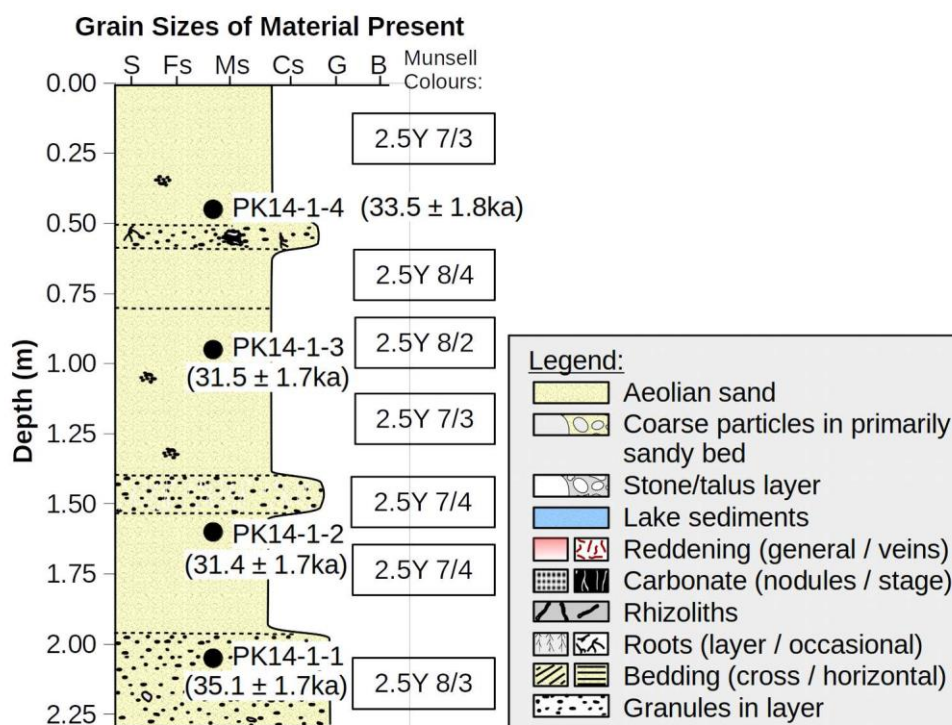


Figure 7.7: Stratigraphy of the aeolian deposit at PK.

Royalty Drive (RD)

This site occupies a valley along the western front of the Cady Mountains (Figure 7.1) and presents a 1.5m section exposed via fluvial activity. The sediments are not exposed to bedrock (Figure 7.8). The lowest unit was active at approximately 70-75ka, with the upper units accumulating in the last 2ka.

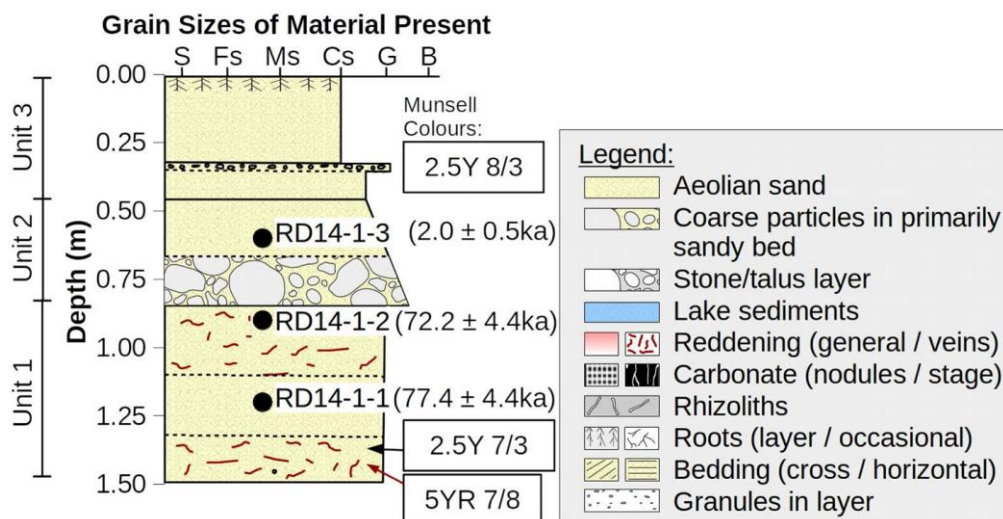


Figure 7.8: Stratigraphy of the aeolian deposit at RD.

Unit 1

The lowest unit comprises cemented fine sand through granules with some carbonate nodule development (mode $\sim 250\mu\text{m}$). Unlike other sites, the material within the unit was reddened as it contained significant 1-5cm long broadly horizontal veins of sand 5YR 7/8 in colour which occur in two bands (0.85-1.1m and 1.3-1.5m) within otherwise unreddened sands of 2.5Y 7/3 in colour.

Unit 2

The second unit is a poorly consolidated mixture of fine to coarse sands (mode $\sim 200\mu\text{m}$) with horizontally aligned angular material composed of granules through to gravel (clasts of $<12\text{cm}$). The unit fines upwards to near-pure sands at the contact with Unit 3. The ages imply that this unit represents a significant unconformity.

Unit 3

The uppermost unit comprises unconsolidated and unbedded sands and silts (mode $\sim 200\mu\text{m}$) with extensive root systems.

Soldier Mountain (SM)

This landform is extensively exposed due to quarrying activity and here two sections are described (Figure 7.10). The lower section is equivalent to section A (545-558m.a.s.l.) (shown in Figure 7.9) from Bateman *et al.* (2012) and the upper portion was sampled from the cross-bedded uppermost unit at the southern end of the quarry (their Unit V) (Figure 7.14).

Unit 1

The basal unit is composed of blue-grey silts/clays through to fine sand and is weakly bedded. It has been interpreted as a lake deposit from the former Lake Manix bed of an unknown age. Bateman *et al.* (2012) described nearby bedrock deposits at a similar stratigraphic position to these deposits and suggested that they form the basal unit of the stratigraphy (this was corroborated by this study).

Unit 2

This unit is a ~2m thick layer of sands, gravels, pebbles and boulders. Coarse material is commonly angular and varies between matrix- and clast-supported within the unit. Matrix material is sandy with a mode of ~150 μ m.

Unit 3

This unit is a thick ~8 m unit composed of fine to coarse sand, but with complex and often discontinuous layers of angular clastic material, commonly only one or two clasts thick. The unit varies between moderately-sorted sands (mode ~200 μ m / D₅₀ ~180 / D₉₀ ~480 μ m) and a poorly-sorted mixture of sand with an additional coarse sand component (mode ~290 μ m / D₅₀ ~ 200 μ m / D₉₀ ~580 μ m) as well as granules through to cobbles. The unit contains carbonate nodules and evidence of rhizoliths associated with both clast and matrix material.

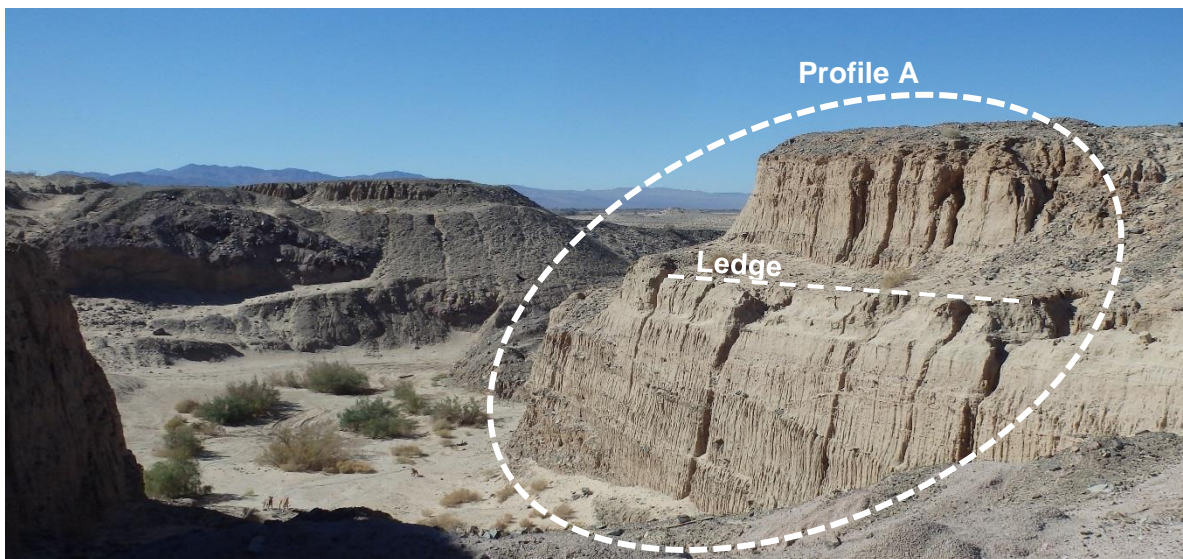


Figure 7.9: Photograph showing the interior of the sedimentary deposit at SM by profile A. Figure looking south-west (Figure 7.10).

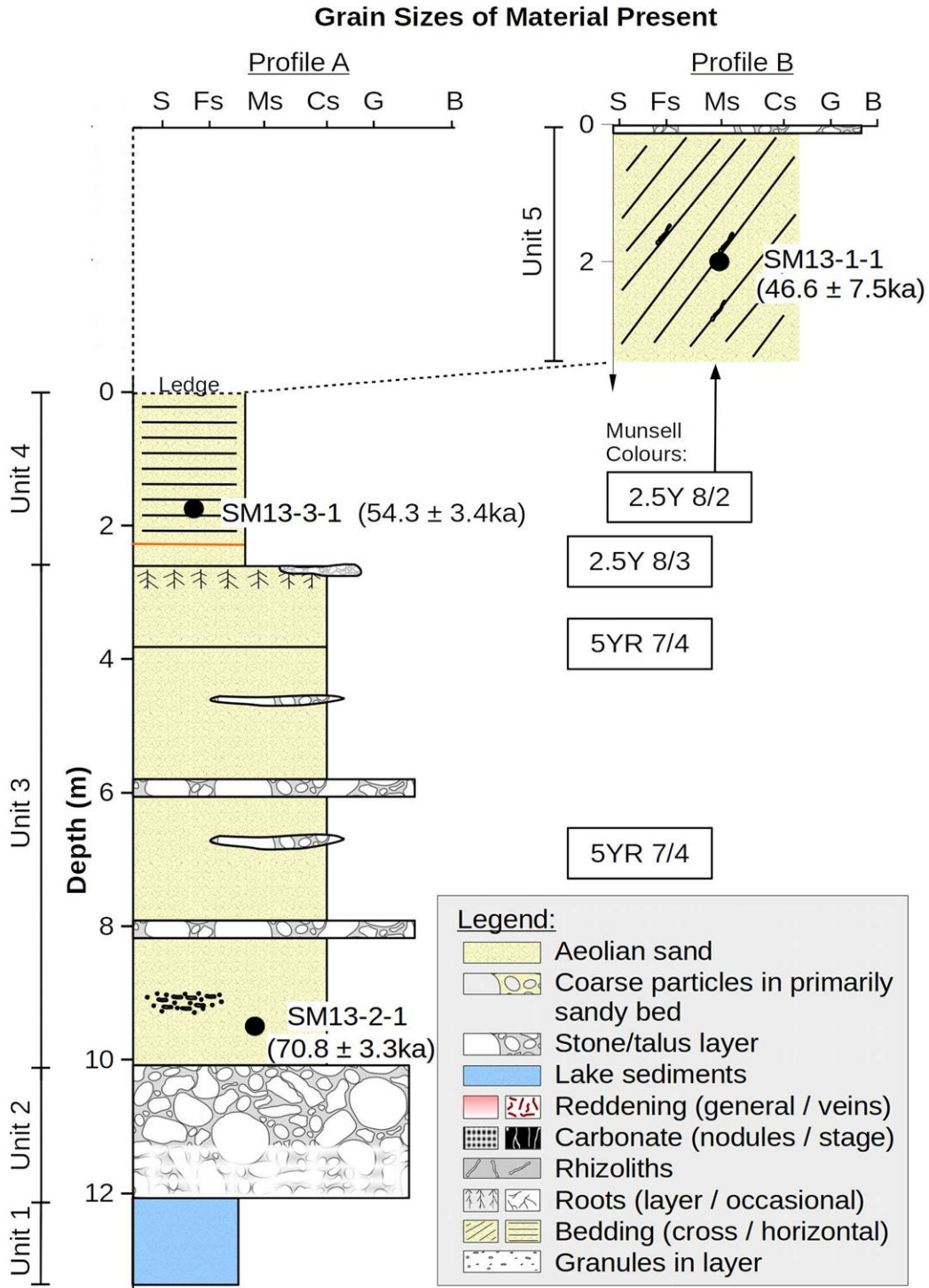


Figure 7.10: Stratigraphy of the aeolian deposit at SM composed of two profiles (A&B).

Unit 4

This unit comprises a poorly-sorted mixture of horizontally-bedded silts and sands (mode $\sim 250\mu\text{m}$) with some coarse sands present ($D_{90} = 512\mu\text{m}$) and a slight pink hue. The upper portion of the unit contains less silt, but the top of the unit is marked by a discontinuous layer of coarse sands and clastic material.

Unit 5

The uppermost unit is a $\sim 3\text{m}$ thick cross-bedded (dip $\sim 30^\circ$; strike to the north) deposit of poorly-sorted cemented fine to coarse sand with a dominant mode of $\sim 170\mu\text{m}$. The unit contains many rhizoliths and carbonate nodules associated with foresets and is overlain by a desert pavement surface formed of material between granule and small boulder in size.

WC

This site comprises a 3.5 m section, which was exposed through fluvial activity and which did not reach the base of the landform. The sands are homogenous and largely structureless (Figure 7.11), comprising unconsolidated and unbedded medium to fine sands (mode $\sim 250\mu\text{m}$) with sporadic granules and pebbles throughout the section and roots towards the top of the section. The landform has a pavement surface of angular to sub-rounded pebbles and cobbles.

This section has described the stratigraphy of the nine sampled sites within the Cady Mountains. One of the most significant observations (from a process perspective) is that coarse-grained (non-aeolian) sediments were observed at all sites, although they differ significantly with regards to the relative proportion, size and structure of coarse-grained materials. To this end, the following section will consider the grain-size characteristics in more detail.

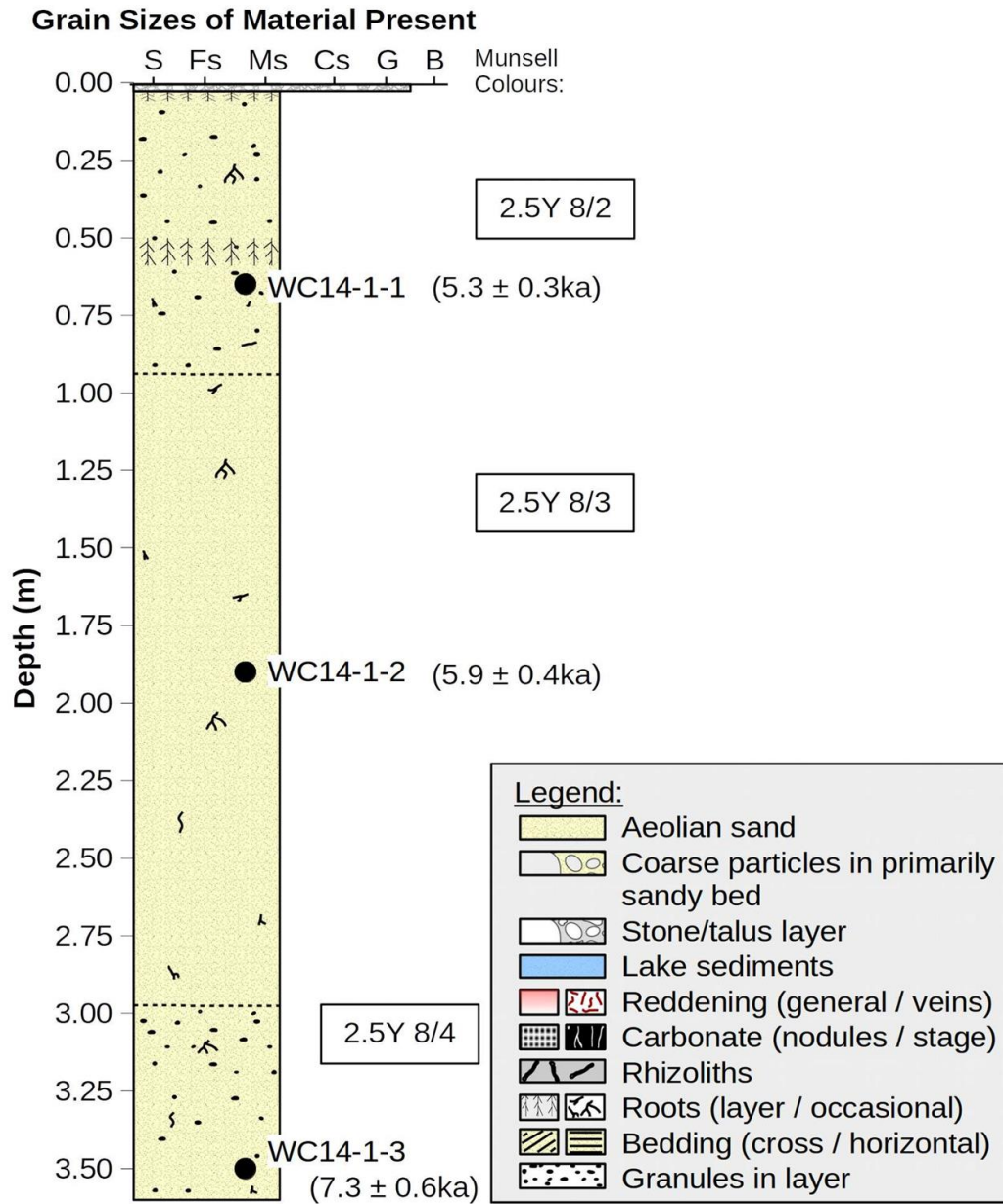


Figure 7.11: Stratigraphy and geochronology of the aeolian deposit at WC.

7.1.4 Textural characteristics and structure of deposits

The textural characteristics of a deposit contain information pertaining to its formative process (Folk, 1974; Ahlbrandt, 1979). Particle size data (for the <2mm size-fraction) indicate that the majority of samples show a similar distribution of moderately-well or moderately sorted sands with a dominant mode around 150-250 μm , with the exception of the fine-grained sediments of the former lake bed (Figure 7.12). Sorting values for the aeolian deposits of the Cady Mountains range from 0.6 phi (moderately-well-sorted) to 2.1 phi (poorly-sorted) and so differ from the well-sorted characteristics which typify aeolian dune crests (Lancaster, 1995). Values of sorting and mean grain size are, however, similar to the sand sheets and sand ramps elsewhere in the Mojave Desert (Lancaster, 1994; Lancaster and Tchakerian, 1996), and are consistent with the incorporation of reworked aeolian sands and silts, lake bed deposits and alluvial fan sediments (each of which differ strongly in their characteristics) and transportation distance (Ahlbrandt, 1979). Where aeolian deposits incorporate other fine- or coarse-grained sediments, a measure of skewness can highlight where deposits have a disproportionately fine-grained or coarse-grained characteristic (Folk and Ward, 1957; Folk, 1974). Skewness values indicate a variability, ranging from strongly coarse skewed (-0.5) to strongly fine skewed (0.8) (Figure 7.13). Plotting the sorting and skewness values distinguishes the fine sediments of the contemporary Mojave River and

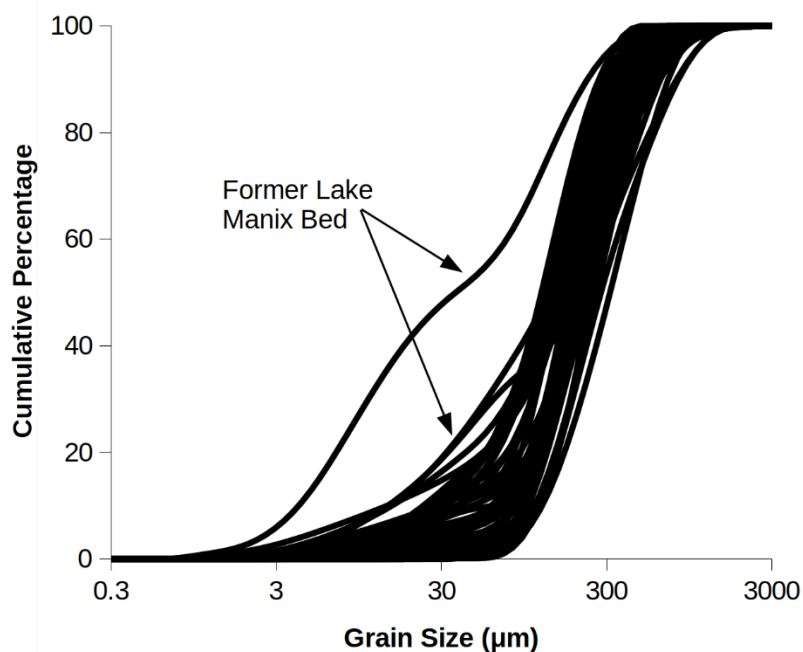


Figure 7.12: Grain size distribution data for the sedimentary units listed above.

MC14 from the majority of the deposits. Within the aeolian deposits there appears to be a spectrum of textural compositions ranging from 0.6-1 phi (e.g. from ER and some CN samples), which are interpreted as aeolian sands, to 1.2-2.2 phi (e.g. several SM units and RD) which contain a greater proportion of coarse-grained material (interpreted as locally-sourced material). The fine-skewed sediments of Unit 4 of SM indicate a tail (rather than a mode) of silts in the 10-63 μ m size fraction, which presumably represents some incorporation of Lake Manix material (Chapter 8).

Although the majority of the sediments are indicative of a significant aeolian-derived component (and are similar to Lancaster, 1994; Lancaster and Tchakerian, 1996), at each of the sites coarse-grained sediments (typically a mixture of gravels, pebbles and occasional cobbles), presumably resulting from fluvial/mass-movement processes, are present. The incorporation of granules and occasionally pebbles into the principally aeolian sediments at ER/PK and the inter-fingering of sands and discontinuous layers of coarse-grained sediment (pebbles to boulders) in the upper portion of CN suggests a closely associated operation of the aeolian and fluvial/hillslope process domains (Wells *et al.*, 2003; Ventra *et al.*, 2017). The relationship between sediment characteristics and process (e.g. a more powerful geomorphic process is required to emplace the ~1m boulders than the frequently observed granules) means that the internal structure of topographically-anchored aeolian deposits relates to the

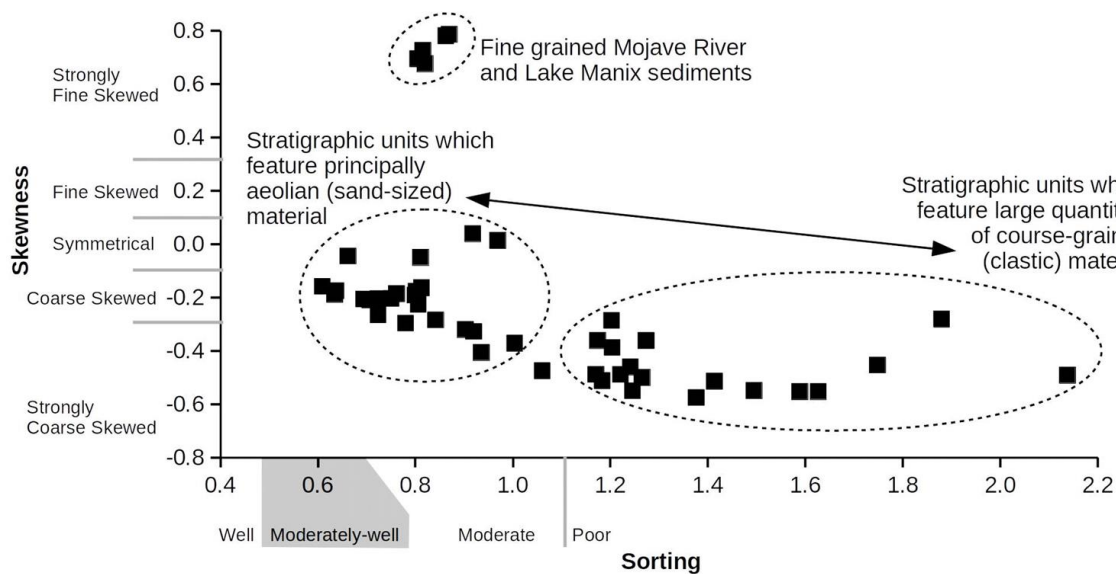


Figure 7.13: Textural characterisation for the sedimentary units described in Section 142. Skewness and sorting parameters after Folk and Ward (1957).

interaction between aeolian and fluvial/hillslope processes which formed the deposit over time (Section 2.2) (Lancaster and Tchakerian, 1996; Bertram, 2003; Bateman *et al.*, 2012).

The internal structure of the sedimentary deposits of the Cady Mountains are shown to be highly variable. For example, CN ranges from units of almost pure (aeolian) sands and silts through to angular clastic material up to the size of >1m boulders (Figure 7.2). By contrast, WC is unstratified and comprises near-homogeneous sands, with occasional granules (Figure 7.11). Different again is the ER site which contains isolated granules and small pebbles through the profile, without stratification (Figure 7.5). At all sites where pebble-sized clasts or larger were present they were typically angular or sub-angular suggesting relative short and/or brief transport distances, presumably from the local hillslopes (Parsons and Abrahams, 2009). Indeed, the site with the roundest clasts, DN, was also the furthest from the mountain front.

Within the field sites of the Cady Mountains three principal arrangements of clasts were observed:

1. Discontinuous layers (often 5-10 clasts thick) associated with lenses of rounded clastic material (Figure 7.15), which were observed within the sediments at CN (Figure 7.2) and PK (Figure 7.7).
2. Individual clasts (ER) or discontinuous stone lines of one or two clast thickness (SM – Figure 7.14)
3. Coarse-grained, angular material within a fine-grained matrix and which varies between clast- and matrix-supported. These were observed at the base of SM (Unit 2 – Figure 7.10).



Figure 7.14: Photograph showing the interior of the landform at Soldier Mountain indicating the location of profile B (Figure 7.10).

Overall, evidence of sedimentology and grain-size characteristics from the Cady Mountains indicate that all sites incorporate non-aeolian material, often within and between the aeolian sands, suggesting contemporaneous operation. High stratigraphic variability was observed both within and between sites, with differences principally relating to the structure and arrangement of clastic material. The mechanisms which are understood to have led to the formation of these arrangements are discussed in Section 8.3.3.

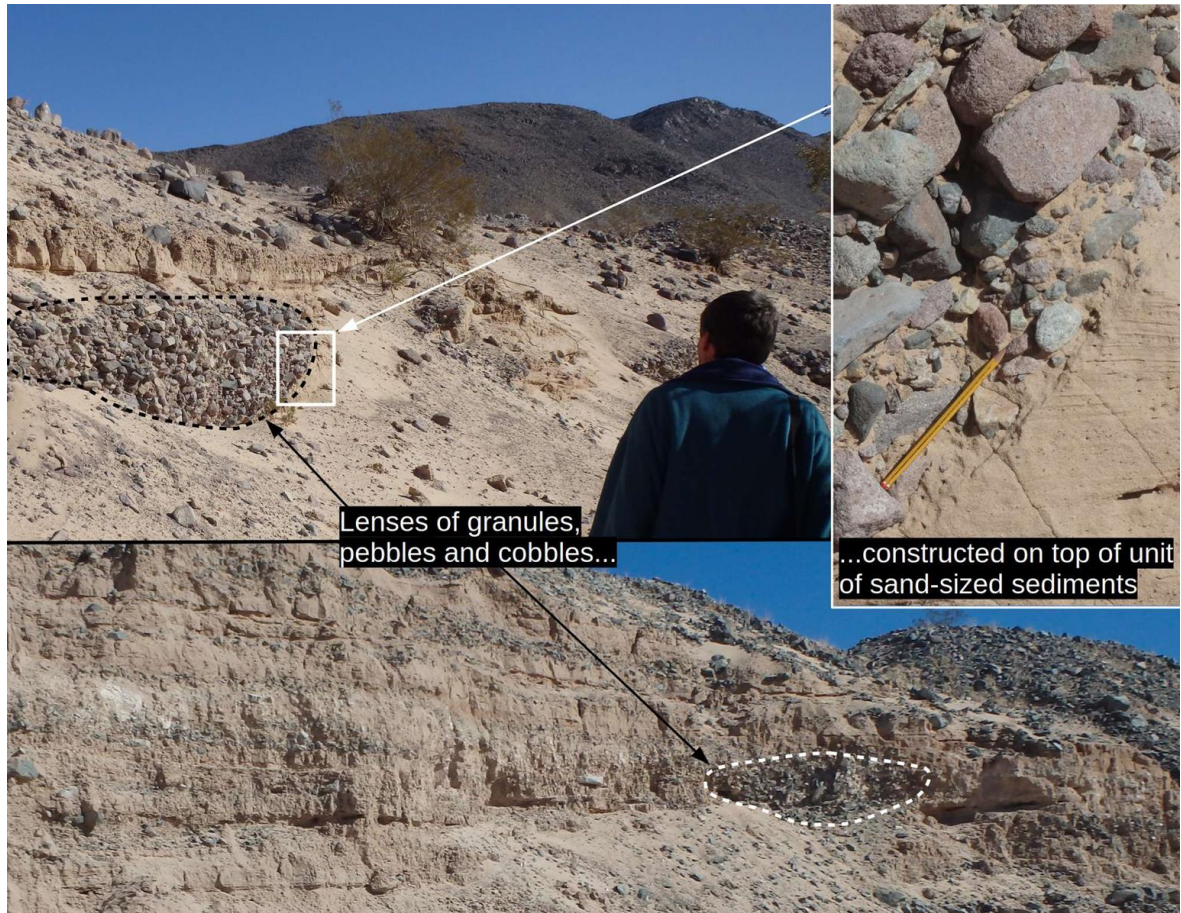


Figure 7.15: Lenses of pebbles, gravel and cobbles observed within the Complex Valley (described in Section 6.2) (upper and inset) and within the CN landform and adjacent (< 50m distance) to the sampled stratigraphy (lower). The lens shown in the upper figure shows evidence of cut-and-fill processes, with what appears to be an unconformity present within the close-up photograph (inset).

7.2 Operation of the aeolian system

The previous section described the stratigraphy and sedimentology of the deposits and also provided a geochronology for nine sites within the Cady Mountains. It was then demonstrated that the landforms developed through the combined operation of the aeolian, fluvial and mass-movement process domains (albeit with variation in their relative influence over time). By collating these data between field sites, Section 7.2 considers how the wider aeolian system has behaved in terms of when it was (in)active, whether this history has a spatio-temporal pattern, what the rate of landform development was and whether the sediments are derived from distinct sources.

7.2.1 Age-based landscape description

Luminescence dating was used to establish a chronology for nine aeolian deposits within the Cady Mountains (Section 4.4 and Chapter 5). Luminescence ages were predominately taken within the layers of sand-sized material, which particle size data suggest are dominated by aeolian sediments (Section 7.1). An overview of the history of aeolian activity is provided in Table 7.2 and on the basis of the available luminescence samples shows that the aeolian system has been operating over the majority of the past >80ka with the exception of two periods at 30ka-11ka and since ~3ka.

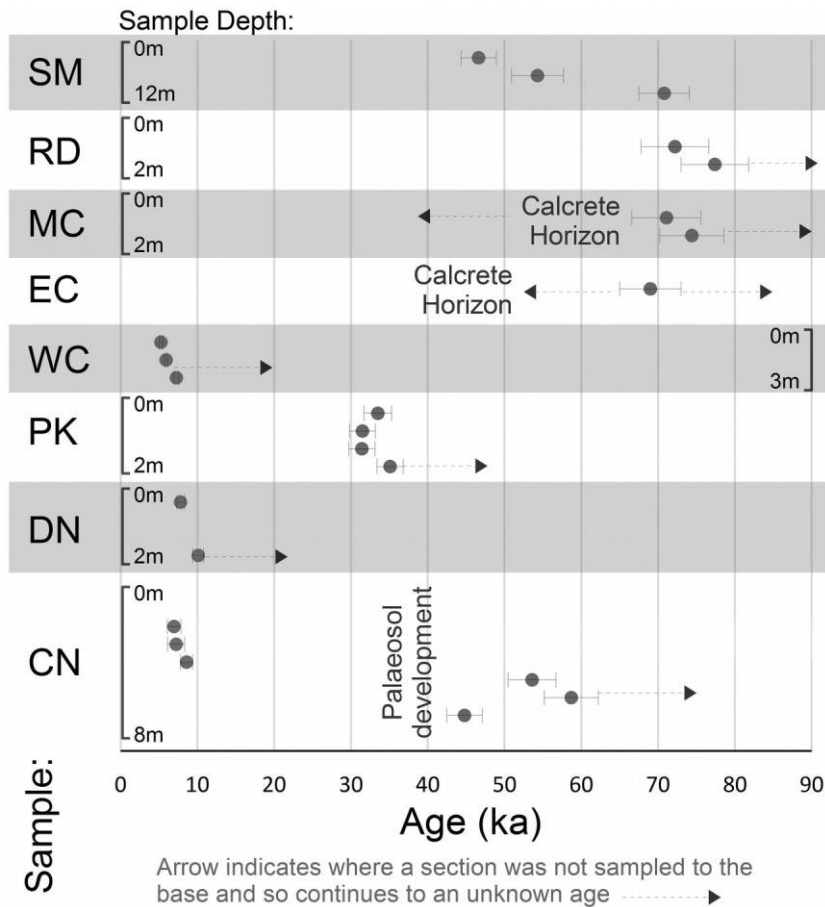


Figure 7.16: Geochronology for the field sites listed in Table 7.1.

Table 7.2: Synthesised history of (in)activity within the aeolian system operating across the Cady Mountains during the last 80ka, based on the evidence presented in Section 7.1.

Age	Description
70-80ka (MIS 5a)	<p>Aeolian activity is recorded at MC and RD between 80ka and 70ka. This was followed by the occurrence of a debris flow at SM before 70ka (undated) as well as the sample taken in the valley at the eastern border of CN (CN-Valley). The palaeosol immediately above the sample implies a period of landscape stability immediately after this time (Figure 7.2). Though no record of activity was established around this time at MC, RD and CN, these landforms were not sampled to their full depth.</p>
60-40ka (MIS 3)	<p>The oldest recorded activity at the main body of CN dates to ~55ka in a unit that is horizontally bedded and contains many calcified root casts (Unit 1). This unit likely represents aeolian accumulation upon a vegetated surface at this site and occurred at a time, within uncertainty, of a similarly bedded aeolian unit within SM (Unit 4). The ages from SM and CN both imply that aeolian activity continued along the northern edge of the mountain block (from ~80ka) until ~40ka. The end of this period is marked by the development of the cross-bedded SM Unit 5 and the partially reddened CN Unit 3.</p> <p>Because the samples at MC and CN-Valley were not taken from the top of the landform it is not known for how long after the youngest age they continued accumulating and so may have been active around this time.</p>
35-30ka (MIS 3)	<p>Aeolian activity is recorded at PK (in the south of the mountain block) between 35ka and 30ka. This site does not sample to the base of the landform and so the initiation date is unknown, though a nearby valley which has eroded into the landform suggests that it may be much thicker (and presumably older).</p>

30-11ka (MIS 2)	None of the sites record activity between 30ka and 11ka. At some point between 45ka and 11ka well developed and laterally continuous palaeosol formed along the northern edge of the mountain block around (and including) CN and CN-Valley.
11-3ka (MIS 1)	CN records activity restarting along the northern edge of the mountain block around 11ka. Over the period from 11ka to 7ka, the landform at CN accumulated as alternating aeolian sands with periodic delivery of coarse-grained (pebble- to boulder-sized) material (Figure 7.2). This activity broadly coincides with aeolian activity in the dune field (DN) around this time.
3ka – present (MIS 1)	Aeolian activity continued at WC until ~3ka. As this did not sample to the base of the landform, initiation date is unknown. Activity is last recorded at ER and RD around 2ka, but these appear to be localised events triggered by fluvial reworking (given the evidence for degradation elsewhere on the landform).

7.2.2 Timings within the aeolian system

Table 7.2 compiles the data presented in Section 7.2 to provide a description of the history of the aeolian system over the past 80ka. However, this record has been created from discrete snapshots of the aeolian system and so the question remains whether this history is broadly continuous or episodic. Luminescence ages, by definition, only sample what has been preserved (Singhvi and Porat, 2008; Chase, 2009; Thomas and Burrough, 2013). Almost all aeolian sedimentary sequences contain breaks in their accumulation history due to the complex nature of their formative processes and subsequent preservation (Singhvi and Porat, 2008; Thomas and Burrough, 2012). It is tempting to interpret records as a series of discrete episodes of activity. However, it has been demonstrated that for linear dunes any apparent patterns drawn from luminescence age distributions can bear a closer relationship to the expected decrease in preservation potential of individual units over time rather than to any “true” episodic accumulation history (Nanson *et al.*, 1992; Telfer and Thomas, 2007; Stone and Thomas, 2008; Hesse, 2014). Given that linear dunes are an accumulating (rather than migrating) free dune form, it is possible that a similar conclusion may also apply for

topographically-anchored dune archives – certainly, caution is appropriate. This being the case, the history of aeolian activity across the mountain block over the last 80ka is proposed to be best divided into four periods. Two of these periods imply significant aeolian activity within the mountain block (>80-30ka and 11ka-3ka) and two represent periods of (relative) geomorphic stability (30-11ka and 3ka-present) (Figure 7.16). The lack of recent luminescence dates suggests a present inactivity of the aeolian system within the Cady Mountains, which is most visibly justified through the minimal contemporary sand accumulation within the Soldier Mountain Quarry (as noted by Lancaster and Tchakerian, 1996; Bateman *et al.*, 2012), although geomorphologically significant events have been observed within the wider Mojave Desert (e.g. Clarke and Rendell, 1998).

Relative stability within a geomorphic system is expected when aeolian, fluvial and hillslope processes are negligible in their influence and, in arid areas, this is often interpreted as more humid periods (Fitzsimmons *et al.*, 2009). During the break in aeolian activity at CN between 45ka and 11ka a well-developed palaeosol formed along the northern edge of the mountain block (notably around CN) which can be traced for some distance. Further pedogenic carbonate development (nodules and rhizoloths), implying surface vegetation cover, is present throughout SM, within one unit at PK and as the carbonate layer in MC. Such evidence is absent in the upper half of CN and at other sites. Reddening is present as continuous layers in CN and MC, as reddened veins at RD and was observed above CN-Valley. Though such development is within the older sections (>30ka), these periods are not necessarily synchronous and may represent a hiatus of only a few hundred years (as Reheis *et al.*, 2015). Mineral magnetic analysis conducted by Bateman *et al.* (2012) suggested that no palaeosol development or hiatus was recorded within SM. However, the reddening and carbonate development at CN are much more pronounced and more extensive than that observed at SM (Bateman *et al.*, 2012). Additionally, the timing of its development broadly matches numerous periods of soil development associated with Lake Manix (40 and 35ka – Reheis *et al.*, 2012; Reheis *et al.*, 2015). Consequently, it is therefore probable that this event was significant across the northern portion of the mountain block and possibly the wider Manix Basin and represents a genuine hiatus in accumulation during the period.

In summary, the record presented here indicates that the aeolian system of the Cady Mountains has been active for the majority of the last 80ka, indeed the “default” state appears

to be of activity somewhere in the mountain block with the exception of a period of stability sometime between 30 ka and 11 ka.

7.2.3 Sediment provenance

The geochemistry of the sediment samples used for deriving luminescence ages does not show clear distinctions in sediment provenance between field sites (Figure 7.17). The ratio of K-Feldspar to Plagioclase for the Cady Mountains is typical for granites or granodiorites and is broadly similar to the sediments of the Kelso Dunes and the Cadiz, Danby and Dale Lake sand sheets to the south (which are also principally sourced from granitic parent material) and unlike the Parker Dunes (principally sourced from the Colorado River) (Muhs *et al.*, 2003; Pease and Tchakerian, 2003; Muhs *et al.*, 2017) (Figure 7.18). Ratios of K/Rb and K/Ba (which represent variability in K-Feldspar composition) show significant overlap between the sediments of the Cady Mountains and contemporary Mojave River, with the fan alluvium of the Providence and Granite Mountains, but not the Kelso Dunes (Figure 7.17).

In summary, geochemical evidence does not suggest that sediments of different provenance can be distinguished across the Cady Mountains (and prospective source areas). The variability is likely to be a function of the variability of source rock types, the mixing of local and distal (principally aeolian) sources of sediments, the recycling of sediments over time

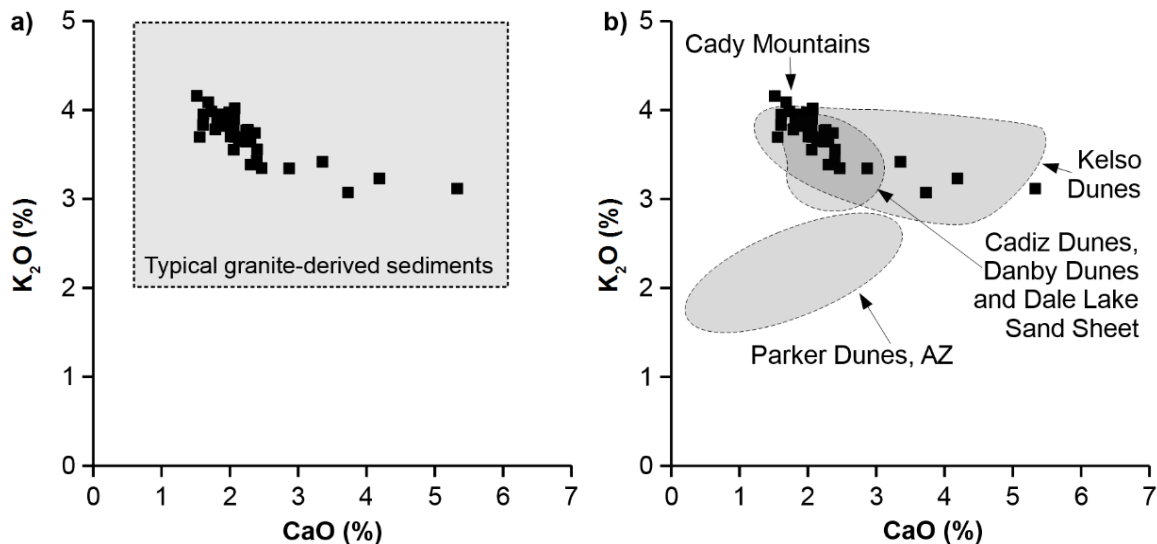


Figure 7.17: The ratio of K₂O (representing K-Feldspar concentration) and CaO (representing Plagioclase feldspar) for Cady Mountain samples (squares). The typical range for granite or granodiorite sediments is plotted in a) and the range of distributions reported by Muhs *et al.* (2003) and Muhs *et al.* (2017) for comparable deposits are shown as dashed shapes in b).

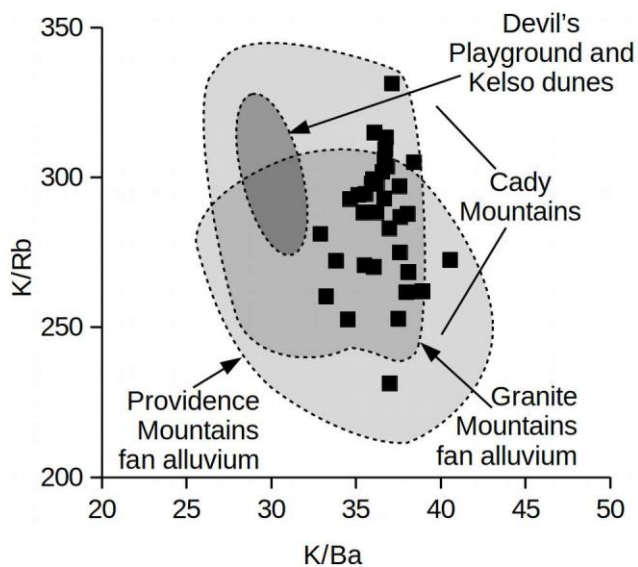


Figure 7.18: Ratios of K/Rb and K/Ba (which represent variability in K-Feldspar composition) for the sedimentary deposits of the Cady Mountains (squares) are shown against the ranges for comparable sediments from Muhs *et al.* (2003) and Muhs *et al.* (2017) (shaded shapes).

and the impact of variable grain-size characteristics between samples (Ramsey *et al.*, 1999; Pease and Tchakerian, 2003; Sweeney *et al.*, 2013)

7.3 Process history of the Cady Mountains

This chapter has outlined the process history of aeolian deposition and landform development in the Cady Mountains. Section 7.1 described the stratigraphy and geochronology at each sampled section, noting that each site comprised a composite structure of sands and coarse-grained (presumably non-aeolian) sediments. Section 7.2 demonstrated that the aeolian system has been operating across the majority of the last 80ka, except for a principal period of shutdown at 30-11ka. Within the Cady Mountains, there is no evidence to indicate that the system operated as discrete sub-systems in terms of any spatio-temporal pattern of aeolian activity or sediment provenance. This aeolian history is punctuated by event-based fluvial/hillslope input, but landforms differ in the proportion and arrangements of coarse sediment within landforms (as three principal arrangement types) even locally. Chapter 8 will use this process history to tease apart the relationship between complex topography and aeolian landform development within the Cady Mountains, by identifying this effect within the history of boundary conditions (especially the variable climatic history) outlined in Chapter 3.

8 Discussion

The purpose of this study was to develop an understanding of how complex mountainous topography influences aeolian deposition, and landform development and preservation. To achieve this, this study has established that topographic control over the distribution and form of aeolian deposits is manifest as characteristic morphologies associated with different accommodation spaces. Within these landforms both the aeolian system and local hillslope processes have influenced/contributed to landform development and preservation.

To this end, this chapter describes the relationship between the distribution and form of aeolian deposits and topography in the Cady Mountains (Section 8.1), infers the drivers for sediment deposition and landform development (Section 8.2), unpicks the influence of complex topography on aeolian deposition and landform development (Section 8.3) and outlines the broader contribution of this study to academic discourse (Section 8.4).

8.1 The relationship between the distribution and form of aeolian deposits and topography

This section discusses how the distribution and form of aeolian deposits is related to the topography of the Cady Mountains. Aeolian deposition has formed a broadly continuous cover across the western portion of the mountain block, which can be subdivided based upon three accommodation space types, each with a characteristic morphology.

8.1.1 Distribution

In Section 6.1 the aeolian deposits of the Cady Mountains were mapped and their distribution and surface form was characterised. Within the mountain block the sand clusters disproportionately to the north and west, forming a broadly continuous cover in these areas. This clustering of sand across the mountain block is typical of the Mojave Desert where much of the sand is concentrated into large aeolian systems (e.g. the “corridors” from Zimelman *et al.*, 1995). Between these areas, much of the region has little sand cover and the piedmont surface is typically of pediment (e.g. Cima Dome and Lucerne Valley) or alluvial fan morphology (e.g. Death Valley). Observed aeolian deposits within the Cady Mountains vary in their thickness, from the thickest deposit being observed where a >15m deep incision was cut into the wedge of accumulated sediments (PK – Figure 6.22) through to areas where the

sand was merely a superficial covering (<50cm) on the bedrock topography (e.g. where WC grades into the hillslopes).

Within the broadly continuous cover of sediments, the form and distribution of the aeolian deposits is related to the elevation, aspect, slope angle and morphometric shape of the topography. Both the Sand Cover and Stone-Covered Sand classes are disproportionately present on or as broad plains or low angled planar slopes. This suggests that a significant proportion of aeolian and fluvial processes have created piedmont landforms in and around the larger topographic obstacles of the mountain block and which tend to have slope angles in the order of two to five degrees (e.g. alluvial fans or sand ramps). That aeolian deposits are preferentially present on/as slopes of a particular aspect and valleys of a particular orientation fits with the previous studies of sand ramp (clusters) which have noted that many features have a common orientation, being frequently aligned with a prominent sand-transporting wind direction (e.g. Zimelman *et al.*, 1995; Lancaster and Tchakerian, 1996; Chojnacki *et al.*, 2010; Ventra *et al.*, 2017; Rowell *et al.*, in press). The implications of the relationship between aeolian deposits and valleys are more nuanced. Sand-filled valleys are disproportionately of a south-westerly to north-westerly orientation, despite the majority of valleys within the mountain block being south- and east-facing (Section 6.1). This difference reflects the existence of a number of large valleys on the north and western boundary of the mountain block which face the contemporary Mojave River and former Lake Manix bed (and their significant potential sediment supply – Chapter 3.3.2) whereas the valleys that are northeast- through southerly-orientated are much less sandy, reflecting the reduced sand cover present at areas around Broadwell Lake generally (Figure 6.11). These observations are symptomatic of how the relationship between the distribution and form of aeolian deposits is manifest as deposits which occur in one of three landscape positions, each of which represent one of three accommodation space types: Plain, Mountain Front and Valley.

8.1.2 Morphology of aeolian deposits within accommodation spaces

The relationship between the distribution and form of aeolian deposits within the Cady Mountains can be conceptualised through three types of accommodation spaces (Section 6.1.4). Accommodation spaces exist as a zone where the interaction of the wind flow and the bedrock topography promotes aeolian deposition (and preservation), with their size relating to the size of the topography (Section 2.1.1). The different accommodation space types are

manifest through characteristic morphologies at the meso-scale. Section 6.2 highlighted that, due to a combination of unambiguous boundaries (e.g. landforms grading into each other) and the close association of the different accommodation space types within the landscape, the aeolian deposits which form within these accommodation spaces will not necessarily create a patchwork of discrete landforms. In this respect the Mountain Front landforms SM (Figure 6.20) and ER (Figure 6.21) are unusual in the landscape for being so well-defined. Across the majority of the Cady Mountains the aeolian deposits form a broadly continuous cover wherein individual landforms grade into one another with no unambiguous boundary to separate those within different accommodation spaces. Plains serve as a good example as they were observed to grade gradually into their surroundings, hence those identified in Section 6.2 were defined through a combination of (a gradual) land cover change and (arbitrary) slope thresholds. Areas where multiple accommodation spaces (of differing types) were present in close proximity were difficult to define because these deposits coalesce, for example into the continuous surface of CN which exists as a planar slope against a topographic obstacle but which is continuous and fills the multiple valleys within the topography which bounds it. In this respect, CN may be thought of as similar to the "sand ramp complexes" (their term) which were described as occurring where the sand had accumulated against and around a complex inselberg by Bertram (2003). As a further example, Ellwein *et al.* (2015) identified climbing and falling dunes which formed in an accommodation space owing to a trapping effect and which were observed to merge into a single feature which was more akin to valley-fill than to discrete climbing and falling landforms.

8.2 Landscape history for the Cady Mountains

None of the landforms discussed by this study are purely aeolian in their composition, with each containing some evidence of hillslope processes (Section 7.1.4). By combining this composite history with timings (provided using luminescence dating), a landscape history for the Cady Mountains can be used to understand how the record of landform development fits with the boundary conditions for the system. To this end, this section outlines the revised landscape history for aeolian activity within the Cady Mountains which highlights how the episodic aeolian history is punctuated by local event-based hillslope deposition.

8.2.1 Updated history of aeolian activity in the region

In the Mojave Desert, past work regarding the timings of aeolian activity has been dominated by the inferred association between the accumulation of the Mojave Desert sand ramps and the Kelso Dunes commonly linking the dune field with a sudden increase in sediment supply after the cutting of Afton Canyon. This sediment was deflated from shoreline, fan-delta and lacustrine sediments within the Soda Lake Basin and the Mojave River Fan after Afton Canyon was cut (~25ka), particularly during intermittent Lake Mojave I and after Lake Mojave desiccated ~8ka (e.g. Lancaster and Tchakerian, 1996; Rendell and Sheffer, 1996; Clarke and Rendell, 1998; Kocurek and Lancaster, 1999; Bateman *et al.*, 2012). The significantly revised history of aeolian activity within the Cady Mountains presented in Chapter 7 indicates that the periods of aeolian activity which followed the draining of Lake Manix were merely a part of a much longer running system, with aeolian activity occurring across the majority of the past ~80ka, except for a principal period of shutdown at 30-11ka. Within the Cady Mountains, the system does not appear to have operated as discrete sub-systems in terms of any spatio-temporal pattern of aeolian activity or sediment provenance. The timing of aeolian activity within the Cady Mountains corresponds with two of three episodes reported (50-36ka, 36-25ka and <14.5ka) within a recent luminescence-derived record of aeolian (sand-sized sediment) accumulation within a desert pavement archive near to the Kelso Dunes (Dietze *et al.*, 2016). The latter period correlates with the reported construction of the widespread aeolian sediments which inter-finger fan complexes at Soda Mountain (adjacent to Silver Lake) and Providence Mountains which developed within the Late Pleistocene-Holocene (LPH) transition between ~14 cal kyr BP and 8 cal kyr BP (recalibrated radiocarbon dates – Wells *et al.*, 1987; McDonald *et al.*, 2003). Similarly, Mahan *et al.* (2007) identified aeolian activity within the Silurian Valley, north of Silver Lake, which spans >52ka to 3.2ka and includes aeolian accumulation within the fan sediments of the LPH transition around ~12ka.

Between ~30ka and ~11ka there is no evidence of aeolian activity within the mountain block, this period spans both the Last Glacial Maximum and Last Precipitation Maximum when Lake Manix reached its most recent high stand (Reheis *et al.*, 2012; Maher *et al.*, 2014). Furthermore the existence of soil and carbonate development from within the CN and EC field sites indicates that a notable hiatus in geomorphic activity occurred (at least along the

northern border of the mountain block) at some point within this period, presumably when the lake was at high stand. Aeolian activity within the landforms of the Cady Mountains is punctuated by event-based fluvial/hillslope input, but landforms differ in the proportion and arrangement of coarse sediment within landforms (as three principal arrangement types) even locally.

8.2.2 Drivers for aeolian deposition and preservation

No aeolian system operates in isolation, as its timings relate to the frequently non-linear interplay of the various drivers which control activity within the system (Lancaster, 2013). This section will describe the interpreted drivers for the emplacement of aeolian and coarse-grained sediments within the Cady Mountains.

Context and drivers for periods of aeolian (in)activity

Aeolian activity occurred at the field sites across the majority of the past ~80ka, with the exception of between 30ka and 11ka and under present conditions. Timings of aeolian activity have been interpreted as episodes which represent periods of greater regional aridity, with any gaps, soils or stone lines within the stratigraphy representing periods of greater humidity (e.g. Nanson *et al.*, 1992; Rendell and Sheffer, 1996; Stokes *et al.*, 1997; Fitzsimmons *et al.*, 2007; Telfer *et al.*, 2012) and often increased fluvial activity (e.g. Telfer *et al.*, 2014; Kumar *et al.*, 2017). However, the association between phases of aeolian activity and regional aridity and the notion that climate-driven switching drives episodes of aeolian or fluvial/colluvial process dominance has begun to be questioned (e.g. Stone and Thomas, 2008; Telfer and Hesse, 2013; Hesse, 2014). Indeed, the widespread mixing/inter-fingering of aeolian and non-aeolian sediments within the same stratigraphic units across the Cady Mountains suggests that processes are occurring within a single geomorphic period and thus that no large switching of states is operating (as concluded by Ventra *et al.*, 2017). Such a system would imply that a more direct control than climate is required to explain the timings of aeolian accumulation within the Cady Mountains.

Luminescence ages indicate that the aeolian system of the Cady Mountains has been active for the majority of the last >80ka, having been relatively inactive between 30ka and 11ka as well as since ~3ka. The former period of inactivity correlates with reddening and soil development around CN, suggesting that the observed gap in the OSL record represents a genuine hiatus in activity during this period (for at least some of the time and at least along

the northern edge of the mountain block). No spatio-temporal pattern of aeolian (in)activity across the mountain block was evident and nor could any discrimination of sediment provenance be confidently made, suggesting that the aeolian system should be considered as a coherent system (rather than multiple distinct systems).

Supply and availability of sand-sized sediments

Significant volumes of pre-sorted, sand-sized sediment have been delivered to the Manix Basin across much of the last 100ka (Chapter 3). Lake Manix has received Mojave River waters for much of this period and the lake level fluctuated from wetland to moderate lake conditions between 80-30ka in phase with periods of greater/lesser river flow (peaks of 90-82ka, 65-55ka, ~45ka, ~35ka and 24-22ka (Robert, 2004; Cyr *et al.*, 2015)) and the avulsion of the lake into the Harper Basin at ~30ka (Section 5.3.2) (Reheis *et al.*, 2012; Reheis *et al.*, 2015). This broadly continuous delivery of sediment suggests that the aeolian system was availability-limited rather than supply-limited during this period. Sediment availability will have varied as the lake level fluctuated within the basin, exposing shoreline and lake bed sediment in the Manix Basin as well as the sediments of the Manix Fan-Delta (Section 3.3.2). The semi-independence of the Manix sub-basins (especially Troy, being adjacent to both the Fan-Delta and the Cady Mountains) is an important constraint on sediment availability (Meek, 1999; Dudash, 2006).

Whilst the Manix Basin contained a perennial lake (before ~25ka), it is expected that even modest lake level fluctuations (~20m – Reheis *et al.*, 2015) exposed sediments previously supplied to the system, making it available for deflation. Such a process is analogous to: (1) the rapid availability of geomorphically significant quantities of sediment from deltaic areas adjacent to the Aral Sea which formed rapidly migrating barchan dunes (Saiko and Zonn, 2000; Issanova *et al.*, 2015); (2) the combination of climate change and the fluctuating Mediterranean sea level led at 35-13ka to changes in sediment supply and availability within coarse-grained alluvial plains with the Nile Delta and which formed a significant sediment source for the Sanai Desert (Stanley and Warne, 1993; Muhs *et al.*, 2013); and (3) the peak of aeolian accumulation during the last glacial in the Black Mesa Region, Colorado, which was driven by the (short-term) availability of sediments deposited by the Little Colorado River onto a floodplain comprising wide, braided channels (Ellwein *et al.*, 2015) (see Section 2.2.2). These examples highlight the role of pre-sorted fluvial sediments for aeolian systems,

whereby even seasonally dry distributary channels (or lake fluctuations) can promote sediment availability.

After Lake Manix desiccated, the whole basin would have become available for deflation. Coupled with this, sediment availability increased out of the LGM as vegetation cover decreased around ~11.5ka (Koehler *et al.*, 2005), coinciding with the re-starting of aeolian activity and landform construction at CN by 9 ± 0.9 ka. After the Mojave River switched to an ephemeral flow regime, periods of sediment availability immediately followed river-flow events (as Clarke and Rendell, 1998; Kocurek and Lancaster, 1999), as was observed for the construction of the Kelso Dunes by Muhs *et al.* (2017) and Sweeney *et al.* (2013).

Stacking of aeolian units

Landform development need not operate as a single phase. At CN the record is split, with two phases of development being separated by evidence of a hiatus along the northern edge of the mountain block at some time between 45ka and 15ka. CN is also interesting as the upper portion of the ramp is highly stratified and includes large volumes of clastic material (discussed below), which highlights the wider observation that there is no clear relationship between accumulation rate and the properties of sedimentary features (e.g. older ramps do not typically contain more units or stone lines) within the aeolian accumulations of the Cady Mountains, as was noted by Rowell *et al.* (in press) for 75 Namibian sand ramps. Other reported ramps have accumulated episodically. The 18m section of sand ramp described by Kumar *et al.* (2017) in Ladakh, northwest India, started accumulating at ~44ka, but principally developed in two phases around 25-17ka and 12-8ka.

Timings of coarse-grained sediment emplacement

The landforms of the Cady Mountains are principally formed of aeolian sediments but are punctuated by coarse-grained material which is inferred to be locally-derived. The proportion and arrangement of stones varies both within and between landforms, with little evidence of discrete aeolian and fluvial/colluvial layers (as Bertram, 2003). Rather, the sediments inter-finger suggesting that the composite stratigraphy formed as the processes operated simultaneously (with some relative balance of influence) (Ventra *et al.*, 2017), creating layers of varying thicknesses which contain sediments from multiple sources (both proximal and distal) (Bertram, 2003; Pease and Tchakerian, 2003). This raises the question regarding the mechanisms (and their drivers) for the emplacement of these stone lines.

The upper portion of CN is interesting because it contains significant (5-15 stones thick) layers of coarse-grained sediment which were deposited at 10-8ka. This period is coincident with unit Qf3 adjacent to Silver Lake (9.3-5.2ka – Harvey and Wells, 2003) which represented the end of a period of widespread fan aggradation across the SW USA following the LPH transition (Miller *et al.*, 2010; Antinao and McDonald, 2013; Antinao *et al.*, 2016). A mechanism analogous to that of alluvial fan aggradation from the feeder valleys at CN would be capable of depositing the quantities of sediment observed both within and upon CN. Across the Mojave periods of fan aggradation have been linked to the interplay of precipitation, temperature and vegetation variation over Milankovitch and sub-Milankovitch timescales (Miller *et al.*, 2010). However, it remains fundamentally uncertain what mechanism(s) explain the observed distribution of fan activity across the SW USA, as chronological data imply that they formed during cool, warm and transition periods (Reheis and Throckmorton, 1993; Dühnforth *et al.*, 2007; Miller *et al.*, 2010; Owen *et al.*, 2014; Dühnforth *et al.*, 2017). Though vegetation change has been cited as a driver of fan aggradation (Bull, 1991), McDonald *et al.* (2003) argued that the Late Pleistocene - Holocene Transition pulse of fan aggradation pre-dated changes in vegetation within the Mojave Desert. Furthermore, Miller *et al.* (2010) argued that storm seasonality was key to determining the impact of an event on the history of fan aggradation with cool-season frontal storms tending to degrade fans/ramps and redistribute sediments down-fan, whereas warm-season monsoonal storms tend to lead to aggradation on ramp surfaces (as Antinao and McDonald, 2013). Fan aggradation in Baja California and the Mojave Desert has also been linked to peaks in summer insolation (Robert, 2004), and hence warm-season monsoonal storms, which were observed through episodes of streamflow and fan aggradation around 65ka and 35ka as well as during the LPH transition (e.g. Antinao and McDonald, 2013; Gray *et al.*, 2014; Owen *et al.*, 2014; Antinao *et al.*, 2016). Based on this, it is expected that the flow-events recorded by Robert (2004) should correlate with timings of fan aggradation (and stone line development) within the Cady Mountains. The ~65ka event post-dates the last recorded activity at MC, RD and EC, as well as the debris flow recorded at the base of SM (~70ka). The PK site records channelised fluvial activity which was deposited coincidentally with ~35ka event described by Robert (2004).

The emplacement of clastic material is not disconnected from climatic history. Rather, the relationship between periods of aeolian activity and climate is more nuanced than a simple switching between aeolian activity during arid periods and fluvial/hillslope activity during fluvial periods.

8.3 The influence of complex topography on aeolian deposition and landform development

Systems of aeolian sediment transport in drylands can be conceptualised using the notion of an ‘integrated pathway of sediments’ which forms a source-to-sink conceptual model of how aeolian systems are manifest in the landscape. In the Mojave Desert this has been related to aeolian transport corridors which occur where sand is transported through basins (Zimbelman *et al.*, 1995), however the aeolian system operating across the Cady Mountains differs in that the transportation of sand is interrupted, and effectively trapped, by the topography of the mountain block. This aeolian system differs from the aeolian transport corridors described by Zimbelman *et al.* (1995) and Clarke and Rendell (1998) in that the topography protrudes into the aeolian system, trapping sediments and forming deposits which coalesce into aprons. Sand was disproportionately observed to the north-westerly side of the mountain block as well as on west-facing (and north-facing by the Manix bed) slopes, i.e. those adjacent to and facing the former Lake Manix Fan-Delta and lake bed. Because there is no indication from sediment provenance data that the Cady Mountains contains multiple aeolian systems which feature sediments from distinct sources, it is proposed that the Cady Mountains fall within a single aeolian transport system (Section 7.2.3). Furthermore, the dominant westerly wind regime (Section 3.2.3) means that the Manix Basin (especially the coarse-grained sediments of the Fan-Delta and shorelines – Section 3.3) is a likely candidate for the principal source areas for the aeolian system. Given enough sediment and time, the aeolian sediments will eventually reach the Broadwell Playa (and perhaps as far as Kelso Dunes), however the lack of aeolian sediments within the eastern slopes of the Cady Mountains suggests that the aeolian system is effectively halted by the complex topography.

The morphology and distribution of aeolian deposits are closely associated with the topography of the mountain block, and this relationship is observed across both the mountain block scale and meso-scales (see below). The aeolian deposits of the mountain block

represent the net-effect of aeolian deposition and landform development as well as the variability in climate and wind regime of the Cady Mountains described in Chapter 3. From this record, the influence of the complex topography needs to be unpicked. That is the purpose of this section.

8.3.1 Role of accommodation spaces

As aeolian sands are transported across the mountain block the topography influences wind flow patterns, trapping sediment within available accommodation spaces (see Section 2.1.1). Sediment deposition and accumulation can themselves modify the wind flow until a depositional surface with an ‘equilibrium slope’ results – when the accommodation space is filled (Pye, 1994; Lancaster and Tchakerian, 1996). As sands progress westwards across the mountain block, it would be expected that sands would fill each accommodation space in turn, creating a spatio-temporal pattern of sediment accumulation. However no spatio-temporal pattern of sediment accumulation was observed within the Cady Mountains (Section 7.2). This is interpreted as a function of both the study only presenting a record of aeolian activity across nine (fairly clustered) sites within the mountain block and because the complex topography allows sand to be moved more easily in some areas compared with others. For example, the strong topographic differences between the area round Soldier Mountain and that in the broad plain within which sits Valley Center Road would result in sand progressing much faster within the latter when compared with the former, thus resulting in a potentially complex spatio-temporal pattern.

8.3.2 Morphology of landforms

Based upon the field evidence of the aeolian deposits of the Cady Mountains (form and materials), a better understanding has been gained about both the morphology and formative process. This can, help to in turn, develop the classification of accommodation space morphologies. The three types of landforms best represent: sand ramps, sand sheets and valley-fill sediments (Figure 8.1).

Sand ramps

Aeolian deposits which accumulate against topographic obstacles are morphologically indicative of topographic dunes. However, the mountain front features described in the Cady Mountains are notable by their composite structure which includes a range of particle sizes including sands, gravels and boulders. This composite structure, a sand ramp morphology,

results from the accumulation (and degradation) of fluvial, aeolian and sediment gravity deposits over time (Tchakerian, 1989; Bertram, 2003; Lancaster and Tchakerian, 2003). Sand ramps sit along a continuum of morphologies with end-members of topographic dunes and fans (Lancaster and Tchakerian, 1996), with their drivers reflecting the interplay of aeolian, fluvial and sediment gravity processes (hence the association with periods of alluvial fan development described above).

Sand sheets

Aeolian deposits which have accumulated as broad plains, were observed to be commonly unbedded and largely without bedforms (with exception of DN). These characteristics are typical of sand sheets (Kocurek and Nielson, 1986; Warren, 2013), though in all cases coarse-grained material was incorporated into the stratigraphy as either stone lines or isolated clasts.

Valley-fill sediments

Sediments form valley-fills, with their compositions varying from those almost devoid of clasts (WC) to the stone-filled (Valley Complex).

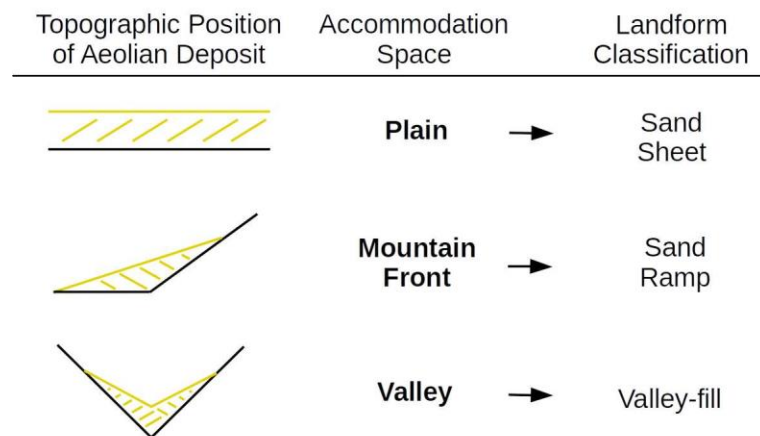


Figure 8.1: Landform classification based upon the three accommodation spaces types from Section 6.2.

Interpretation

This interpretation of the landscape into sand sheets, sand ramps and valley-fills mirrors Ellwein *et al.* (2015) where they noted that “deposits in similar landscape positions” (interpreted to distinguish topographic dunes from sand sheets) share similar geomorphic histories. Within this classification it is observed that, where accommodation spaces are

simple in shape, occur in isolation and under a constant wind regime, then a simple delimitable landform can develop. However, the relationship is more nuanced where topography is more complex owing to the interference of wind flow patterns, the overprinting of deposits and the coalescence of morphologies where accommodation spaces occur in close proximity.

As an example of this, SM is very well-defined within its semi-circular embayment which is the first topographic obstacle the sand has reached after travelling across the Manix Basin. ER is also well-defined against large topography, but these examples are unusual within the landscape of the Cady Mountains. Similarly, many well-defined sand ramps were described as occurring against inselbergs, such as the Namibian sand ramps described by Bertram (2003) and Rowell *et al.* (in press). However, across the majority of the Cady Mountains, the points of flow separation and flow interference which this creates (Xiao *et al.*, 2014), coupled with the close association of different accommodation spaces and space types within the landscape (Section 6.2), leads to landforms which are poorly defined because they coalesce (as observed by Ellwein *et al.*, 2015). Where enough accommodation spaces have filled then the broadly continuous (yet morphologically variable) sand cover observed in the Cady Mountains can result (as was described for a lower relief environment by Telfer *et al.*, 2014). These observations would imply that the deposits have developed through a space-filling process whereby sand accumulated within topographic lows (accommodation spaces) until they are “full”, masking much of the smaller-scale topography in the process (or even the large topography of PK – Figure 6.22). The larger bedrock topography rises above the aeolian deposits as mountain peaks and prominent ridges or, where aeolian sediments are present, they form a thin covering which wraps around the large-scale topography (as was typically observed at higher elevations – Figure 6.6). Areas of Rock Surfaces present upon smaller topographic obstacles and within passes (for example upon the smaller mountains of the Western Front and the undulations present along Valley Center Road) were heavily ventifacted as sand saltated across their surface (Figure 6.24) (Laity, 1992).

8.3.3 Hillslope sediment

Understandings of sand ramp construction dynamics have recognised the interplay between the processes of aeolian construction and the processes of stone line development over time. This interplay has been interpreted as reflecting either a shift between periods of time of

aeolian activity (more arid periods and of geomorphic stability and talus accumulations – Lancaster and Tchakerian, 1996; Kumar *et al.*, 2017) or where the stone lines represent short-term geomorphic events within a wider aeolian history (Bertram, 2003; Bateman *et al.*, 2012; Ventra *et al.*, 2017). The record of fluvial/hillslope activity within the Cady Mountains is variable in the proportions and the arrangement of locally-derived sediments present within the observed landforms (Section 7.1.4). The inter-fingering of aeolian and fluvial/hillslope sediments within the same sedimentary units (e.g. CN) suggest that these processes operated contemporaneously. Furthermore, the timings and arrangements of hillslope sediments within the mountain block suggest that this is locally determined rather than showing a common history of stone line development.

Additionally, Rowell *et al.* (in press) suggested that accommodation spaces have a control on overland flow which should, in turn, influence sediment delivery to the topographically-controlled aeolian deposits. Some association here is observed. Landforms situated either towards the valley toe (Valley Complex – Figure 7.15) or at the outlet of multiple valley-bounded channels (CN) were observed to feature lenses of fluvially-derived sediments and a greater proportion of large-clastic material in their stratigraphy than the deposit at the head of a valley (WC), perhaps suggesting that the size of the fluvial system’s catchment for stones may be a control over this. Similarly, at SM, where the stone lines were often only one-clast thick, there was only a small catchment for coarse-grained sediments (Figure 7.14). The limited size of the dataset here means that this requires further investigation before any conclusions can be drawn.

8.3.4 Landform persistence / preservation

Wind tunnel studies would suggest that (e.g. Tsoar, 1983; Howard, 1985; Xianwan *et al.*, 1999), if the wind regime is constant, once sediments have been deposited within accommodation spaces any subsequent sand simply climbs up and passes over the accumulation (as Zimbelman *et al.*, 1995). However, in the real world, once sediments have been deposited within accommodation spaces their preservation is variable, effectively relating to pseudo-random/stochastic fluvial/hillslope events which degrade the landforms (Telfer and Hesse, 2013). Luminescence dating indicates that the persistence of the aeolian deposits can be significant. The sand ramp at Soldier Mountain shows a long persistence, with no evidence for a significant modification of the sand ramp for >45ka. The CN field site

shows a more complex history with the lower portion having been preserved for >45ka and the upper portion having accumulated upon it before itself being preserved for ~10ka. By contrast RD shows valley-fill sediments which have been preserved for ~70ka at the base, although the younger upper unit (~2ka) is suggestive of degradation/reworking of the sediments within this valley, especially due to the adjacent valleys along the Western Front featuring sand accumulation to a greater elevation. Over the timescales of interest here, sediments have been deposited and preserved for >80ka, which is enough to be effectively permanent.

The preservation of a landform is associated with its local topography and hence the accommodation space. Rowell *et al.* (in press) described how the distributions of sand within a Namibian field site could be related to accommodation space characteristics such as topographic shape and potential for overland flow generation because significant fluvial activity can inhibit accumulation/preservation of aeolian sediments. Where fluvial activity can generate sufficient power it can also erode existing sediments, as observed at the cut and fill sequence shown in Figure 7.15. Accordingly, CN contains the largest volumes of clastic material (both within and upon the landform) and sits at the outflow of a number of fluvial systems. By contrast SM and WC contain much less hillslope sediment and are within a small embayment and a small valley respectively – and so will not experience such significant fluvial activity. Such observations suggest that the degradation of the geomorphic record is highly localised in its impact, depending on event-based phenomena and (for example) the routing of fluvial channels.

The presence of stones on the surface of an aeolian accumulation (e.g. SM and CN) will likely hinder the erosion of the aeolian sediments beneath (by either deflation/fluvial processes) and thus protect its existence within the landscape (Rowell *et al.*, in press). The precise mechanisms for forming the stone lines within and upon sand ramps remain uncertain (Bateman *et al.*, 2012), however there is evidence from within the Cady Mountains that stones can be transported onto, and incorporated into, the aeolian sediments. If fluvial processes are in part responsible for stone line development (which appears to be the case at CN, for example), then it may become important to distinguish aggradational events (summer monsoonal storms) from degradational events (large winter storms) (Miller *et al.*, 2010). The power of fluvial processes (as indicated by particle size of sediments in the ramp) for

aggrading/degrading a landform is related to the local topographic conditions (e.g. steepness, catchment size, etc.) (Bull, 1991; Sorriso-Valvo *et al.*, 1998; Miller *et al.*, 2010). The surface of the deposit can also be protected by a calcrete layer (as at MC) or by a duricrust (as was reported for the Aus Ramp in Namibia – Bertram, 2003; Rowell *et al.*, in press) and which also indicate long-term preservation.

8.3.5 Summary

This effect of topography in the Cady Mountains is that, where accommodation spaces occur in isolation, a simple, delimitable landform can develop, but that the relationship is more nuanced where topography is more complex owing to interference of wind flow patterns, the overprinting of deposits and the coalescence of morphologies where accommodation spaces occur in close proximity. After unpicking the effect of the boundary conditions it appears that the distribution of aeolian deposition and landform development in space is related to the mountain block topography, and the distribution across time is related to the history of the boundary conditions.

8.4 Broader considerations

This section briefly discusses the implications of the findings of this study for other researchers in the western Mojave Desert, which were not directly addressed above.

8.4.1 Approach

At one of the few sites (the sand ramp at Soldier Mountain) to have received multiple luminescence chronologies (Section 3.1.1), these geochronologies indicate strongly contrasting landscape histories. The timings of aeolian construction at Soldier Mountain from this study indicate that the development of the sand ramp occurred between 70ka and 45ka. These diverge considerably from those reported by both Rendell and Sheffer (1996) and Bateman *et al.* (2012) which concluded that the ramp's construction occurred episodically across the last >20ka and that the ramp accumulated rapidly between 12ka and 8ka respectively. Chapter 5 demonstrated that the divergence of these geochronologies was related to then unknown limitations with their respective luminescence dating approaches. For the former, feldspar IRSL chronologies did not correct for anomalous fading or sensitivity change during measurement which can lead to D_e underestimation if not corrected for (Huntley and Lamothe, 2001; Auclair *et al.*, 2003). For the latter, quartz OSL experiences either signal contamination or malign properties which can lead to severe underestimations

of D_e (Lawson *et al.*, 2012; Lawson *et al.*, 2015). By contrast feldspar pIR-IRSL protocols provide ages in good accordance with independent chronologies at the two lake sites (Section 5.3).

Because much of the history of aeolian activity within the Mojave Desert was derived using IRSL₅₀ ages (not fading corrected), an implication of this study is that these ages may represent underestimates of their “true” deposition. Wells *et al.* (2003) and McDonald *et al.* (2003) observed widespread aeolian sediments which inter-finger fan complexes at Soda Mountain (adjacent to Silver Lake) and Providence Mountains, with radiocarbon dates indicating phases of aeolian activity around ~16ka and ~7ka (recalibrated). The ~16ka age fits between the two Silver Lake high stands (when the lake briefly dried) and the ~7ka age after it desiccated (Wells *et al.*, 2003; Owen *et al.*, 2007). Aeolian (fine sediment) accumulation within a desert pavement archive close to the Cima Dome shows three episodes of accumulation: 50-36ka, 36-25ka and <14.5ka – the onset of the latter pavement formation also correlates with an aeolian period recorded by Wells *et al.* (2003) and McDonald *et al.* (2003) (Dietze *et al.*, 2016). The above records do not suggest that additional luminescence dates would radically amend the landscape history of the Kelso Dunes over the last 16ka, but its history may be older than this.

8.4.2 Timing of lake stands

The revised geochronology presented by this study corresponds well with the ~10ka high stand reported by Owen *et al.* (2007) at Silver Lake (Lake Mojave I). Similarly, timings from Harper Lake indicate the occurrence of a ~29ka high stand, suggesting that either there were multiple high stands within the lake (as Meek, 1999) or that there was a single high stand but which was younger than was proposed by Garcia *et al.* (2014).

9 Conclusions

The aim of this project was:

To understand how complex mountainous topography influences aeolian deposition, and landform development and preservation.

This thesis has demonstrated that:

1. Accommodation spaces locally promote deposition, having the effect of interrupting the aeolian system through a trapping effect.
2. The form of the aeolian deposits is related to the topography of the mountain block and is manifest as deposits which represent three accommodation space types, each having a characteristic morphology (sand ramps, sand sheets and valleys).
3. Aeolian morphologies which develop within accommodation spaces cannot necessarily be delimited into a discrete patchwork of aeolian landforms because, in many cases, they lack distinct boundaries and because of the close association of the different accommodation space types within the landscape.
4. Timings of process activity within the Cady Mountains cover the majority of the last 80ka and appear to be associated with variations in sediment supply and availability in the Manix Basin. Across this time, coarse-grained sediments appear as event-based and highly localised deposits (both of which are related to climate) which inter-finger with the predominantly aeolian sediments. This indicates that these processes operated contemporaneously rather than as some switching between states of aeolian and hillslope process dominance.
5. Topographically-anchored aeolian deposits within these accommodation spaces can be highly persistent features within the landscape, with some landforms being preserved (and unmodified) for >45ka.

Broader research implications

Alongside the principal findings of the research (which link with the project's aim), a number of other findings were made which have implications for other research undertaken within the Mojave Desert.

6. Previous luminescence-derived geochronologies from the Mojave Desert indicated wildly conflicting landscape histories and this observation is explained by these methods underestimating the 'true' timings of aeolian activity (to varying extents).
7. Malign quartz properties were demonstrated to limit their application for luminescence dating within the Mojave Desert. Rather, the suitability of a K-Feldspar post-IR IRSL technique was demonstrated through an assessment using two independently dated lake sites where comparable ages were derived.
8. A revised geochronology is provided which indicated that aeolian activity has occurred within the Cady Mountains for the majority of the last ~80ka, with the exception of a hiatus at 30-11ka and the lack of activity observed over the last ~3ka.
9. Luminescence ages from the Harper Lake bed indicate the occurrence of a ~29ka high stand.

10 References

- AHLBRANDT, T. S. 1979. Textural Parameters of Eolian Deposits. *In*: MCKEE, E. D. (ed.) *A Study of Global Sand Seas: Geological Survey Professional Paper 1052*. Washington DC: United States Department of the Interior.
- AITKEN, M. J. 1985. *Thermoluminescence Dating*, London, Academic Press.
- AITKEN, M. J. 1998. *An Introduction to Optical Dating*, Oxford, Oxford University Press.
- ANDERSON, J. R. 1971. Land Use Classification Schemes Used in Selected Recent Geographic Applications of Remote Sensing. *Photogrammetric Engineering & Remote Sensing*, 37, 379-387.
- ANDREWS, E. D., ANTWEILER, R. C., NEIMAN, P. J. & RALPH, F. M. 2004. Influence of ENSO on flood frequency along the California coast. *Journal of Climate*, 17, 337-348.
- ANTINAO, J. L. & MCDONALD, E. 2013. An enhanced role for the Tropical Pacific on the humid Pleistocene–Holocene transition in southwestern North America. *Quaternary Science Reviews*, 78, 319-341.
- ANTINAO, J. L., MCDONALD, E., RHODES, E. J., BROWN, N., BARRERA, W., GOSSE, J. C. & ZIMMERMANN, S. 2016. Late Pleistocene-Holocene alluvial stratigraphy of southern Baja California, Mexico. *Quaternary Science Reviews*, 146, 161-181.
- AUCLAIR, M., LAMOTHE, M. & HUOT, S. 2003. Measurement of anomalous fading for feldspar IRSL using SAR. *Radiation Measurements*, 37, 487-492.
- BAGNOLD, R. A. 1941. *The physics of blown sand and desert dunes*, New York, Dover Publications.
- BAILEY, R. M. 2010. Direct measurement of the fast component of quartz optically stimulated luminescence and implications for the accuracy of optical dating. *Quaternary Geochronology*, 5, 559-568.
- BAILEY, R. M., SMITH, B. W. & RHODES, E. J. 1997. Partial bleaching and the decay form characteristics of quartz OSL. *Radiation Measurements*, 27, 123-136.
- BANERJEE, D., BØTTER-JENSEN, L. & MURRAY, A. S. 2000. Retrospective dosimetry: estimation of the dose to quartz using the single-aliquot regenerative-dose protocol. *Applied Radiation and Isotopes*, 52, 831-844.
- BARTLEIN, P. J., ANDERSON, K. H., ANDERSON, P. M., EDWARDS, M. E., MOCK, C. J., THOMPSON, R. S., WEBB, R. S., WEBB III, T. & WHITLOCK, C. 1998.

Paleoclimate simulations for North America over the past 21,000 years. *Quaternary Science Reviews*, 17, 549-585.

BATEMAN, M. D., BOULTER, C. H., CARR, A. S., FREDERICK, C. D., PETER, D. & WILDER, M. 2007. Preserving the palaeoenvironmental record in Drylands: Bioturbation and its significance for luminescence-derived chronologies. *Sedimentary Geology*, 195, 5-19.

BATEMAN, M. D., BRYANT, R. G., FOSTER, I. D. L., LIVINGSTONE, I. & PARSONS, A. J. 2012. On the formation of sand ramps: A case study from the Mojave Desert. *Geomorphology*, 161-162, 93-109.

BATEMAN, M. D. & CATT, J. A. 1996. An absolute chronology for the raised beach and associated deposits at Sewerby, East Yorkshire, England. *Journal of Quaternary Science*, 11, 389-395.

BAUER, B. O., DAVIDSON-ARNOTT, R. G. D., HESP, P. A., NAMIKAS, S. L., OLLERHEAD, J. & WALKER, I. J. 2009. Aeolian sediment transport on a beach: Surface moisture, wind fetch, and mean transport. *Geomorphology*, 105, 106-116.

BEATLEY, J. C. 1974. Phenological Events and Their Environmental Triggers in Mojave Desert Ecosystems. *Ecology*, 55, 856-863.

BENSON, L., LUND, S., NEGRINI, R., LINSLEY, B. & ZIC, M. 2003. Response of North American Great Basin Lakes to Dansgaard–Oeschger oscillations. *Quaternary Science Reviews*, 22, 2239-2251.

BENSON, L. V., LUND, S. P., SMOOT, J. P., RHODE, D. E., SPENCER, R. J., VEROSUB, K. L., LOUDERBACK, L. A., JOHNSON, C. A., RYE, R. O. & NEGRINI, R. M. 2011. The rise and fall of Lake Bonneville between 45 and 10.5 ka. *Quaternary International*, 235, 57-69.

BENSON, L. V., SMOOT, J. P., LUND, S. P., MENSING, S. A., FOIT, F. F. & RYE, R. O. 2013. Insights from a synthesis of old and new climate-proxy data from the Pyramid and Winnemucca lake basins for the period 48 to 11.5 cal ka. *Quaternary International*, 310, 62-82.

BERRY, E., HOUSER, R. K. & LANE, W. G. 1981. *A Wind Energy Assessment of the Southern California Desert, Project Windesert, Final Report, Volume I.*

BERTRAM. 2003. *Late Quaternary sand ramps in south-western Namibia-Nature, origin and palaeoclimatological significance.*

BHATTARAI, B. 2011. Assessment of mangrove forests in the Pacific region using Landsat imagery. *Journal of Applied Remote Sensing*, 5, 053509.

BIRD, B. W. & KIRBY, M. E. 2006. An Alpine Lacustrine Record of Early Holocene North American Monsoon Dynamics from Dry Lake, Southern California (USA). *Journal of Paleolimnology*, 35, 179-192.

- BLAZEVIC, M. A., KIRBY, M. E., WOODS, A. D., BROWNE, B. L. & BOWMAN, D. D. 2009. A sedimentary facies model for glacial-age sediments in Baldwin Lake, Southern California. *Sedimentary Geology*, 219, 151-168.
- BLUMBERG, D. 2006. Analysis of large aeolian (wind-blown) bedforms using the Shuttle Radar Topography Mission (SRTM) digital elevation data. *Remote Sensing of Environment*, 100, 179-189.
- BULL, W. B. 1991. *Geomorphic Response to Climatic Change*, Oxford, Oxford University Press.
- BULLARD, J. E. & LIVINGSTONE, I. 2002. Interactions between aeolian and fluvial systems in dryland environments. *Area*, 34, 8-16.
- BULLARD, J. E., WHITE, K. & LIVINGSTONE, I. 2011. Morphometric analysis of aeolian bedforms in the Namib Sand Sea using ASTER data. *Earth Surface Processes and Landforms*, 36, 1534-1549.
- BURROUGH, S. L., THOMAS, D. S. G., BAILEY, R. M. & DAVIES, L. 2012. From landform to process: Morphology and formation of lake-bed barchan dunes, Makgadikgadi, Botswana. *Geomorphology*, 161-162, 1-14.
- BUYLAERT, J.-P., JAIN, M., MURRAY, A. S., THOMSEN, K. J., THIEL, C. & SOHBATI, R. 2012a. A robust feldspar luminescence dating method for Middle and Late Pleistocene sediments. *Boreas*, 41, 435-451.
- BUYLAERT, J. P., JAIN, M., MURRAY, A. S., THOMSEN, K. J. & LAPP, T. 2012b. IR-RF dating of sand-sized K-feldspar extracts: A test of accuracy. *Radiation Measurements*, 47, 759-765.
- BUYLAERT, J. P., MURRAY, A. S., THOMSEN, K. J. & JAIN, M. 2009. Testing the potential of an elevated temperature IRSL signal from K-feldspar. *Radiation Measurements*, 44, 560-565.
- BYERS 1960. Geologic Investigations of Southern California Deserts. *Geological Society Bulletin*, 1089.
- CARDINALE, M., KOMATSU, G., SILVESTRO, S. & TIRSCH, D. 2012. The influence of local topography for wind direction on Mars: two examples of dune fields in crater basins. *Earth Surface Processes and Landforms*, 37, 1437-1443.
- CARR, A. S., ARMITAGE, S. J., BERRÍO, J.-C., BILBAO, B. A. & BOOM, A. 2016. An optical luminescence chronology for late Pleistocene aeolian activity in the Colombian and Venezuelan Llanos. *Quaternary Research*, 85, 299-312.
- CAYAN, D. R., REDMOND, K. T. & RIDDLE, L. G. 1999. ENSO and Hydrologic Extremes in the Western United States. *Journal of Climate*, 12, 2881-2893.

- CHAPLIN, J. & BRABYN, L. 2013. Using remote sensing and GIS to investigate the impacts of tourism on forest cover in the Annapurna Conservation Area, Nepal. *Applied Geography*, 43, 159-168.
- CHASE, B. 2009. Evaluating the use of dune sediments as a proxy for palaeo-aridity: A southern African case study. *Earth-Science Reviews*, 93, 31-45.
- CHEN, Y., LI, S.-H. & LI, B. 2013. Residual doses and sensitivity change of post IR IRSL signals from potassium feldspar under different bleaching conditions. *Geochronometria*, 40.
- CHOJNACKI, M., BURR, D. M., MOERSCH, J. E. & WRAY, J. J. 2014. Valles Marineris dune sediment provenance and pathways. *Icarus*, 232, 187-219.
- CHOJNACKI, M., MOERSCH, J. E. & BURR, D. M. 2010. Climbing and falling dunes in Valles Marineris, Mars. *Geophysical Research Letters*, 37.
- CLARKE, M. L. 1996. IRSL Dating of Sands: Bleaching Characteristics at Deposition Inferred From the Use of Single Aliquots. *Radiation Measurements*, 26, 611-620.
- CLARKE, M. L. & RENDELL, H. M. 1998. Climate change impacts on sand supply and the formation of desert sand dunes in the south-west U.S.A. *Journal of Arid Environments*, 39, 517-531.
- CLARKE, M. L., RICHARDSON, C. A. & RENDELL, H. M. 1995. Luminescence dating of Mojave desert sands. *Quaternary Science Reviews*, 14, 783-789.
- COHEN, T. J., NANSON, G. C., LARSEN, J. R., JONES, B. G., PRICE, D. M., COLEMAN, M. & PIETSCH, T. J. 2010. Late Quaternary aeolian and fluvial interactions on the Cooper Creek Fan and the association between linear and source-bordering dunes, Strzelecki Desert, Australia. *Quaternary Science Reviews*, 29, 455-471.
- COLAROSSO, D., DULLER, G. A. T. & ROBERTS, H. M. 2017. Exploring the behaviour of luminescence signals from feldspars: Implications for the single aliquot regenerative dose protocol. *Radiation Measurements*.
- CONGALTON, R. G. 1991. A review of assessing the accuracy of classifications of remotely sensed data. *Remote Sensing of Environment*, 37, 35-46.
- CONNIN, S. L., BETANCOURT, J. & QUADE, J. 1998. Late Pleistocene C4 plant dominance and Summer Rainfall in the Southwestern United States from Isotopic Study of Herbivore Teeth. *Quaternary Research*, 50, 179-193.
- COOKE, R. U., WARREN, A. & GOUDIE, A. S. 1993. *Desert geomorphology*, UCL Press.
- COX, B. F., HILLHOUSE, J. W. & OWEN, L. A. 2003. Pliocene and Pleistocene evolution of the Mojave River, and associated tectonic development of the Transverse Ranges and Mojave Desert, based on borehole stratigraphy studies and mapping of

- landforms and sediments near Victorville, California. *In: ENZEL, Y., WELLS, S. G. & LANCASTER, N. (eds.) Paleoenvironments and paleohydrology of the Mojave and southern Great Basin deserts.* Geological Society of America.
- CUNNINGHAM, A. C. & WALLINGA, J. 2010. Selection of integration time intervals for quartz OSL decay curves. *Quaternary Geochronology*, 5, 657-666.
- CYR, A. J., MILLER, D. M. & MAHAN, S. A. 2015. Paleodischarge of the Mojave River, southwestern United States, investigated with single-pebble measurements of ^{10}Be . *Geosphere*, 11, 1158-1171.
- DAWELBAIT, M. & MORARI, F. 2008. Limits and Potentialities of Studying Dryland Vegetation Using the Optical Remote Sensing. *Italian Journal of Agronomy*, 3, 97 - 106.
- DIBBLEE, T. W. & BASSETT, A. M. 1966. Geologic Map of the Newberry Quadrangle San Bernardino County, California. *Miscellaneous Geologic Investigations Map 461.* U.S. Geological Survey.
- DIETZE, M., DIETZE, E., LOMAX, J., FUCHS, M., KLEBER, A. & WELLS, S. G. 2016. Environmental history recorded in aeolian deposits under stone pavements, Mojave Desert, USA. *Quaternary Research*, 85, 4-16.
- DOKKA, R. K. 1986. Patterns and modes of early Miocene crustal extension, central Mojave Desert, California. *Geological Society of America Special Paper*, 208, 75-95.
- DOKKA, R. K. & TRAVIS, C. J. 1990. Late Cenozoic strike-slip faulting in the Mojave Desert, California. *Tectonics*, 9, 311-340.
- DUDASH, S. 2006. Preliminary Surficial Geologic Map of a Calico Mountains Piedmont and Part of Coyote Lake, Mojave Desert, San Bernardino County, California. *USGS Open-File Report*.
- DÜHNFORTH, M., DENSMORE, A. L., IVY-OCHS, S., ALLEN, P. & KUBIK, P. W. 2017. Early to Late Pleistocene history of debris-flow fan evolution in western Death Valley (California) using cosmogenic ^{10}Be and ^{26}Al . *Geomorphology*, 281, 53-65.
- DÜHNFORTH, M., DENSMORE, A. L., IVY-OCHS, S., ALLEN, P. A. & KUBIK, P. W. 2007. Timing and patterns of debris flow deposition on Shepherd and Symmes creek fans, Owens Valley, California, deduced from cosmogenic ^{10}Be . *Journal of Geophysical Research: Earth Surface*, 112, n/a-n/a.
- DULLER, G. A. T. 1997. Behavioural studies of stimulated luminescence from feldspars. *Radiation Measurements*, 27, 663-694.
- DULLER, G. A. T. 2003. Distinguishing quartz and feldspar in single grain luminescence measurements. *Radiation Measurements*, 37, 161-165.
- DULLER, G. A. T. 2004. Luminescence dating of quaternary sediments: recent advances. *Journal of Quaternary Science*, 19, 183-192.

- DULLER, G. A. T. 2008. Single-grain optical dating of Quaternary sediments: why aliquot size matters in luminescence dating. *Boreas*, 37, 589-612.
- DULLER, G. A. T. 2012. Improving the accuracy and precision of equivalent doses determined using the optically stimulated luminescence signal from single grains of quartz. *Radiation Measurements*, 47, 770-777.
- DURCAN, J. A. & DULLER, G. A. T. 2011. The fast ratio: A rapid measure for testing the dominance of the fast component in the initial OSL signal from quartz. *Radiation Measurements*, 46, 1065-1072.
- ELBELRHITI, H., ANDREOTTI, B. & CLAUDIN, P. 2008. Barchan dune corridors: Field characterization and investigation of control parameters. *Journal of Geophysical Research: Earth Surface*, 113, n/a-n/a.
- ELLWEIN, A. L., MAHAN, S. A. & MCFADDEN, L. D. 2015. Impacts of climate change on the formation and stability of late Quaternary sand sheets and falling dunes, Black Mesa region, southern Colorado Plateau, USA. *Quaternary International*, 362, 87-107.
- ENZEL, Y. 1992. Flood frequency of the Mojave River and the formation of late Holocene playa lakes, southern California, USA. *Holocene*, 2, 11-18.
- ENZEL, Y., BROWN, W. J., ANDERSON, R. Y., MCFADDEN, L. D. & WELLS, S. G. 1992. Short-Duration Holocene Lakes in the Mojave River Drainage-Basin, Southern California. *Quaternary Research*, 38, 60-73.
- ENZEL, Y., CAYAN, D. R., ANDERSON, R. Y. & WELLS, S. G. 1989. Atmospheric circulation during Holocene lake stands in the Mojave Desert: evidence of regional climate change. *Nature*, 341, 44-47.
- ENZEL, Y. & WELLS, S. G. 1997. Extracting Holocene paleohydrology and paleoclimatology information from modern extreme flood events: An example from southern California. *Geomorphology*, 19, 203-226.
- ENZEL, Y., WELLS, S. G. & LANCASTER, N. 2003. Late Pleistocene lakes along the Mojave River, southeast California.
- EVANS, I. S. 1972. General geomorphology, derivatives of altitude and descriptive statistics. Chorley RJ (ed) *Spatial analysis in geomorphology*. Harper and Row. NY, 17-90.
- EVANS, I. S. 2012. Geomorphometry and landform mapping: What is a landform? *Geomorphology*, 137, 94-106.
- EVANS, J. R. 1962. Falling and climbing sand dunes in the Cronese Cat Dune. *The Journal of Geology*, 70, 107-113.
- FEATHERS, J. 2015. Luminescence dating at Diepkloof Rock Shelter – new dates from single-grain quartz. *Journal of Archaeological Science*, 63, 164-174.

- FEATHERS, J. K. & PAGONIS, V. 2015. Dating quartz near saturation – Simulations and application at archaeological sites in South Africa and South Carolina. *Quaternary Geochronology*.
- FISHER, P., WOOD, J. & CHENG, T. 2004. Where is Helvellyn? Fuzziness of multi-scale landscape morphometry. *Transactions of the Institute of British Geographers*, 29, 106-128.
- FISHER, P., WOOD, J. & CHENG, T. 2005. Fuzziness and Ambiguity in Multi-Scale Analysis of Landscape Morphometry. In: PETRY, F. E., ROBINSON, V. B. & COBB, M. A. (eds.) *Fuzzy Modeling with Spatial Information for Geographic Problems*. Berlin, Heidelberg: Springer Berlin Heidelberg.
- FITZSIMMONS, K. E., MAGEE, J. W. & AMOS, K. J. 2009. Characterisation of aeolian sediments from the Strzelecki and Tirari Deserts, Australia: Implications for reconstructing palaeoenvironmental conditions. *Sedimentary Geology*, 218, 61-73.
- FITZSIMMONS, K. E., RHODES, E. J., MAGEE, J. W. & BARROWS, T. T. 2007. The timing of linear dune activity in the Strzelecki and Tirari Deserts, Australia. *Quaternary Science Reviews*, 26, 2598-2616.
- FOLK, R. L. 1974. *Petrology of sedimentary rocks*, Hemphill Publishing Company.
- FOLK, R. L. & WARD, W. C. 1957. Brazos River Bar: A Study in the Significance of Grain Size Parameters. *Journal of Sedimentary Petrology*, 27, 3-26.
- FONJI, S. F. & TAFF, G. N. 2014. Using satellite data to monitor land-use land-cover change in North-eastern Latvia. *Springerplus*, 3.
- FOODY, G. M. 1992. On the compensation for chance agreement in image classification accuracy assessment. *Photogrammetric engineering and remote sensing*, 58, 1459-1460.
- FRAGOULIS, D. V. & READHEAD, M. L. 1991. Feldspar inclusions and the anomalous fading and enhancement of thermoluminescence in quartz grains. *International Journal of Radiation Applications and Instrumentation. Part D. Nuclear Tracks and Radiation Measurements*, 18, 291-296.
- FU, X. & LI, S.-H. 2013. A modified multi-elevated-temperature post-IR IRSL protocol for dating Holocene sediments using K-feldspar. *Quaternary Geochronology*, 17, 44-54.
- FUCHS, M. & LANG, A. 2009. Luminescence dating of hillslope deposits—A review. *Geomorphology*, 109, 17-26.
- FUCHS, M. & WAGNER, G. A. 2003. Recognition of insufficient bleaching by small aliquots of quartz for reconstructing soil erosion in Greece. *Quaternary Science Reviews*, 22, 1161-1167.
- GALBRAITH, R. F. 2003. A simple homogeneity test for estimates of dose obtained using OSL. *Ancient TL*, 21, 75-77.

- GALBRAITH, R. F., ROBERTS, R. G., LASLETT, G. M., YOSHIDA, H. & OLLEY, J. M. 1999. OPTICAL DATING OF SINGLE AND MULTIPLE GRAINS OF QUARTZ FROM JINMIUM ROCK SHELTER, NORTHERN AUSTRALIA: PART I, EXPERIMENTAL DESIGN AND STATISTICAL MODELS*. *Archaeometry*, 41, 339-364.
- GARCIA, A. L., KNOTT, J. R., MAHAN, S. A. & BRIGHT, J. 2014. Geochronology and paleoenvironment of pluvial Harper Lake, Mojave Desert, California, USA. *Quaternary Research*, 81, 305-317.
- GLAZNER, A. F., BARTLEY, J. M. & WALKER, D. J. 1989. Magnitude and significance of Miocene crustal extension in the central Mojave Desert, California. *Geology*, 17, 50-53.
- GLAZNER, A. F., WALKER, D. J., BARTLEY, J. M. & FLETCHER, J. M. 2002. Cenozoic evolution of the Mojave block of southern California. *Geological Society of America Memoir*, 195, 19-41.
- GLIGANIC, L. A., JACOBS, Z. & ROBERTS, R. G. 2012. Luminescence characteristics and dose distributions for quartz and feldspar grains from Mumba rockshelter, Tanzania. *Archaeological and Anthropological Sciences*, 4, 115-135.
- GLOVER, K. C., MACDONALD, G. M., KIRBY, M. E., RHODES, E. J., STEVENS, L., SILVEIRA, E., WHITAKER, A. & LYDON, S. 2017. Evidence for orbital and North Atlantic climate forcing in alpine Southern California between 125 and 10 ka from multi-proxy analyses of Baldwin Lake. *Quaternary Science Reviews*, 167, 47-62.
- GODFREY-SMITH, D. I., HUNTLEY, D. J. & CHEN, W. H. 1988. Optical dating studies of quartz and feldspar sediment extracts. *Quaternary Science Reviews*, 7, 373-380.
- GRAY, H. J., OWEN, L. A., DIETSCH, C., BECK, R. A., CAFFEE, M. A., FINKEL, R. C. & MAHAN, S. A. 2014. Quaternary landscape development, alluvial fan chronology and erosion of the Mecca Hills at the southern end of the San Andreas Fault zone. *Quaternary Science Reviews*, 105, 66-85.
- GRIFFITHS, P. G., WEBB, R. H., FISHER, M. & MUTH, A. 2009. Plants and ventifacts delineate late Holocene wind vectors in the Coachella Valley, USA. *Aeolian Research*, 1, 63-73.
- GUÉRIN, G. & MERCIER, N. 2011. Determining gamma dose rates by field gamma spectroscopy in sedimentary media: Results of Monte Carlo simulations. *Radiation Measurements*, 46, 190-195.
- HAGAR, D. J. 1966. *Geomorphology of Coyote Valley, San Bernardino County, California*. MS, University of Massachusetts.
- HALFEN, A. F., JOHNSON, W. C., HANSON, P. R., WOODBURN, T. L., YOUNG, A. R. & LUDVIGSON, G. A. 2012. Activation history of the Hutchinson dunes in east-central Kansas, USA during the past 2200 years. *Aeolian Research*, 5, 9-20.

- HALFEN, A. F., LANCASTER, N. & WOLFE, S. 2015. Interpretations and common challenges of aeolian records from North American dune fields. *Quaternary International*.
- HAMMOND, R. & MCCULLAGH, P. S. 1978. *Quantitative Techniques in Geography: An Introduction*, Oxford, Oxford University Press.
- HARRISON, S. 2001. On reductionism and emergence in geomorphology. *Transactions of the Institute of British Geographers*, 26, 327-339.
- HARVEY, A. M. & WELLS, S. G. 2003. Late Quaternary variations in alluvial fan sedimentologic and geomorphic processes, Soda Lake basin, eastern Mojave Desert, California. *In*: ENZEL, Y., WELLS, S. G. & LANCASTER, N. (eds.) *Paleoenvironments and paleohydrology of the Mojave and southern Great Basin deserts*. Geological Society of America.
- HENDY, I. L. & KENNETT, J. P. 2000. Dansgaard-Oeschger Cycles and the California Current System: Planktonic foraminiferal response to rapid climate change in Santa Barbara Basin, Ocean Drilling Program Hole 893A. *Paleoceanography*, 15, 30-42.
- HENGL, T. 2006. Finding the right pixel size. *Computers & Geosciences*, 32, 1283-1298.
- HEREFORD, R., WEBB, R. H. & LONGPRE, C. I. 2004. Precipitation History of the Mojave Desert Region, 1893–2001. *USGS Factsheet 117*. U.S. Geological Survey.
- HESSE, P. P. 2014. How do longitudinal dunes respond to climate forcing? Insights from 25 years of luminescence dating of the Australian desert dunefields. *Quaternary International*.
- HOWARD, A. D. 1985. Interaction of sand transport with topography and local winds in the north Peruvian coastal desert. *In*: BARNDORFF-NIELSEN, O. E., MØLLER, J. T., RASMUSSEN, K. R. & WILLETTS, B. B. (eds.) *Proceedings of International Workshop on the Physics of Blown Sand*. Aarhus: University of Aarhus.
- HUNTLEY, D. J. & BARIL, M. R. 1997. The K content of the K-feldspars being measured in optical dating or in thermoluminescence dating. *Ancient TL*, 15, 11-13.
- HUNTLEY, D. J. & HANCOCK, R. G. V. 2001. The Rb contents of the K-feldspar grains being measured in optical dating. *Ancient TL*, 19, 43-46.
- HUNTLEY, D. J. & LAMOTHE, M. 2001. Ubiquity of anomalous fading in K-feldspars and the measurement and correction for it in optical dating. *Canadian Journal of Earth Sciences*, 38, 1093-1106.
- IBARRA, D. E., EGGER, A. E., WEAVER, K. L., HARRIS, C. R. & MAHER, K. 2014. Rise and fall of late Pleistocene pluvial lakes in response to reduced evaporation and precipitation: Evidence from Lake Surprise, California. *Geological Society of America Bulletin*, 126, 1387-1415.

- ISSANOVA, G., ABUDUWAILI, J., GALAYEVA, O., SEMENOV, O. & BAZARBAYEVA, T. 2015. Aeolian transportation of sand and dust in the Aral Sea region. *International Journal of Environmental Science and Technology*, 12, 3213-3224.
- JACOBS, Z. 2008. Luminescence chronologies for coastal and marine sediments. *Boreas*, 37, 508-535.
- JACOBS, Z., HAYES, E. H., ROBERTS, R. G., GALBRAITH, R. F. & HENSHILWOOD, C. S. 2013. An improved OSL chronology for the Still Bay layers at Blombos Cave, South Africa: further tests of single-grain dating procedures and a re-evaluation of the timing of the Still Bay industry across southern Africa. *Journal of Archaeological Science*, 40, 579-594.
- JAIN, M. & ANKJÆRGAARD, C. 2011. Towards a non-fading signal in feldspar: Insight into charge transport and tunnelling from time-resolved optically stimulated luminescence. *Radiation Measurements*, 46, 292-309.
- JAIN, M., MURRAY, A. S. & BØTTER-JENSEN, L. 2003. Characterisation of blue-light stimulated luminescence components in different quartz samples: implications for dose measurement. *Radiation Measurements*, 37, 441-449.
- JAIN, M. & SINGHVI, A. K. 2001. Limits to depletion of blue-green light stimulated luminescence in feldspars: implications for quartz dating. *Radiation Measurements*, 33, 883-892.
- JEFFERSON, G. T. 2003. Stratigraphy and paleontology of the middle to late Pleistocene Manix Formation, and paleoenvironments of the central Mojave River, Southern California. *Geological Society of America Special Papers*, 368, 43-60.
- JENSEN, J. R. 2005. *Introductory Digital Image Processing: A Remote Sensing Perspective*, Prentice Hall.
- KARS, R. H., BUSSCHERS, F. S. & WALLINGA, J. 2012. Validating post IR-IRSL dating on K-feldspars through comparison with quartz OSL ages. *Quaternary Geochronology*, 12, 74-86.
- KARS, R. H., REIMANN, T., ANKJÆRGAARD, C. & WALLINGA, J. 2014a. Bleaching of the post-IR IRSL signal: new insights for feldspar luminescence dating. *Boreas*, n/a-n/a.
- KARS, R. H., REIMANN, T. & WALLINGA, J. 2014b. Are feldspar SAR protocols appropriate for post-IR IRSL dating? *Quaternary Geochronology*, 22, 126-136.
- KHIRY, M. A. 2007. *Spectral Mixture Analysis for Monitoring and Mapping Desertification Processes in Semi-arid Areas in North Kordofan State, Sudan*. Doctor of Natural Science, Technische Universität Dresden.

- KIRBY, M. E., FEAJKINS, S. J., BONUSO, N., FANTOZZI, J. M. & HINER, C. A. 2013. Latest Pleistocene to Holocene hydroclimates from Lake Elsinore, California. *Quaternary Science Reviews*, 76, 1-15.
- KIRBY, M. E., KNELL, E. J., ANDERSON, W. T., LACHNIET, M. S., PALERMO, J., EEG, H., LUCERO, R., MURRIETA, R., AREVALO, A., SILVEIRA, E. & HINER, C. A. 2015. Evidence for insolation and Pacific forcing of late glacial through Holocene climate in the Central Mojave Desert (Silver Lake, CA). *Quaternary Research*, 84, 174-186.
- KIRBY, M. E., LUND, S. P. & BIRD, B. W. 2006. Mid-Wisconsin sediment record from Baldwin Lake reveals hemispheric climate dynamics (Southern CA, USA). *Palaeogeography, Palaeoclimatology, Palaeoecology*, 241, 267-283.
- KIRBY, M. E., ZIMMERMAN, S. R. H., PATTERSON, W. P. & RIVERA, J. J. 2012. A 9170-year record of decadal-to-multi-centennial scale pluvial episodes from the coastal Southwest United States: a role for atmospheric rivers? *Quaternary Science Reviews*, 46, 57-65.
- KLASEN, N., FIEBIG, M. & PREUSSER, F. 2016. Applying luminescence methodology to key sites of Alpine glaciations in Southern Germany. *Quaternary International*, 420, 249-258.
- KOCUREK, G. & LANCASTER, N. 1999. Aeolian system sediment state: Theory and Mojave Desert Kelso dune field example. *Sedimentology*, 46, 505-515.
- KOCUREK, G. & NIELSON, J. 1986. Conditions favourable for the formation of warm-climate aeolian sand sheets. *Sedimentology*, 33, 795-816.
- KOEHLER, P. A., ANDERSON, R. S. & SPAULDING, W. G. 2005. Development of vegetation in the Central Mojave Desert of California during the late Quaternary. *Palaeogeography, Palaeoclimatology, Palaeoecology*, 215, 297-311.
- KULONGOSKI, J. T., HILTON, D. R., IZBICKI, J. A. & BELITZ, K. 2009. Evidence for prolonged El Nino-like conditions in the Pacific during the Late Pleistocene: a 43ka noble gas record from California groundwaters. *Quaternary Science Reviews*, 28, 2465-2473.
- KUMAR, A., SRIVASTAVA, P. & MEENA, N. K. 2017. Late Pleistocene aeolian activity in the cold desert of Ladakh: A record from sand ramps. *Quaternary International*, 443, 13-28.
- KÜSTER, M., FÜLLING, A., KAISER, K. & ULRICH, J. 2014. Aeolian sands and buried soils in the Mecklenburg Lake District, NE Germany: Holocene land-use history and pedo-geomorphic response. *Geomorphology*, 211, 64-76.
- LACHNIET, M. S., DENNISTON, R. F., ASMEROM, Y. & POLYAK, V. J. 2014. Orbital control of western North America atmospheric circulation and climate over two glacial cycles. *Nat Commun*, 5, 3805.

- LAITY, J. E. 1992. Ventifact evidence for Holocene wind patterns in the east-central Mojave Desert. *Zeitschrift für Geomorphologie, Supplementband*, 84, 73-88.
- LAITY, J. E. & BRIDGES, N. T. 2009. Ventifacts on Earth and Mars: Analytical, field, and laboratory studies supporting sand abrasion and windward feature development. *Geomorphology*, 105, 202-217.
- LAMOTHE, M., AUCLAIR, M., HAMZAOUI, C. & HUOT, S. 2003. Towards a prediction of long-term anomalous fading of feldspar IRSL. *Radiation Measurements*, 37, 493-498.
- LANCASTER, N. 1988. Development of Linear Dunes in the Southwestern Kalahari, Southern-Africa. *Journal of Arid Environments*, 14, 233-244.
- LANCASTER, N. 1993. Kelso Dunes. *National Geographic Research and Exploration*, 9, 444-459.
- LANCASTER, N. 1994. Controls on aeolian activity Some new perspectives from the Kelso Dunes, Mojave Desert, California. *Journal of Arid Environments*, 27, 113-125.
- LANCASTER, N. 1995. *Geomorphology of Desert Dunes*, London, Routledge.
- LANCASTER, N. 1997. Response of eolian geomorphic systems to minor climate change: Examples from the southern Californian deserts. *Geomorphology*, 19, 333-347.
- LANCASTER, N. 2013. 13.9 Climate Change and Aeolian Processes A2 - Shroder, John F. *Treatise on Geomorphology*. San Diego: Academic Press.
- LANCASTER, N. & TCHAKERIAN, V. P. 1996. Geomorphology and sediments of sand ramps in the Mojave Desert. *Geomorphology*, 17, 151-165.
- LANCASTER, N. & TCHAKERIAN, V. P. 2003. Late Quaternary eolian dynamics, Mojave Desert, California. Special Paper of the Geological Society of America.
- LANGBEIN, W. B. & SCHUMM, S. A. 1958. Yield of sediment in relation to mean annual precipitation. *Eos, Transactions American Geophysical Union*, 39, 1076-1084.
- LAWSON, M. J., DANIELS, J. T. M. & RHODES, E. J. 2015. Assessing Optically Stimulated Luminescence (OSL) signal contamination within small aliquots and single grain measurements utilizing the composition test. *Quaternary International*, 362, 34-41.
- LAWSON, M. J., RODER, B. J., STANG, D. M. & RHODES, E. J. 2012. OSL and IRSL characteristics of quartz and feldspar from southern California, USA. *Radiation Measurements*, 47, 830-836.
- LEIGHTON, C. L., THOMAS, D. S. G. & BAILEY, R. M. 2014. Reproducibility and utility of dune luminescence chronologies. *Earth-Science Reviews*, 129, 24-39.

- LI, B., JACOBS, Z., ROBERTS, R. G. & LI, S.-H. 2014. Review and assessment of the potential of post-IR IRSL dating methods to circumvent the problem of anomalous fading in feldspar luminescence. *Geochronometria*, 41, 178-201.
- LI, B. & LI, S.-H. 2006. Comparison of estimates using the fast component and the medium component of quartz OSL. *Radiation Measurements*, 41, 125-136.
- LI, B. & LI, S.-H. 2011. Luminescence dating of K-feldspar from sediments: A protocol without anomalous fading correction. *Quaternary Geochronology*, 6, 468-479.
- LI, B. & LI, S. H. 2008. Investigations of the dose-dependent anomalous fading rate of feldspar from sediments. *Journal of Physics D: Applied Physics*, 41.
- LI, B., ROBERTS, R. G. & JACOBS, Z. 2013. On the dose dependency of the bleachable and non-bleachable components of IRSL from K-feldspar: Improved procedures for luminescence dating of Quaternary sediments. *Quaternary Geochronology*, 17, 1-13.
- LI, S.-H. 1994. Optical dating: Insufficiently bleached sediments. *Radiation Measurements*, 23, 563-567.
- LIVINGSTONE, I., BRISTOW, C., BRYANT, R. G., BULLARD, J., WHITE, K., WIGGS, G. F. S., BAAS, A. C. W., BATEMAN, M. D. & THOMAS, D. S. G. 2010. The Namib Sand Sea digital database of aeolian dunes and key forcing variables. *Aeolian Research*, 2, 93-104.
- LIVINGSTONE, I. & WARREN, A. 1996. *Aeolian geomorphology : an introduction*, Harlow, Longman.
- LOWICK, S. E., PREUSSER, F. & WINTLE, A. G. 2010. Investigating quartz optically stimulated luminescence dose-response curves at high doses. *Radiation Measurements*, 45, 975-984.
- LOWICK, S. E., TRAUERSTEIN, M. & PREUSSER, F. 2012. Testing the application of post IR-IRSL dating to fine grain waterlain sediments. *Quaternary Geochronology*, 8, 33-40.
- LYLE, M., HEUSSER, L., RAVELO, C., ANDREASEN, D., OLIVAREZ LYLE, A. & DIFFENBAUGH, N. 2010. Pleistocene water cycle and eastern boundary current processes along the California continental margin. *Paleoceanography*, 25.
- LYLE, M., HEUSSER, L., RAVELO, C., YAMAMOTO, M., BARRON, J., DIFFENBAUGH, N. S., HERBERT, T. & ANDREASEN, D. 2012. Out of the tropics: the Pacific, Great Basin lakes, and late Pleistocene water cycle in the western United States. *Science*, 337, 1629-33.
- MABBUTT, J. A. 1977. *Desert Landforms*, Canberra, Australian National University Press.

- MAHAN, S. A., MILLER, D. M., MENGES, C. M. & YOUNT, J. C. 2007. Late Quaternary stratigraphy and luminescence geochronology of the northeastern Mojave Desert. *Quaternary International*, 166, 61-78.
- MAHER, K., IBARRA, D. E., OSTER, J. L., MILLER, D. M., REDWINE, J. L., REHEIS, M. C. & HARDEN, J. W. 2014. Uranium isotopes in soils as a proxy for past infiltration and precipitation across the western United States. *American Journal of Science*, 314, 821-857.
- MAHOWALD, N. M., BRYANT, R. G., DEL CORRAL, J. & STEINBERGER, L. 2003. Ephemeral lakes and desert dust sources. *Geophysical Research Letters*, 30, n/a-n/a.
- MAROULIS, J. C., NANSON, G. C., PRICE, D. M. & PIETSCH, T. 2007. Aeolian-fluvial interaction and climate change: source-bordering dune development over the past ~100ka on Cooper Creek, central Australia. *Quaternary Science Reviews*, 26, 386-404.
- MARTINSON, D. G., PISIAS, N. G., HAYS, J. D., IMBRIE, J. D., MOORE, T. C. & SHACKLETON, N. J. 1987. Age dating and isotopic analyses of sediment core RC11-120. *Supplement to: Martinson, DG et al. (1987): Age Dating and the orbital theory of the ice ages: development of a high-resolution 0 to 300,000-year chronostratigraphy. Quaternary Research*, 27, 1-29, [https://doi.org/10.1016/0033-5894\(87\)90046-9](https://doi.org/10.1016/0033-5894(87)90046-9). PANGAEA.
- MASON, J. A., SWINEHART, J. B., HANSON, P. R., LOOPE, D. B., GOBLE, R. J., MIAO, X. & SCHMEISSER, R. L. 2011. Late Pleistocene dune activity in the central Great Plains, USA. *Quaternary Science Reviews*, 30, 3858-3870.
- MAYYA, Y. S., MORTHEKAI, P., MURARI, M. K. & SINGHVI, A. K. 2006. Towards quantifying beta microdosimetric effects in single-grain quartz dose distribution. *Radiation Measurements*, 41, 1032-1039.
- MCDONALD, E. V., MCFADDEN, L. D. & WELLS, S. G. 2003. Regional response of alluvial fans to the Pleistocene-Holocene climatic transition, Mojave Desert, California. In: ENZEL, Y., WELLS, S. G. & LANCASTER, N. (eds.) *Paleoenvironments and paleohydrology of the Mojave and southern Great Basin deserts*. Geological Society of America.
- MEEK, N. 1990. *Late Quaternary Geochronology and Geomorphology of the Manix Basin, San Bernardino County, California*. PhD, University of California.
- MEEK, N. 1994. The stratigraphy and geomorphology of Coyote basin, central Mojave Desert, California. *San Bernardino County Museum Association Quarterly*, 41, 5-13.
- MEEK, N. 1999. New discoveries about the Late Wisconsinan history of the late Mojave River system. *San Bernardino County Museum Association Quarterly*, 46, 113-117.
- MEEK, N. 2000. The Late Wisconsinan History of the Afton Canyon area. *San Bernardino County Museum Association Quarterly*, 47, 32-34.

- MEEK, N. 2004. Mojave River history from an upstream perspective. *In: REYNOLDS, R. E. (ed.) 2004 Desert Symposium. Zzyzx Desert Studies Center.*
- MEJDAHL, V. 1979. THERMOLUMINESCENCE DATING: BETA-DOSE ATTENUATION IN QUARTZ GRAINS. *Archaeometry*, 21, 61-72.
- MILIAREISIS 2000. Extraction and deliniation of alluvial fans from DEM and landsat imagery. *Photogrammetric Engineering & Remote Sensing*, 66.
- MILIAREISIS, G. C. 2001. Extraction of bajadas from digital elevation models and satellite imagery. *Computers & Geosciences*, 27, 1157-1167.
- MILLER, D. M., SCHMIDT, K. M., MAHAN, S. A., MCGEEHIN, J. P., OWEN, L. A., BARRON, J. A., LEHMKUHL, F. & LÖHRER, R. 2010. Holocene landscape response to seasonality of storms in the Mojave Desert. *Quaternary International*, 215, 45-61.
- MINÁR, J., EVANS, I. S. & KRCHO, J. 2013. 14.3 Geomorphometry: Quantitative Land-Surface Analysis A2 - Shroder, John F. *Treatise on Geomorphology*. San Diego: Academic Press.
- MOSELEY, G. E., EDWARDS, R. L., WENDT, K. A., CHENG, H., DUBLYANSKY, Y., LU, Y., BOCH, R. & SPÖTL, C. 2016. Reconciliation of the Devils Hole climate record with orbital forcing. *Science*, 351, 165-168.
- MUHS, D. R. & HOLLIDAY, V. T. 1995. Evidence of active dune sand on the great plains in the 19th century from accounts of early explorers. *Quaternary Research*, 43, 198-208.
- MUHS, D. R., LANCASTER, N. & SKIPP, G. L. 2017. A complex origin for the Kelso Dunes, Mojave National Preserve, California, USA: A case study using a simple geochemical method with global applications. *Geomorphology*, 276, 222-243.
- MUHS, D. R., REYNOLDS, R. L., BEEN, J. & SKIPP, G. 2003. Eolian sand transport pathways in the southwestern United States: importance of the Colorado River and local sources. *Quaternary International*, 104, 3-18.
- MUHS, D. R., ROSKIN, J., TSOAR, H., SKIPP, G., BUDAHN, J. R., SNEH, A., PORAT, N., STANLEY, J.-D., KATRA, I. & BLUMBERG, D. G. 2013. Origin of the Sinai–Negev erg, Egypt and Israel: mineralogical and geochemical evidence for the importance of the Nile and sea level history. *Quaternary Science Reviews*, 69, 28-48.
- MUNYIKWA, K., VAN DEN HAUTE, P., VANDENBERGHE, D. & DE CORTE, F. 2000. The age and palæoenvironmental significance of the Kalahari Sands in western Zimbabwe: a thermoluminescence reconnaissance study. *Journal of African Earth Sciences*, 30, 941-956.
- MURRAY, A. S. & MEJDAHL, V. 1999. Comparison of regenerative-dose single-aliquot and multiple-aliquot (SARA) protocols using heated quartz from archaeological sites. *Quaternary Science Reviews*, 18, 223-229.

- MURRAY, A. S. & OLLEY, J. M. 2002. PRECISION AND ACCURACY IN THE OPTICALLY STIMULATED LUMINESCENCE DATING OF SEDIMENTARY QUARTZ: A STATUS REVIEW. *Geochronometria*, 21, 1-16.
- MURRAY, A. S. & ROBERTS, R. G. 1997. Determining the burial time of single grains of quartz using optically stimulated luminescence. *Earth and Planetary Science Letters*, 152, 163-180.
- MURRAY, A. S. & WINTLE, A. G. 2000. Luminescence dating of quartz using an improved single-aliquot regenerative-does protocol.
- MURRAY, A. S. & WINTLE, A. G. 2003. The single aliquot regenerative dose protocol: potential for improvements in reliability. *Radiation Measurements*, 37, 377-381.
- NAGGY, E. A. & MURRAY, B. 1996. Plio-Pleistocene deposits adjacent to the Manix Fault: implications for the history of the Mojave River and transverse ranges uplift. *Sedimentary Geology*, 103, 9-21.
- NANSON, G. C., PRICE, D. M. & SHORT, S. A. 1992. Wetting and Drying of Australia over the Past 300 Ka. *Geology*, 20, 791-794.
- NEUDORF, C. M., ROBERTS, R. G. & JACOBS, Z. 2012. Sources of overdispersion in a K-rich feldspar sample from north-central India: Insights from De, K content and IRSL age distributions for individual grains. *Radiation Measurements*, 47, 696-702.
- NIAN, X., BAILEY, R. M. & ZHOU, L. 2012. Investigations of the post-IR IRSL protocol applied to single K-feldspar grains from fluvial sediment samples. *Radiation Measurements*, 47, 703-709.
- NORINI, G., ZULUAGA, M. C., ORTIZ, I. J., AQUINO, D. T. & LAGMAY, A. M. F. 2016. Delineation of alluvial fans from Digital Elevation Models with a GIS algorithm for the geomorphological mapping of the Earth and Mars. *Geomorphology*, 273, 134-149.
- OERTER, E. J., SHARP, W. D., OSTER, J. L., EBELING, A., VALLEY, J. W., KOZDON, R., ORLAND, I. J., HELLSTROM, J., WOODHEAD, J. D., HERGT, J. M., CHADWICK, O. A. & AMUNDSON, R. 2016. Pedothem carbonates reveal anomalous North American atmospheric circulation 70,000-55,000 years ago. *Proc Natl Acad Sci U S A*, 113, 919-24.
- OLLEY, J., CAITCHEON, G. & MURRAY, A. 1998. The distribution of apparent dose as determined by Optically Stimulated Luminescence in small aliquots of fluvial quartz. *Quaternary Science Reviews*, 17, 1033-1040.
- OLOFSSON, P., FOODY, G. M., STEHMAN, S. V. & WOODCOCK, C. E. 2013. Making better use of accuracy data in land change studies: Estimating accuracy and area and quantifying uncertainty using stratified estimation. *Remote Sensing of Environment*, 129, 122-131.

- OSTER, J. L., MONTAÑEZ, I. P., SHARP, W. D. & COOPER, K. M. 2009. Late Pleistocene California droughts during deglaciation and Arctic warming. *Earth and Planetary Science Letters*, 288, 434-443.
- OWEN, L. A., BRIGHT, J., FINKEL, R. C., JAISWAL, M. K., KAUFMAN, D. S., MAHAN, S., RADTKE, U., SCHNEIDER, J. S., SHARP, W., SINGHVI, A. K. & WARREN, C. N. 2007. Numerical dating of a Late Quaternary spit-shoreline complex at the northern end of Silver Lake playa, Mojave Desert, California: A comparison of the applicability of radiocarbon, luminescence, terrestrial cosmogenic nuclide, electron spin resonance, U-series and amino acid racemization methods. *Quaternary International*, 166, 87-110.
- OWEN, L. A., CLEMMENS, S. J., FINKEL, R. C. & GRAY, H. 2014. Late Quaternary alluvial fans at the eastern end of the San Bernardino Mountains, Southern California. *Quaternary Science Reviews*, 87, 114-134.
- PAN, M., WU, Y., ZHENG, Y. & TAN, L. 2014. Holocene aeolian activity in the Dinggye area (Southern Tibet, China). *Aeolian Research*, 12, 19-27.
- PARSONS, A. J. & ABRAHAMS, A. D. 2009. *Geomorphology of desert environments*.
- PEASE, P. P. & TCHAKERIAN, V. P. 2003. Geochemistry of sediments from quaternary sand ramps in the southeastern Mojave Desert, California. *Quaternary International*, 104, 19-29.
- PHELPS, G. A., BEDFORD, D. R., LIDKE, D. J., MILLER, D. M. & SCHMIDT, K. M. 2012. Preliminary Surficial Geologic Map of the Newberry prings 30' x 60' Quadrangle, California. *Open-File Report*
- PIGATI, J. S., MILLER, D. M., BRIGHT, J. E., MAHAN, S. A., NEKOLA, J. C. & PACES, J. B. 2011. Chronology, sedimentology, and microfauna of groundwater discharge deposits in the central Mojave Desert, Valley Wells, California. *Geological Society of America Bulletin*, 123, 2224-2239.
- PIKE, R. J., EVANS, I. S. & HENGL, T. 2009. Chapter 1 Geomorphometry: A Brief Guide. In: HENGL, T. & REUTER, H. I. (eds.) *Developments in Soil Science*. Elsevier.
- PRESCOTT, J. R. & HUTTON, J. T. 1994. Cosmic ray contributions to dose rates for luminescence and ESR dating: Large depths and long-term time variations. *Radiation Measurements*, 23, 497-500.
- PREUSSER, F., CHITHAMBO, M. L., GÖTTE, T., MARTINI, M., RAMSEYER, K., SENDEZERA, E. J., SUSINO, G. J. & WINTLE, A. G. 2009. Quartz as a natural luminescence dosimeter. *Earth-Science Reviews*, 97, 184-214.
- PYE, K. 1994. *Sediment Transport and Depositional Processes*, Oxford, Blackwell Scientific Publications.

- PYE, K. & TSOAR, H. 1990. The Formation of Sand Seas and Dune Fields. *Aeolian Sand and Sand Dunes*. First Edition ed. London: Unwin Hyman Ltd.
- QIAN, G., DONG, Z., LUO, W. & LU, J. 2011. Mean airflow patterns upwind of topographic obstacles and their implications for the formation of echo dunes: A wind tunnel simulation of the effects of windward slope. *Journal of Geophysical Research*, 116.
- QIN, J. T. & ZHOU, L. P. 2012. Effects of thermally transferred signals in the post-IR IRS L SAR protocol. *Radiation Measurements*, 47, 710-715.
- QUADE, J., FORESTER, R. M. & WHELAN, J. F. 2003. Late Quaternary paleohydrologic and paleotemperature change in southern Nevada. In: ENZEL, Y., WELLS, S. G. & LANCASTER, N. (eds.) *Paleoenvironments and paleohydrology of the Mojave and southern Great Basin deserts*. Geological Society of America.
- RAILSBACK, L. B., BROOK, G. A., ELLWOOD, B. B., LIANG, F., CHENG, H. & EDWARDS, R. L. 2015. A record of wet glacial stages and dry interglacial stages over the last 560kyr from a standing massive stalagmite in Carlsbad Cavern, New Mexico, USA. *Palaeogeography, Palaeoclimatology, Palaeoecology*, 438, 256-266.
- RAMSEY, M. S., CHRISTENSEN, P. R., LANCASTER, N. & HOWARD, D. A. 1999. Identification of sand sources and transport pathways at the Kelso Dunes, California, using thermal infrared remote sensing. *Geological Society of America Bulletin*, 111, 646-662.
- READHEAD, M. L. 2002. Absorbed dose fraction for ^{87}Rb β particles. *Ancient TL*, 20, 25-28.
- REHEIS, M. & MILLER, D. M. 2010. Environments of nearshore lacustrine deposition in the Pleistocene Lake Manix basin. In: REYNOLDS, R. E. & MILLER, D. M. (eds.) *Overboard in the Mojave: 20 Million Years of Lakes and Wetlands. Proceedings from the 2010 Desert Symposium, Zzyzx, California*.
- REHEIS, M. & REDWINE, J. L. 2008. Lake Manix shorelines and Afton Canyon terraces: Implications for incision of Afton Canyon. In: REHEIS, M. C., HERSHLER, R. & MILLER, D. M. (eds.) *Late Cenozoic drainage history of the southwestern Great Basin and lower Colorado River region: geologic and biotic perspectives*. Geological Society of America Special Publication.
- REHEIS, M. & THROCKMORTON, C. K. 1993. Climatic Control of Late Quaternary Sedimentation on the Leidy Creek Fan in Fish Lake Valley, Nevada-California - Implications for Geomorphic Processes in Semiarid Climates. In: BENSON, L. V. (ed.) *Proceedings of the Workshop "Ongoing Paleoclimatic Studies in the Northern Great Basin*.
- REHEIS, M. C., ADAMS, K. D., OVIATT, C. G. & BACON, S. N. 2014. Pluvial lakes in the Great Basin of the western United States—a view from the outcrop. *Quaternary Science Reviews*, 97, 33-57.

- REHEIS, M. C., BRIGHT, J., LUND, S. P., MILLER, D. M., SKIPP, G. & FLECK, R. J. 2012. A half-million-year record of paleoclimate from the Lake Manix Core, Mojave Desert, California. *Palaeogeography, Palaeoclimatology, Palaeoecology*, 365-366, 11-37.
- REHEIS, M. C., MILLER, D. M., MCGEEHIN, J. P., REDWINE, J. R., OVIATT, C. G. & BRIGHT, J. 2015. Directly dated MIS 3 lake-level record from Lake Manix, Mojave Desert, California, USA. *Quaternary Research*, 83, 187-203.
- REIMANN, T., THOMSEN, K. J., JAIN, M., MURRAY, A. S. & FRECHEN, M. 2012. Single-grain dating of young sediments using the pIRIR signal from feldspar. *Quaternary Geochronology*, 11, 28-41.
- REIMANN, T., TSUKAMOTO, S., NAUMANN, M. & FRECHEN, M. 2011. The potential of using K-rich feldspars for optical dating of young coastal sediments – A test case from Darss-Zingst peninsula (southern Baltic Sea coast). *Quaternary Geochronology*, 6, 207-222.
- RENDELL, H. M., CLARKE, M. L., WARREN, A. & CHAPPELL, A. 2003. The timing of climbing dune formation in southwestern Niger: fluvio-aeolian interactions and the rôle of sand supply. *Quaternary Science Reviews*, 22, 1059-1065.
- RENDELL, H. M. & SHEFFER, N. L. 1996. Luminescence dating of sand ramps in the Eastern Mojave Desert. *Geomorphology*, 17, 187-197.
- RETALLACK, G. J. 1988. Field Recognition of Paleosols. *Geological Society of America Special Paper*, 216, 1-20.
- RHODES, E. J. 2007. Quartz single grain OSL sensitivity distributions: Implications for multiple grain single aliquot dating. *Geochronometria*, 26, 19-29.
- RHODES, E. J. 2011. Optically Stimulated Luminescence Dating of Sediments over the Past 200,000 Years. *Annual Review of Earth and Planetary Sciences*, 39, 461-488.
- RHODES, E. J. 2015. Dating sediments using potassium feldspar single-grain IRSL: Initial methodological considerations. *Quaternary International*, 362, 14-22.
- RICH, J. 2013. A 250,000-year record of lunette dune accumulation on the Southern High Plains, USA and implications for past climates. *Quaternary Science Reviews*, 62, 1-20.
- ROBERT, C. 2004. Late Quaternary variability of precipitation in Southern California and climatic implications: clay mineral evidence from the Santa Barbara Basin, ODP Site 893. *Quaternary Science Reviews*, 23, 1029-1040.
- ROBERTS, H. M. 2012. Testing Post-IR IRSL protocols for minimising fading in feldspars, using Alaskan loess with independent chronological control. *Radiation Measurements*, 47, 716-724.

- RODER, B., LAWSON, M., RHODES, E. J., DOLAN, J., MCAULIFFE, L. & MCGILL, S. 2012. Assessing the potential of luminescence dating for fault slip rate studies on the Garlock fault, Mojave Desert, California, USA. *Quaternary Geochronology*, 10, 285-290.
- ROSKIN, J., KATRA, I. & BLUMBERG, D. G. 2013. Late Holocene dune mobilizations in the northwestern Negev dunefield, Israel: A response to combined anthropogenic activity and short-term intensified windiness. *Quaternary International*, 303, 10-23.
- ROSS, T. M. 1995. North-south-directed extension, timing of extension, and vertical-axis rotation of the southwest Cady Mountains, Mojave Desert, California. *Geological Society of America Bulletin*, 107, 793-811.
- ROUSE, J. W. 1974. Monitoring vegetation systems in the Great Plains with ETRS. In: FREDEN, MERCANTI & BECKER (eds.) *Third Earth Resources Technology Satellite-1 Symposium- Volume I: Technical Presentations*.
- ROWAN, A. V., ROBERTS, H. M., JONES, M. A., DULLER, G. A. T., COVEY-CRUMP, S. J. & BROCKLEHURST, S. H. 2012. Optically stimulated luminescence dating of glaciofluvial sediments on the Canterbury Plains, South Island, New Zealand. *Quaternary Geochronology*, 8, 10-22.
- ROWELL, A., THOMAS, D., BAILEY, R., STONE, A., GARZANTI, E. & PADOAN, M. in press. Controls on sand ramp formation in southern Namibia. *Earth Surface Processes and Landforms*, n/a-n/a.
- ROWLANDS, P., JOHNSON, H., RITTER, E. & ENDO, A. 1982. The Mojave Desert. In: BENDER, G. L. (ed.) *Reference Handbook on the Deserts of North America*. Westport: Greenwood Press.
- SAIKO, T. A. & ZONN, I. S. 2000. Irrigation expansion and dynamics of desertification in the Circum-Aral region of Central Asia. *Applied Geography*, 20, 349-367.
- SHARP, R. P. 1966. Kelso Dunes, Mojave Desert, California. *Geological Society of America Bulletin*, 77, 1045-1074.
- SILVESTRO, S., DI ACHILLE, G. & ORI, G. G. 2010a. Dune morphology, sand transport pathways and possible source areas in east Thaumasia Region (Mars). *Geomorphology*, 121, 84-97.
- SILVESTRO, S., FENTON, L. K., VAZ, D. A., BRIDGES, N. T. & ORI, G. G. 2010b. Ripple migration and dune activity on Mars: Evidence for dynamic wind processes. *Geophysical Research Letters*, 37, L20203.
- SINGARAYER, J. S. & BAILEY, R. M. 2003. Further investigations of the quartz optically stimulated luminescence components using linear modulation. *Radiation Measurements*, 37, 451-458.
- SINGHVI, A. K. & PORAT, N. 2008. Impact of luminescence dating on geomorphological and palaeoclimate research in drylands. *Boreas*, 37, 536-558.

- SMEDLEY, R. K., DULLER, G. A. T. & ROBERTS, H. M. 2015. Bleaching of the post-IR IRSL signal from individual grains of K-feldspar: Implications for single-grain dating. *Radiation Measurements*, 79, 33-42.
- SMITH, B. & VARZI, A. C. 2000. Fiat and Bona Fide Boundaries. *Philosophy and Phenomenological Research*, 60, 401.
- SMITH, B. W. & RHODES, E. J. 1994. Charge Movements in Quartz and Their Relevance to Optical Dating. *Radiation Measurements*, 23, 329-333.
- SMITH, M. J. & PAIN, C. F. 2009. Applications of remote sensing in geomorphology. *Progress in Physical Geography*, 33, 568-582.
- SMITH, R. S. U. 1984. Eolian geomorphology of the Devil's Playground, Kelso Dunes and Silurian Valley, CA. In: DOHRENWEND, J. C. (ed.) *Surficial Geology of the Eastern Mojave Desert, California*. 14 ed.: Geological Society of America.
- SORRISO-VALVO, M., ANTRONICO, L. & LE PERA, E. 1998. Controls on modern fan morphology in Calabria, Southern Italy. *Geomorphology*, 24, 169-187.
- SPELZ, R. M., FLETCHER, J. M., OWEN, L. A. & CAFFEE, M. W. 2008. Quaternary alluvial-fan development, climate and morphologic dating of fault scarps in Laguna Salada, Baja California, Mexico. *Geomorphology*, 102, 578-594.
- STANLEY, D. J. & WARNE, A. G. 1993. Nile Delta: Recent Geological Evolution and Human Impact. *Science*, 260.
- STEFFEN, D., PREUSSER, F. & SCHLUNEGGER, F. 2009. OSL quartz age underestimation due to unstable signal components. *Quaternary Geochronology*, 4, 353-362.
- STEVENS, T., MARKOVIĆ, S. B., ZECH, M., HAMBACH, U. & SÜMEGI, P. 2011. Dust deposition and climate in the Carpathian Basin over an independently dated last glacial–interglacial cycle. *Quaternary Science Reviews*, 30, 662-681.
- STOKES, S., KOCUREK, G., PYE, K. & WINSPEAR, N. R. 1997. New evidence for the timing of aeolian sand supply to the Algodones dunefield and East Mesa area, southeastern California, USA. *Palaeogeography, Palaeoclimatology, Palaeoecology*, 128, 63-75.
- STONE, A. E. C. & THOMAS, D. S. G. 2008. Linear dune accumulation chronologies from the southwest Kalahari, Namibia: challenges of reconstructing late Quaternary palaeoenvironments from aeolian landforms. *Quaternary Science Reviews*, 27, 1667-1681.
- SWEENEY, M. R., MCDONALD, E. V. & MARKLEY, C. E. 2013. Alluvial sediment or playas: What is the dominant source of sand and silt in desert soil vesicular A horizons, southwest USA. *Journal of Geophysical Research: Earth Surface*, 118, 257-275.

- SWEET, M. L., NIELSON, J., HAVHOLM, K. & FARRELLEY, J. 1988. Algodones dune field of southeastern California: case history of a migrating modern dune field. *Sedimentology*, 35, 939-952.
- TCHAKERIAN, V. P. 1989. *Late Quaternary aeolian geomorphology, east-central Mojave Desert, California*. PhD, University of California.
- TCHAKERIAN, V. P. 1991. Late Quaternary aeolian geomorphology of the Dale Lake sand sheet, southern Mojave Desert, California. *Physical Geography*, 12, 347-369.
- TELFER, M. W., BAILEY, R. M., BURROUGH, S. L., STONE, A. E. S., THOMAS, D. S. G. & WIGGS, G. S. F. 2010. Understanding linear dune chronologies: Insights from a simple accumulation model. *Geomorphology*, 120, 195-208.
- TELFER, M. W. & HESSE, P. P. 2013. Palaeoenvironmental reconstructions from linear dunefields: recent progress, current challenges and future directions. *Quaternary Science Reviews*, 78, 1-21.
- TELFER, M. W., MILLS, S. C. & MATHER, A. E. 2014. Extensive Quaternary aeolian deposits in the Drakensberg foothills, Rooiberge, South Africa. *Geomorphology*, 219, 161-175.
- TELFER, M. W. & THOMAS, D. S. G. 2007. Late Quaternary linear dune accumulation and chronostratigraphy of the southwestern Kalahari: implications for aeolian palaeoclimatic reconstructions and predictions of future dynamics. *Quaternary Science Reviews*, 26, 2617-2630.
- TELFER, M. W., THOMAS, Z. A. & BREMAN, E. 2012. Sand ramps in the Golden Gate Highlands National Park, South Africa: Evidence of periglacial aeolian activity during the last glacial. *Palaeogeography, Palaeoclimatology, Palaeoecology*, 313-314, 59-69.
- TEODORO, A. C. & GONCALVES, H. 2012. A Semi-Automatic Approach for the Extraction of Sandy Bodies (Sand Spits) From IKONOS-2 Data. *Ieee Journal of Selected Topics in Applied Earth Observations and Remote Sensing*, 5, 634-642.
- THIEL, C., BUYLAERT, J.-P., MURRAY, A., TERHORST, B., HOFER, I., TSUKAMOTO, S. & FRECHEN, M. 2011. Luminescence dating of the Stratzing loess profile (Austria) – Testing the potential of an elevated temperature post-IR IRSL protocol. *Quaternary International*, 234, 23-31.
- THOMAS, D. S. G., BATEMAN, M. D., MEHRSHAHI, D. & O'HARA, S. L. 1997. Development and environmental significance of an eolian sand ramp of last-glacial age, central Iran. *Quaternary Research*, 48, 155-161.
- THOMAS, D. S. G. & BURROUGH, S. L. 2012. Interpreting geoproxies of late Quaternary climate change in African drylands: Implications for understanding environmental change and early human behaviour. *Quaternary International*, 253, 5-17.

- THOMAS, D. S. G. & BURROUGH, S. L. 2013. Luminescence-based dune chronologies in southern Africa: Analysis and interpretation of dune database records across the subcontinent. *Quaternary International*.
- THOMSEN, K. J., MURRAY, A. S., JAIN, M. & BØTTER-JENSEN, L. 2008. Laboratory fading rates of various luminescence signals from feldspar-rich sediment extracts. *Radiation Measurements*, 43, 1474-1486.
- TRAUERSTEIN, M., LOWICK SALLY, E., PREUSSER, F. & VEIT, H. 2017. Testing the suitability of dim sedimentary quartz from northern Switzerland for OSL burial dose estimation. *Geochronometria*.
- TSOAR, H. 1983. Wind Tunnel Modeling of Echo and Climbing Dunes. 38, 247-259.
- VENTRA, D., RODRÍGUEZ-LÓPEZ, J. P. & DE BOER, P. L. 2017. Sedimentology and preservation of aeolian sediments on steep terrains: Incipient sand ramps on the Atacama coast (northern Chile). *Geomorphology*, 285, 162-185.
- VERMEESCH, P. & DRAKE, N. 2008. Remotely sensed dune celerity and sand flux measurements of the world's fastest barchans (Bodélé, Chad). *Geophysical Research Letters*, 35.
- WALLINGA, J. 2002a. On the Detection of OSL Age Overestimation Using Single-Aliquot Techniques. *Geochronometria*, 21, 17-26.
- WALLINGA, J. 2002b. Optically stimulated luminescence dating of fluvial deposits: a review. *Boreas*, 31, 303-322.
- WALLINGA, J., BOS, A. J. J., DORENBOS, P., MURRAY, A. S. & SCHOKKER, J. 2007. A test case for anomalous fading correction in IRSL dating. *Quaternary Geochronology*, 2, 216-221.
- WALLINGA, J., MURRAY, A. & WINTLE, A. 2000. The single-aliquot regenerative-dose (SAR) protocol applied to coarse-grain feldspar. *Radiation Measurements*, 32, 529-533.
- WARREN, A. 2013. *Dunes: Dynamics, Morphology, History*, John Wiley & Sons.
- WASSON, R. J. & HYDE, R. 1983. Factors determining desert dune type. *Nature*, 304, 337-339.
- WELLS, S. G., BROWN, W. J., ENZEL, Y., ANDERSON, R. Y. & MCFADDEN, L. D. 2003. Late Quaternary geology and paleohydrology of pluvial Lake Mojave, southern California. In: ENZEL, Y., WELLS, S. G. & LANCASTER, N. (eds.) *Paleoenvironments and paleohydrology of the Mojave and southern Great Basin deserts*. Geological Society of America.

- WELLS, S. G., MCFADDEN, L. D. & DOHRENWEND, J. C. 1987. Influence of late Quaternary climatic changes on geomorphic and pedogenic processes on a desert piedmont, Eastern Mojave Desert, California. *Quaternary Research*, 27, 130-146.
- WHITTOW, J. B. 1984. *The Penguin dictionary of physical geography*, Penguin books Hamondsworth.
- WIGGENHORN, H. 1994. IrsL Dating of K-Feldspar at Elevated-Temperatures and Infrared Bleaching of TL. *Radiation Measurements*, 23, 387-391.
- WIGGS, G. F. S., BULLARD, J. E., GARVEY, B. & CASTRO, I. 2002. Interactions between airflow and valley topography with implications for aeolian sediment transport. *Physical Geography*, 23, 366-380.
- WILSON, I. G. 1973. Ergs. *Sedimentary Geology*, 10, 77-106.
- WINCHESTER, V. & CHAUJAR, R. K. 2002. Lichenometric dating of slope movements, Nant Ffrancon, North Wales. *Geomorphology*, 47, 61-74.
- WINOGRAD, I. J., COPLEN, T. B., LANDWEHR, J. M., RIGGS, A. C., LUDWIG, K. R., SZABO, B. J., KOLESAR, P. T. & REVESZ, K. M. 1992. Continuous 500,000-Year Climate Record from Vein Calcite in Devils Hole, Nevada. *Science*, 258, 255-260.
- WINOGRAD, I. J., LANDWEHR, J. M., COPLEN, T. B., SHARP, W. D., RIGGS, A. C., LUDWIG, K. R. & KOLESAR, P. T. 2006. Devils Hole, Nevada, $\delta^{18}O$ record extended to the mid-Holocene. *Quaternary Research*, 66, 202-212.
- WINTLE, A. G. 1973. Anomalous Fading of Thermo-luminescence in Mineral Samples. *Nature*, 245, 143-144.
- WINTLE, A. G. 1997. Luminescence dating: Laboratory procedures and protocols. *Radiation Measurements*, 27, 769-817.
- WINTLE, A. G. & ADAMIEC, G. 2017. Optically stimulated luminescence signals from quartz: A review. *Radiation Measurements*, 98, 10-33.
- WINTLE, A. G., LANCASTERT, N. & EDWARDS, S. R. 1994. Infrared stimulated luminescence (IRSL) dating of late-Holocene aeolian sands in the Mojave Desert, California, USA. *The Holocene*, 4, 74-78.
- WINTLE, A. G. & MURRAY, A. S. 2006. A review of quartz optically stimulated luminescence characteristics and their relevance in single-aliquot regeneration dating protocols. *Radiation Measurements*, 41, 369-391.
- WONG, C. I., POTTER, G. L., MONTAÑEZ, I. P., OTTO-BLIESNER, B. L., BEHLING, P. & OSTER, J. L. 2016. Evolution of moisture transport to the western U.S. during the last deglaciation. *Geophysical Research Letters*, 43, 3468-3477.
- WOOD, J. 1996. *The Geomorphological Characterisation of Digital Elevation Models*. PhD, University of Leicester.

- WOOD, J. 2009. Chapter 14 Geomorphometry in LandSerf. *In: TOMISLAV, H. & HANNES, I. R. (eds.) Developments in Soil Science*. Elsevier.
- WORMAN, S. L., MURRAY, A. B., LITTLEWOOD, R., ANDREOTTI, B. & CLAUDIN, P. 2013. Modeling emergent large-scale structures of barchan dune fields. *Geology*.
- XIANWAN, L., SEN, L. & JIANYOU, S. 1999. Wind tunnel simulation experiment of mountain dunes. *Journal of Arid Environments*, 42, 49-59.
- XIAO, J., QU, J., YAO, Z., PANG, Y. & ZHANG, K. 2014. Morphology and formation mechanism of sand shadow dunes on the Qinghai-Tibet Plateau. *Journal of Arid Land*, 7, 10-26.
- YANG, Y., QU, Z., SHI, P., LIU, L., ZHANG, G., TANG, Y., HU, X., LV, Y., XIONG, Y., WANG, J., SHEN, L., LV, L. & SUN, S. 2014. Wind regime and sand transport in the corridor between the Badain Jaran and Tengger deserts, central Alxa Plateau, China. *Aeolian Research*, 12, 143-156.
- ZHENG-CAI, Z., ZHI-BAO, D., QING, W. & CHAN-WEN, J. 2015. Wind regimes and aeolian geomorphology in the western and southwestern Tengger Desert, NW China. *Geological Journal*, 50, 707-719.
- ZIMBELMAN, J. R., WILLIAMS, S. H. & TCHAKERIAN, V. P. 1995. Sand Transport Paths In The Mojave Desert, Southwestern United States. *In: TCHAKERIAN, V. P. (ed.) Desert Aeolian processes*. London: Chapman & Hall.

11 Appendix

Chi Square tables showing the significance of any relationship between the land cover classes (Sand Cover, Stone-Covered Sands and Rock Surfaces) and each of the morphometric parameters/features from Section 6.1. Significance was inferred where the Chi Square (χ^2) value was larger than the critical threshold (where $p = 0.01$) and is indicated using a ⁺.

Land cover and elevation:

Land Cover	n	X ²
Sand Cover	115202	19224 ⁺
Stone-Covered Sands	257042	55964 ⁺
Rock Surfaces	559020	27386 ⁺

Land cover and aspect:

Land Cover	n	X ²
Sand Cover	83571	40128 ⁺
Stone-Covered Sands	138273	23680 ⁺
Rock Surfaces	502030	19832 ⁺

Land cover and slope angle:

Land Cover	n	X ²
Sand Cover	115202	8316 ⁺
Stone-Covered Sands	257041	103884 ⁺
Rock Surfaces	559020	63161 ⁺

Land cover and morphometric feature classes:

Land Cover	n	X ²
Sand Cover	115140	5409 ⁺
Stone-Covered Sands	256996	101177 ⁺
Rock Surfaces	559011	57963 ⁺

Land cover and valley orientation:

Land Cover	n	X ²
Sand Cover	1315	577 ⁺
Stone-Covered Sands	1463	192 ⁺
Rock Surfaces	8754	173 ⁺